RICE UNIVERSITY

Tailoring vessel morphology *in vivo*

by

Daniel Joseph Gould

A THESIS SUBMITTED IN PARTIAL FULFILLMENT OF THE REQUIREMENTS FOR THE DEGREE

Doctor of Philosophy

APPROVED, THESIS COMMITTEE

Dr. Mary E Dickinson, Associate Professor,

Department of Molecular Physiology and Biophysics,

Baylor College of Medicine

Dr. Jennifer L West, Isabel C. Cameron

Professor, Chair of Bioengineering

Dr. Peter Y Lwigale, Assistant Professor,

Department of Biochemistry & Cell Biology

Dr. K Jane Grande-Allen, Associate Professor,

Department of Bioengineering

Houston, Texas

September, 2011

Abstract

Tailoring vessel morphology *in vivo*

By

Daniel J Gould

Tissue engineering is a rapidly growing field which seeks to provide alternatives to organ transplantation in order to address the increasing need for transplantable tissues. One huge hurdle in this effort is the provision of thick tissues; this hurdle exists because currently there is no way to provide prevascularized or rapidly vascularizable scaffolds. To design thick, vascularized tissues, scaffolds are needed that can induce vessels which are similar to the microvasculature found in normal tissues. Angiogenic biomaterials are being developed to provide useful scaffolds to address this problem.

In this thesis angiogenic and cell signaling and adhesion factors were incorporated into a biomimetic poly(ethylene glycol) (PEG) hydrogel system. The composition of these hydrogels was precisely tuned to induce the formation of differing vessel morphology. To sensitively measure induced microvascular morphology and to compare it to native microvessels in several tissues, this thesis developed an image-based tool for quantification of scale invariant and classical measures of vessel morphology. The tool displayed great utility in the comparison of native vessels and remodeling vessels in normal tissues. To utilize this tool to tune the vessel response *in vivo*, Flk1::myr-mCherry fluorescently labeled mice were implanted with Platelet Derived Growth Factor-BB (PDGF-BB) and basic Fibroblast

Growth Factor (FGF-2) containing PEG-based hydrogels in a modified mouse corneal angiogenesis assay. Resulting vessels were imaged with confocal microscopy, analyzed with the image based tool created in this thesis to compare morphological differences between treatment groups, and used to create a linear relationship between space filling parameters and dose of growth factor release. Morphological parameters of native mouse tissue vessels were then compared to the linear fit to calculate the dose of growth factors needed to induce vessels similar in morphology to native vessels. Resulting induced vessels did match in morphology to the target vessels. Several other covalently bound signals were then analyzed in the assay and resulting morphology of vessels was compared in several studies which further highlighted the utility of the micropocket assay in conjunction with the image based tool for vessel morphological quantification. Finally, an alternative method to provide rapid vasculature to the constructs, which relied on pre-seeded hydrogels encapsulated endothelial cells was also developed and shown to allow anastamosis between induced host vessels and the implanted construct within 48 hours.

These results indicate great promise in the rational design of synthetic, bioactive hydrogels, which can be used as a platform to study microvascular induction for regenerative medicine and angiogenesis research. Future applications of this research may help to develop therapeutic strategies to ameliorate human disease by replacing organs or correcting vessel morphology in the case of ischemic diseases and cancer.

Thesis Acknowledgements

Firstly and most importantly I would like to thank my thesis mentor and committee. Dr. Dickinson spent timeless hours towards my tutelage and her mentorship and guidance is greatly appreciated. Also Dr. West helped particularly early in my training, graciously allowing me to spend the first six months in her lab, learning the basics of PEG-Based hydrogels. Her lab environment was a great help to me, and the atmosphere is truly fun and inspiring. Also Dr. Grande-Allen has spent many hours with me, and has been helpful in the thesis process, but also as a mentor, and I greatly appreciated the opportunity to teach in her course.

In the MSTP offices at Baylor Kathy Crawford and Vanessa Hatfield provided support and Dr. Sharon Plon has served as a great role model, and a strong advocate for me.

Two teachers have made a lasting impact on me, Joan Valentine, my mentor at UCLA, and Francis Kretzer, my histology professor at Baylor College of Medicine. Frank is the greatest educator I have ever met, a gentle soul with a fantastic sense of humor and cunning wit. He made me better as a student and as a person, turning me on to teaching and mentoring.

I would like to thank my mother, who has listened, and always makes me feel better. My father, Dr. Gould, a mentor, a teacher and a friend. His support throughout my life has helped me to reach for high goals, and I have done so in order to make him proud. My brother Joshua, a true genius has inspired me with his creativity and brilliance. Naomi and Rebecca remind me to be a good person, and help me to learn how to translate my thoughts and interests. Finally, Grandpa Sol, who was a scientist as well who described the first known condition of hyperactivity, with several methods for treatment using cognitive therapy, biofeedback and other techniques. He fostered a sense of awe and exploration in me at a young age. My father made me a physician, my mother made me a teacher and my grandfather made me a scientist. I think about him every day, and his memory is a blessing.

I want to thank my friends, especially Ted Lambert, Max Agnew, David Gibson, and Dr. Lisa Mouzi. They kept me sane, but they also kept me fun, and I know without a doubt I can rely on them.

Funding for this research project came from the American Heart Association, in the form of a predoctoral fellowship, 10PRE4190021.

Finally I would like to thank all the research scientists who helped to bring us to this wonderful age, where engineering human tissues is a reality. This work rests on the shoulders of giants.

TABLE OF CONTENTS

Figures

Tables

1. Background and Significance

The focus of this thesis is the rational design of angiogenic tissue engineering scaffolds which can induce the formation of a microvascular host response. This contribution is critical to the field because recently developed tissue engineering products for use in humans lack microvascularization. These successfully engineered thin tissue components include cartilage, bladder and cornea. The lack of microvascularization limits the types of tissue replacements that can be engineered. In order to better understand the need for microvascularization, a basic discussion on the demand for tissue engineering, an overview of current strategies employed by tissue engineering and some successes and challenges within the field must first be presented.

1.1 Motivation: The Increasing Need for and Cost of Transplantation Fuels Demand for Tissue Engineering

Many disease processes in the United States involve the destruction or damage of organs and tissues. The cause of destruction of these tissues can originate from ischemic insult triggered by cardiovascular disease, infection, auto-immune attack, cancerous invasion, genetic conditions or toxic exposure.

Hundreds of conditions can contribute to the destruction of host organs and ultimately necessitate either assistance of organ function or complete organ transplantation in the host. The most common diseases requiring organ transplant include Polycystic Kidney Disease, Diabetes Mellitus, Chronic Obstructive Pulmonary Disease, Idiopathic Pulmonary Fibrosis, Hypertension, Coronary Heart Disease, Cardiomyopathy, Short Gut Syndrome, Cirrhosis and Hepatitis (Graham 2010). In the US, there are currently over 100,000 people awaiting organ transplantation (figure 1-1). Those awaiting organ transplantation mostly need kidney transplantation or liver transplantation these represent approximately 90% of the people on organ waiting lists. Both liver and kidney tissues are extremely well vascularized, with complex microvascular networks to allow for the diffusion and excretion of waste products and the reabsorption of nutrients and metabolites. There are countless other conditions involving many tissues for which there are no current transplantable methods to alleviate their disease, or to allow recovery of function.

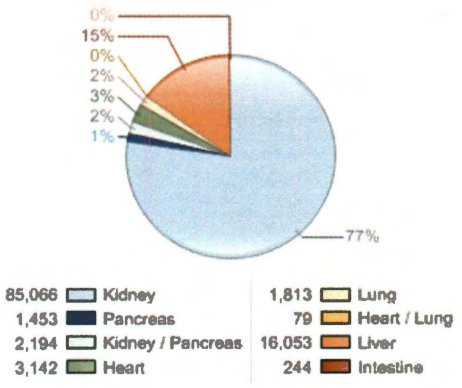

Figure 1-1: Waiting list for transplantation. Current statistics for total number of people on the waiting list for an organ transplant are broken down by organ type (United Network of Organ Sharing, May 2010).

One important consideration of transplantation is the cost associated with this dramatic surgical procedure and the maintenance of the graft for many years

following surgery. Of those awaiting transplantation, around 20% will receive their organ per year, and the cost for organ transplantation in the first year alone will range between $275,000 for a pancreas and $1.1 million for a heart-lung or intestine transplant (Graham 2010). Roughly $200,000 of the total cost for organ transplant comes from procurement and immunosuppressants in the first year, however, over time immunosuppression can contribute an additional $200,000 to the total cost of transplantation (Graham 2010). Furthermore, the process of immunosuppression, though vital to the success of the transplant, can leave the host at risk for numerous infections and the drugs themselves often cause unwanted side effects. One proposed alternative to tissue transplantation is the development of new tissues and organs derived from cells extracted from the host using technology developed in the field of tissue engineering. The argument for this technology is that it will decrease monetary and human costs by eliminating post transplant immunosuppression and the transportation and surgical costs for procurement of donor organs. Also tissue engineering could provide new options for previously untreatable diseases.

Tissue engineering is a relatively new field of research, which may have roots in ancient practices but was best presented in the landmark paper of Langer and Vacanti in 1993 (Langer and Vacanti 1993). Tissue engineering involves the use of three critical ingredients, cells, scaffolding, and cytokines to fabricate tissues as a therapeutic (Langer and Vacanti 1993; Mikos 2006). The goal of this field is to replace damaged tissues and organs, in order to provide a greater pool of resources for those awaiting transplantation, as well as to reduce the costs of organ replacement, by

reducing immunosuppression required (using host cells) and reducing procurement costs. Furthermore, tissue engineering serves to provide new therapeutic solutions for conditions of tissue loss where transplantation is not currently possible. In many disease conditions this new field will help to better the available treatments by contributing vascularized tissue constructs for implantation; this is particularly relevant to many diseases involving a compromised vascular system.

1.2. Limitations of Tissue Engineering: Current Approaches

Tissue engineering has yet to address the issue of *solid, thick tissues,* requiring nutrient delivery over more than 150 microns, which is the transport limit of diffusion for most metabolic substrates (Vacanti; Vacanti, Vacanti et al. 2007). The focus of many labs is to develop *microvascularized tissue engineered constructs*, in order to provide a solution to the diffusion problem, and to ultimately design and develop thick tissues or whole organs to replace damaged tissues (Hoganson, Pryor et al. 2008). This represents a major hurdle to tissue engineering and the fabrication of a microvascularized or rapidly perfused tissue construct is a highly sought after goal (Vacanti, Vacanti et al. 2007). One strategy towards this goal is to develop prevascularized constructs for implantation (Hoganson, Pryor et al. 2008), while other strategies focus on rapid vascular invasion and perfusion (Atala 2006). The main focus of this thesis is to develop rapidly vascularized scaffolds that recreate vascular space-filling properties similar to those found in normal, functional tissues, to provide

adequate perfusion of implanted constructs. In addition to this approach, the prevascularization of implants *in vitro* and then the development of a specialized implantation scheme to stimulate anastomosis with induced host vessels *in vivo* is also achieved, in order to provide proof of principle for an alternative method to overcome the thick tissue hurdle in tissue engineering.

Previous attempts have been made to provide prevascularized tissue engineering scaffolds. These attempts have included the use of mesenchymal stem cells in conjunction with Human Umbilical Vein derived Endothelial Cells (HUVECs- a common source of endothelial cells) to form vessel beds in the cranial window of scid mice (Au, Tam et al. 2008). Also similar attempts have been made with the use of human embryonic stem cells which were differentiated into endothelial cells, then implanted into the scid mouse through a cranial window and likewise showed vascular integration (see figure 1-2) (Wang, Au et al. 2007). Although both of these methods were successful at demonstrating vessel integration in the brain, neither used brain derived endothelial cells, and both

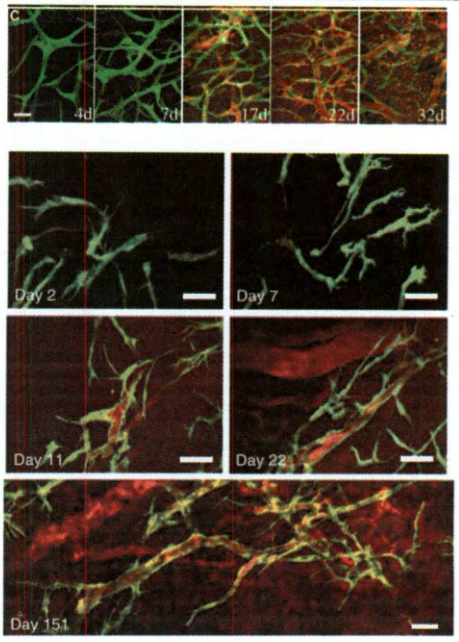

Figure 1-2 : Incorporated Endothelial Constructs. Adapted from Wang et al and Au et al. In the top panels, endothelial cells are labeled with GFP and co-cultured and implanted with bone marrow derived mesenchymal cells. They form robust vascular networks in the scid mouse cranial window, which persist for 140 days. In the five panels below, endothelial cells derived from human embryonic stem cells are labeled green with GFP and are similarly implanted and shown to be perfused at day 11.

created functional vessels in this system, but the monitoring of the mice using a cranial window is complex and requires many precautions and considerations, as the mice have compromised immune systems. A better model would allow for facile monitoring in non-immune compromised mice to determine if vascular networks for tissue engineering applications could stand the test of implantation. In this thesis I have helped develop a model that allows for the *in vivo* study of vascularization in non-immune compromised, fluorescently labeled mice. In order to effectively induce microvascularization of engineered constructs in our laboratory model, a basic understanding of vessel biology is instrumental and will be described in the next section.

1.3. Blood Vessels

1.3.1 Vascular development and basic structure

Most blood vessels consist of tubes of endothelium, surrounded by a muscular layer and an adventitial layer, tube diameters vary based on the distance of vessels from the heart and the function of those vessels.

Smaller vessels contain an intimal endothelial layer, though the medial smooth muscle layer may be attenuated to as few as three smooth muscle cells, or may be replaced entirely by single pericytes (figure 1-3, adapted from (Kovacic 2009)).

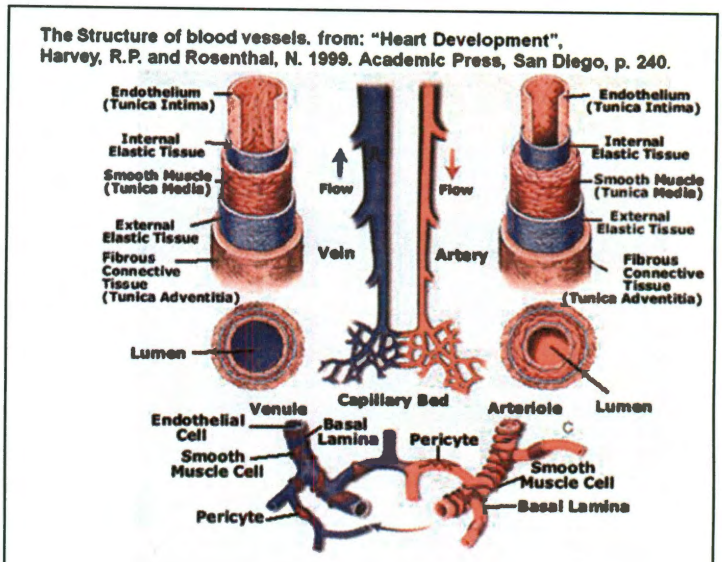

Figure 1-3: The structure of blood vessels, adapted from Kovacic et al, 2009.

Capillaries form immediately from adjacent arterioles in most tissues with the only cell remaining between the capillary and the perfused tissue being the pericyte. Pericytes spread across the capillary to help regulate permeability either through contractile force or direct signaling and help maintain the basement membrane in these regions (Bohnsack 2003; Carmeliet 2005). In several tissues where diffusion is the main function, there are capillaries without high levels of resident pericytes. In all tissues, the pericyte is critical to the stability and function of vessels. One factor known to be responsible for the recruitment of the pericyte is Platelet Derived Growth Factor-BB (PDGF-BB) (Carmeliet 2005), and a schematic of the process of mural cell recruitment is shown in figure 1-4. Vessels require this supportive element and thus, any attempt at formation of a microvasculature *in vivo* should be demonstrated to recruit similar type cells.

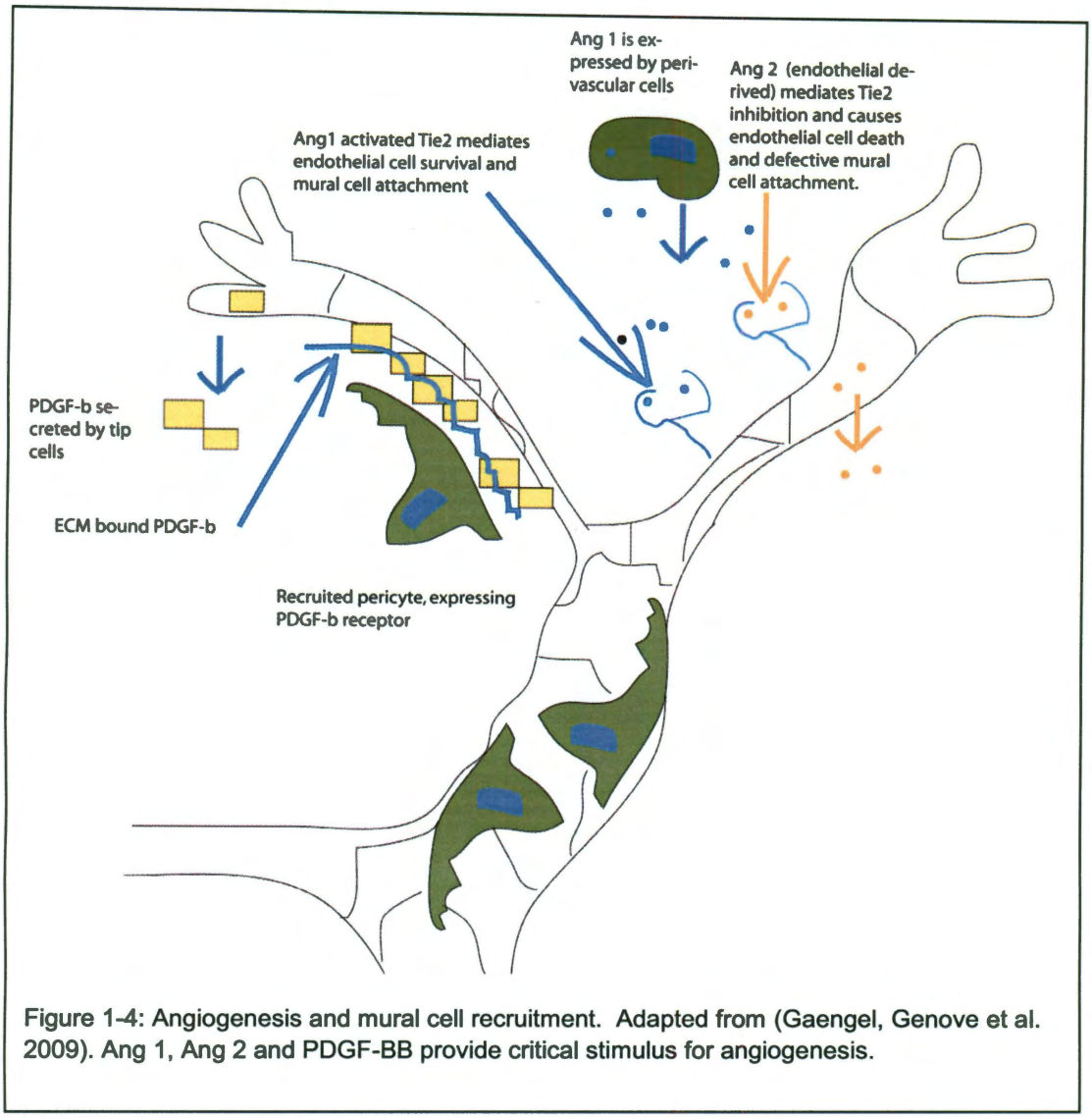

Figure 1-4: Angiogenesis and mural cell recruitment. Adapted from (Gaengel, Genove et al. 2009). Ang 1, Ang 2 and PDGF-BB provide critical stimulus for angiogenesis.

Early in development, vessel formation is dictated by the local development of endothelial cell progenitors into a primitive vessel network. After development of the primitive vessel network, pericytes and other mural cells may be recruited to the vasculature, via signaling through PDGF-BB to aid in the formation of mature microvessels (Carmeliet 2005).

For the purposes of this thesis, special focus will be centered on the microvasculature of tissues. Within developing tissues, molecules like Vascular Endothelial Growth Factor -A (VEGF-A) and Semaphorins dictate the areas of vessel invasion and formation. Some supporting cells secrete diffusible factors like VEGF-A to help recruit endothelial cells, while the endothelial cells secrete diffusible PDGF-BB to help recruit pericytes, which in turn stabilize the vessel networks (Bautch 2009). This process is likely in flux during angiogenesis in tissues. The process of angiogenesis has been widely studied to help treat ischemic diseases through direct administration of angiogenic agents and angioproliferative diseases through the use of angiostatic agents (Carmeliet 2005; Beenken and Mohammadi 2009). A greater understanding of the process of angiogenesis is helpful in the design of vascularized tissue engineering scaffolds.

1.3.2 Angiogenesis

Angiogenesis is directed through the initiation of a response from nearby vessels to some diffusible cytokine, often VEGF-A (Carmeliet 2005; Bautch 2009).

The vessel endothelial cell reacts to the signal and an angiogenic tip cell buds from the vessel. This tip cell migrates towards the chemotactic signal and additional endothelial cells migrate and proliferate to extend towards the signal concentration gradient (Carmeliet 2005). A tubule is formed behind the tip cell from fusing cell vesicles. The tip cell secretes PDGF-BB, which becomes bound to the matrix proteoglycans and diffuses to recruit pericytes, which migrate towards the new vessel tubes (Gaengel, Genove et al. 2009). At the site of the new vessels, endothelial cells secrete Angiopoietin 2 (Ang2) which is a soluble ligand for the tyrosine kinase receptor Tie2 and perivascular cells release Ang1 which activates Tie2 (Gaengel, Genove et al. 2009). Tie-2 mediates endothelial cell survival and mural cell attachment, and thus the recruitment of pericytes is critical to the stability of new vessel beds (Gaengel, Genove et al. 2009). Later, mural cells communicate with endothelial cells through gap junctions to stabilize vessels. Also, other signals from the EGD1-Rac pathway regulate N-

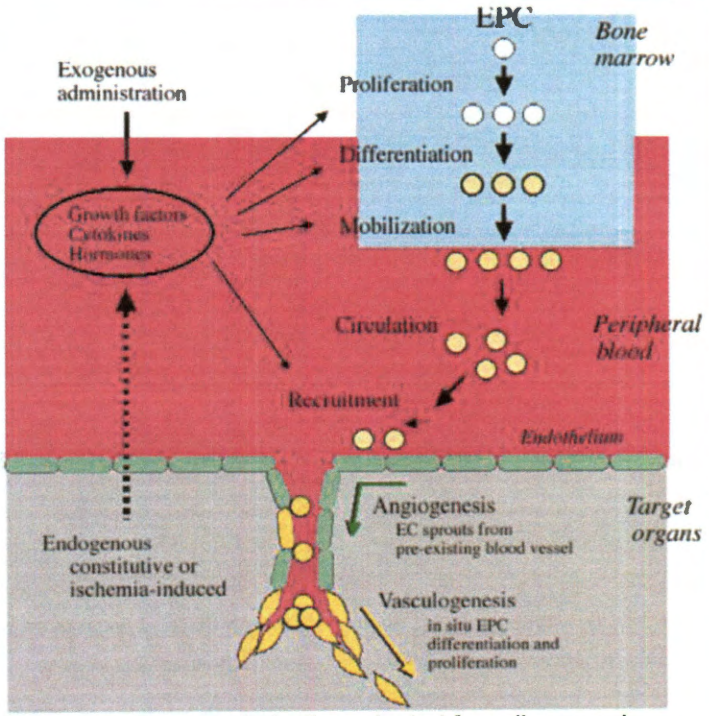

Figure 1-5: Neovascularization adapted from (Isner and Asahara 1999).

Cadherin trafficking and thus mural cell adhesion. Therapeutic neovascularization involves angiogenesis, not only inducing sprouting from existing vessels, but also recruiting endothelial progenitor cells (EPCs) for *in situ* differentiation and proliferation (Isner and Asahara 1999) (figure 1-5).

1.3.3 Growth Factors for Angiogenesis

Two key factors involved in angiogenesis are basic fibroblast growth factor (FGF2) and platelet derived growth factor-BB (PDGF-BB). FGF2 signals through FGF receptors (FGFRs) and regulates many events in development, including mesoderm patterning and organ development (Kimelman and Kirschner 1987; Welm 2002). FGF2 also regulates key physiological functions involved in angiogenesis and wound repair (Turner and Grose). FGFs are glycoproteins, which bind matrix components and heparin sulphate proteoglycans (HPSGs) from the cell surface (Ori, Wilkinson et al. 2008). They are released from matrix by proteases and heparinases to bind the cell surface HSPGs, which stabilize their interactions with their receptors. FGF acts through four conserved tyrosine kinase receptors and one non tyrosine kinase receptor, which may down regulate signaling (figure 1-6) (Wiedemann and Trueb 2000).

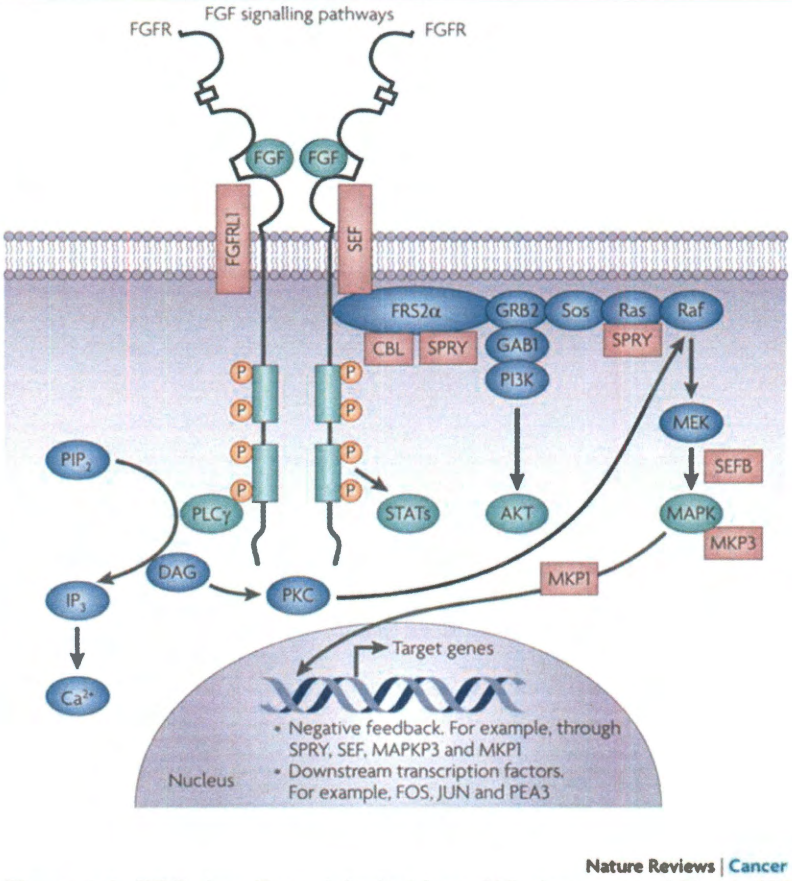

Figure 1-6: FGF signalling. Adapted from (Wiedemann and Trueb 2000). Fgf signaling is involved in many processes in the cell, and can be transduced through the PIP-IP3 cascade, as well as through STATS and through AKT and MAPK pathways.

The receptors exhibit ligand driven dimerization and signaling (Welm 2002), through tyrosine kinase dependent auto phosphorylation of the FGFR intracellular tail, which then serves as a docking site for many adaptor proteins and other signaling proteins which may trigger RAS, RAF, MAPK PI3K and AKT pathways (Wiedemann and Trueb 2000). FGF-2 binds FGFR2 isoform IIIc to initiate vessel formation by stimulating endothelial cell proliferation and vessel stabilization (Werner and Grose 2003) by inducing migration and proliferation of smooth muscle cells (Parsons-Wingerter, Elliott et al. 2000).

This process is selective for small vessels in the arterial tree (Parsons-Wingerter, Elliott et al. 2000). Furthermore, FGF-2 induces production of matrix metalloproteinases (MMPs), secreted by ECs to allow migrating blood vessels to penetrate extracellular matrix (ECM) (Bikfalvi, Klein et al. 1997; Davis 2008). Hypoxia induced FGF-2 production in macrophages regulates expression of key angiogenic molecules, such as collagenases, β1 integrins, and urokinase type plasminogen activator (Werner and Grose 2003). Platelet Derived Growth Factor (PDGF) is chemotactic for wound healing cells in the body. It stimulates fibroblast production of ECM and myofibroblast growth and contraction (Werner and Grose 2003). There are four different monomers of PDGF (A,B,C and D), and the homodimer PDGF-BB signals through the tyrosine kinase receptor PDGFRB with the highest affinity to recruit supporting pericytes and stabilize new vessel formation (Heldin and Westermark 1999). Hypoxia, shear stress, and growth factors induce endothelial cells at the sprouting tip of capillaries to release PDGF-BB (Cao 2003).

PDGF-BB aids in vessel stabilization by stimulating production of extracellular matrix proteins that compose the basement membrane, including fibronectin, collagen, and proteoglycans. PDGF-BB also stimulates secretion of collagenases, key for cell migration (Cao 2003). These factors can be used for therapeutic vascularization. Notably, PDGF-BB has been FDA approved in a recombinant form for the treatment of diabetic and pressure ulcers, and is the only drug FDA approved for chronic wound care (Stephan, Olivera et al. 2008). Furthermore, gene delivery of PDGF-BB with adenovirus has been found effective and is in FDA trials (Margolis, Crombleholme et al. 2000).

Cao et al. demonstrated that PDGF-BB and FGF-2 have a synergistic effect when used in a 4:1 concentration on blood vessel growth and stability (Cao 2004) as compared to the use of each growth factor alone through the use of a corneal micropocket assay *in vivo*. Vessels generated by VEGF-A are more fenestrated and appear less stable and less well organized compared to those generated by FGF-2 (Cao 2003). Although VEGF can induce vascularization of the cornea, new vessels do not persist longer than 70 days (Cao 2003). A more stable network can be formed with the use of PDGF-BB and FGF-2 (Cao 2003) which persists at least 210 days (figure 1-7). Therefore, PDGF-BB and FGF-2 induce more stable vessels by recruiting pericytes to promote formation of vascular networks which persist after the withdrawal of the factors for over a year (Cao 2003). These factors will provide necessary signaling to nearby vessels to trigger stable vessel invasion and perfusion of

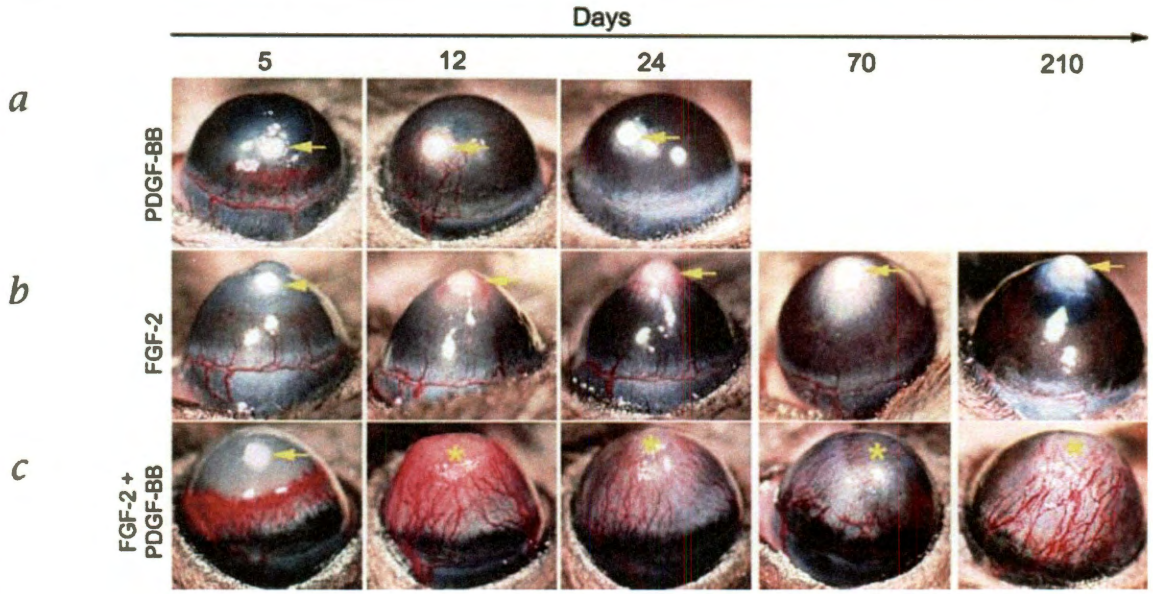

Figure 1-7: Growth Factors for Angiogenesis in the Cornea. Adapted from (Cao 2003). In these experiments, Combinations of PDGF and FGF were shown to generate longer lasting stable vessels than the use of either factor alone in a corneal angiogenesis assay.

implanted tissue constructs. Beyond signaling molecules for angiogenesis, the basic scaffolding material for the tissue scaffolds also needs to carefully be selected.

1.4. Engineering Microvascular Constructs

1.4.1 Poly (ethylene-glycol) (PEG) hydrogels as a model scaffold

Many scaffolds exist for the process of tissue engineering. One category includes natural materials, like collagen, fibrin, alginate and agarose, while another category includes synthetic materials, like poly(dimethyl siloxane) (PDMS), poly(ethylene glycol) (PEG) and poly(ethylene terephthalate)(PET), also known as Dacron (Liu, Xia et al. 2007). Natural materials are desirable because they are known to be biologically compatible, they contain many biological substrates, and they are easily derived and they are generally less expensive to render than synthetics. Some of the limitations of natural materials include the presence of biological infectious agents, chemical pathogens from their decellularization, generalized inconsistency with their composition, immunogenicity in hosts and the inability to tightly control all properties of the scaffold (Liu, Xia et al. 2007). In contrast, synthetic materials are less likely to be biologically contaminated, they are less immunogenic and their composition is more tightly controlled, offering a truly blank slate for scaffold design (Liu, Xia et al. 2007).

In particular, PEG is a useful synthetic material because it is hydrophilic and may be rendered cross-linkable through addition of acrylate chains or other linking agents (Zisch, Lutolf et al.). The hydrophilic nature of PEG hydrogels allows them to resist protein adsorption, rendering them mostly bioinert. This makes them more

biocompatible because they typically do not form granulomatous or highly fibrous capsules when implanted. They are mechanically tunable by varying the molecular weight and the gel weight percentage, so that they can mimic natural stiffnesses within the cellular environment.

The functionalization and crosslinking of PEG may be achieved through reaction of PEG with acryloyl chloride to form PEGDA (figure 1-8). PEGDA then may be reacted with cysteine-bound peptides via a Michaelis addition to generate cell

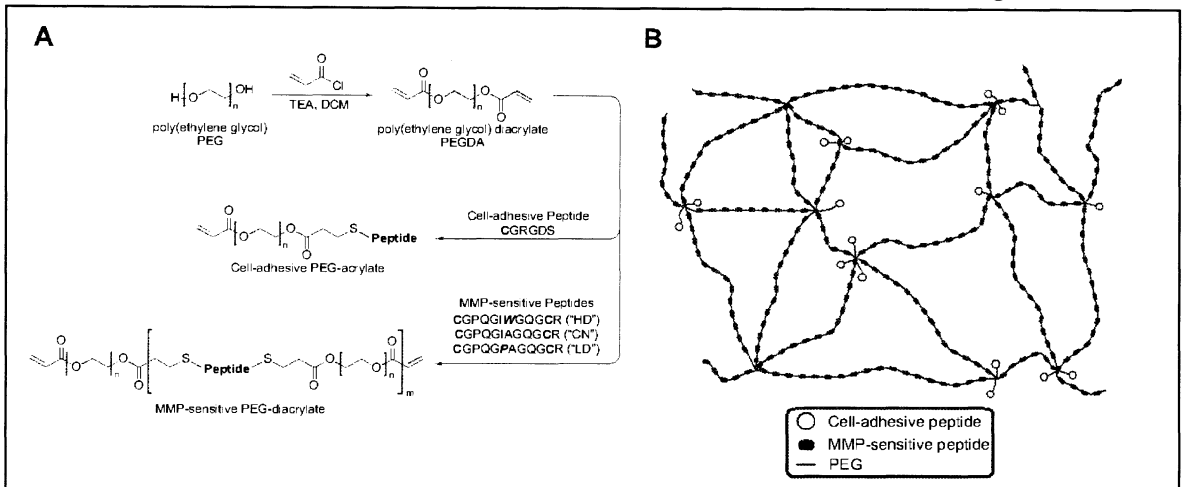

Figure 1-8: PEG functionalization and cross-linking. Adapted from (Miller, Shen et al.).

adhesive (with RGDS), growth stimulating (with PDGF-BB), or MMP-sensitive PEG-acrylate chains. Alternatively, PEG-Succinimidyl Carboxymethyl (PEG-SMC) may be readily conjugated to pre-synthesized cell adhesive peptides (figure 1-9) which may also be commercially purchased (RGDS). Biodegradable hydrogels may be prepared by reacting dissolved GGGPQGIWGQGK (abbreviated PQ), peptide with acryloyl-PEG-SMC to incorporate PQ into the polymer backbone (Lutolf, Lauer-Fields et al. 2003). Ultimately, the resultant chains which have PEG-PQ-PEG can be crosslinked in the presence of the photoinititator 2,2-dimethoxy-2-

phenylacetophenone (acetophenone) dissolved in N-vinylpyrrolidone (NVP) (300 mg/mL), in order to generate a free-radical driven photopolymerization. This step allows for the formation of hydrogels in relatively gentle conditions so that crosslinking can be done in the presence of sensitive growth factors and even **with cells**, to form virtually any shape hydrogel for implantation.

Biomimetic (PEG) hydrogel scaffolds have demonstrated tremendous utility in the design of tissue engineered constructs (Cosgriff-Hernandez, Hahn et al.;

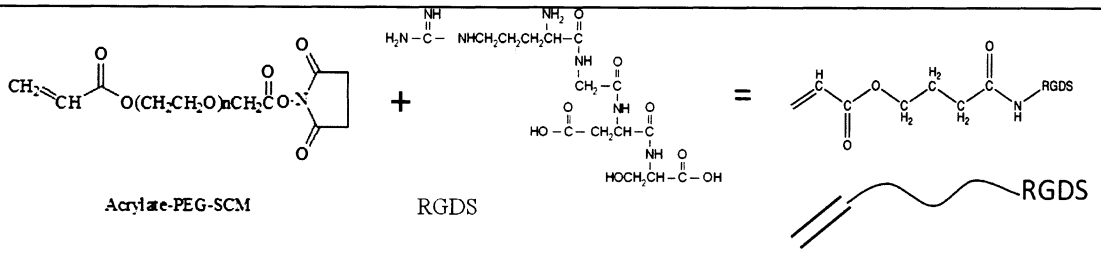

Figure 1-9: PEG SMC conjugation to RGDS

Gonzalez, Gobin et al. 2004; DeLong, Gobin et al. 2005). Modified hydrogels allow for biological activity, through the incorporation of cell adhesion peptides (Zisch, Lutolf et al. 2003) and growth factors (West and Hubbell 1998; Mann, Gobin et al. 2001; Moon, Saik et al. 2010), as well as through incorporation of degradable peptides within the backbone of the polymer (West and Hubbell 1998). Hydrogels sensitive to degradation by MMPs were developed by West and Hubbel in 1998 by synthesis of block co-polymers of PEG and degradable peptides, flanked with acrylate chains which are photopolymerizable (West 2006). Other cell-adhesion molecules which have been functionalized to PEG include YIGSR and IKAVAV, derived from laminin and REDV and KQAGDV from fibronectin (Gonzalez, Gobin et al. 2004). The laminin derivatives may provide promise as they have been shown to stimulate

human mesenchymal stem cell survival and neuronal differentiation *in vitro* (Delcroix, Schiller et al.). Many more cell adhesive signals will likely be developed, based on integrin domains, and will provide greater functionality of the PEG hydrogel system. For this project, degradable PEG-PQ-PEG based hydrogels will be utilized as a scaffold for engineering a niche and studying induced vasculature *in vivo* in a modified mouse corneal micropocket assay.

1.4.2 The Modified Corneal Micropocket Assay: The mouse cornea as an in vivo transplantation site

Kenyon *et al.* pioneered the use of a mouse corneal micropocket assay to show the angiogenic potential of growth factors (Kenyon 1996). The mouse corneal micropocket angiogenic assay is a well- studied model for assaying the activity of pro- or anti-angiogenic factors *in vivo* for several reasons. Importantly, the cornea is avascular in the native state, allowing for the optical clarity needed for vision to take place. The avascular nature of the cornea allows for facile differentiation of angiogenic responses and vascular patterns (Ambati and Sakurai 2006). All vessels present in the cornea after implantation of growth factors can thus be attributed to the growth factors.

To allow for the adequate transmission of light, the cornea must remain avascular, and thus transparent. The undisturbed cornea maintains its avascular nature with several factors, including the soluble inhibitor of VEGF sflt1 (Chang, Gabison et al. 2001; Ambati and Sakurai 2006), pigment epithelium derived factor,

and many tethered anti-matrix metalloproteinases within the corneal stroma (Chang, Gabison et al. 2001). This balance is relatively robust, and in humans, few disease states lead to vascularization of the cornea, including hypoxic conditions (from extended contact lens use) and massive inflammatory conditions, in which a predominant leukocytic response is initiated (Ellenberg, Azar et al.). Anti-angiogenic factors may be overcome with the addition of soluble growth factors, including VEGF and this has been shown by many groups (Kenyon 1996; Rogers 2007). The cornea has proven an acceptable location to study angiogenesis, and has been used in many studies of cancer therapeutics (Streilein 2003) .

Besides being angiogenically privileged, the cornea is also immune privileged (Cursiefen 2007), thus it provides an acceptable niche for implantation of foreign materials and cells (Cursiefen 2007) which might typically trigger an immune response in other implant locations within the host. Previously, cancer cells have been shown to survive and be angiogenic when implanted into the cornea (Kim, Li et al. 1993). This serves as support for the idea that cells may be encapsulated within a scaffold containing diffusible growth factors, then implanted within the cornea and studied without triggering a large immune response. The immune privileged state is actively maintained by the reduced expression of major histocompatability complex (MHC) class I and reduced numbers of immune cells expressing MHC class II (Ellenberg, Azar et al.). Furthermore, an immunosuppressive environment is maintained by the presence of soluble factors such as α-melanocyte-stimulating hormone and vasoactive intestinal polypeptide (Chang, Gabison et al. 2001; Cursiefen

2007). The immune privileged state of the cornea, along with the angiogenic privilege it exhibits provides an environment for *in vivo* studies of tissue constructs, to allow for optimization of angiogenesis and implanted cell survival and differentiation. Several other *in vivo* methods have been developed for implantation of tissue constructs, including the dorsal skin fold apparatus, and intra-abdominal omental implantation, both of which are problematic when assessing neovascularization, because they both contain background vessels.

Previous work performed in the laboratories of both Dickinson and West has served to modify the cornea micropocket assay using PEG hydrogels as a delivery vehicle in an effort to generate tissue constructs (figure 1-10) (Moon, Saik et al.

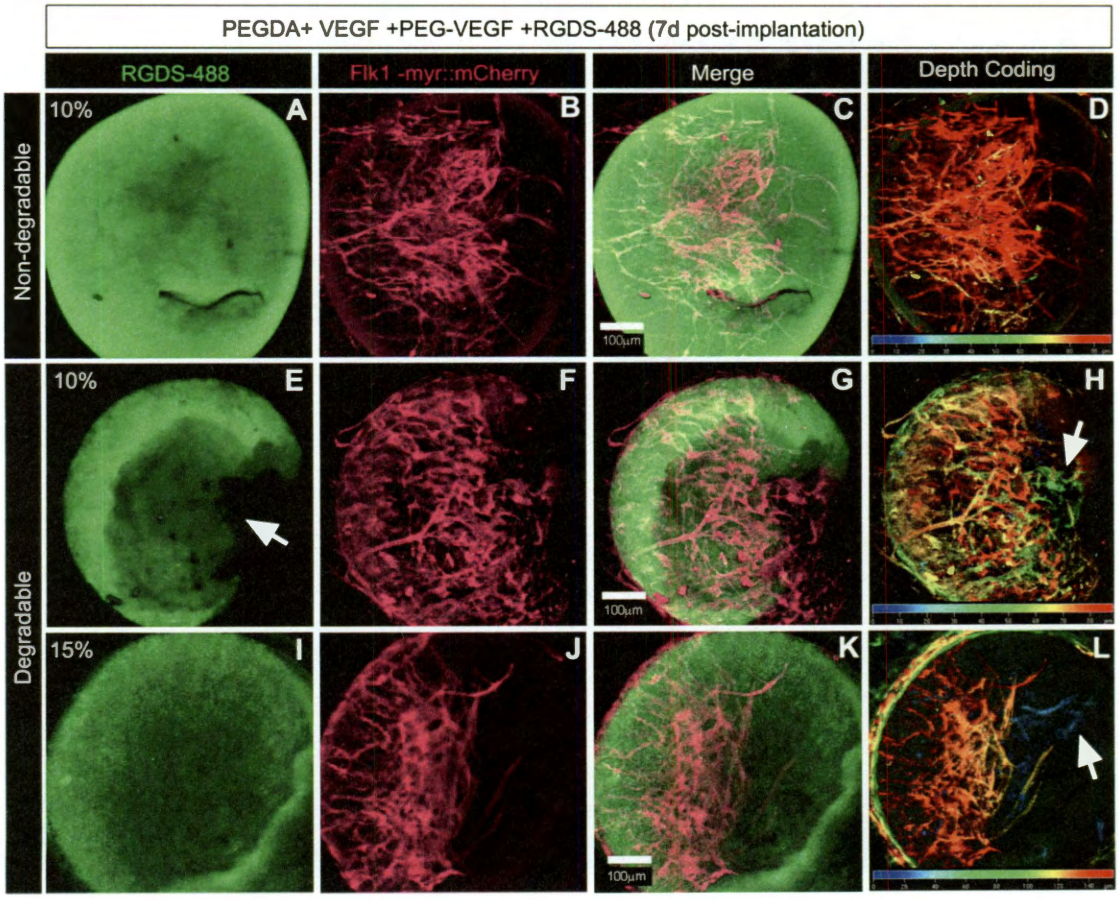

Figure 1-10: This figure demonstrates several implanted hydrogels containing (PQ) degradable sequences in the backbone allow for MMP-mediated degradation by invading vessels(E-L). From Moon et al 2010.

2010). Hydrogels have been rendered degradable by the host *in vivo* through incorporation of matrix metalloproteinase (MMP) sensitive cleavable cross links into the polymer backbone (PEG-GGGPQGIWGQGK-PEG) (West and Hubbell 1998), (Soo-Hong, Jordan et al. 2005; Moon, Saik et al. 2010). Matrix metalloproteinases (MMPs) 2 and 9 are secreted by invading host vessels and degrade the PQ peptide sequence within the backbone of the polymer. *MMPs 2 and 9* are particularly important because they are known to be important in the host angiogenic response and they are found to be secreted by endothelial cells, in response to FGF-2 making degradation into the gel relatively specific (Haas 2005). The typical host response of the cornea to implanted hydrogels lacking growth factors involves a thickening of perilimbic vessels proximal to the implant site (Moon, Saik et al. 2010; Poche, Saik et al. 2010). However, this represents a relatively weak reaction in comparison to the vascularization seen with the inclusion of diffusible angiogenic factors. The vascularization is particularly easy to assess and image, because the mouse used in these studies contains and endothelial bound fluorophore, mCherry, which is expressed via the FLK1 marker with a myristoylation sequence which binds the fluorophore to endothelial cell membranes. This allows for excellent vascular labeling and imaging.

The *in vivo* micropocket assay allows for the study of vascularization of fabricated tissue constructs, and the next step is to define the parameters for the optimization of angiogenesis within this environment.

1.5 Cell Based Methods for Prevascularization

One method to create vascularized constructs involves pre-vascularization of either the recipient site or the construct containing the encapsulated cells with endothelial cells, to ensure rapid anastomosis and perfusion. This has previously been demonstrated *in vivo* using human umbilical vein endothelial cells (HUVECS) with fibroblasts in co-culture, where *in vitro* culture required 7 days and *in vivo* time to perfusion was 5 days (Chen, Aledia et al. 2008). Another suitable line for this application is the brain derived endothelial line (b.end3 or bend cells) (Montesano, Pepper et al. 1990; Omidi, Campbell et al. 2003). These cells are appealing because they are thought to induce a barrier similar to that seen in the blood-brain barrier. This means they can induce a unique vascular bed that will allow for the diffusion of those nutrients needed for survival of neural cells, and they may inhibit the passage of metabolites and other blood soluble factors into the new neural tissue which may be damaging. Bend cells have been studied *in vitro*, and remain viable and proliferate after encapsulation. They also form tubules *in vitro* (Montesano, Pepper et al. 1990) and when encapsulated in PEG-PQ-PEG hydrogels and then grown in culture (Saik and Gould in submission). Although many other cell types have been attempted for implantation to aid vascularization, this project will focus on bend cells for the purpose of developing a rapidly vascularizable construct or scaffold for the delivery of neural stem cells and other cell types.

1.6. Measurement of Vessel Morphology

In this thesis, I induce vessel growth using soluble and tethered growth factors in order to tune the vascular response *in vivo*, providing a robust system for control of angiogenesis for biomaterials and tissue engineering applications. In order to tune the microvasculature, I have developed a quantification method of the vessel response in this thesis. Vessels can be characterized in many ways, and have been in order to study vascular disease, cancer progression and basic physiological properties (Less, Skalak et al. 1991). Vessels induced by growth factors as described above can be categorized similar to the manner proposed by Rogers *et al.* (Rogers 2007) where they applied a subjective grading system to the types of vessels grown into the gel, as well as a slit-lamp measurement of vessel area, calculated by estimating length of vessels and clock hours (radial length). This method is only relevant to characterizing the intensity of vascular response in the cornea. More inclusive and descriptive measurements of vessels for the purposes of mimicking their structure are necessary.

There is vast literature concerning the quantification of vessel morphology, from initial studies of vessel length and diameter to more complex physiological, molecular and higher level structural or super structural analysis (Jain, Schlenger et al. 1997). These include vascular length, surface area, volume, number of vessels in the network, fractal dimensions of the network (Masters 2004), and basement membrane formation (col 4 deposition) (McKay, Gedeon et al. 2008; Gould,

Vadakkan et al. 2010; Yang, Yu et al. 2010; Gould Submitted- In preparation). The classical measures are not scale invariant, and they may change as the focus region or the region of interest of vessels decreases, they do not account for the change in scale seen. Ideally, scale invariant measures of vessel morphology should be determined in order to allow for scale up in design to engineer methods for angiogenesis. Also, any characterization of quantification scheme should incorporate an automated approach, in order to allow for the processing of tremendous numbers of images of the vessels in question. This thesis provides an automated method to examine the scale-invariant space filling parameters of vessels.

1.6.1 Automated methods to measure vessel morphology

Algorithms have been developed in the past to aid segmentation with pattern recognition (W. E. Higgins 1989), model based approaches, tracking approaches, artificial intelligence approaches, neural network based approaches and miscellaneous tube-like object detection (Kirbas C 2004). These methods help to define vascular morphology, but in the case of new biological tools, including membrane-based labels of vessels, the classical measures which require extraction using automated methods fail for several reasons (Kirbas C 2004). The labels are not homogenous which may be due to biological phenomena, and vessel closing algorithms are required to artificially fill in vessel segments and to ignore this information (Gould, Vadakkan et al. 2010). Given the modified micropocket assay is conducted in membrane labeled

Flk1-myr::mCherry mice, classification should take into account the distribution of the fluorophore when characterizing morphology.

One automated program developed to analyze images of vasculature is VESGEN 2D (Mary, Patricia et al. 2009), which determines local vessel diameter, tortuosity, and avascular spacing. It correlates these measures with hierarchical branch organizations. The creators of VESGEN suggest that specific growth factors induce "signature fingerprints" within the morphology of generated vessels, which are *hierarchically dependent (McKay, Gedeon et al. 2008)*. Though generalities can be made about the vessel structures using classical measurements of vessel morphology, including average vessel diameter and branch distance, a more comprehensive measure of global vessel morphology based on **space filling properties** may be helpful in demonstrating subtle differences between tissues. *This is particularly relevant in the case of membrane labeled vessels, in which subtle variations in signal may indicate biologically relevant information.* Furthermore, this algorithm (VESGEN) and classical methods fail to characterize differences seen in engineered vessels, as the vessel structures are not hierarchically ordered and they grow not in developmental context, but in response to inducing growth factors.

1.6.2 Space-filling measures: Vessel Density, Fractal Dimension, Generalized Fractal Dimensions and Lacunarity

The density of vessels occupying a tissue has implications for the exchange of oxygen and nutrients, and this concept is not difficult to relate to many tissues, in

terms of function. Vessel density has been measured in the past, using algorithms which count occupied pixels and divide these by the total number of pixels for a given image size, performing a density calculation (Penn and Gay 1992). This by itself provides information on the amount of space filled by vessels, but the measure is not scale invariant, and therefore it fails to be a good tool for comparison across different tissue beds. In contrast, fractal analysis, which is a scale-invariant measure of how vessels fill space (Masters 2004), in conjunction with lacunarity analysis, which is a scale-invariant measure of the distribution of empty space around vessels, provides for comparison across different vessels in tissue beds (Lopes and Betrouni 2009). In the 1960's the adjective 'fractal' was first used by mathematical Benoit Mandelbrot to describe objects with complex geometry which can only be described by a non-integer dimension using non-euclidean geometry (Mandelbrot 1963; Mandelbrot 1982; Lopes and Betrouni 2009). This means these objects look similar at different scales. In Euclidean geometry, a line is represented as having a dimension of 1, and a box has a dimension of 2, (existing in x and y coordinates), but branching and complex structures exist somewhere in between, with a fractional dimension, hence the term, "fractal". Perfectly formed snowflakes and leaves are fractals, as are patterns created by diffusion limited processes; also regularly branching structures exhibit measurable fractal properties. The underlying process which forms these objects can be determined by the fractal dimension, as is the case in diffusion limited processes (Lopes and Betrouni 2009). In reality, no snowflakes, leaves, or human vessels are truly completely described with a single fractal dimension alone. Subtle

variations in growth or fluctuations during formation affect the morphology of these objects. To better characterize these objects, multifractal analysis which measures generalized fractal dimensions can be applied to determine if an object is a simple monofractal or if there are fluctuations in the underlying self similarity (Lopes and Betrouni 2009). Multifractal analysis can detect these fluctuations and can provide more information about the space an object fills, and might provide insight into the underlying processes which affected the formation or the remodeling of that structure. Lacunarity is a complementary measure of the empty space surrounding objects, and it quantifies the distribution of the empty space surrounding complex objects. Fractal dimension and lacunarity analysis are ideal for quantifying complexity and space-filling in vascular mesh-like or distributory networks. These properties help to robustly differentiate patterns with differing levels of branching and heterogeneity.

Tools in image analysis have recently been developed to help create global characterization schemes for biological systems (Baish and Jain 2000) and include fractal dimension (Mandelbrot 1982), lacunarity analysis (Tolle, McJunkin et al. 2008) and multifractal analysis (Posadas, Gimenez et al. 2001; Gould, Vadakkan et al. 2011). These methods have demonstrated great promise in biological applications, including in the diagnosis of lung cancer (Al-Kadi and Watson 2008), osteoporosis (Zaia, Eleonori et al. 2006) and melanoma (Gilmore, Hofmann-Wellenhof et al. 2009). And more recently they have been applied to segregate pathological retinal angiogenesis (Avakian, Kalina et al. 2002) from normal retinal vasculature (Stosic, Tatijana et al. 2006).

These tools help to assess the space-filling nature of vessels. In images of vessels labeled with dextran, the lumens of these vessels are completely filled and are easy to trace using classical hierarchical methods. The tracing methods break down when applied to membrane-labeled vessels which are now available in biology (either through genetic conjugation of a fluorophore or immunohistochemistry) because of uneven distribution of labels on the vessels. More information can be extracted from the distribution of these labels using space filling methods, instead of hierarchical tracing algorithms. Since the non-homogeneous distribution of labels on vessels may be biologically relevant, space-filling measures may provide more information than classical morphological measures. In this project, these new methods are applied in the automated study of vessels generated within tissue scaffolds providing a new classification tool for vessels. *These methods* have helped aid design of microvascularized constructs for tissue engineering strategies in this thesis. This contribution could be critical to the design of vascularized scaffolds for use in transplantation.

1.7 Thesis Overview

In Conclusion, tissue engineering is a rapidly developing field which promises to create new tissues from stem cells, scaffolds, and biological factors to repair diseased or damaged organs. In order to best repair tissues after damage, replacement angiogenic scaffolds could be best optimized by mimicking normal vascular morphology. The focus of my thesis has been to determine new ways to quantify the microvasculature *in vivo*, and in angiogenic engineered constructs. I applied this method to vessels induced in the modified corneal micropocket assay and found that the vessel response is *tunable* and that it is possible to induce vessels which are similar to those found in native tissues. Finally I have implanted brain derived endothelial cells in a two-step adaptation of the mouse corneal micropocket assay to provide a tool for rapid anastomosis with induced host vessels.

In the following chapters, I describe the primary results of this thesis project. First, I discuss the development of a new image-based tool for the study of scale invariant parameters of vessel morphology. This tool provided critical information about vessels and their response *in vivo* to growth factors, and information which may be utilized in future design, given the scalable nature of the morphology data. Second, I describe the use of this tool in the design of induced vascular beds. Host vessels were induced *in vivo* in a mouse corneal micropocket assay to recapitulate vessels in native host tissues. Third, I used other covalently bound factors to tune vessel induction *in vivo*. Finally I describe a novel implantation scheme to allow for

anastomosis between encapsulated endothelial cells and the host induced vascular response in a corneal micropocket. This thesis serves to provide a platform for the study of anastomosis and perfusion of implanted tissue engineered constructs *in vivo* by providing a protocol for future optimization of angiogenic scaffolds and cell-based therapeutics. This *in vivo* platform may be applied in future studies of native and diseased vessel morphology, angiogenic biomaterials, and implanted cell constructs. Ultimately, this project has contributed to the field of bioengineering by furthering knowledge in these areas, moving towards the goal of implantable tissue engineered constructs.

Chapter 2: *Multifractal and Lacunarity Analysis of Microvascular Morphology and Remodeling*

This chapter is adapted from the article titled "Multifractal and Lacunarity Analysis of Microvascular Morphology and Remodeling" (Gould, Vadakkan et al. 2010) published in the journal *Microcirculation*, available online Feb 6th 2011.

This chapter outlines the adaptation of space filling measures used previously to study vessels along with classical methods to quantify vessel morphology and to characterize microvessels. Furthermore, it adapts the use of a new technique, multifractal analysis, previously used to examine multiscale systems and retinal vessel morphology. The technique is applied to stable vessel beds in skin and muscle, remodeling vasculature and vessels in the neural stem cell niche, the sub ependymal zone (SEZ) in the brain to identify fractal dimension, lacunarity and density of vessels to aid in their future design.

Classical measures of vessel morphology, including diameter and density, have been employed by other research groups to study microvasculature in endothelial membrane labeled mice. These measurements prove sufficient to differentiate vascular beds for some studies; however, they are less well suited for quantifying changes in microcirculatory networks lacking hierarchical structure, like those occurring in the microvasculature in many organs. This study demonstrates that

automated multifractal analysis and lacunarity may be implemented with classical methods like density, vessel diameter and branching to quantify microvascular morphology. Using multifractal analysis and lacunarity, an automated extraction tool with a processing pipeline to characterize 2D representations of 3D microvasculature is presented by this work. The application of this analysis is in images taken from four tissue types and the hyaloid vasculature during remodeling. This study demonstrates that individual vessel networks possess specific multifractal spectra, which serve as 'fingerprints' in that they are each individual and distinguishable. The networks analyzed are shown to be multifractal by this work. Also, when compared, kidney microvasculature has the largest fractal dimension and the lowest lacunarity versus microvasculature networks in the cortex, skin, and thigh muscle. During hyaloid remodeling, there were differences in multifractal spectra reflecting the functional developmental transition from a space filling vasculature which nurtures the lens to a less dense vasculature as it regresses, to permit unobstructed vision. This work shows that multifractal analysis and lacunarity are valuable additions to classical measures of vascular morphology and will have utility in future studies of normal, developing, engineered and pathological tissues.

2.1 Introduction

Vessel morphology in any tissue depends on genetic control during development, remodeling related to hemodynamics and metabolic demand, and

pathological events. Thus, significant changes occur in vessel architecture during vessel remodeling in normal development (Lucitti, Jones et al. 2007; Poché 2009), in response to physiological changes, such as increased oxygenation demands (Bergman and Ullberg 1998), and as a result of pathology as in the case of vessels in tumors (Dajnowiec and Langille 2007). Quantitative analysis of changes in vessel architecture provides a powerful means to assess functional changes (West, Brown et al. 1997; Murray (1926); Kurz (1997)) and to establish prognosis in the case of pathological conditions (Sabo, Boltenko et al. 2001; Lin 2008). Moreover, for tissue engineering applications, it is important to use quantitative methods to describe vessel structures in order to develop truly biomimetic vascularized scaffolds (Hoganson, Pryor et al. 2008; Grayson, Martens et al. 2009). Thus, there has been a great emphasis on defining and developing methods to quantify these important changes in vessel morphology.

Previously developed methods to quantify vessel morphology include the mean diameter of vessels, mean length of vessel segments, branch angle, vessel area density (the fraction of image area occupied by the vessels), and vessel length density (the fraction of image area occupied by the skeleton of the vessels). Moreover, hierarchically branched vessels have been further characterized by more elaborate methods, such as by allocating the branching order to the measures described above (McKay, Gedeon et al. 2008; Yang, Yu et al. 2010). However, such methods are generally applied to vessel trees with clear parent to daughter branch architectures (Stosic, Tatijana et al. 2006). While these measurements are adequate for many

studies, including those of larger vessel segments like the branches of the great arteries and pulmonary vasculature (Horsfield 1978), they are less well suited for quantifying changes in microcirculatory networks that lack hierarchical structure and have a more homogeneous distribution of vessel diameters. Thus, to more aptly describe these networks, more advanced methods that determine the space filling properties of these networks have been implemented.

One measurement of the space filled by an object if density, and vessel density is the simplest expression of how vessels fill a space (Fontanini G 1995; Claudio, Anna et al. 1999; Uzzan, Nicolas et al. 2004) and can be measured from images of vessels by counting the number pixels that contain part of the vessel image and dividing these by the total number of pixels for a given image (Penn and Gay 1992). This value by itself provides information on the amount of space filled by vessels, but the density is not scale invariant, and therefore it fails to be a good tool for comparison across different tissue beds. More recently, fractal analysis has been used to describe the space filling properties of vessels (Masters 2004) and offers an improvement over density, as it is a scale-invariant measure of the space filled by an object. The term 'fractal' was first used by Mandelbrot to describe objects with complex geometry which occupy non-integer dimensions (Mandelbrot 1963; Mandelbrot 1982; Lopes and Betrouni 2009). Fractal objects look similar at different length scales, and in the late 1980s, fractal analysis was used to describe patterns of retinal vessels (Masters 1989). The fractal dimension, D_0 also known as the Hausdorff-Besicovitch dimension is used to describe the fractal properties of a

structure (Mandelbrot 1982) and is most commonly determined with the box counting algorithm (see figure 2.1). For the box counting algorithm, a binary image of an object (where pixels either have a value of 1 or 0) is partitioned into several boxes each of width ε. Then, the number of boxes $N(\varepsilon)$ that contain at least one signal pixel (a pixel with a value equal to 1) is enumerated. The procedure is repeated for different values of ε. The fractal dimension is determined by plotting $\log(N(\varepsilon))$ versus $\log(\varepsilon)$ and determining the slope of the linear region of the plot (Baish and Jain 2000). Thus, the fractal dimension is a single value that reflects the minimum dimension of the space required to embed the object. Numerous studies have applied this analysis to quantify changes in the vasculature (Masters 1989; Parsons-Wingerter, Elliott et al. 2000; Sabo, Boltenko et al. 2001; Stosic, Tatijana et al. 2006; Grayson, Martens et al. 2009; Doubal, MacGillivray et al. 2010).

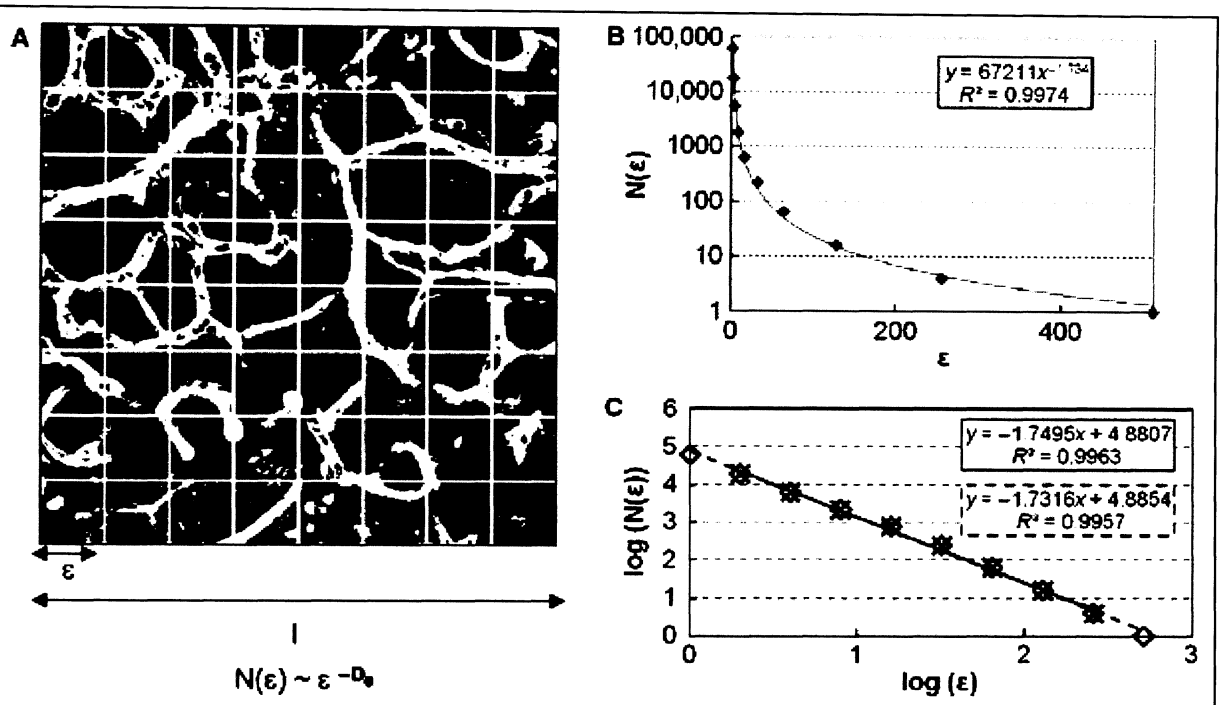

Figure 2.1: Determination of the fractal dimension of an object. A schematic of the box counting algorithm is shown here. Note, the grid has box width ε, and as ε decreases, the total number of boxes N(ε) increases (figure A). In the case of a fractal N(ε) is related to ε by the relation $N(\varepsilon) \sim \varepsilon^{-D_0}$. D_0 is defined as the box counting fractal dimension. Figure B shows the plot of N(ε) vs. ε. The log-log plot is shown in figure C along with the linear fits to the plot. Two equations are shown in the upper right hand corner of figure C. The first one corresponds to the linear fit to all points; the second one corresponds to the linear fit to the data excluding the lowest and highest ε values. The lowest ε value corresponds to the width of the pixel in the image; the largest ε value corresponds to the bounding size of the image. Therefore, it is reasonable to define the linear region of the log-log plot as between the limiting values. The R^2 values in both cases are close to 1. The standard errors of the slopes of the lines based on linear regression are 0.10 and 0.09 respectively. The slopes of the lines are not significantly different. Hence, for this project, all points will be used to calculate the slope of the linear region (fractal dimension).

Although vessels can be considered as fractal structures, two problems arise from using the fractal dimension alone. First, although the fractal dimension describes how much space is filled, this value does not indicate the distribution of that object within the space filled by the object. To address this limitation, Mandelbrot introduced lacunarity to further characterize fractal objects (29). Lacunarity is a parameter that describes the distribution of the sizes of gaps or lacunae surrounding the object within the image. Greater lacunarity reflects a greater size distribution of the lacunae, or said in another way, a higher degree of "gappiness". Lacunarity can be used to distinguish objects with similar fractal dimensions because some objects with the same or similar fractal dimension will fill the space differently (Mandelbrot 1982), but lacunarity can also be used independently as a general tool for describing spatial patterns (Plotnick, Gardner et al. 1996). Lacunarity is routinely measured using a gliding box algorithm (Masters 2004; Tolle, McJunkin et al. 2008). The algorithm is described briefly as follows: an ε x ε box with width ε is placed at the top left corner of an image. The number of signal pixels in the box is counted. The box is then glided one pixel to the right and the number of pixels in the ε x ε box is counted. The process is repeated until the box reaches the bottom right corner of the image. If ℓ is the size of the image, the number of boxes of width ε is $N(\varepsilon) = (\ell - \varepsilon + 1)^2$. The width ε of the box is chosen such that its numerical value is equal to 2,4,8,.., ℓ. For each box width ε, the following two quantities are measured: the sum of the number of signal pixels in each box $Q_1 = \sum_i p(i,\varepsilon)$ and the sum of the square of the number of signal

pixels in each box $Q_2 = \sum_i p(i,\varepsilon)^2$. Lacunarity $L(\varepsilon)$ at a box size ε is defined as $(N(\varepsilon) \times Q_2) / Q_1^2$. The value $p(i,\varepsilon)$ is the number of signal pixels in the i^{th} box and $i \in [\ell, N(\varepsilon)]$. In the gliding box algorithm, the box of size ε is placed over each pixel in the image and $p(i,\varepsilon)$ is calculated for each box centered on the i^{th} pixel. Thus, lacunarity measurement adds significantly to the description of an object with a known fractal dimension because it describes the empty space around the object, and thus it relates how the object fills space.

The second limitation of simple fractal analysis is that it assumes that vessels can be described by a single fractal dimension alone, when in reality, complex structures exist with subsets of regions having different scaling properties. In fact, very few examples exist of structures with perfect monofractal geometries. For example, although theoretical structures with monofractal behavior can be generated, such as Koch's snowflake, numerical models of naturally occurring snowflakes in fact exhibit multifractal behavior (Wolf 1996) because subtle variations in growth or fluctuations during formation affect the geometry of these objects. Also although simple fractal processes were initially proposed to adequately describe the formation of Diffusion Limited Aggregates (DLAs) (Matsushita, Sano et al. 1984; Meakin, Stanley et al. 1985); recently these processes have been shown to be better described using generalized fractal dimensions in a multifractal approach (Lee and Stanley 1988; Block, von Bloh et al. 1990; Vicsek and et al. 1990; Chaudhari, Sanders Yan et al. 2002). Thus, in many cases, multifractal analysis provides more information about the space-filling properties than the fractal dimension (D_0) alone (Lopes and Betrouni

2009). One recent example of the application of multifractal analysis to vessel structures has been in the vessels of the retina. These vessels were first assumed to follow a simple fractal pattern (Masters 1989) but have more recently been shown to be multifractal in nature (Stosic, Tatijana et al. 2006).

One can measure the generalized fractal dimensions in order to construct the multifractal spectra by modifying the box-counting algorithm. The simple box-counting fractal dimension method only quantifies the number of boxes that contain signal pixels, ignoring the density of signal pixels (representing intensity fluctuation) in each box at all box widths (ε). For multifractal analysis, one must consider the density of signal pixels in each box (Chhabra 1989) as shown by Posadas et al. 2003 (Posadas, Gimenez et al. 2003). A detailed description of this analysis is in the Materials and Methods section. The benefit of this multifractal technique was first recognized in its application in geography and polymer chemistry (Milne 1991; Lam 1993; Kats and Kutarov 1996), but very recently it has demonstrated utility in its application to vasculature (Stosic, Tatijana et al. 2006; Doubal, MacGillivray et al. 2010; Grauslund, Green et al. 2010; Sng, Sabanayagam et al. 2010).

Here three new methods are described: fractal analysis, multifractal analysis and lacunarity analysis to characterize microvessels of a transgenic mouse in which a fluorescent protein (mCherry) fused to a myristoylation tag is expressed in endothelial cells under the control of Flk1 promoter elements (Larina 2009). Using an image processing pipeline and automated statistical methods, traditional measures of vessel morphology (diameter, area density) are combined with fractal dimension and

lacunarity as well as with multifractal analysis using images of microcirculatory networks in several different tissues and in the regressing hyaloid vasculature. In this study it was found that indeed all of the vessel networks analyzed have multifractal geometries. Moreover, classical measures alone were found to be insufficient to distinguish differences in microvascular structures from images of different tissues; however, such differences could be detected from comparisons of multifractal spectra and the lacunarity parameter. Finally, multifractal and lacunarity analysis was shown to provide the most sensitive measure of changes in vessel morphology associated with hyaloid vessel regression.

2.2 Materials and Methods

2.2.1 Image Acquisition

Images of Flk1-myr::mCherry labeled vessels were acquired from fixed, sectioned tissues obtained from euthanized Flk1-myr::mCherry transgenic animals in accordance with an IACUC approved animal protocol at Baylor College of Medicine. Confocal images were obtained using an LSM 510 META (Carl Zeiss) confocal microscope and a C-Apochromat 40x/1.2 water immersion lens. A 543 nm laser was used to excite the mCherry fluorophore, and z-stacks of vessels labeled by mCherry were collected. Z-stacks of 17.5 um thick sections of the tissues were collected such

that the step size between two successive images in the z-stacks was 2.5 um. Each 8-bit image in the z-stack consisted of 512 x 512 pixels.

2.2.2. Image Processing

Images of the vascular beds were processed by first converting Zeiss LSM z-stacks to maximum intensity projections using ImageJ software (Rasband 2010). A significant variation in signal intensity was not detected from the top to the bottom of the stack; therefore, no correction was applied along the z-stack before taking the maximum intensity projection. The custom contrast enhancement methods used to threshold the images were chosen such that the weakest signal in the projected image was captured in the thresholded image. Next, projected images were exported to Adobe Photoshop CS2 and the unsharp mask filter with a radius of 12 pixels was applied to improve image quality by intensifying the vascular patterns while decreasing background noise in nearby regions. The unsharp mask is a high-pass filter that removes the low frequency noise component of the image and enhances the high frequency signal component. Finally, images were further processed using a series of MATLAB programs that are freely available from the MATLAB central exchange to threshold and binarize the images so they would be suitable for the designed algorithms (see references). First, 8 bit images were binarized by applying an intensity threshold of 10 (Bemis 2005), and the raw images were overlapped with the thresholded images (Gould 2010). The intensity value that gave the best overlap, such

that the original vessel structures were preserved while the background noise was diminished, was chosen as the threshold; uniformly this value was 10 in the case of the images in this study. Figure 2.2 summarizes the image processing steps. Therefore, after the threshold was applied, the image was binarized such that all pixels with a value above 10 were designated as a value of one (referred to as signal pixels) and all those below were designated as zero (referred to as empty pixels). Several other MATLAB programs were then used to determine the vessel density, lacunarity, fractal dimension and multifractal spectrum of the binary images of blood vessels (Moisy 2006; Vadakkan 2009; Vadakkan 2009). Figure 2.2 A is the projection image of a 17.5 micron thick stack of images from a section of the cerebral cortex vasculature of a Flk1-myr::mCherry mouse expressing the fluorescent protein mCherry in the vasculature. The pre-processing steps consisted of applying an unsharp mask filter to improve image quality (figure 2.2 C) and then applying an intensity threshold to binarize the grayscale image. Note that the binarized image (figure 2.2 D) has gaps (black pixels) within the vessel surface (white pixels). These gaps in the surface markers represent an example of intensity variation inherent in any membrane based label. Morphological closing algorithms (Eddins 2007) may serve to fill the gaps; however, because this intensity variation is likely to be biologically relevant as little manipulation as possible of these images provides the clearest picture of true vessel morphology. The finalized processed image was overlapped with the original image to demonstrate preservation of vessel diameters (2.2E). Furthermore, the vessel diameters were measured in the two images and histograms were compared

to identify the distribution of vessel diameters and to compare the original and processed image, in order to demonstrate that the processing step did not change the vessel diameters significantly (2.2F, 2.2G).

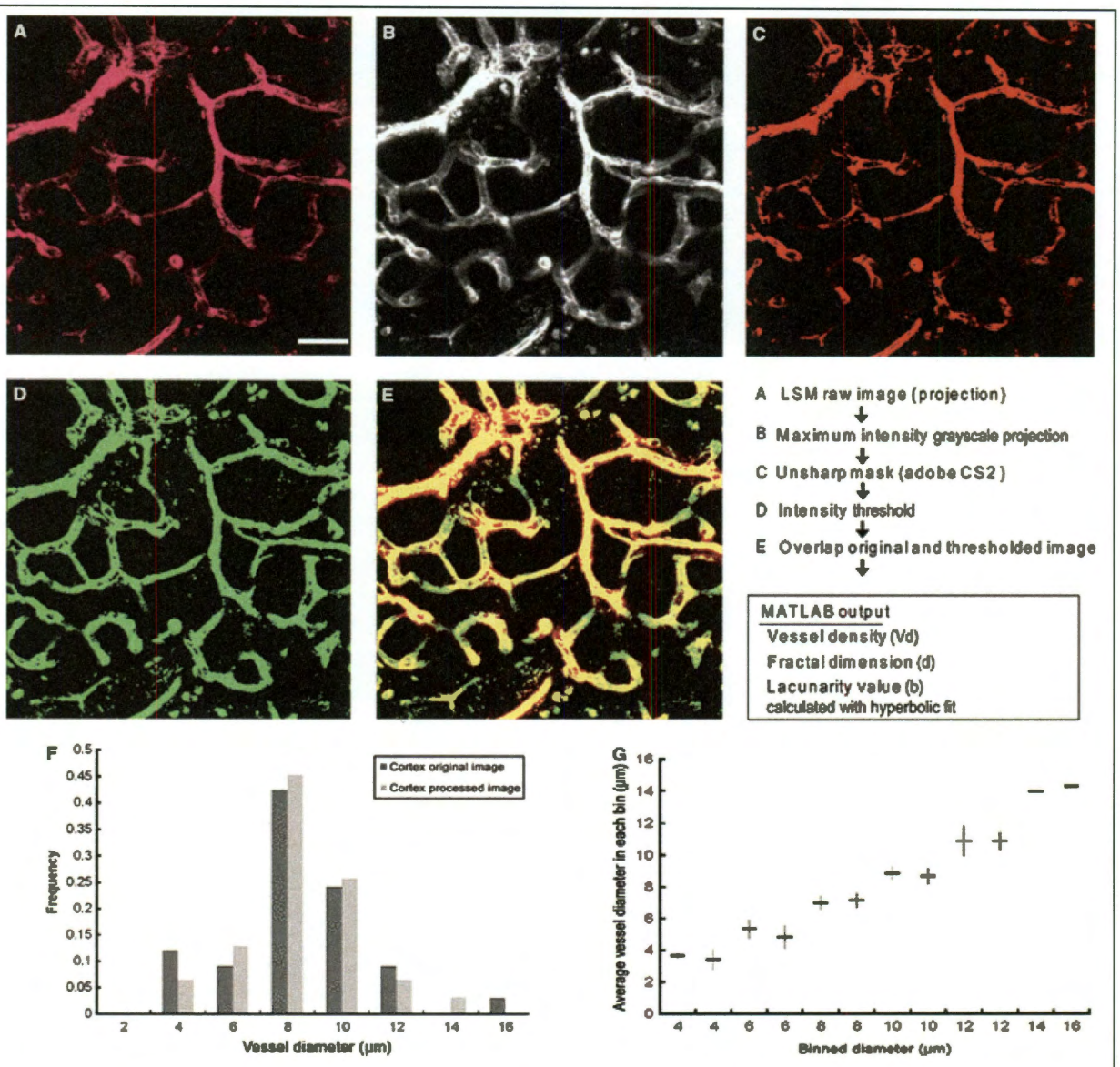

Figure 2.2: A flow chart of image contrast enhancement. Figure A is the maximum intensity projection image of a 17.5 um thick confocal z-stack of cortex vasculature at post natal day 6 (P6). The vessels are tagged by the fluorescent marker mCherry. Figure B is the grayscale image obtained by maximum intensity projection of the z-stack used in figure A. Figure C was obtained from figure B by applying an unsharp mask filter (radius 12). Figure D is the binary image obtained from figure C by applying an intensity threshold of 10 using a MATLAB program (Bemis 2005). The original image in figure A is then overlapped with the image in figure D to check whether the thresholded image is a good representation of the original image. Regions in yellow show the overlap between the two images (figures A and D) in figure E. Importantly the vessel diameters from the original and the processed images do not differ significantly thus the processing steps preserve critical information about the original vessel beds for analysis and comparison. The similarities in the histograms of the vessels (figure F) and the similarities of the average vessel diameters within each bin (figure G) support this observation. Note the gaps on the vessel surface due to thresholding. Vessel density, box counting dimension, and lacunarity obtained by applying the set of operations mentioned above are listed in table 2.1. Scale bar = 50 micrometers.

2.2.3. Vessel Morphology Analysis

After processing the images to ensure retention of key biological features, the binary images were then subjected to several algorithms to determine the fractal dimension, lacunarity and multifractal spectra. These methods are briefly described below.

2.2.4. Box Counting Fractal Dimension (D_0)

The fractal dimension was measured by overlaying a binary image of a vascular system with a grid of boxes and counting the number of boxes, $N(\varepsilon)$, that contain at least one signal pixel (Baish and Jain 2000). The fractal dimension (D_0) was determined from the slope of the linear region in the log-log plot of $N(\varepsilon)$ versus ε and is sometimes referred to as the capacity dimension. The number of boxes at given box width ε was assumed to scale with the box width as $N(\varepsilon) \sim \varepsilon^{-D0}$. The numerical values of the widths of the boxes used are 1, 2, 4, 8, …, 512 (maximum number of pixels) (see Figure 2.1). Although these box widths were chosen so that all length scales are represented, data points corresponding to a box width of a single pixel and the maximum width of pixels were eliminated in a second calculation to exclude an effect from noise or finite size effect (Figure 2.1, dashed box) and showed no significant difference. In fact the fractal dimension for the middle range of values only (4, 8, … and 64 pixels) was also determined and was found to be no different

from the data presented in Figure 2.1 (data not shown). The similar values for the slope were expected because vessel diameters ranged from 4 to 16 um, corresponding to box width sizes of 8-32 pixels, and the middle region represented that range of box sizes. For the experimental images all length scales are included since some continuous vessel segments span nearly the width of the field of view. However, it was confirmed that the data were not influenced by noise or finite size effect for each data set by comparing the slope over the entire range with the slope obtained from the middle set of values (4-64 pixels).

Fractal analysis required binarized images and considered boxes as positive (containing at least one signal pixel) or negative (containing no signal pixels). In images of membrane labeled vessels because the number of signal pixels is different from one box to another for any given box width (figure 2.1) simple box counting analysis is insufficient to fully characterize these complex vessel structures. In order to address this issue a multifractal method was developed and employed and will be described in a later section. It is important to note that the use of erosion or skeletonization methods was avoided in order to maintain intensity variations which could likely be biologically relevant. In this study the measurement of the box counting fractal dimension D_0 is performed using a MATLAB program available free online through the MATLAB central database (Moisy 2006).

2.2.5. Lacunarity

The fractal analysis allows for the determination of the dimension of the images, but in order to determine an independent measure of how the vessels in these images are distributed in space, lacunarity analysis provides the best parameter. Lacunarity was measured using a custom MATLAB program (Vadakkan 2009) based on the gliding box algorithm (Tolle, McJunkin et al. 2008). The lacunarity at a box size ε was defined as $L(\varepsilon) = (N(\varepsilon) \times Q_2) / Q_1^2$. $Q_1 = \sum_i p(i,\varepsilon)$ and the sum of the square of the number of signal pixels in each box $Q_2 = \sum_i p(i,\varepsilon)^2$. In the vascular patterns analyzed, the lacunarity function $L(\varepsilon)$ resembled a hyperbola; therefore, the lacunarity function was fitted with the hyperbolic function, $L(\varepsilon) = b / \varepsilon^a + c$ (Zaia, Eleonori et al. 2006) in which b (referred to as the lacunarity parameter) is related to the concavity of the hyperbola. A low b value defines a hyperbola with wide concavity (high lacunarity); meaning that a low b value describes an object with a high distribution of empty gaps throughout, or a high level of "gappiness". For fractal patterns, the lacunarity plot is a straight line on a log-log graph. Taking the logarithm of the hyperbolic function $L(\varepsilon) = b/\varepsilon^a + c$ the out put is $\ln(L(\varepsilon)-c) = \ln(b) - a \ln(\varepsilon)$, which is the equation of a straight line. The linear relationship justifies the choice of the hyperbolic function. The use of the hyperbolic function is further supported by the R^2 values obtained from the fitting of the function to the data points.

2.2.6. Generalized Fractal Dimensions and Multifractal Analysis

Lacunarity in conjunction with fractal dimension can provide information on how much space is filled by an object and how it is distributed within space, but they only provide discrete parameters that are not continuous over a range of dimensions. Multifractal analysis provides information on how an object fills space, but also provides information about how the entropy within an image changes as a function of the scale used to investigate it, as well as how the scale affects similarity or correlation within the image. Furthermore, Multifractal analysis yields a continuous spectrum representing the amount of space filled by the object, as well as the distribution of that object within space and allows for greater comparison of like objects, by providing useful shape features of the curve of the spectra, including symmetry and heterogeneity features which can be used to distinguish similar objects. Here, we seek to determine the generalized fractal dimensions of the vascular structures in order to determine if they are, indeed, multifractal. Multifractal analysis takes intensity variations like those seen in membrane labeled vessels (figure 2.2) into account by measuring pixel density within a box (Posadas, Gimenez et al. 2003).

Pixel Density

Pixel density in any given box is defined as the number of signal pixels in that box divided by the number of signal pixels in the entire image. A signal pixel in a

binary image is defined as a pixel whose intensity is 1 after thresholding to form a binary image. In a binary image, the number of signal pixels / (the number of signal pixels + empty pixels (total Pixels)) is defined as the pixel density.

Generalized Fractal Dimensions

The generalized fractal dimensions are defined through the scaling relation $\sum_i [P_i(\varepsilon)]^q \sim \varepsilon^{\tau(q)}$, where $\tau(q) = (q-1) D_q$, $q \in (-\infty, +\infty)$, and $i \in [1, N(\varepsilon)]$ (Posadas, Gimenez et al. 2003). The numerical values of D_q corresponding to different values of q are the generalized fractal dimensions of a structure. For a simple fractal (also called a monofractal structure), D_q is independent of the value of q. D_0, D_1, and D_2, are called respectively, the box counting dimension (also capacity dimension), the entropy dimension, and the correlation dimension. D_0, D_1, and D_2 are related by the inequality $D_0 \geq D_1 \geq D_2$ in the case of a multifractal. Conversely, the equality holds in the case of a simple fractal. A vascular structure is considered a multifractal structure only if there is a statistically significant difference between D_0, D_1, and D_2.

A description of the generalized fractal dimensions in a manner similar to the box counting dimension is made by changing the variables from (q, τ) to (α, f) such that $\alpha = \partial\tau / \partial q$ and $f(\alpha) = \alpha q - \tau$. This transformation, called a Legendre transformation (Frisch and Vergassola, 1991, (Meneveau and Sreenivasan 1991) has been used before to relate the D(q) spectrum to the f(α) spectrum (Stosic, Tatijana et al. 2006).

The number of boxes $N(\alpha)$ for which the probability $P_i(\varepsilon)$ has exponents between α and $\alpha + d\alpha$ scales as $\varepsilon^{-f(\alpha)}$. Thus, $f(\alpha)$ is the fractal dimension of the set of boxes for which the exponent is α. *The plot of $f(\alpha)$ against $\alpha(q)$ is referred to as the multifractal spectrum* in this and other papers (Posadas, Gimenez et al. 2003; Stosic, Tatijana et al. 2006). The comparison of these spectra in a multifractal analysis as defined by Chhabra and Jensen (Chhabra 1989) is described later in this work.

Measuring Generalized Dimensions and Generating a Multifractal Spectrum

To measure the generalized fractal dimensions of a binary image, the binary image is overlaid with $N(\varepsilon)$ boxes each of width ε. Associated with each box of index i is a measure $P_i(\varepsilon)$, which is defined as the number of signal pixels in the i^{th} box of width ε divided by the total number of signal pixels in the image (pixel density). Determining q with respect to $P_i(\varepsilon)$ is given by the equation given below.

$$\mu_i(q,\varepsilon) = [P_i(\varepsilon)]^q / \sum_i [P_i(\varepsilon)]^q \qquad (1)$$

$\mu_i(q,\varepsilon) \in [0,1]$ for each value of q. In this case, we used q ranges from -2 to +2 in steps of 0.1. Also, $\sum_i [P_i(\varepsilon)]^q \sim \varepsilon^{\tau(q)}$. Importantly, the value of $\tau(q)$ is determined by taking the slope of $\log(\sum_i [P_i(\varepsilon)]^q)$ versus $\log(\varepsilon)$.

$f(q)$ and $\alpha(q)$ are determined using the following two equations:

$$f(q) = \lim_{\varepsilon \to 0} [\{ \sum_i \mu_i(q,\varepsilon) \log(\mu_i(q,\varepsilon)) \} / \log \varepsilon] \qquad (2)$$

$$\alpha(q) = \lim_{\varepsilon \to 0} [\{ \sum_i \mu_i(q,\varepsilon) \log(P_i(\varepsilon)) \} / \log \varepsilon] \qquad (3)$$

The functions f(q) and $\alpha(q)$ (equations 2 and 3) represent the moments of the distribution P_i. The values of these functions for each of the values of q allow us to construct the multifractal spectrum. Equations 2 and 3 can thus be used to determine $f(\alpha)$ for each $\alpha(q)$ (Posadas, Gimenez et al. 2003). The multifractal spectrum is the f (α) - α curve defined by the equation given below.

$$f(\alpha) = \alpha q - \tau(q).$$

A flowchart depicting the construction of the multifractal spectra is included in figure 2.3. A program written for this project in MATLAB was used to calculate the functions f(q) and $\alpha(q)$ using the equations above (available online, see references). Figure 2.3 demonstrates this analysis on one of the images of the retinal vessels depicted later, in 2.6 D. The image of retinal vessels is first overlaid with a grid and q is determined as described above. Then, $\tau(q)$ is measured for each value of q, given that $\tau(q)$ is the slope of $\log(\sum_i [P_i(\varepsilon)]^q)$ versus $\log(\varepsilon)$. For each ε, equations 1, 2, and 3 are calculated for all values of q. $\tau(q)$ is then plotted versus q for each value of q (figure 2.3 A). The equation used to estimate $\tau(q)$ is shown in the text within the box. Two lines have been drawn upon the figure A to illustrate the change in slope in the $\tau(q)$ spectrum (arrowheads). This change in slope is a characteristic of a multifractal. Figure B shows the plots of f(q) and $\alpha(q)$. f(q) is the slope of the line obtained by plotting $(\sum_i \mu_i(q,\varepsilon) \log(\mu_i(q,\varepsilon)))$ against $\log \varepsilon$. $\alpha(q)$ is the slope of the line obtained by plotting $(\sum_i \mu_i(q,\varepsilon) \log(P_i(\varepsilon)))$ against $\log \varepsilon$. The equations used to calculate f(q) and

$\alpha(q)$ are shown in the Figure B. Finally the multifractal spectrum is determined an plotted as the multifractal spectrum is the f (α) - α curve defined by the equation f (α) = αq - $\tau(q)$. Figure C is the multifractal spectrum of the image of vessels in figure 2.6 D.

By construction, $\mu_i(q,\varepsilon) \in [0,1]$ for each value of q. In this set of experiments, for each value of q, linear fits to the plots of numerators versus denominators in the above equations were used to calculate f(q) and $\alpha(q)$. All q values in the range from -2 to +2 were used to calculate f(q) and $\alpha(q)$. The q values were increased in steps of 0.1 (Posadas, Gimenez et al. 2003; Stosic, Tatijana et al. 2006). The linearity of fits was assessed using R^2 values. The multifractal spectra of the

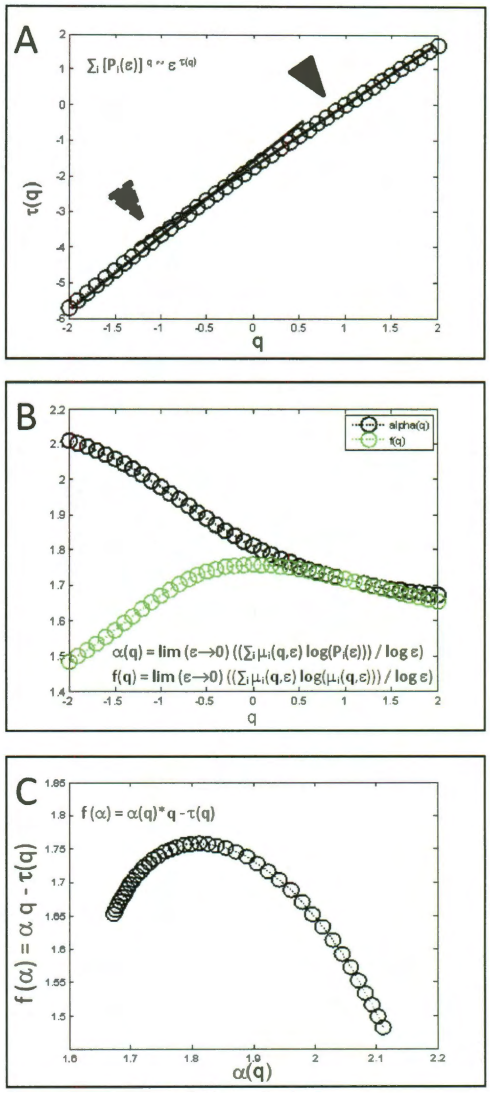

Figure 2.3: Work flow in the multifractal analysis. The image of the retinal vessel in figure 2.6 D is used to demonstrate the multifractal analysis step by step. First, $\tau(q)$ is measured for each value of q. For each ε, equations 1, 2, and 3 are calculated for all values of q. $\tau(q)$ is the slope of $\log(\sum_i [P_i(\varepsilon)]^q)$ versus $\log(\varepsilon)$. Figure A shows the plot of $\tau(q)$ versus q. The equation used to estimate $\tau(q)$ is shown in the text within the box. Two lines have been drawn upon the figure A to illustrate the change in slope in the $\tau(q)$ spectrum (arrowheads). Such a change in slope is a characteristic of a multifractal. Figure B shows the plots of f(q) and $\alpha(q)$. f(q) is the slope of the line obtained by plotting $(\sum_i \mu_i(q,\varepsilon) \log(\mu_i(q,\varepsilon)))$ against $\log \varepsilon$. $\alpha(q)$ is the slope of the line obtained by plotting $(\sum_i \mu_i(q,\varepsilon) \log(P_i(\varepsilon)))$ against $\log \varepsilon$. The equations used to calculate f(q) and $\alpha(q)$ are shown in the Figure B. Figure C is the multifractal spectrum of the image in figure 2.6 D. The multifractal spectrum is the f (α) - α curve defined by the equation f (α) = αq - $\tau(q)$.

binary images were obtained by plotting f(α) against α(q); only α(q) values with an R^2 value above 0.95 were considered for plotting and comparison.

In conducting the multifractal analysis, and in all of the measurements, 2D projections from 3D z-stacks were used. To understand if the process of projection changed our measurements, the analysis on each slice from the z stack was conducted and then compared the average values for each parameter to the projection image values (figure 2.4). There were slight, but insignificant, differences between the slice averages and the projection values for vessel density, fractal dimension and lacunarity

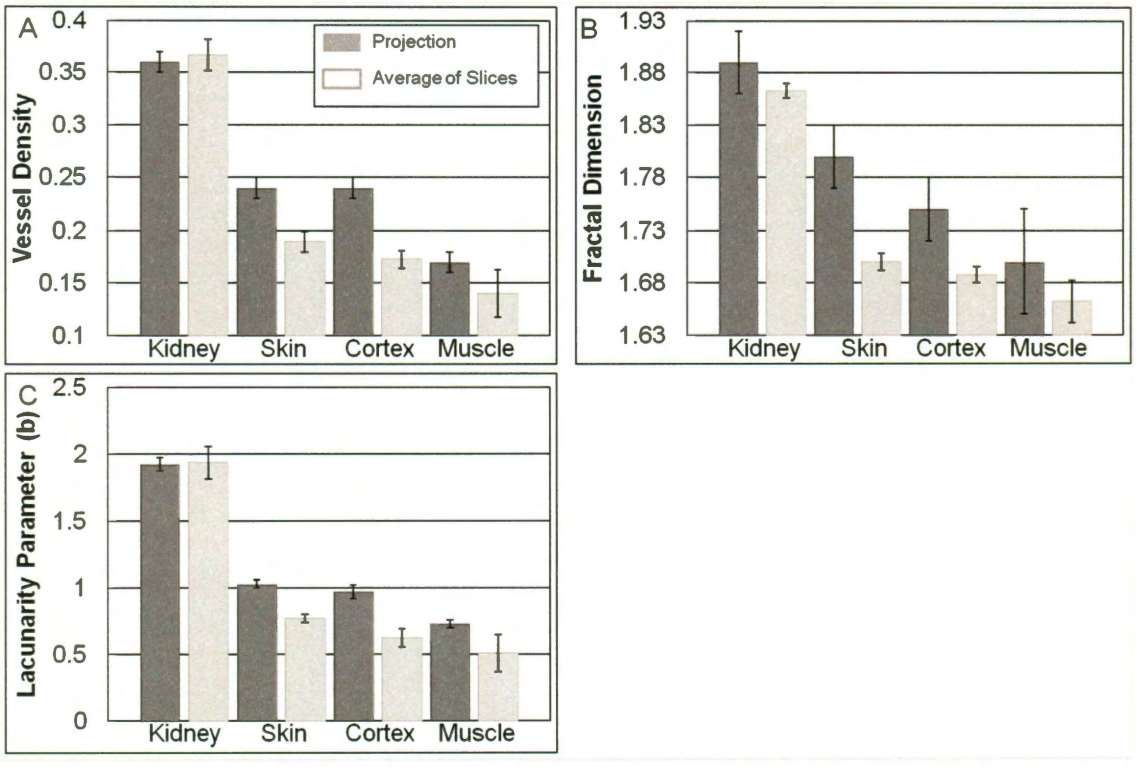

Figure 2.4: Comparison of slice-by-slice means versus projection means. The vessel density, fractal dimension and lacunarity were measured as described in the manuscript for each image in the z-stack (figure A). Next the average values and the standard deviations of vessel density, fractal dimension and lacunarity were calculated. The mean values obtained from slice-by-slice analysis of the z-stack are plotted alongside the mean values obtained from projection images of vessels (figures A-C). Similar trends in the morphological parameters are seen between the two groups. Thus for the vessel images used in this manuscript, projection analysis is similar to the slice by slice analysis in detecting trends between the vessel images.

for each tissue type. Importantly, the trends were preserved between tissue types, and the values increased as predicted in the projection cases.

The multifractal analysis was compared in similar fashion (figure 2.5). The overlap between the spectra of each slice and the projected spectra again showed that the trends between tissue types were preserved as well.

The methods described above were demonstrated to be robust in analysis of images of vessels from different tissues. The results of the application of these tools to images of vessel beds are described below.

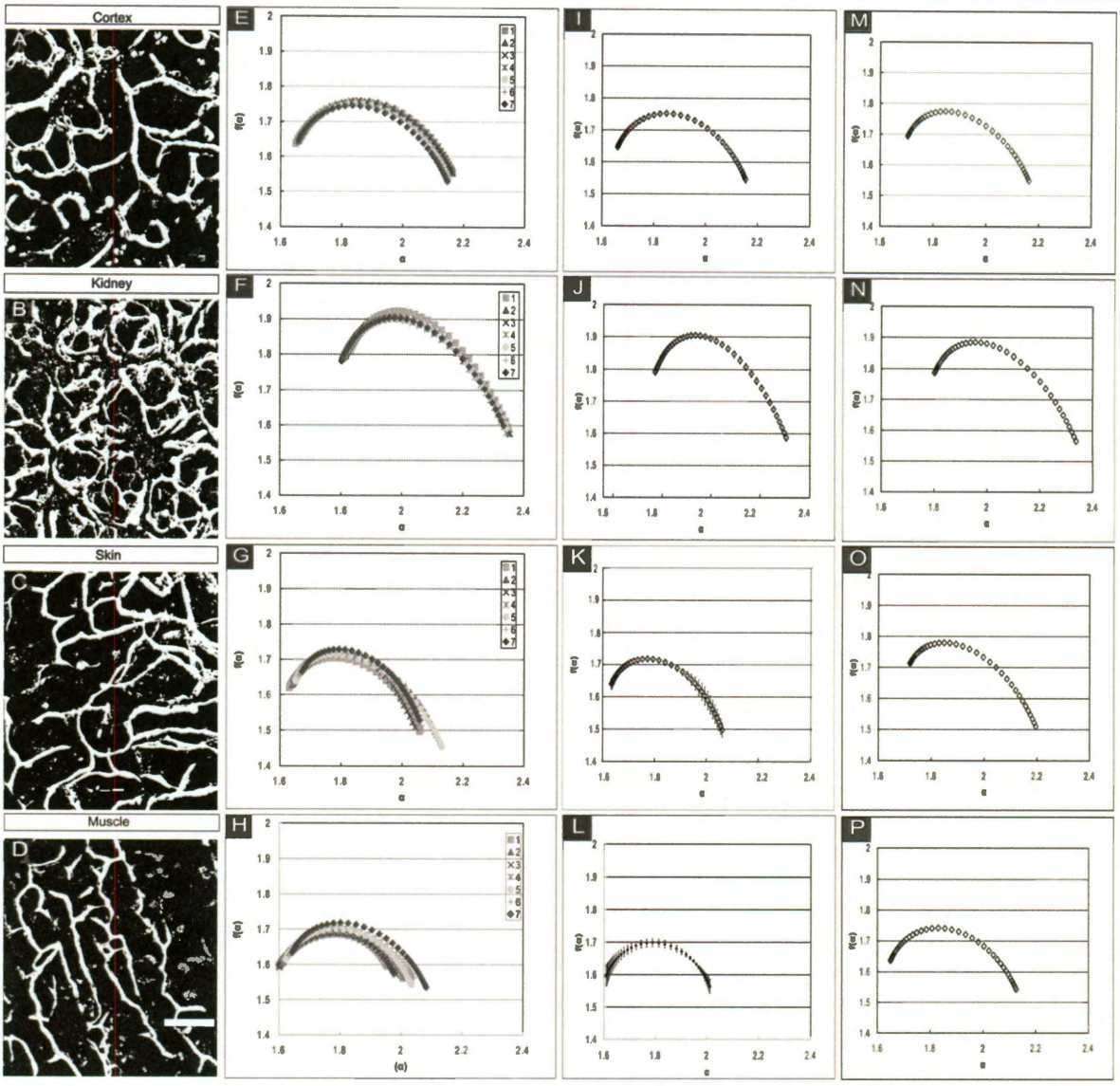

Figure 2.5: Validation of the use of two dimensional projections via comparison of multifractal analysis applied to projection images and to slice by slice analysis. Here, the individual images comprising the z-stacks for all of the tissue beds were each individually subjected to multifractal analysis. This figure summarizes the raw data for each of the seven images comprising the stacks in the column labeled E-H. I-L shows the average value of the points on the various multifractal spectra derived from each individual slice. Because the raw data appeared relatively similar, this average was plotted with error bars representing the standard deviation at each value of f(α) for α. In the final column labeled M-P, the multifractal spectra for the projected images are shown for comparison to the average values. The trends between I-L and between M-P are similar and both reflect changing generalized fractal dimensions between vessel beds. In the vascular beds discussed in this paper, the thickness of the z-stacks of the tissue was 17.5 micrometers. If the z-stacks were much thicker, then the projected image of the vessels could overlap and would be measured as occupying more space (due to a contribution from vessel elements in other planes). In fact, it is possible to fully fill the projected image space with vessel elements by increasing the number of slices in the z-stack and consequently increasing the tissue thickness sampled. In this case, a fractal dimension of 2 will be measured as the upper limit of the projection images. Our analysis demonstrates that the projection images of the vessels are sufficient to demonstrate differences between vessels from different tissues, and that the projection process itself does not significantly alter the dataset. Scale bar= 100 micrometers.

Data Analysis

Vessel density, lacunarity, fractal dimension and multifractal spectra were measured from images of vessels from the, cortex, kidney, skin, and thigh muscle of mice at postnatal day 6 (P6), and hyaloid vasculature from P0-P10 (Moisy 2006; Vadakkan 2009; Vadakkan 2009). Vessel diameters were measured manually by using the length measurement tool in the overlay menu in the Zeiss LSM image browser. Statistical significance of the differences between diameters, densities, fractal dimensions, lacunarity parameters, and generalized fractal dimensions among different tissue types and remodeling vascular patterns was tested with ANOVA analysis and post hoc- Tukey's Test. The error estimates of the box counting dimension and generalized fractal dimensions are based on linear regression analysis of the linear fitting of the log/log plot of the curves associated with each of the moments using MS Excel. Error estimates of the lacunarity parameters were based on the jackknife method (Efron 1979; Harris 1998) (described below). The hyperbolic function is non-linear, and thus the jackknife method was used to calculate error estimates of the least squares parameters. In comparing fractal dimension, generalized dimensions, and lacunarity, the statistical significance between a pair of data sets was tested by checking whether the mean values of the pair overlap with each other after adding or subtracting the error estimates to their respective mean values.

Below is a description that proves that $D_q = D_0$ regardless of the value of q.

For a monofractal, $P_i(\varepsilon) \sim \varepsilon^{D0}$ (fractal dimension is same in each box i).

$\sum_i [P_i(\varepsilon)] = 1$ (normalization condition)

$\sum_I \sim \varepsilon^{-D0}$ (substituting for $P_i(\varepsilon)$)

$\sum_i [P_i(\varepsilon)]^q = \varepsilon^{qD0} \sum_I = \varepsilon^{(q-1)D0} \sim \varepsilon^{(q-1)Dq}$

Therefore, $D_q = D_0$ regardless of the value of q. For a given spatial structure such as a vascular bed, fractal dimension need not be same in each box. Typically D_q is a monotonically decreasing function of q. So the inequality $D_0 > D_1 > D_2$ holds. A test vascular tree and the corresponding D_q versus q plot are shown to illustrate the above arguments below in figure 2.6.

Jackknife method:

The hyperbolic function is non-linear. To estimate the errors in the least squares parameters when a non-linear fit is performed, the jackknife method has been shown to be reliable (Efron 1979). Briefly, the jackknife can be described as follows. Consider a data set of N measurements. In the first iteration using the jackknife method, the first measurement of the data set is removed and the least squares values of the parameters are estimated from all remaining measurements. In the second iteration, the second value is removed (but the first value is included) and the least squares values are again estimated. In the third iteration, the third value is removed and so on. The procedure is repeated by sequentially removing each measurement in the data set so that N-1 values are considered in each iteration.

2.3 Results and Discussion

The methods have now been described in great detail for the application of quantifying microvessel morphology. The purpose of this study was to develop and to test these automated methods to distinguish the complexity between different vessel beds. To compare measurements of space filling properties (fractal dimension, multifractal spectra and lacunarity parameter) with more traditional measures of vessel diameter and density, new analytical tools have been developed and validated in this project. A simple box counting method was used to measure fractal dimension (figure 2.1) and then modified to allow for measurements of the generalized box counting dimensions (multifractal analysis). These methods were used in conjunction with a gliding box algorithm as described in the methods section to quantify the lacunarity of images of the vessel structures. In addition to these measurements, the pre-processing pipeline was developed to allow for image cleanup and conversion to binary format to preserve vessel morphology and space-filling characteristics of the fluorescent vessel label (figure 2.2).

To validate the MATLAB program created in this study (Vadakkan 2009), five validation steps were employed. First, a multifractal analysis of three monofractal structures, a straight line (figure 2.6 A), a checkerboard (2.6 B), and a Sierpinski carpet (2.6 C), and then similar analysis of an image of the retinal vasculature (2.6 D), which has a known multifractal organization was conducted. Figure 2.6 E-H represent the generalized dimensions obtained from images A-D, respectively. As expected, in the case of the straight line, all values of q (the generalized dimensions) were equal to 1 and the multifractal spectrum condensed to a point (figure 2.6 A, E). Similarly, for the checkerboard, the output from the program matched the known generalized

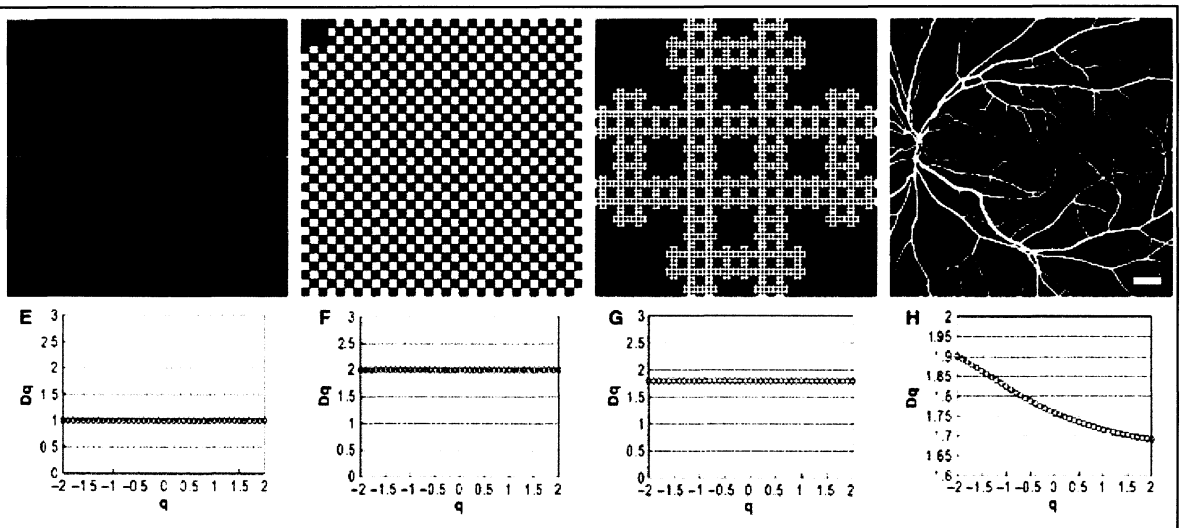

Figure 2.6: Multifractal analysis of a straight line (A), checkerboard (B), Sierpinski carpet (C) and retinal vasculature (D). The generalized dimensions of the line in A were all equal to 1 (E). The generalized dimensions of the checkerboard (B) were all equal to 2 (F). C is a monofractal called a Sierpinski carpet with a fractal dimension of 1.79. The generalized dimensions of the carpet were equal to 1.79 (G). D is the image of retinal vessels taken from the database for retinal images called STARE (Glodbaum 2010). The vasculature is different from the three patterns discussed above in that the space filling property of the vasculature cannot be described by a single dimension as in the previous cases. A set of generalized dimensions is required to characterize the retinal vascular pattern (H). The retinal vasculature is an example of a multifractal found in nature. In fact, in nature most objects are quasi fractal and must be measured with generalized dimensions to fully capture their behavior. All monofractals represent a special case of multifractal behavior in which all generalized dimensions are equal. Scale bar= 200 micrometers.

dimensions as all values were equal to 2 (figure 2.6 B, F). Third, the fractal dimension of a modified Sierpinski carpet (a self similar fractal) with a known fractal dimension of 1.79 was measured. The generalized fractal dimensions (D_0, D_1, D_2) that was measured using the program created in this project all matched this value as expected for a monofractal (figure 2.6 C,G). Next, an image of blood vessels from the retina, obtained from the retinal vascular database, STARE was analyzed (Glodbaum 2010) (figure 2.6 D, H). Retinal vessels have been shown to have a multifractal organization (Stosic, Tatijana et al. 2006). Here it was similarly found that D_0, D_1, D_2 had different values, demonstrating the multifractal nature of this vessel bed. Finally, the program was tested by acquiring two images of the same field of view by scanning one image (figure 2.7 A) and then rotating the scan field by 5^0 (figure 2.7 B). Xu et al., have previously demonstrated that the generalized fractal dimensions are rotationally invariant (Xu, Ji et al. 2009), and as expected, no difference was found between these values for the rotated images analyzed here (figure 2.7 C,D). Also, for all the data mentioned above, it was confirmed that the box counting dimension D_0 measured from the multifractal program created here (Vadakkan 2009) was indistinguishable from the box counting dimension measured using another program written by a different author (Moisy 2006). These tests indicated that this study's program generated data consistent with expected outcomes given control images. These validation steps have shown that the multifractal method written for this study can be applied to images of vessels to extract a value for the simple fractal dimension which

is similar to the values calculated by other, simpler, algorithms available online which determine only the discrete fractal dimension.

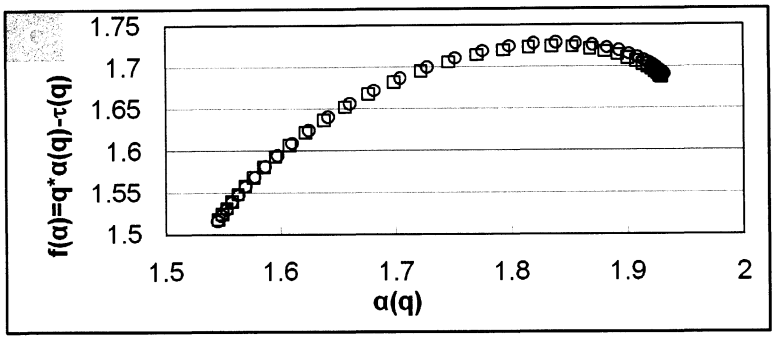

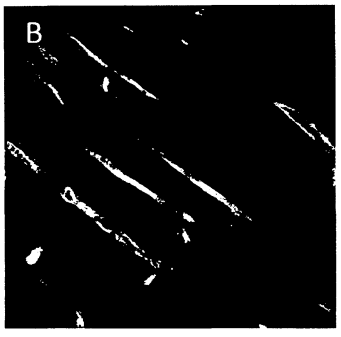

	D_0	D_1	D_2
Skin	1.73 ± 0.08	1.63 ± 0.02	1.58 ± 0.03
Rotated Image	1.73 ± 0.08	1.62 ± 0.02	1.57 ± 0.03

Figure 2.7: Rotational invariance of the fractal dimension. This figure shows images of vessels from the skin of Flk1-myr::mCherry mice, (figures A and B). Figures A and B are taken in the same location, but figure B is rotated 5 degrees counterclockwise. Figure C depicts the overlap of the multifractal spectra of images A and B. The generalized fractal dimensions measured from the spectra show no difference between the original image and the rotated image. Our findings are similar to the findings of Xu et al., and demonstrate that these measures are invariant under rotation (Xu, Ji et al. 2009). Scale bar = 50 micrometers.

To compare traditional measures of diameter and density with more complex measures of fractal dimension, multifractal spectra and lacunarity parameter, images of Flk1-myr::mCherry labeled microvessels from multiple tissue types were used. Figure 2.8 shows thresholded confocal images of Flk1-myr::mCherry labeled vessels in mice taken from the cortex, kidney, skin and thigh muscle at postnatal day 6 (P6).

From these images, the mean vessel diameter, vessel density, fractal dimension (D_0), the generalized fractal dimensions (D_0, D_1, D_2) and the lacunarity parameter (b) were determined as described in the methods section. These measurements are summarized in table 2.1, where measurements from the control images shown in figure 2.6 are also included to provide a comparison of monofractal and multifractal images.

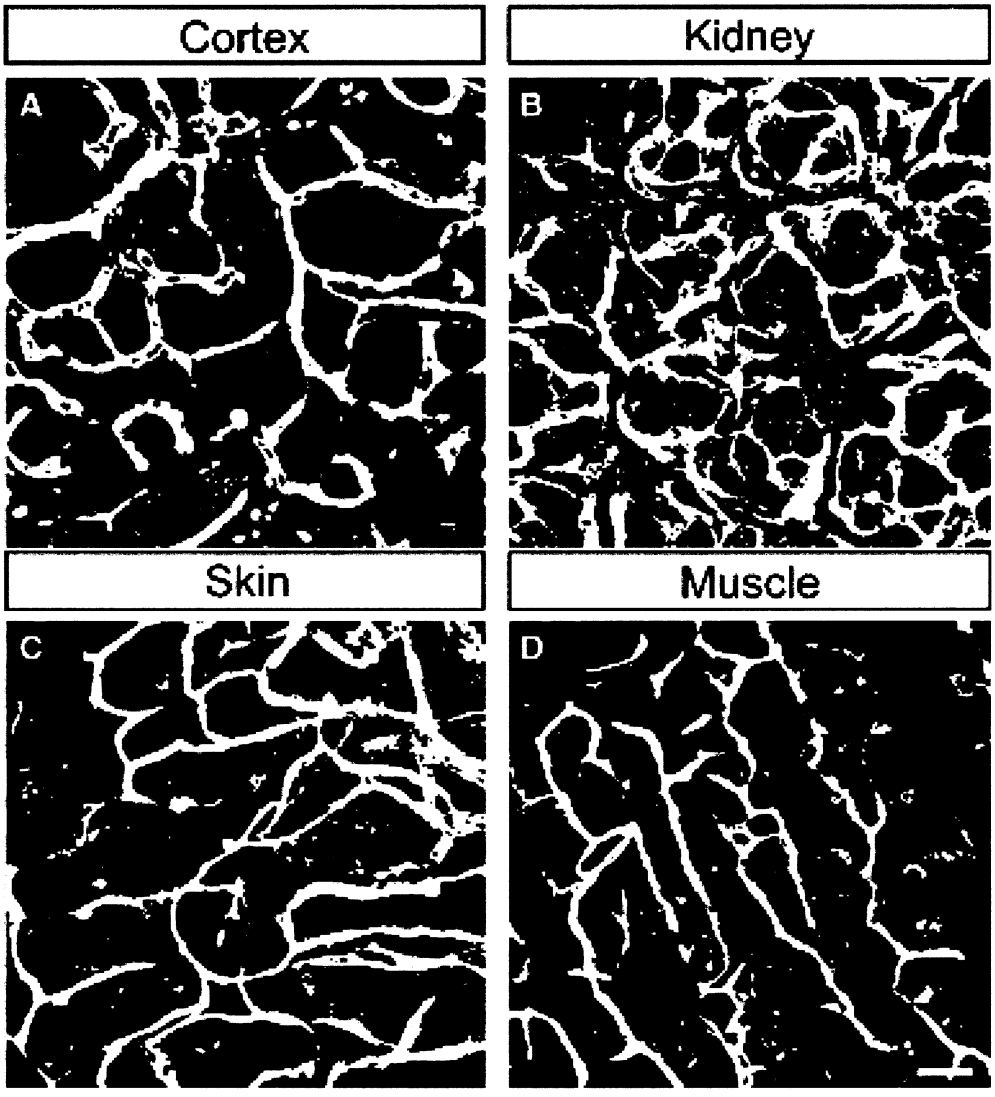

Figure 2.8: Thresholded confocal images of microvessels in four different tissues taken from postnatal day 6 (P6) of Flk1-myr::mCherry mice. Figure A is the thresholded image of the vasculature in the cortex, B is kidney, C is skin and D is muscle (vastus medialus). Scale bar = 50 micrometers.

Upon determination of the classical measures, a statistically significant difference was found in the diameters between the images from cortex and muscle ($p<0.01$), as well as images from kidney and skin ($P<0.05$), and images from kidney and muscle microvasculature ($p<0.01$). Comparisons between other groups showed no significant difference in diameters. The vessel density measurements from images of vessels were indistinguishable between the image of skin and the image of cortex, but both of these differed significantly from the kidney and muscle images. Density measurements from the kidney and muscle images also differed statistically from each other. Next the fractal dimension, generalized dimensions and lacunarity of vessel structures were analyzed in images of the four tissues (table 2.1).

	Vessel diameter (μm)	Vessel density	Fractal dimension	Generalized fractal dimensions			b (Lacunarity parameter)
				D_0	D_1	D_2	
Line				1.00 ± 0.00	1.00 ± 0.00	1.00 ± 0.00	0.00
Checker				2.00 ± 0.00	2.00 ± 0.00	2.00 ± 0.00	0.00
Sierpinski carpet				1.79 ± 0.02	1.79 ± 0.02	1.79 ± 0.02	0.40 ± 0.01
Retinal vessels				1.75 ± 0.06	1.72 ± 0.04	1.69 ± 0.03	0.49 ± 0.01
Kidney	8.55 ± 1.93	0.36 ± 0.01	1.89 ± 0.02	1.88 ± 0.03	1.84 ± 0.02	1.82 ± 0.02	1.92 ± 0.08
Skin	7.27 ± 1.63	0.24 ± 0.01	1.80 ± 0.03	1.78 ± 0.04	1.74 ± 0.03	1.73 ± 0.02	1.03 ± 0.03
Cortex	8.45 ± 2.20	0.24 ± 0.01	1.75 ± 0.03	1.77 ± 0.04	1.73 ± 0.03	1.71 ± 0.03	0.97 ± 0.05
Muscle	6.51 ± 1.41	0.17 ± 0.01	1.70 ± 0.05	1.74 ± 0.06	1.68 ± 0.04	1.66 ± 0.03	0.73 ± 0.03

Table 2.1: Microvascular Morphology Quantification. The set of vessel morphological measurements corresponding to the binary images in figure 2.8, and the generalized dimensions and lacunarity from the four test cases from figure 2.6 are summarized. Generalized fractal dimensions obtained from multifractal spectra correspond to q = 0, 1 and 2, respectively. The lacunarity parameter *b* was estimated based from the hyperbolic fit. Taken together, the data in the table suggest that generalized dimensions D_0, D_1, and D_2 as well as the parameter *b* can be used to characterize the difference in the morphology of the beds even when differences between mean diameters of the vessels are less pronounced. The test cases of the sierpinski carpet and the retinal vessels contrast monofractal and multi fractal behavior. Error estimates of vessel diameters are the standard deviations of the measured vessel diameter segments in each image. Error estimates of vessel area density were calculated by partitioning the images into boxes of different widths and then averaging over the vessel densities obtained using boxes of different widths. Regression of these values provided an R^2 of at least 0.98 in all cases. The error estimates of box counting dimension and generalized fractal dimensions are standard errors estimated using a regression analysis in MS excel. The error values of lacunarity are standard deviations measured using the jackknife method (Efron 1979; Harris 1998). In all cases, R^2 values of the fits were greater than or equal to 0.98 for lacunarity, fractal dimension and generalized dimension regression analysis.

The fractal dimension analysis clearly showed that there are differences in the space filling properties in all of these images. Although vessel density and fractal dimension are both measures of how vessels occupy space, they do not always correlate because variations in vessel diameter can alter density but may not alter fractal dimension. However, for these images, where vessel diameters were

comparable, there was a significant correlation between vessel density and fractal dimension measured using the box counting algorithm ($R^2 = 0.99$, table 2.1). These data suggest that complexity increases with added vessel elements in these cases.

To determine whether the vessel structures in these images had a multifractal or monofractal character the control cases from figure 2.6 were used as a baseline for comparison of monofractal to multifractal behavior of the different tissues. What was found were distinct values for D_0, D_1, D_2 from images of all four tissues, indicating

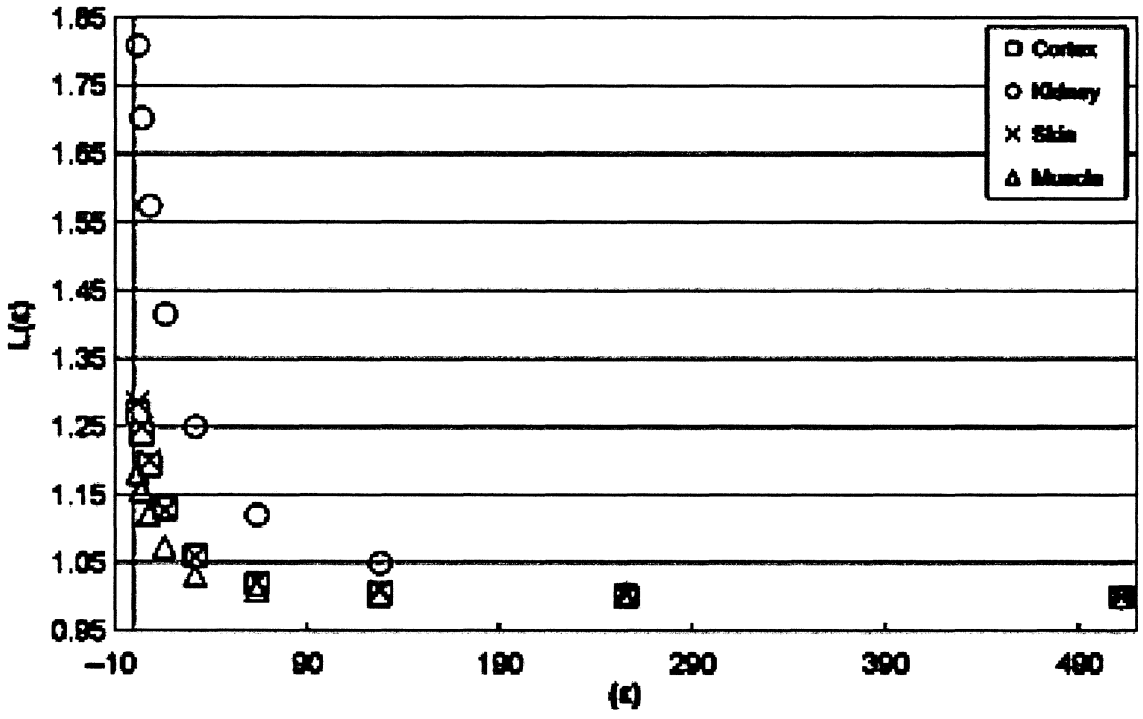

Figure 2.9: A graph of lacunarity values L(ε) versus the box widths (ε) for various tissues. The lacunarity plots overlap in the case of skin and cortex, while the plots in the case of kidney and muscle tissues are well separated from each other and also from the plots of cortex and skin.

that, indeed, these vessel structures have a multifractal organization. The gaps or lacunae in the vascular patterns were quantified by measuring the lacunarity parameter *b* in each case. Figure 2.9 shows the lacunarity values measured from the

confocal images of various tissues. In all cases the data for box widths were able to be fitted in the range from 8 to 512 with the hyperbolic function listed above ($L(\varepsilon) = b / \varepsilon^a + c$) with $R^2 > 0.98$. The hyperbolic function corresponding to the kidney had the largest lacunarity parameter *b* (meaning it has the lowest lacunarity) while that of the muscle had the smallest lacunarity parameter *b*. The difference in lacunarity parameters was representative of the fact that the image of the muscle vessels had a wide range of gap sizes compared to the kidney, and thus, muscle vessels had the highest lacunarity. The *b* values for the various images of vessels in the tissues are summarized in table 2.1. The lacunarity analysis complemented the fractal dimension by adding information about how the vessels filled the space, reflected in the distribution of lacunae. It was observed in these data sets that as the fractal dimension went up, the lacunarity parameter *b* increased meaning the lacunarity decreased (see table 2.1). This is as one might expect, since when vessel branches are more dense, there is less available space between vessels, limiting the size distribution of the lacunae. However, this is not to say that the relationship between lacunarity and fractal dimension is fixed. It is important to consider that large vessels that may occupy the same amount of space in tissue as smaller, more highly branched vessels (same vessel density), but may not impose the same limits to the size of lacunae or have the same fractal dimension. Thus, considering both of these independent measures provides more information about how the vessels fill the tissue space.

In addition to considering the generalized fractal dimensions (D_0, D_1, D_2), the multifractal spectrum can be plotted to visualize the distribution of the space occupied by vascular structures. Figure 2.10 shows the multifractal spectra corresponding to vasculature in different tissues. The peak value of the multifractal spectra corresponds to D_0. The $f(\alpha)$ values to the left and right of D_0 correspond to positive and negative values of q, respectively. Since $\alpha(q)$ values are estimated from the linear fits to the

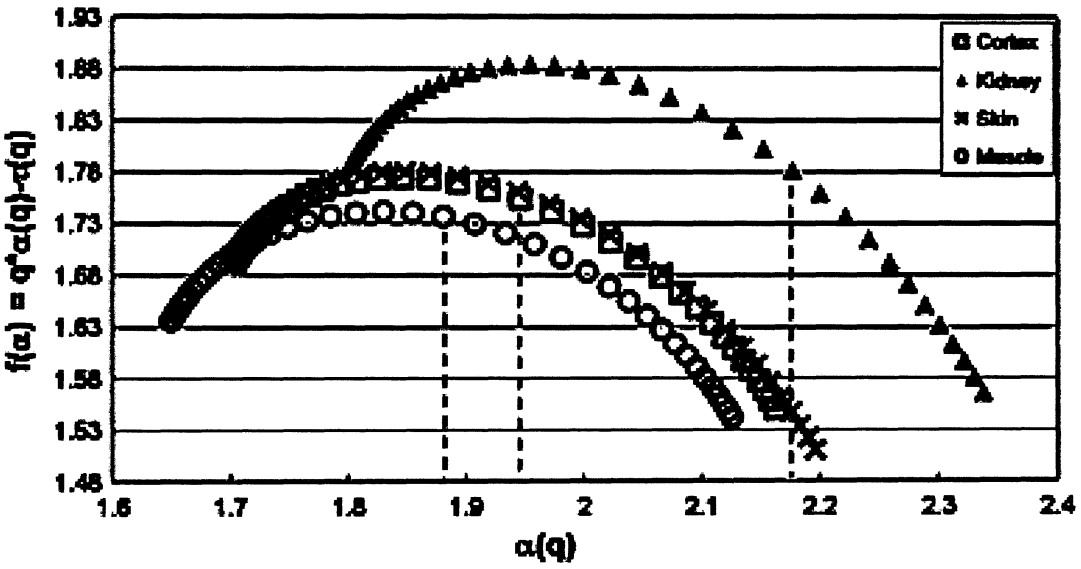

Figure 2.10: The multifractal spectra of the images of vascular patterns presented in figure 2.8. The spectra corresponding to patterns with larger lacunarity are shifted to the lower α range and have lower maxima in comparison to patterns with smaller lacunarity. Dashed lines indicate values of α beyond which the R^2 values associated with the linear fits in the evaluation of α fall below 0.95. $f(\alpha)$ values with α values whose R^2 above 0.95 lie to the left of the dashed lines.

equations described earlier, values of $q > 0$ and $q < 0$ for which $R^2 > 0.95$ were used (Posadas, Gimenez et al. 2003). The cut off values for $q < 0$ with $R^2 < 0.95$ are represented by dashed lines on the spectra. The shift in the peaks of the spectra from

top to bottom (figure 2.10) is due to differences in the values of D_0 (table 2.1), corresponding to the apex of the spectrum.

For example, the kidney vessels occupy more space than the muscle vessels, and hence their D_0 values were significantly higher. The images from cortex and skin are difficult to compare, and this analysis allowed us to show that they have similar morphology based on their space filling properties. The spectra derived from vessel images from the four tissues were also shifted with respect to the x-axis, the value for $\alpha(q)$. It was found that multifractal spectra corresponding to smaller fractal dimension (D_0) and larger lacunarity (smaller lacunarity parameter *b*) were shifted to smaller values of the $f(\alpha)$ - α space. While the lacunarity parameter is not necessarily related to the multifractal spectra, others have also observed a correlation between the lacunarity and the shift of the spectra in the $f(\alpha)$ - α space (Posadas, Gimenez et al. 2003; Stosic, Tatijana et al. 2006).

From the multifractal spectra, two other observations could be made (figure 2.11). First, figure 2.11 A shows the plot of $\alpha(0)$ versus D_0 for the various tissues discussed above. The magnitude of the difference in the values of $\alpha(0)$ and D_0 is a measure of heterogeneity of the vascular pattern, which is defined as the range of scaling exponents required to characterize the pattern. Second, a key feature of multifractal behavior is heterogeneity in scaling behavior of different regions of the pattern. Thus, the multifractal behavior can also be directly assessed from $\alpha(0)$ and D_0 , in addition to comparing the values obtained from the generalized fractal dimensions (D_0, D_1, D_2) (table 2.1). If the data points lie

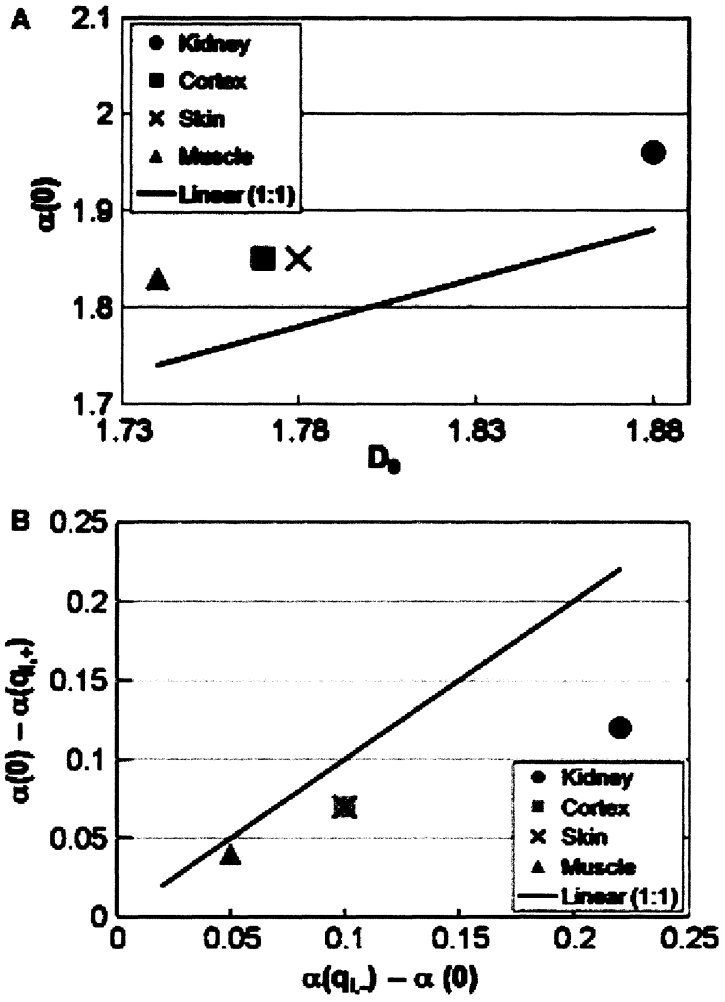

Figure 2.11: Assessment of multifractal behavior and curve symmetry. The homogeneity of a structure can be determined by the proximity of its data point to the 1:1 line on the $\alpha(0) - D_0$ plot, and the symmetry of a multifractal spectrum can be assessed by the proximity of its widths to the 1:1 line on the $\alpha(0) - \alpha(q_{i,+})$ versus $\alpha(q_{i,-}) - \alpha(0)$ plot. A shows that the patterns in figure 4 are heterogeneous and thus cannot be described by box counting dimension alone. B shows the asymmetry of the multifractal spectra of images from different tissue types. The spectra of cortex, skin, and muscle are more symmetric than the spectrum of kidney.

on the 1:1 line, the pattern is homogeneous and can be characterized by D_0 alone. The data points from the images of the tissue vasculature do not lie on the 1:1 line; in fact, they all deviate from this line (figure 2.11 A). Deviation from the 1:1 line indicates that the microvascular patterns discussed above are heterogeneous and are more appropriately described by the multifractal spectra rather than by their box counting dimensions alone. This process is similar to the heterogeneity analysis described in Posadas et al. (Posadas, Gimenez et al. 2003). The symmetry of the multifractal spectrum offers further information about the distribution of fractal dimensions of the vessel pattern (i.e., the space that is occupied by the vessels in the images). The symmetry of the multifractal spectrum can be assessed by measuring the widths $(\alpha(q_{i,-}) - \alpha(0))$ and $(\alpha(0) - \alpha(q_{i,+}))$ (Posadas, Gimenez et al. 2003). The values of $q_{i,-}$ and $q_{i,+}$ correspond to negative and positive values of q taken from the range of q values over which the multifractal scaling was observed. The spectrum is symmetric if the two widths are equal. In the context of soil structures, massive structures with low porosity have been shown to have asymmetric spectra (Posadas, Gimenez et al. 2003).

In the present context, vascular beds with high density and low lacunarity should have relatively asymmetric spectra. For the images of kidney, cortex, skin, and muscle vessels, the widths of the spectra are shown in figure 2.11 B. The data points for cortex, skin, and muscle were closer to the 1:1 line than the data point for kidney vessels. Thus the multifractal spectra of cortex, skin, and muscle vessels were more symmetric compared to the spectrum of kidney vessels. Asymmetry in the multifractal spectra of the kidney may be related to the fact that the vascular network

is characterized by high vessel density, high fractal dimension, and low lacunarity, which may all contribute to relative asymmetry of the multifractal spectra compared to other vascular beds.

The studies above indicate that multifractal analysis is valuable in identifying significant differences between vessels in different tissues. Next it was tested whether these methods could be used to describe changes during vessel remodeling within the same tissue. Vessel regression was studied by analyzing images from the hyaloid vasculature in the eyes of neonatal mouse pups. The hyaloid vessels make up a transient vessel network that nurtures the lens during embryonic development. These vessels regress just before birth in humans and postnatally in rodents by macrophage-mediated vessel pruning to eliminate vessels that would otherwise obstruct vision (Lang and Bishop 1993; Zhu, Madigan et al. 2000; Poché 2009). Figure 2.12 A-D are grayscale confocal microscope images of the hyaloid vasculature of Flk1-myr::mCherry mice from ages postnatal day 0 (P0) to P10, which demonstrate this regression. Again, vessel diameter, vessel density, fractal dimension, generalized fractal dimensions and the lacunarity parameter were measured and are shown in table 2.2.

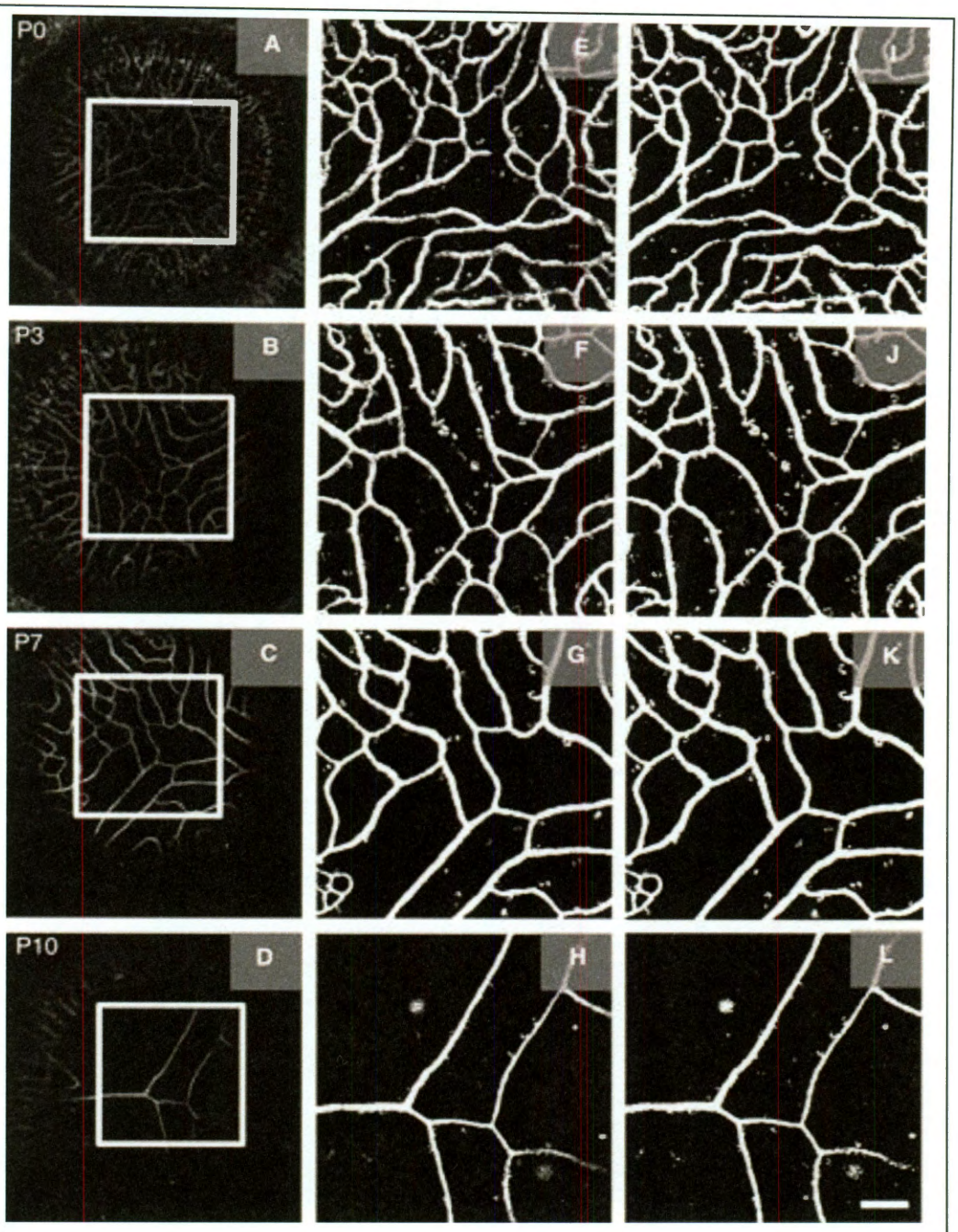

Figure 2.12: Hyaloid regression in the postnatal mouse. Figures A-D are grayscale confocal microscope images of hyaloid vasculature in the retina of a Flk1-myr::mCherry mouse taken from P0 to P10. P refers to the postnatal stage of the mouse imaged, as in postnatal day 0 through day 10. Figures E-H are images of the regions in figures A-C first cropped and dilated to occupy 512 x 512 pixels, then modified with an unsharp mask in Adobe CS2 with radius set to 12. Figures I-L are binary images obtained from D-F after applying an intensity threshold. Scale bar = 50 micrometers.

The only significant differences between mean vessel diameters were between the P0, P3 and P7 vessel diameters in comparison to the P10 stage (P=0.01). There was no significant difference in vessel diameter between P0, P3 and P7 vessels in the hyaloid vasculature (P>0.05) (table 2; figure 2.13 A) as determined by ANOVA and post hoc Tukey's tests. During the vessel regression process, it was clear that vessel density decreased from P0 to P10 (table 2.2). Reduction in vessel density corresponds with the functional vascular transition from nurturing the lens at P0 to clearing the visual path at P10. When the fractal dimension and generalized fractal dimensions were examined at successive postnatal stages, differences were found between D_0, D_1, D_2, again indicating that the hyaloid vasculature exhibited multifractal behavior. Furthermore, the generalized fractal dimensions decreased from P0 to P10, while lacunarity increased (parameter *b* decreased) (table 2.2) as the regressing vessels occupied less space. In fact, fractal dimension and vessel density at all stages of remodeling were linearly correlated (figure 2.13 B, R^2=0.99). This was an interesting observation but the complete meaning of this observation remains to be understood. The singular discrete values of the parameters are reported below, however the multifractal spectra are valuable for reasons stated above, and they are demonstrated below.

Age	Vessel diameter (μm)	Vessel density	Fractal dimension	Generalized fractal dimensions			*b* (Lacunarity parameter)
				D_0	D_1	D_2	
P0	12.98 ± 2.63	0.26 ± 0.01	1.76 ± 0.03	1.78 ± 0.04	1.75 ± 0.03	1.73 ± 0.03	1.67 ± 0.12
P3	11.83 ± 3.45	0.22 ± 0.01	1.72 ± 0.03	1.73 ± 0.04	1.70 ± 0.03	1.69 ± 0.03	1.08 ± 0.06
P7	12.43 ± 2.65	0.19 ± 0.01	1.69 ± 0.03	1.69 ± 0.04	1.66 ± 0.03	1.66 ± 0.03	0.85 ± 0.03
P10	9.60 ± 3.31	0.07 ± 0.01	1.49 ± 0.06	1.52 ± 0.08	1.47 ± 0.03	1.46 ± 0.04	0.19 ± 0.01

Table 2.2: Morphological Remodeling of the Mouse Hyaloid Vasculature. The various quantities that may be used to quantify the time evolution of the hyaloid vasculature in the images 2.12 I-L are tabulated here. Collectively, the data strongly support the claim that D_0, D_1, D_2, and *b* can be used to capture changes in vessel morphology even when the differences in mean vessel diameters at various developmental stages are less pronounced. Errors were estimated as in table 2.1. In all cases, the R^2 values from regression analysis were equal to or greater than 0.98.

The multifractal spectra of the remodeling stages during hyaloid regression are shown in figure 2.13 C. As in the previous data set, an inverse correlation was observed between D_0 and lacunarity. The spectrum on the top right corresponds to P0, which has the largest D_0 and also the smallest lacunarity, and the spectrum on the bottom left corresponds to P10, with the smallest D_0 and largest lacunarity. It was noted that the deviation between D_0, D_1, D_2 was smaller for the hyaloid vasculature than for the deviations seen for the same values in images from other vessel beds (table 2.2 vs. table 2.1). This prompted further analysis of the heterogeneity from the multifractal spectra.

Figure 2.13 D shows that while the images of the vessels all exhibited multifractal behavior, the values were closer to the 1:1 line than in figure 2.11, and thus were less heterogeneous than the images of vessels from the other tissues. Figure 2.13 E demonstrates the symmetry of the curves, and it is clearly seen that P3 and P7 vessels lie closer to the 1:1 line than P0 and P10 vessels, meaning P3 and P7 possess more symmetric spectra than P0 and P10. The higher asymmetry in the spectrum of

P0 is partly due to the presence of more vessels and thus higher complexity in the image at P0. In P10 there was more empty space in the image of the vessels, and due to the relatively low contribution of the vessels to the image, the curve was asymmetric and the corresponding data point laid above the 1:1 line (more empty space than vessels causes this shift). Thus, the pattern of regression was obvious from plotting the multifractal spectra, even when there are incremental differences that could not be readily distinguished visually, as between P3 and P7 hyaloid vessels (2.12 J vs. K). Thus, these data provided a convenient and robust way to quantify changes associated with developing vessels, such as regressing vessel networks.

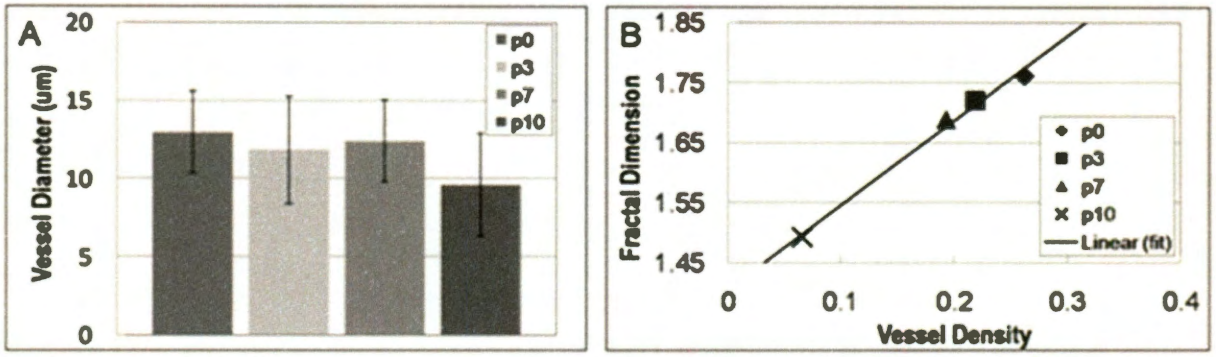

Figure 2.13: Multifractal analysis of the hyaloid vasculature during regression. Figure A shows the average diameters of the vessels in the images 2.12 I-L. The only significant differences between vessel diameters are between the P0, P3, P7 stage vessels and P10 stage vessels ($P<0.01$). There is no significant difference in vessel diameter between the P0, P3, and P7 images of vessels in the hyaloid. Here, there is significant correlation between vessel densities and box counting dimensions (B, $R^2=0.99$).

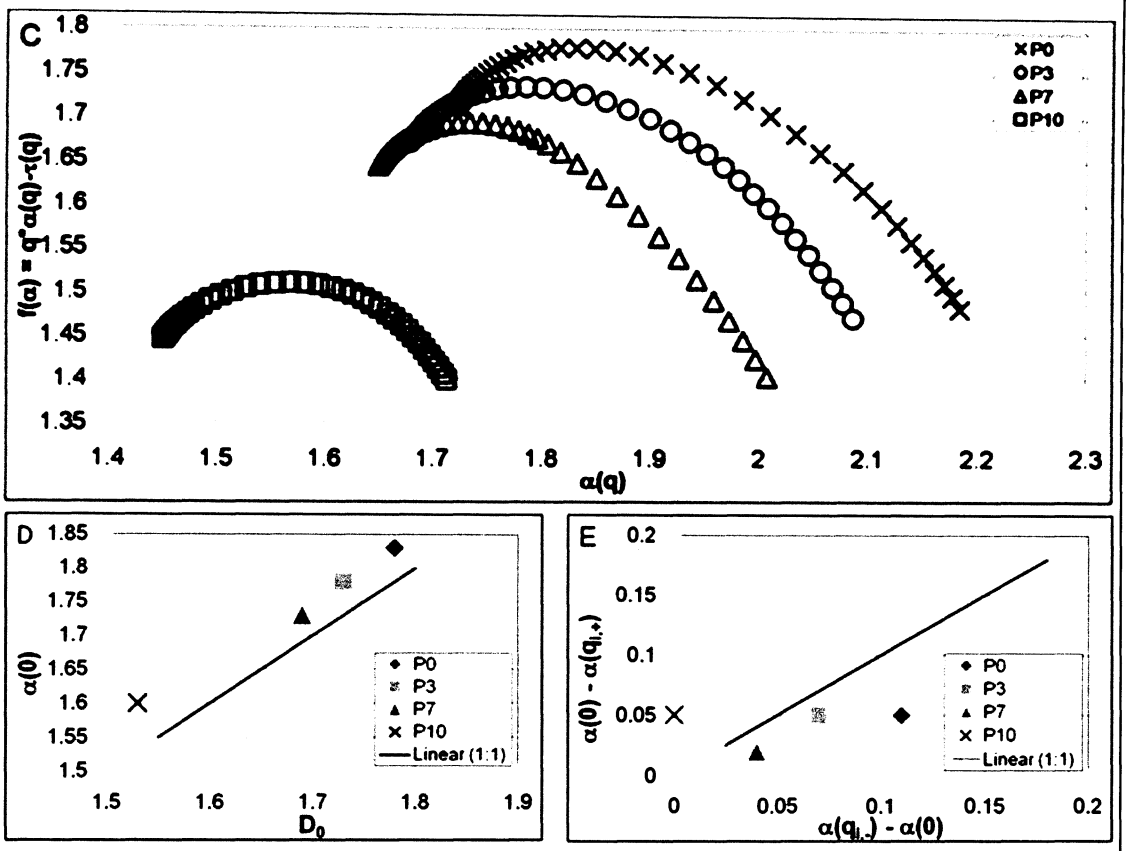

Figure 2.13 continued: Figure C shows the multifractal spectra of binary images 2.12 I-L. The spectrum at the top right corresponds to the hyaloid vasculature at P0. The pattern has the largest box counting dimension D_0 and the smallest lacunarity. The pattern on day P10 has the smallest box counting dimension D_0 and the largest lacunarity and is at bottom left. D shows the heterogeneity analysis and compares P0-P10. Figure E is the symmetry comparison of the spectra of P0-P10 hyaloid vessels. 2.13D is the heterogeneity analysis of the spectra from the hyaloid vessels. The values for the hyaloid vessels are closer to the 1:1 line than in figure 2.11, and thus are less heterogeneous than the images of vessels from the other tissues. In figure E the symmetry data points for P3 and P7 vessels lie closer to the 1:1 line than P0 and P10 vessels. This means P3 and P7 are more symmetric than P0 and P10. The higher asymmetry in the spectrum of P0 is partly due to the presence of more vessels and thus higher complexity in the image at P0. In P10 there is more empty space in the image of the vessels. Due to the relatively low contribution of the vessels to the image, the curve is asymmetric and the corresponding data point lies above the 1:1 line (more empty space than vessels causes this shift).

The final goal of this study was to image and analyze vessels from the stem cell niche in the sub ependymal zone of the mouse brain. Towards this effort, images of the native neural stem cell niche, the sub-ependymal zone (SEZ), were analyzed to identify the vessel density, fractal dimension and lacunarity. Figure 2.14 demonstrates the projections of vessels that were measured from this tissue. In A-C projections of the 56 um thick stacks taken medially from the ventricle wall were shown. Figures D-I show projections of 22um thick stacks extracted as a subset from the 56um thick image set. Measurements on both the subventricular zone and the nascent striatum were recorded and compared using a pair wise t test assuming unequal variance. The vessel density (0.12 vs. 0.19 $p<0.01$), fractal dimension (1.66 vs. 1.78 $p<0.01$) and lacunarity (0.49 vs. 0.87 $p<0.01$) were significantly different in the SEZ, compared to the nearby striatum (J-L). The fractal dimension, lacunarity and vessel density have not previously been reported in this fashion. This information provides valuable insight into the scale invariant distribution of vessels within the specialized neuro vascular niche, and is yet another example of the application of this new method to quantify vessel morphology.

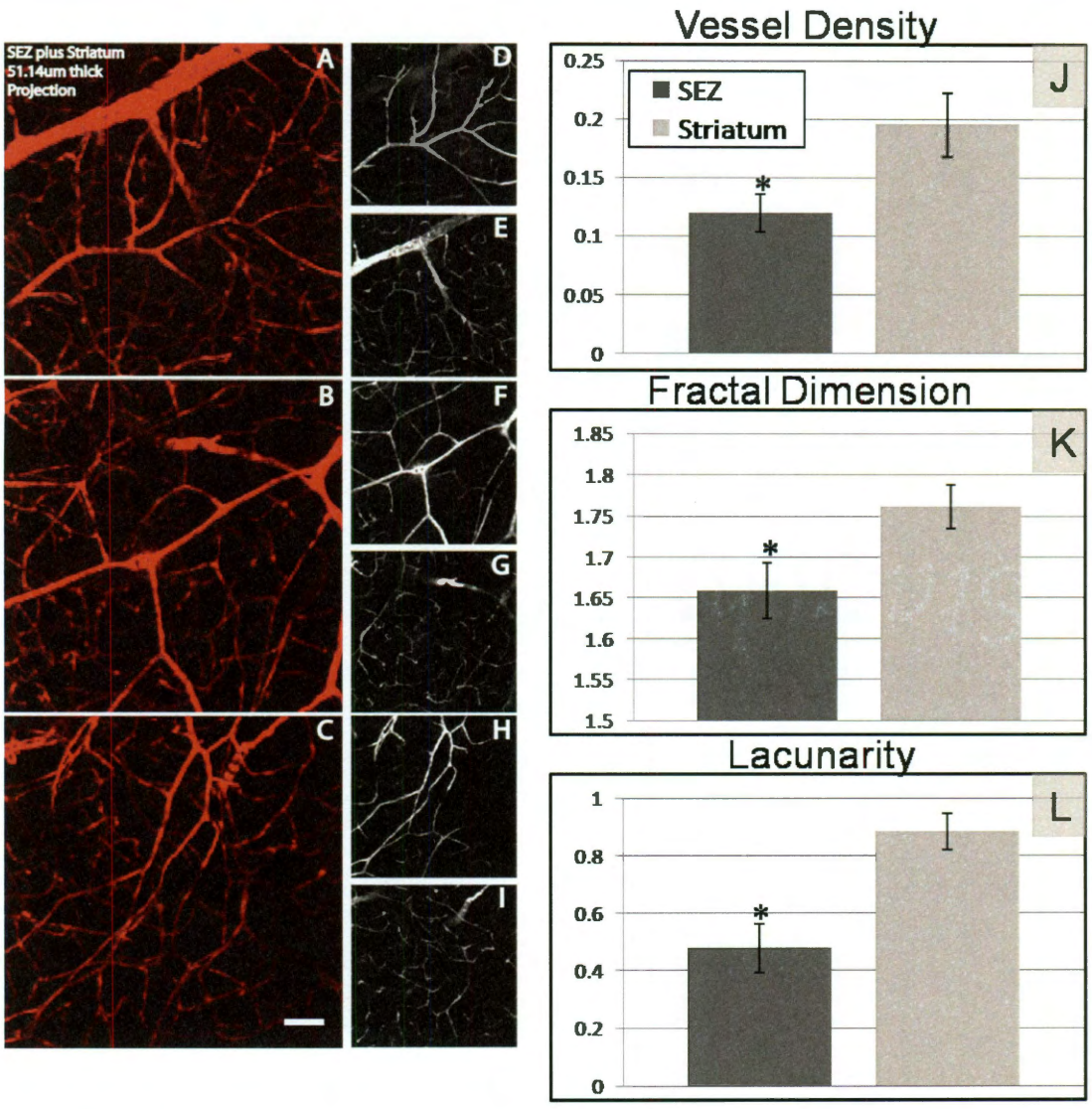

Figure 2.14: Analysis of the sub-ependymal zone (SEZ). The native vessels are shown in A-C and the stacks which represent the overlying SEZ and underlying cortex extracted from these three dimensional image sets are shown to the right, as D, F, H and E, G, I respectively. In J-L the morphological parameters are measured from the images of the SEZ, represented by D, F, and H. Scale bar = 100 micrometers.

2.4 Conclusions

Here, it was demonstrated that multifractal analysis and lacunarity can be used to compare and describe the morphology of microvasculature labeled with a fluorescent protein reporter from different tissues along with more common measures used for differentiating vasculature (like in the case of vessel diameter). It was found that even in scenarios where changes in mean vessel diameter were not robust at determining changes in vascular morphology, such as remodeling of the hyaloid vasculature, multifractal spectra and lacunarity parameters could be used to reveal significant changes in vessel structure. Such an automated analysis could link morphology with control and experimental parameters in vascular patterns within developing, pathological, or engineered tissues. This approach is likely to be particularly useful for evaluating subtle differences or pathologies where vessel diameters are fairly constant and is well suited for making comparisons over time, as shown here in the evaluation of the hyaloid vessels.

Simple fractal analysis has proven useful in analyzing retinal vessels to differentiate patients with lacunar-type stroke from normal patients (Doubal, MacGillivray et al. 2010), to determine macro- and microvascular complications in type 1 diabetes (Grauslund, Green et al. 2010), and to follow progression of chronic kidney failure (Sng, Sabanayagam et al. 2010). Only recently has the multifractal approach been instituted, and it has proven effective in discerning pathological

vessels from normal vessels in the case of proliferative diabetic retinopathy (Stosic, Tatijana et al. 2006). Although these studies have been conducted in retinal vessels because they are easily imaged *in vivo*, we propose that multifractal analysis could be further applied to other tissues from mice with labeled vasculature in a variety of disease models. Furthermore, it could be used to examine biopsied human specimens to more completely characterize developmental and diseased states, as well as the processes of neovascularization and vessel remodeling.

The findings of the Doubal, Sng and Grausland helped establish the value of the scale invariant fractal dimension in quantifying changes in complexity and how those may reflect disease states of the vasculature. Stosic took the use of the multifractal analysis and brought this technology to the retinal vasculature and retinal disease states. The method in this thesis expands upon the use of the multifractal analysis and highlights the spectral fingerprint that is given in each image to help first validate the natural geometries are multifractal, and then to summarize the morphological findings with a complex spectral curve. Today there are many more labs focusing on the use of these tools to best quantify morphological changes in vessels.

Given the utility of this method in vessel analysis, the scale-invariant parameters should be used in the future to help to develop our understanding of vessel morphology and complexity.

Chapter 3: Tailoring Vascular Morphology

In this chapter, I optimize angiogenic growth factor release from engineered hydrogels to induce and support the formation of stable microvasculature resembling vessels from stable, native tissues and niches. I start off with a brief introduction of important techniques used in this chapter, and then I describe the findings used in tuning the vessel response to match skin and muscle (3.1) as well as to match vessels found in the sub ventricular zone of the brain (3.2). Section 3.1 from this chapter is taken from the publication, "Tailoring vessel morphology" by Gould DJ, Saik JE, Vadakkan TJ, West JL, Dickinson ME., now in preparation for submission to *Tissue Engineering*.

3.1 Introduction:

Biomaterials can provide a local, controlled delivery system for release of angiogenic growth factors as potential treatments for ischemic disease or to improve blood supply to engineered tissues. Precise control over delivery of these growth factor concentrations is necessary to induce desired cellular responses (Tayalia and Mooney 2009). Several polymer delivery strategies have emerged to control growth factor delivery (Tayalia and Mooney 2009). For instance, growth factors can be incorporated into a polymer precursor solution prior to polymerization to entangle factors within a scaffold following polymer crosslinking. Growth factors are then released from the

scaffold via diffusion, establishing a concentration gradient. Growth factor delivery for angiogenesis has been achieved using natural scaffolds (Cascone, Sim et al. 1995; Greisler 1996; Schroeder-Tefft, Bentz et al. 1997; Yao, Roderfeld et al. 2006; Nillesen, Geutjes et al. 2007) as well as synthetic polymers (Cascone, Sim et al. 1995; Nimni 1997; Mann, Gobin et al. 2001; Zisch, Lutolf et al. 2003; Biondi, Ungaro et al. 2008; Gobin (2002)). Scaffolds delivering vascular endothelial growth factor (VEGF) have been used to induce dose dependant, pro-angiogenic responses including increased vascularization, pericyte coverage, and vessel perfusion (Davies, Dobner et al. 2008). VEGF dose and temporal distribution was also found to govern endothelial cell phenotype in an *in vitro* model as well as regulating optimal angiogenic sprouting *in vivo* (Silva and Mooney).

Although many growth factors have been shown to have angiogenic properties, the majority of work has focused on three growth factors: vascular endothelial growth factor (VEGF), platelet derived growth factor (PDGF-BB), and fibroblast growth factor (FGF-2). VEGF, released in response to hypoxia, stimulates endothelial cells to migrate, proliferate, and differentiate (Nomi, Miyake et al. 2006). VEGF has been widely used to induce angiogenesis, but VEGF-induced vessels have been shown to be unstable, leaky and hemorrhagic (Jain 2005; Jain, Au et al. 2005). Hypoxia can also stimulate macrophages to release FGF-2, which triggers endothelial cell proliferation and migration, and regulates the expression of key angiogenic molecules, such as collagenases and β1 integrins (Bikfalvi, Klein et al. 1997). FGF-2 induces migration and proliferation of smooth muscle cells (Jackson and Reidy 1993) which may help stabilize new vessel beds. PDGF-BB is another factor important in angiogenesis, which is released by endothelial tip cells in response to hypoxic conditions. This growth factor is

involved in the stabilization of developing capillaries by recruiting pericytes and inducing them to produce the extracellular matrix proteins that constitute the basement membranes of functional blood vessels. In addition, PDGF-BB has been implicated as a key factor in anastamosis formation (Cao, Brakenhielm et al. 2003; Gaengel, Genove et al. 2009).

Cao et al. demonstrated the utility of PDGF-BB and FGF-2 in combination in comparison to VEGF alone, by using hydron pellets to deliver these factors to the mouse cornea to study the angiogenic response (Cao 2004). In their study, the use of PDGF-BB or VEGF-A alone led to total vessel regression by 24 days and by 70 days for FGF-2-induced vessels (Cao, Brakenhielm et al. 2003; Cao 2004). Notably, vessels formed in response to the combination of FGF-2 and PDGF-BB were stable for over 210 days. Implantation of individual factors led to a transient vessel response, which was shown by removing pellets containing the factors from the eye 6 days after implantation. This caused total vessel regression within one week in all samples except those containing the combination of PDGF-BB and FGF-2. VEGF-A-induced vessels which were highly leaky, where vessels formed in response to PDGF-BB and FGF-2 remodeled into well-defined branching and organized structures that were not leaky when perfused with fluorescent dextran (Cao, Brakenhielm et al. 2003). As an indicator of vessel maturity 25 days after implantation, 70% of vessels formed in response to PDGF-BB and FGF-2 were desmin positive as compared to only 40% for FGF-2 induced vessels (at this point all PDGF-BB induced vessels had regressed). The addition of VEGF antagonists confirmed the VEGF-independent vessel formation using PDGF-BB and FGF-2 (Cao, Brakenhielm et al. 2003). Findings were corroborated in the hind limb ischemia model, which showed that PDGF-BB and FGF-2 increased collateral vessel growth and paw blood perfusion,

and vessels were well-organized and stable for over 60 days. The synergistic response was later found to result from FGF-2 activation of transcription of the PDGF-BB receptor in endothelial cells. PDGF-BB in turn, induces a positive feedback signal by amplifying FGF-2 expression in vascular mural cells (Cao, Cao et al. 2008).

In light of the data showing that the combination of FGF-2 and PDGF-BB promote the formation of more stable vessel structures than VEGF, there is now growing interest in using these factors to promote tissue repair by inducing vessel growth into biomaterial scaffolds for tissue engineering. In this study, the goal was to determine the relationship between growth factor dose and the morphology of induced vessels. Furthermore, it was important to determine whether varying concentrations of FGF-2 and PDGF-BB result in predictable alterations in vessel morphology and to test whether the morphological features of the induced vessels could be tailored to mimic vessel morphology found in natural, endogenous tissues. To assess the morphology of induced or natural vessel beds, traditional criteria such as vessel diameter and density were utilized along with scale-invariant measures of the space-filling properties of vessels such as the fractal dimension (D_0) and lacunarity. Recently the utility of such advanced methods to characterize vessel morphology has been shown (Gould, Vadakkan et al. 2010) . To deliver varying concentrations of growth factors, poly(ethylene glycol) (PEG) diacrylate, a photocrosslinkable and biocompatible polymer was chosen to deliver angiogenic growth factors in a local, controlled manner. These hydrogels were modified with an immobilized RGD peptide (a sequence commonly found in fibronectin and other cell-adhesive proteins) (DeLong, Gobin et al. 2005; Moon 2008) and rendered proteolytically degradable in response to migrating cells by incorporating matrix

metalloproteinase (MMP) sensitive cleavable peptide sequences into the polymer backbone (West and Hubbell 1999; Moon 2008; Moon, Saik et al. 2010). The photocrosslinking process enables inclusion of releasable growth factors prior to crosslinking for local, controlled delivery to induce host vessel invasion (Leslie-Barbick, Moon et al. 2009). For the *in vivo* analysis of induced vessels, hydrogels were implanted into the mouse cornea using a mouse corneal micropocket angiogenesis model in transgenic mice expressing *Flk1-myr::mCherry* in a model that has been extensively developed (Moon, Saik et al. 2010; Poche, Saik et al. 2010). The external nature of the cornea allows for facile surgical implantation and high-throughput analysis, the induced vessels can be quantitatively examined microscopically using high resolution methods, and angiogenesis is induced into an otherwise avascular tissue, facilitating morphological analysis (Gaudric, N'Guyen et al. 1992; Auerbach, Lewis et al. 2003).

This corneal implantation, when coupled with a quantitative method for studying vessels proved to be a valuable platform for inducing and quantifying vessel morphology in this study. The host vessel response was then probed for tunability and finally was optimized to allow for tailoring of the vessel response to match target vessel morphology.

3.2 Inducing Tunable Vessel Morphology

Hypothesis: *The space filling properties of induced vessels have a dose-dependent relationship to pro-angiogenic growth factor concentration, which can be used to fine tune morphology to match parameters of vasculature in tissues.*

The specific goals of this study are to define whether varying concentrations of FGF-2 and PDGF-BB result in predictable alterations in vessel morphology and to test whether the morphological features of the induced vessels mimic morphologies found in natural, functional vessels in endogenous tissues.

3.2.1 Materials and Methods

The experimental design for this aim is described here. The hypothesis was tested with the use of the corneal micropocket angiogenesis assay to implant degradable hydrogels into the mouse cornea for *in vivo* monitoring of vascular formation (figure 3.1). Hydrogels were loaded with Platelet Derived Growth Factor BB (PDGF-BB) and Fibroblast Growth Factor 2 (FGF2), which induce stable vessel growth and mural cell recruitment (Bohnsack 2003; Cao 2003; Cao 2004). The release kinetics of these

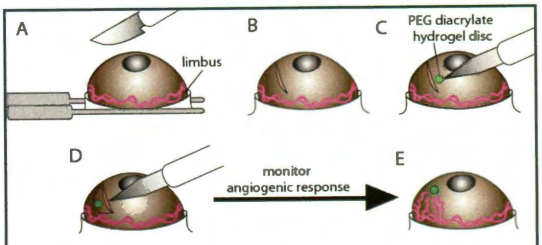

3.1: Implantation of hydrogels into the cornea to define optimal vessel ingression and perfusion. PEG hydrogel discs are inserted into an incision made in the cornea (A-D). The cornea is monitored over time to determine the extent of the angiogenic response (E).(Poche, Saik et al. 2010)

factors (FGF2 and PDGF-BB) had already been characterized *in vitro* by collaborators in the West lab (figure 3.2). Several doses of these growth factors were tested *in vivo* to generate a curve of the response of vessel formation, in order to determine the relationship between implanted growth factor concentrations and the amount of the construct that invading vessels ultimately occupy.

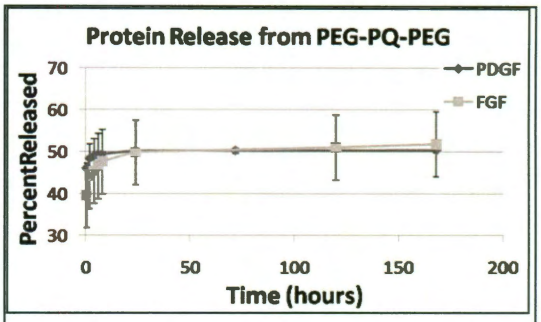

Figure 3.2: Growth factor release from degradable hydrogels *in vitro. J Saik personal communication.*

One goal in the design of these constructs was rapid host vascularization. Invading vessels must reach the target implant within a short period of time, to allow for the efficient delivery of metabolites and oxygen, and thus permit survival of implanted cells. As previously stated, 7-14 days was chosen to provide the ideal engraftment environment; in addition, as little time as possible for vessel invasion could allow for rapid perfusion of the newly implanted grafts. Beyond efficient delivery of nutrients, function of the tissue vasculature should be the next most important consideration. The goal of tissue engineering is to recapitulate closely tissue; therefore the goal was the recreation of as many of the morphological characteristics of the natural tissue niche as are possible.

A dose response curve was compared to known space filling values measured from vessel beds in other tissues, including skin, the thigh muscle, and the sub-ependymal zone (SEZ) in order to interpolate the concentration of PDGF-BB and FGF2 needed to recapitulate the vascular morphology. Rigorous morphometric

analysis to compare the resulting induced vasculature to endogenous vessels was undertaken.

3.2.1.1 Synthesis and Purification of Proteolytically Degradable and Cell Adhesive Polymer Derivatives

Proteolytically degradable hydrogels were prepared by incorporating a peptide sensitive to MMP2 and MMP9, GGGPQGIWGQGK (abbreviated PQ), into the PEG backbone to generate the enzyme-cleavable PEG-PQ-PEG (West and Hubbell 1998). Fmoc chemistry was used to synthesize the PQ peptide on an APEX 396 solid phase peptide synthesizer (Aapptec), and the resulting peptide was then characterized using Matrix Assisted Laser Desorption Ionization Time Of Flight Mass Spec. Dissolved PQ peptide was reacted with dry acryloyl-PEG-SCM (3,400 Da; Laysan, Arab, AL) at a 2.1:1 PEG-SCM: PQ molar ratio and characterized using a gel permeation chromatography (GPC) system with a PLgel column (5μm, 500Å, Polymer Laboratories, Amherst, MA) and an evaporative light scattering (ELS) detector (Polymer Laboratories). PEG-RGDS was prepared similarly by reacting acryloyl-PEG-SCM with RGDS (American Peptide, Sunnyvale, CA) at a molar ratio of 1.1:1 in the presence of DMSO. Fluorescently tagged PEG-RGDS used to enable visualization of implanted gels was synthesized by reacting PEG-RGDS with Alexa Fluor® 488 carboxylic acid, succinimidyl ester (Invitrogen) at a 10:1 molar ratio of dye: PEG-RGDS in dimethylformamide as previously described (Moon, Saik et al. 2010).

3.2.1.2 Hydrogel Fabrication

Hydrogels were prepared for crosslinking using a stock solution of the photoinititator 2,2-dimethoxy-2-phenylacetophenone (acetophenone) dissolved in N-vinylpyrrolidone (NVP) (300 mg/ml). The prepolymer solution was prepared to contain a 10% polymer weight percentage (100 mg/ml) of PEG-PQ-PEG, 3.5 μmol/ml PEG-RGDS, 10 μl/ml acetophenone stock solution, and angiogenic growth factors. Four different concentrations of proteins for the dose escalation were tested: (1) 10 ng FGF-2 and 40 ng PDGF-BB (low dose), (2) 40 ng FGF-2 and 160 ng PDGF-BB (medium dose), (3) 80 ng FGF-2 and 320 ng PDGF-BB, and (4) 160 ng FGF-2 and 640 ng PDGF-BB (high dose shown in figures 6 and 3). Hydrogels were prepared by injecting 0.12 μl of the pre-polymer solution in between two precleaned, sigmacoted (Sigmacote, Sigma Aldrich) glass slides spaced by a 0.005 inch thick poly(tetra fluoroethylene) spacer and secured with binder clips to make a 0.005 inch high, cylindrical implant with a radius roughly 300 microns. The gels were exposed to UV light (B-200SP UV lamp, UVP, 365 nm, 10 mW/cm^2) for two minutes to allow crosslinking and immediately implanted into the cornea micropocket as described below.

3.2.1.3 FLK1-myr::mCherry Mice

Mice expressing the mCherry fluorophore via the Flk1 promoter have previously been characterized (Larina 2009). Mice used in this study were from the colony established in the Dickinson lab at Baylor College of Medicine containing fluorescently labeled endothelial cells, and all experiments were in accordance with an IACUC and AALAS approved animal protocol at Baylor College of Medicine. These mice allowed for visualization and imaging of blood vessels for this study.

3.2.1.4 The Corneal Micropocket Assay

An incision was made in the cornea with a micro knife at approximately 50 microns depth. Next, a Von-Graefe cataract knife was used to separate the stromal layer, allowing the formation of a micropocket. This process is depicted in figure 3.3. PEG based hydrogel implants were placed in the corneal pocket with great reproducibility 500 microns away from the limbus and checked for goodness of fit. For each treatment group five animals were studied. The number of animals selected was based on a power calculation assuming $\sigma = 0.30$, which was based on pilot studies. Controls included opposite eye sham surgery, which showed no vascular response in the nearby limbic region, and implantation of hydrogels not containing growth factors, which produced a similar response to the sham surgery. These controls are published in similar work from these authors (Poché 2009).

3.2.1.5 Analysis of Angiogenic Response

Several different growth factor groups were implanted for analysis, including one group with FGF-2, one group with PDGF-BB and one group containing both factors in a 1:4 ratio, respectively (as previously described). At designated timepoints, eyes were excised from euthanized mice, and the cornea was dissected and flatmounted by cutting the cornea in four locations 90 degrees apart, creating a relatively flat corneal surface (figure 3.3). Imaging regions were chosen by selecting a region within the original implant site where vessels had grown. Three slightly overlapping regions covering the vascularized area were selected for each sample. Confocal images of Flk1-myr::mCherry labeled vessels were acquired from flatmounted corneas containing the tissue constructs using an LSM 510 META (Carl Zeiss) confocal microscope and a C-Apochromat 40x/1.2NA water immersion lens. A 543 nm laser was used to excite the mCherry fluorophore, and 22 micron thick z-stacks of vessels labeled by mCherry directly on the scaffolds were collected such that the step size between two successive images in z-stacks was 1.1 microns. This thickness was chosen because previous studies of vasculature where similar parameters were measured used these dimensions for tissue imaging (Gould, Vadakkan et al. 2010). Each 8-bit image in the z-stacks consists of 512 x 512 pixels. In the final step, each image was subjected to quantification, and the measured parameters were compared. The variation of all samples was less than 10% so each sample's measurements were averaged, to determine the measured fractal, vessel density or lacunarity value. Within the low dose treatment subset of the FGF-2 only

group, examples of implants were found that had vessels growing near the implants but not upon the surface of the hydrogel. These cases accounted for around 40% of the implants attempted in this dose group, thus making it impossible to quantify and compare space-filling measures for all implants. Given that finding, in the implantations that were possible to compare, similar trends to the other low dose treatment groups were found.

3.2.1. 6 Vessel Branch Points and Diameters

Vessel branching was quantified using the LSM image browser to count the total number of branch points per three dimensional image fields in each image of vessels. Diameters were likewise quantified, and the results were compared using ANOVA with post hoc Tukey's test.

3.2.1. 7 Image processing

Images of the vascular beds were processed as described in figure 3.3. This method was designed to replicate the method described in previous studies used to quantify microvessel morphology (Gould, Vadakkan et al. 2010). Briefly, stacks of the vessels were projected then thresholded in order to create binary images for processing. Thresholds were kept constant between images of vessel beds to ensure comparison methods. Figure 3.3 (A-D) summarizes the employed image pre-

processing pipeline. Images of vessels were first converted to projections using Image J and then converted to 8-bit grayscale. These projected images were opened in Adobe Photoshop and had an unsharp mask applied to them, which serves as a high-pass filter to remove haziness from around the vessels while preserving vessel

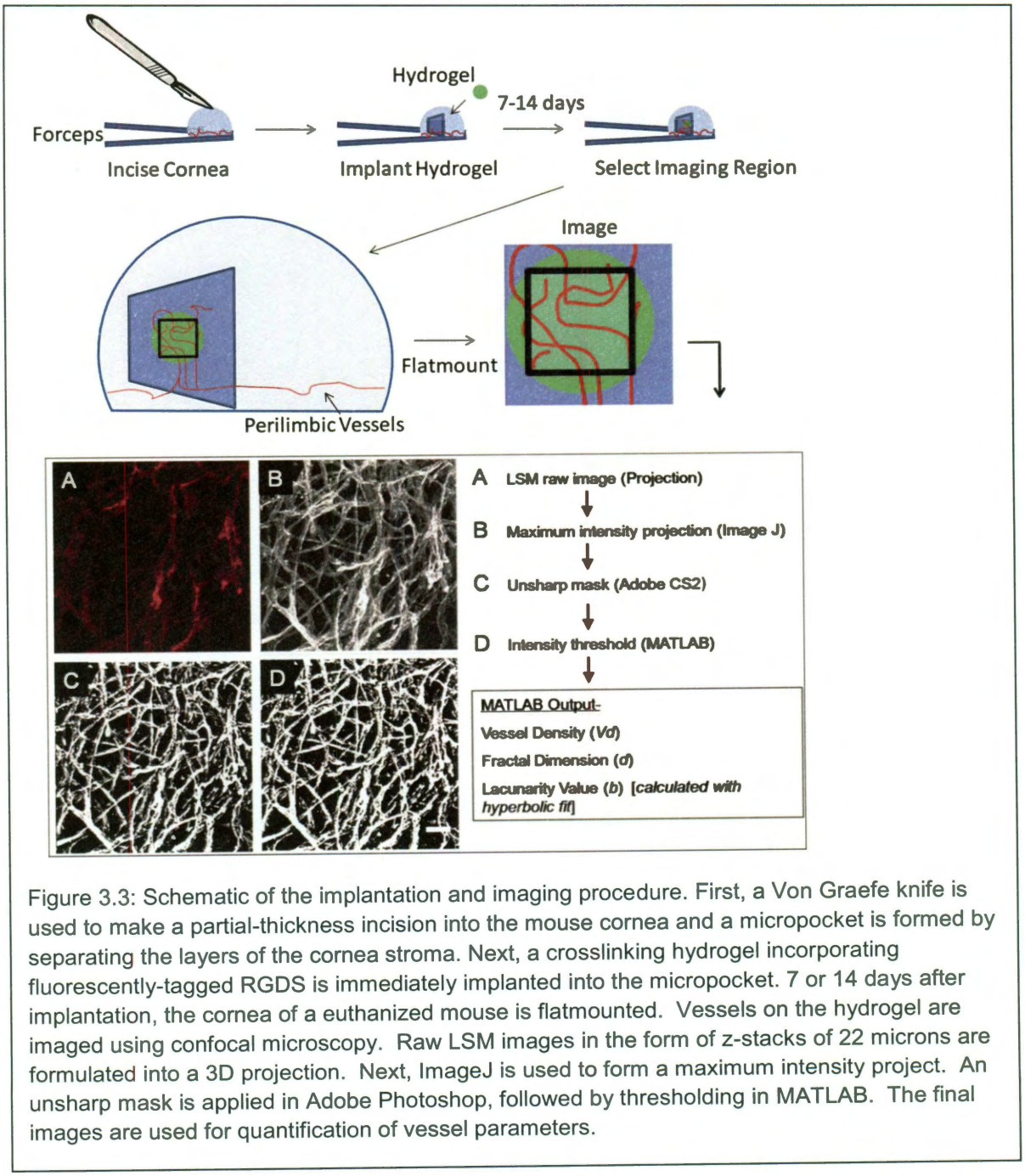

Figure 3.3: Schematic of the implantation and imaging procedure. First, a Von Graefe knife is used to make a partial-thickness incision into the mouse cornea and a micropocket is formed by separating the layers of the cornea stroma. Next, a crosslinking hydrogel incorporating fluorescently-tagged RGDS is immediately implanted into the micropocket. 7 or 14 days after implantation, the cornea of a euthanized mouse is flatmounted. Vessels on the hydrogel are imaged using confocal microscopy. Raw LSM images in the form of z-stacks of 22 microns are formulated into a 3D projection. Next, ImageJ is used to form a maximum intensity project. An unsharp mask is applied in Adobe Photoshop, followed by thresholding in MATLAB. The final images are used for quantification of vessel parameters.

diameters. The finished grayscale image was opened in MATLAB, and a threshold of 90 was applied, based on the ability to maintain vessel diameter with no significant erosion or dilation seen between the original images and the thresholded image.

3.2.1. 8 Fractal Dimension, Lacunarity, and Multifractal Spectra

Induced vessel morphology was assessed by imaging vessels and applying algorithms developed and described in Gould et al.(Gould, Vadakkan et al. 2010) to determine vessel density, diameter, fractal dimension, and lacunarity. Also, the programs used to extract these parameters are available online through the MATLAB central file exchange (Vadakkan 2009; Vadakkan 2009; Gould, Vadakkan et al. 2010).

3.2.1.9 Vessel Density Measurement

Briefly, to calculate vessel density, a binary image was created. Subsequently, the total number of pixels containing signal (white pixels) were determined and divided by the total number of pixels in the image (512x512) to output vessel density.

3.2.1. 10 Fractal Dimension

The fractal dimension was calculated using a box counting algorithm (Moisy 2006; Lopes and Betrouni 2009). Here, a grid was applied to the binarized image of the vessels. Within this grid the length of the boxes determined is ε. Next, the number of positive boxes (containing at least one white pixel) was counted, called N (ε). Finally epsilon vs. N (ε) was plotted and shown to have a logarithmic function (figure 3.4 B). Finally, the log (ε) vs. log (N (ε)) was plotted, and the slope was determined from the plot (figure 3.4 C). The slope is D_0, the fractal dimension.

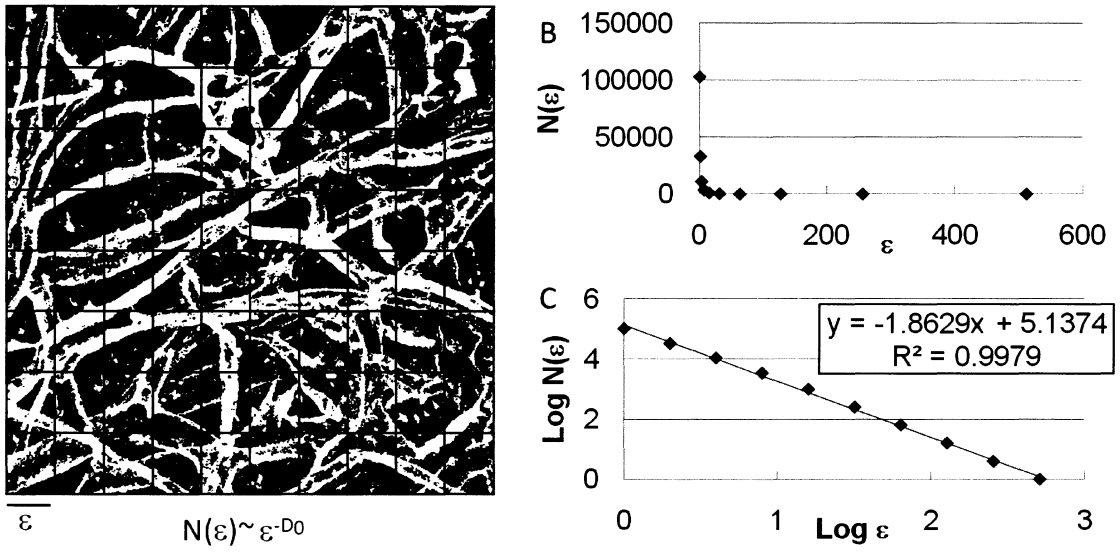

Figure 3.4: Measurement of the Fractal Dimension Using a Box-counting Algorithm. Here, A demonstrates the application of a grid to the image of engineered vessels. After applying a grid, positive boxes (containing at least one white pixel) are counted. B shows the plot of positive box number versus box size. C shows the log (positive boxes) versus log (box size) plot. The slope of this line is the fractal dimension.

3.2.1. 11 Lacunarity

The lacunarity parameter (b) was routinely measured using a gliding box algorithm (Masters 2004; Tolle, McJunkin et al. 2008). Briefly, an ε x ε box with width ε was placed at the top left corner of an image. The number of white pixels in the box was counted. The box was then glided to the right (one pixel) and the number of pixels in the ε x ε box was counted. The process was repeated until the box reaches the bottom right corner of the image. If ℓ is the size of the image, the number of boxes of width ε is $N(\varepsilon) = (\ell-\varepsilon+1)^2$. The width ε of the box is chosen such that its numerical value is equal to 2, 4, 8,..,ℓ. For each box width ε, both the sum of the number of signal pixels in each box $Q_1 = \sum_i p(i,\varepsilon)$ and the sum of the square of the number of signal pixels in each box $Q_2 = \sum_i p(i,\varepsilon)^2$ are measured. Lacunarity $L(\varepsilon)$ at a box size ε is defined as $(N(\varepsilon) \times Q_2) / Q_1^2$. $p(i,\varepsilon)$ is the number of signal pixels in the i^{th} box and $i \in [1, N(\varepsilon)]$. In the gliding box algorithm, the box of size ε is placed over each pixel in the image and $p(i,\varepsilon)$ is calculated for each box centered on the i^{th} pixel. Therefore the lacunarity measurement adds to the description of an object with a known fractal dimension, in describing the empty space around the object, thus relating how the object fills space.

3.2.1.12 Multifractal Analysis

The multifractal method described in the methods section of chapter two was implemented in this study to examine the morphology of vessels induced with the combination of PDGF and FGF from the 14 day time point. Symmetry and heterogeneity analysis of the curves was performed in order to examine the High, Medium and Low dose treatments, in order to provide information about each multifractal distribution.

All of these methods were used to analyze images of blood vessels induced in response to varying doses of growth factors, in order to better understand host vessel induction, and to better tune the hydrogel implants to induce vessels with a desired morphology. The results from this process are described below.

3.2.2 Results: Vessel Induction

3.2.2.1 Induction of Vessels and Morphological Analysis

Three different concentrations (doses) of PDGF-BB and/or FGF-2 were used to induce vessel formation on PEG-based hydrogels implanted into the mouse cornea micropocket. Growth factors were used individually to attempt to parse out individual effects and in combination to investigate synergistic effects. Resulting

vessels were imaged 7 and 14 days after implantation (figure 3.5 A, B), and the resultant vessel morphology varied based on dose. Space-filling morphological parameters including fractal dimension, vessel density, and lacunarity were used to quantify resulting vessel morphology. Clear trends in the values of the morphological parameters were present, where higher dose treatments yield higher vessel density, greater fractal dimension and a higher lacunarity parameter *b*, reflecting less lacunae or open space between vessels versus lower dose treatments (figure 3.5 C, D). These trends were confirmed using statistical tests (ANOVA and Tukey's post hoc analysis), which indicated a significant difference between high and low dose groups at 7 and 14 days in all treatment groups, ($p<0.05$) when using the vessel density and fractal dimension analysis.

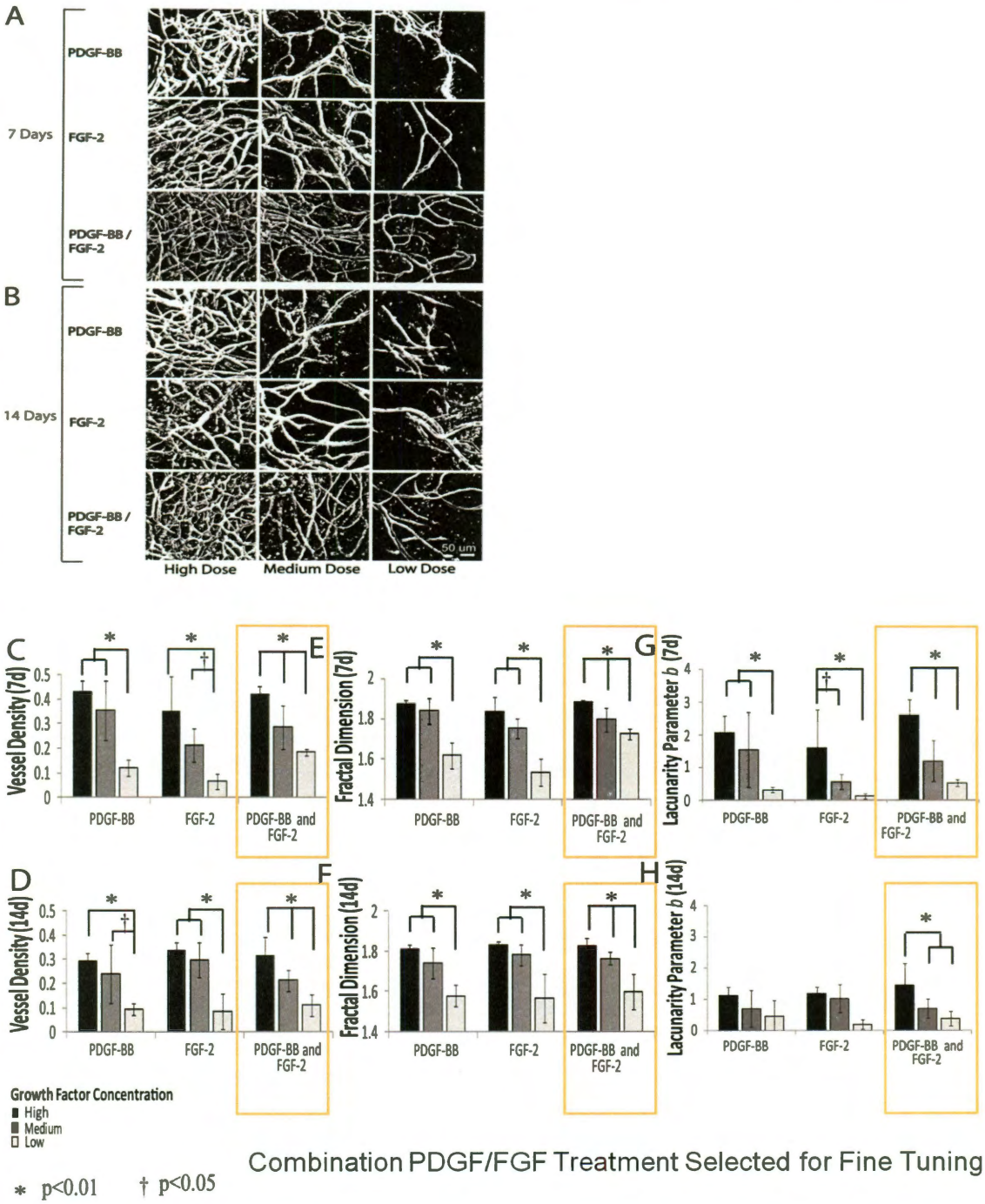

Figure 3.5 : Growth Factor Dose Induces Differing Vessel Morphology. 7 days (A) and 14 days (B) after implantation, vessels were visible in response to PDGF-BB and/or FGF-2 at three different concentrations. Vessel density, fractal dimension, and lacunarity were measured to quantify the vascular response (C-H). 7 Days after implantation, vessel density, fractal dimension and lacunarity parameter b were found to increase as growth factor dose increased (C, E, G). 14 days after implantation, similar trends in vessel density, fractal dimension and lacunarity parameter were observed in response to the growth factors PDGF-BB and FGF-2 at similar dose concentrations (D, F, H). For this study high dose was 640:160ng PDGF-BB: FGF-2, medium was 160:40ng PDGF-BB: FGF-2, low dose was 40:10ng PDGF-BB: FGF-2.

In order to compare the differences between the individual experimental groups, between growth factor types, across dose concentrations, and at seven and fourteen days, ANOVA with post-hoc Tukey's tests were performed on each measured morphological parameter dataset. All of the observations for vessel density, fractal dimension, lacunarity, branch points, and vessel diameters are included in tables in the appendix (Tables A1-A5). Importantly, for brevity the key differences and observations are highlighted in the rest of this section, which helped to determine the best concentrations and types of factors to use as well as the best timepoint for tuning the microvasculature to mimic vessels from normal tissues.

Three key findings were present: first, there were significant differences in all cases between high and low dose groups, indicating a dynamic range of vessel morphology ($p<0.01$), second, the PDGF / FGF combination group at 14 days exhibited significant differences between high, medium and low dose groups using vessel density, fractal dimension, and lacunarity ($p<0.05$), and third, other groups lacked the same level of separation between dose groups.

At the 7 day timepoints, lacunarity proved significantly different amongst dose groups. However, at 14 days the differences between high and low dose groups were not significant except in the PDGF / FGF combination group which showed differences between all three dose groups ($p<0.01$) at 7 and 14 days. In all treatment cases, the high dose groups were significantly higher in vessel density and fractal dimension, while in some, the medium dose groups were significantly different from either the low or the high dose groups, but not both.

The high dose in all treatment groups exhibited vessel densities of around 40% at 7 days and near 35% at 14 days. Although these trends suggest remodeling, no significant difference within groups and doses in the density from 7 to 14 days was observed. In comparison to the 7 day vessels, the 14 day vessels were visually observed to have lower diameters, and the branching was similarly observed to be slightly lower in some groups (figure 3.5 A,B). Within the PDGF / FGF combination group, the high, medium and low dose groups were significantly different in branching morphology ($p<0.01$) at 7 days, with high dose exhibiting the greatest branching (74±5.5) versus medium (56±3.8) and low (17±5.0) dose groups (figure 3.6 A). At 14 days similar differences within this treatment group were seen ($p<0.05$). This level of separation between doses with branching was not seen in the FGF and PDGF alone groups. Similar trends were observed for vessel diameters, within dose groups at 7 days, in that there were differences between high, medium and low dose groups in the case of FGF or PDGF / FGF ($p<0.01$). In the PDGF alone treatment, there was only a significant difference between medium and low dose groups ($p<0.01$) (figure 3.6 C).

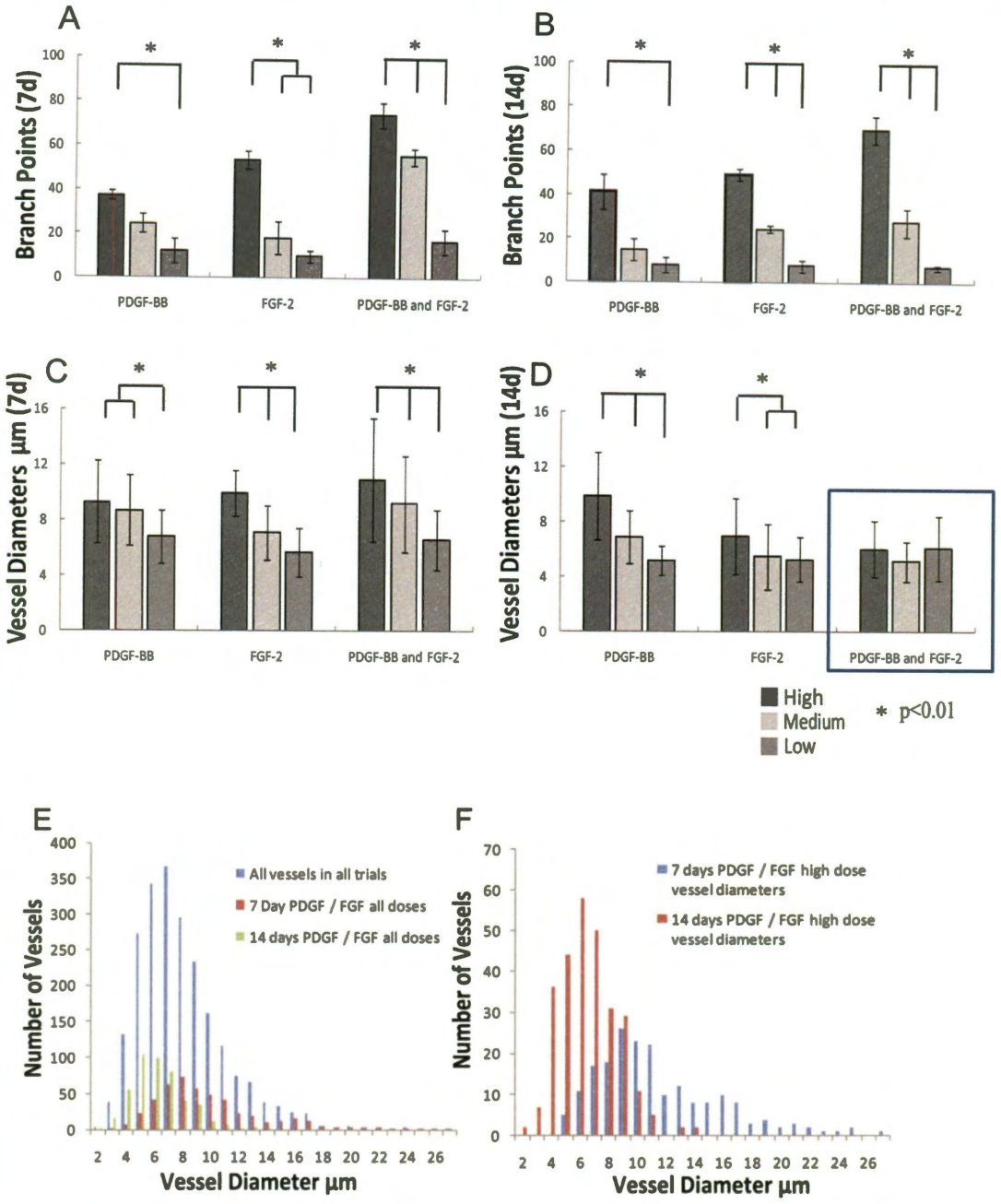

Figure 3.6: Branch point and vessel diameter comparisons. Branching was quantified, by counting the number of branch points using the LSM image browser software in the three dimensional z stacks of the different vessel structures at 7 and 14 days (A, B). Diameters of vessels were measured in similar fashion at 7 and 14 days (C, D) and a histogram was plotted to elaborate on the differences between vessel diameters (E). Interestingly, there were not significant differences between branching from 7 to 14 days in all groups except the medium dose group in the combination PDGF-BB / FGF-2 treatment group ($p<0.05$). In the case of the vessel diameters, there were significant changes in treatment groups between 7 and 14 days, however, the differences that were apparent within treatments, between doses at seven days ($p<0.01$) were not seen in the 14 day timepoint in the PDGF-BB / FGF-2 combination treatment group. This suggests the combination group induces vessels with relatively stable branching and relatively uniform vessel diameter distribution at 14 days, reflected by the histogram in (F) which shows an increased fraction of 6-8um diameter vessels.

One important change highlighted by diameter measurements was the difference within dose groups and within specific dose levels between 7 and 14 days. In each group, with the exception of the PDGF only high dose group, there was a significant decrease in the average vessel diameter between the time points at 7 and 14 days ($p<0.05$). Also at 14 days, the only group which had no significant difference between high, medium and low dose groups was the PDGF / FGF containing group.

In contrast, the PDGF alone and FGF alone groups showed significant differences between the high and low dose groups, and medium and high dose groups ($p<0.05$). These data indicated that at 14 days, the vessel branches were relatively stable and that the vessel diameters are more uniform particularly in the PDGF / FGF combination group. In summary, the key findings were that significant differences in the vessel density, fractal dimension, and lacunarity were supported by similar differences in branching; that the branching differences were only consistently different in the combination treatment, and that the only group with relatively equally distributed vessel diameters in all three treatment groups was the combination treatment group. Importantly, vessels induced in response to encapsulated growth factors exhibit a tunable morphological range, and the combination treatment with PDGF and FGF provides the best range for fine tuning and optimization.

3.2.2.2. Multifractal Analysis of Induced Vessels

Multifractal Analysis was performed on the images of vessels induced with the combination of PDGF and FGF at the 14 day timepoint. This analysis provided for a spectral analysis of the three different treatment groups.

	Sample 1	Error	Sample 2	Error	Sample 3	Error		
Low Dose							Average	Error(sum)
D0	1.658485	0.03	1.582185	0.03	1.696165	0.02	1.64561195	0.04690416
D1	1.581964	0.01	1.535058	0.01	1.624481	0.01	1.58050109	0.01732051
D2	1.559515	0.01	1.511986	0.01	1.598304	0.01	1.55660168	0.01732051
Medium Dose	Sample 1	Error	Sample 2	Error	Sample 3	Error	Average	Error(sum)
D0	1.835848	0.01	1.767277	0.02	1.815202	0.02	1.80610901	0.03
D1	1.79356	0.01	1.709314	0.01	1.737585	0.01	1.74681961	0.01732051
D2	1.778735	0.01	1.682708	0.01	1.703069	0.01	1.7215039	0.01732051
High Dose	Sample 1	Error	Sample 2	Error	Sample 3	Error	Average	Error(sum)
D0	1.92452	0.02	1.907061	0.03	1.921928	0.03	1.91783617	0.04690416
D1	1.891114	0.02	1.867499	0.02	1.882057	0.02	1.88022326	0.03464102
D2	1.875454	0.02	1.849198	0.02	1.862768	0.02	1.86247342	0.03464102

Table 3.1: Generalized Fractal Dimensions of the Dose Escalation Samples. Here the generalized fractal dimensions are provided for each of the measured samples. The Average values are also presented along with the additive error for each calculation.

First, in order to determine if the images of the objects were in fact multifractal, all of the generalized dimensions were recorded from the algorithm and the three different values for each of the samples in each of the three groups were recorded. Next, the error estimates were determined using the same methods from chapter 2, whereby the linear regression analysis was performed on each log/log plot of the moments from each of the generalized dimensions. These values are reported in Table (3.1), where the average measured generalized dimensions are reported along with the error estimates. The generalized dimensions are distinctly different, as reflected by the error estimates for each moment in each sample, satisfying the requirement for the provision of a multifractal. The plot of the generalized dimensions is shown in figure 3.7, with the separation between each generalized dimension, and the additive error associated with each moment is represented by the error bars plotted on the graph. This graph helps to summarize the finding that the induced vessels in each treatment dose at 14 days possess multifractal behavior, and that they possess relatively different morphological structure, including distinctly different generalized dimensions. It is important to stipulate that the determination of multifractal behavior of each object is based on the analysis of each image and the separation of the generalized dimensions as dictated in table 3.1. Additive error bars in the graph from figure 3.7 do overlap in the case of the low and medium dose groups and are not indicative of whether or not each image represents an object with multifractal behavior.

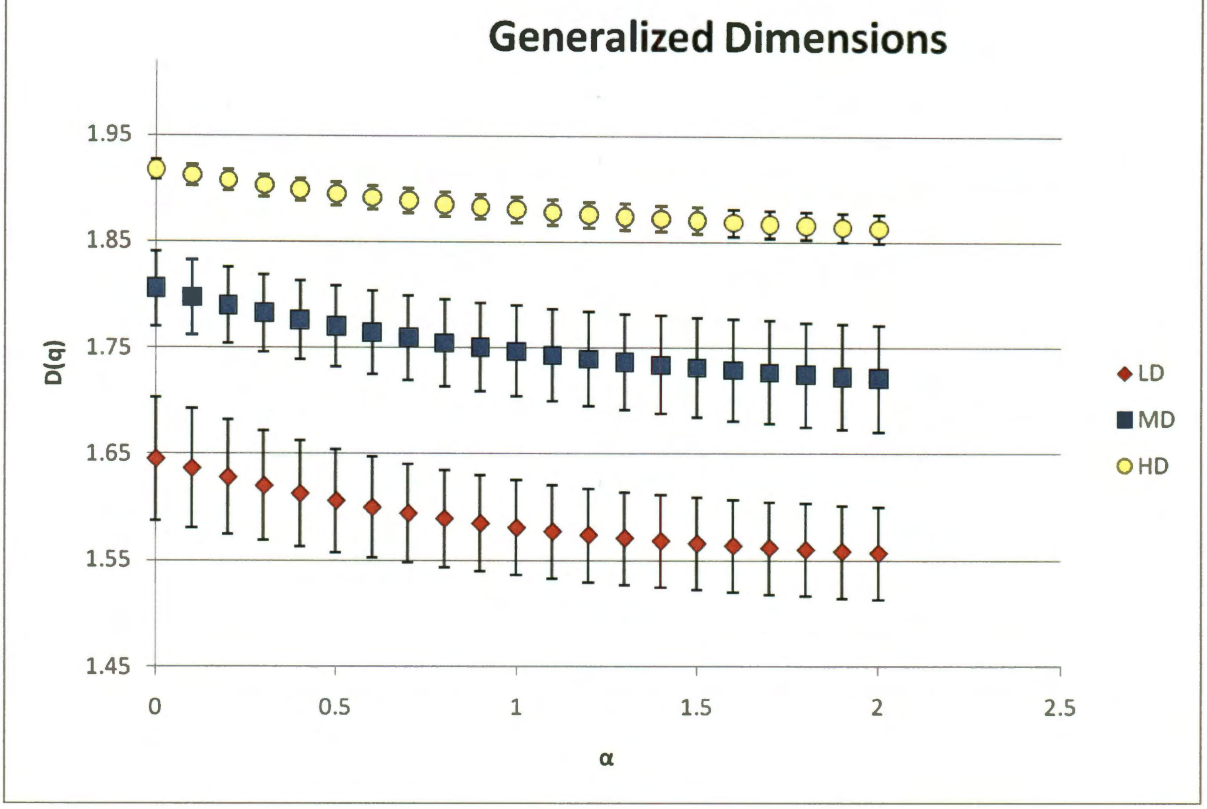

Figure 3.7 : Generalized Fractal Dimension Plots. This graph shows the moments calculated for D(q) at each value of alpha, and the X values 0, 1, and 2 represent the moments of the Generalized Dimensions, D0, D1 and D2. The error bars come from the measured error at each moment of the plot, based on the linear regression of each linear fit for each moment. Since error bars represent the additive error of each of the three groups, their overlap does not exclude multifractal behavior. The determination of multifractal behavior is based on each image and is determined based on the error between dimensions as reported in table 3.1.

Finally, the spectral output from the algorithm was plotted and is shown in figure 3.8. This figure helps to summarize the finding that each group of doses, low, medium and high, induced vessels which were multifractal and morphologically different. The spectra reflect the finding that high dose treatment led to the induction of vessels with relatively high complexity and low distribution of avascular space, as

represented by the upward and rightward shift of the spectral peak. This is in comparison to the medium dose treatment and the low dose treatment. The relationship of the spectral peaks of each sample mimic the findings of the simple fractal analysis from the previous section, where with greater doses there is increasing complexity and decreasing distribution of avascular space.

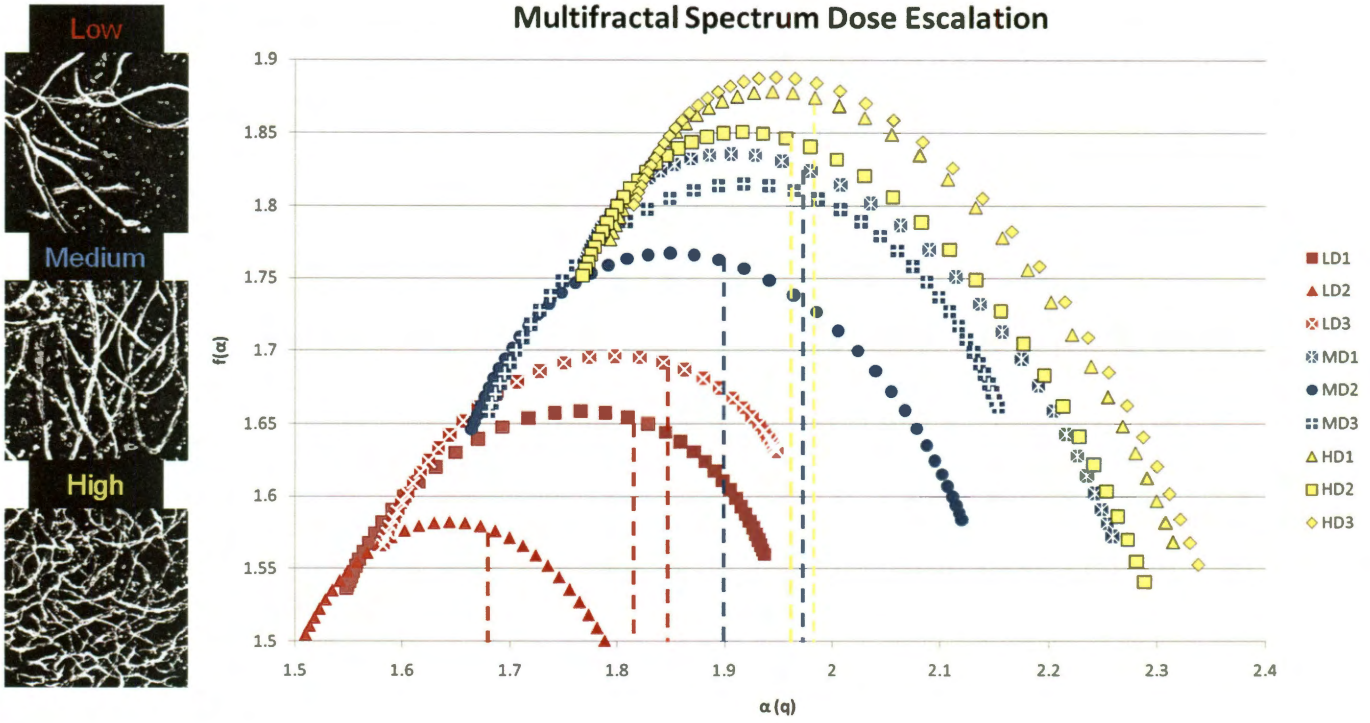

Figure 3.8: Multifractal Spectral Analysis of the Dose Escalation Combination PDGF/FGF Treatment at 14 days. This spectral graph helps to summarize the morphological differences between low, medium and high dose treatments at 14 days, as reflected by the images of each treatment group, shown to the left. The spectra shift upward and to the right with increasing dose, indicating increasing complexity of vessel morphology along with decreasing distribution of avascular space. The dashed lines indicate the cutoff values for which the r^2 values of the linear fit for the approximation for the corresponding alpha values fall below 0.95.

Spectral analysis was then subjected to heterogeneity and symmetry analysis, to confirm multifractal behavior, and to examine the differences in the shape of each of the spectral curves. This is depicted in figure 3.9.

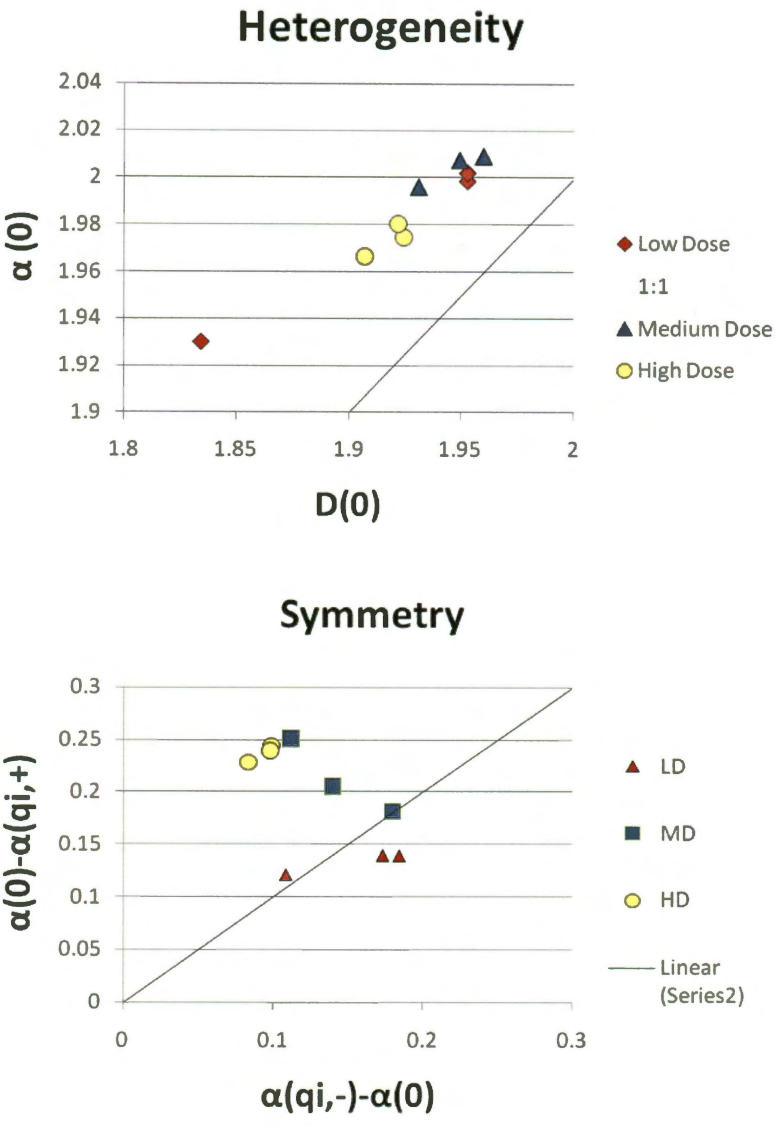

Figure 3.9: Heterogeneity and Symmetry Analysis. The Multifractal spectra were subjected to a Heterogeneity and symmetry analysis, in the same method as described in chapter two. The heterogeneity analysis helps to confirm the multifractal behavior of each of the samples, as the plotted values are not on the 1:1 line. Symmetry analysis helps to show that the High dose vessels have much more contribution of the overall image coming from the complex vascular space, in comparison to the medium dose treatment and the low dose treatment. The lose dose treatment group falls below the 1:1 line, indicating the avascular space contributes more to the spectrum than the vascular space in the images.

Spectral analysis helped to provide more information about the nature of the induced vessels as well as the differences in the shape of their morphological spectra. Heterogeneity analysis confirmed that the spectra were heterogeneous and did represent objects with multifractal behavior, as represented by the fact that the values do not fall on the 1:1 line. Symmetry analysis provided information about the differences in the shapes of the spectral output for each dose treatment group. In the symmetry analysis, high dose treatment was shown to induce vessels where the vascular portion of the image accounted for more of the complexity of the object, as reflected by the points which fall above the 1:1 line. This was in comparison to the medium and low dose groups, where the points are closer to the 1:1 line, and in these images, the non vascular space contributes more to the spectral output. In the low dose treatment group, the non vascular space actually contributes more to the morphology of the object than the vascular space and this is why two values fall below the 1:1 line. In total, heterogeneity and symmetry analysis help to further scrutinize the differences seen in the multifractal spectra.

In summary, multifractal analysis of the combination treatment group at 14 days helped to provide more information about the morphology of the vessels induced. This analysis helped to show the induced microvascular beds are multifractal in nature and that they possess differing complexity. Induction with combination PDGF and FGF at 14 days yields vessel beds which exhibit multifractal behavior with different doses being capable of inducing vessel morphology with

discrete generalized dimensions and multifractal spectra with differing heterogeneity and symmetry.

3. 3 Recapitulating Native Tissue Vessel Morphology of Skin and Muscle

3.3.1 Methods

The PDGF / FGF treatment group at 14 days was selected to fine tune the vascular response, in order to interpolate the necessary concentrations to recapitulate vessel morphology observed in native tissues (Gould, Vadakkan et al. 2010). A fitting function was applied to each set of data at each time point for each recorded parameter (vessel density, fractal dimension, lacunarity).

In order to induce target vessel morphology, the dose response of each of the treatment groups was plotted, and the relationship between dose and fractal dimension was determined. Using this information along with the known fractal dimensions of various tissues from chapter 2, dose concentrations were calculated which would be capable of induction of the target morphology, given the location on the interpolation curve.

New angiogenic hydrogels were implanted in the mouse corneal micropocket assay, containing combination doses of PDGF and FGF based on the calculations from the interpolation. These hydrogels were followed for 14 days and then the animals were sacrificed and the induced vessel morphology within the constructs,

designed to mimic host tissue vessels was analyzed for comparisons. In each experiment, where the induced mimetic tissues were designed to mimic host vessels, images of the tissues were analyzed using the algorithm described in chapter two. Pair wise comparisons were made for each experiment between the induced mimetic and host vessels, using a two tailed t test assuming unequal variance in order to compare vessel branching and diameter.

3.3.2 Results : Skin and Muscle Induced Mimetic Vessels

The best fits were seen for all measurements in the combination PDGF / FGF group, which had r^2 values which were greater than those of the FGF only and PDGF only groups (which were no higher than r^2=0.77) at both 7 and 14 days. Importantly, the r^2 values were the highest for the 14 day timepoint in the PDGF / FGF treatment group (r^2=0.94 at 14 days, compared to 0.80 at 7 days).

The fractal dimension from each combination PDGF / FGF group at 14 days was plotted versus the original dose used (figure 3.10 A). Linear fits were then applied to the data in order to interpolate the dose of PDGF and FGF necessary to induce vessels with a known target fractal dimension (figure 3.10 A). Figure 3.10 shows the original data (fractal dimension, vessel density, and lacunarity) from the dose escalation using the combination PDGF / FGF treatment group, plotted with the linear fit shown and the 95% confidence intervals plotted above and below. Native skin and muscle tissues from the same fluorescent mouse system were imaged prior to

this study to identify the target fractal dimensions at 1.80 ± 0.03 and 1.70 ± 0.05, (Gould, Vadakkan et al. 2010). The growth factor concentrations necessary to reproduce these fractal dimensions (Gould, Vadakkan et al. 2010) were determined based on the linear regression in Figure 3.10, the growth factor concentrations corresponding to the measured fractal dimension from the intact tissues were as follows: 46 ng FGF-2; 184 ng PDGF-BB for skin, solid line; 22 ng FGF-2; 89 ng PDGF-BB for thigh muscle, dashed line.

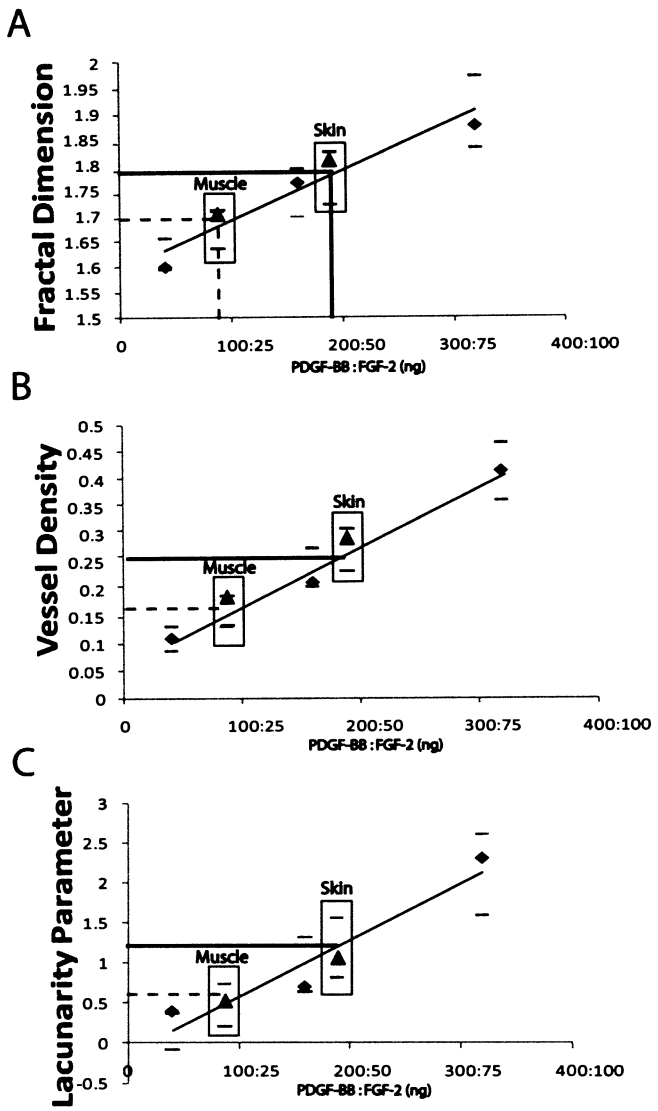

Figure 3.10: Morphological Parameters Used to Calculate a Linear Fit. Fractal dimension (A), vessel density (B) and lacunarity parameter b (C) were plotted against dose released. A linear fit was applied to the data, with R^2 values over 0.9 in each parameter based plot. Linear fit equations were used to back calculate doses necessary to recapitulate vessels with given morphological parameters. The doses were based on the linear plot for the fractal dimension. The measured values for the induced vessels using the interpolated skin and muscle doses are plotted and indicated by the triangle symbols. The 95% confidence intervals are noted as small bars above and below each value. The linear fit for the fractal dimension (A) had an r^2 value of 0.92. For vessel density the fit was $r^2 = 0.96$, for lacunarity $r^2 = 0.92$.

Implants containing the doses of growth factors needed to recapitulate skin and muscle vessel morphologies showed a similar visual appearance to native vessel counterparts (figure 3.11 A and B, C and D). Interestingly, even though the fractal dimension was used to tune the vascular response, the muscle and skin vasculature morphological parameters of lacunarity and vessel density also followed a linear fit. This is shown in figure 3.10, in which all the measured parameters are plotted with a triangle, and are highlighted with a surrounding box. These plotted values represent the actual measured values of the parameters from the tuned constructs, with a 95% confidence interval plotted. Furthermore, established vessel quantification parameters

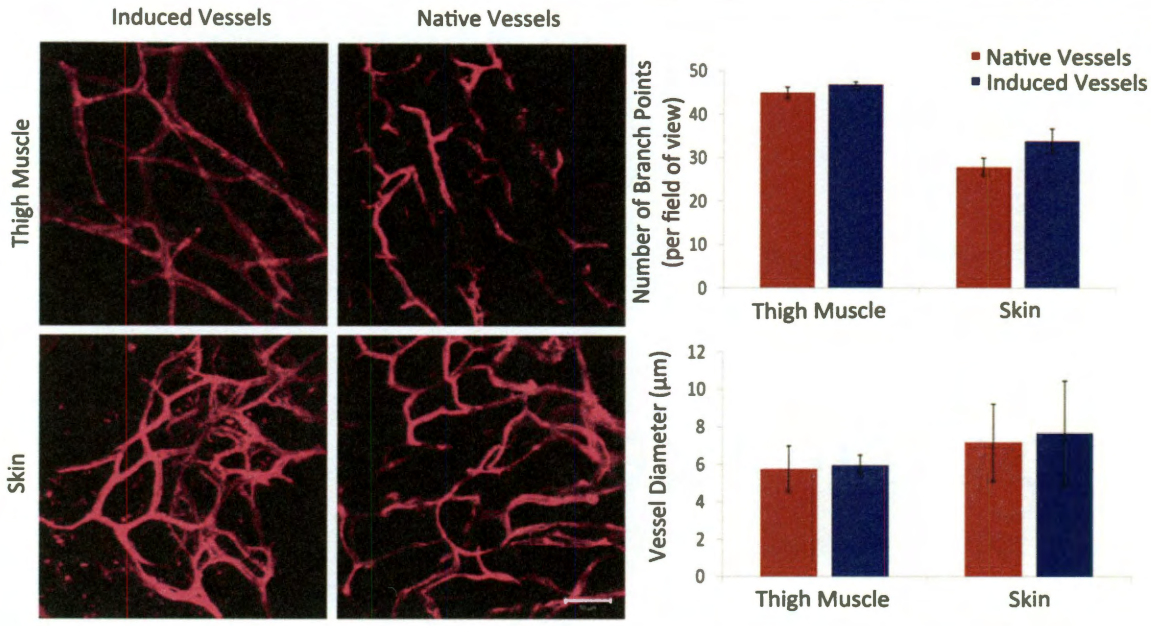

Figure 3.11: Recapitulation of Native Vessels. Induced vessels (A) meant to mimic the native vessels in thigh muscle (B) and similar vessels (C) induced to recapitulate skin vessels (D) were imaged and analyzed. Vessels induced with the hydrogel system using doses for thigh muscle and skin vasculature (A and C) are visually similar to native vessels in thigh muscle and skin (B and D). Additionally, analysis of vessel diameter and branch points indicates no significant difference between native vessel and induced vessel morphological characteristics (E and F) p=0.68 and 0.11 for branch point comparisons of native and induced muscle and skin, p=0.48 and 0.55 for vessel diameter comparisons of native and induced muscle and skin. Scale bar = 50 micrometers.

of vessel diameter (p=0.55 and 0.48 for skin and muscle) and branch points (p=0.11 and 0.68) indicate no statistically significant difference between the induced vessels and the native vessels (figure 3.11 E,F). Table 3.2 provides the complete set of measurements from the induced vessels in the dose escalation experiments (induced mimetic vessels), as well as the similar measurements from the native tissues (measured native vessels). By using space filling morphological parameters such as fractal dimension to design growth factor dosing regimens we were able to tune the response of subsequent vessel formation in terms of characteristics such as vessel diameter and branch points.

Experimental Doses					
320/80 ng (PDGF-BB/FGF-2)	0.41 ± 0.08	1.88 ± 0.03	2.30 ± 0.52	5.42 ± 0.39	84.20 ± 4.02
160/40 ng (PDGF-BB/FGF-2)	0.21 ± 0.04	1.76 ± 0.03	0.70 ± 0.31	6.24 ± 0.22	33.00 ± 5.39
40/10 ng (PDGF-BB/FGF-2)	0.10 ± 0.06	1.59 ± 0.12	0.35 ± 0.23	7.41 ± 0.64	16.00 ± 4.85
Measured Native Vessels					
Skin (native)	0.24 ± 0.01	1.80 ± 0.03	1.03 ± 0.03	7.15 ± 2.05	28.00 ± 2.06
Muscle (native)	0.17 ± 0.01	1.70 ± 0.05	0.73 ± 0.03	5.76 ± 1.20	43.00 ± 1.83
Induced Mimetic Vessels					
Skin Dose	0.29 ± 0.05	1.81 ± 0.04	1.04 ± 0.32	7.65 ± 2.80	32.30 ± 5.00
Muscle Dose	0.18 ± 0.02	1.70 ± 0.05	0.53 ± 0.19	5.97 ± 0.51	47.00 ± 14.20

Table 3.2: Complete Set of Measurements from Dose Escalation and Mimetic Vessel Induction. This table provides the complete set of morphological output parameters for the dose escalation studies as well as the induced mimetic tuning experiments. Notice that the induced mimetic vessels matched the vessel morphology of the target tissues.

3.4 Mimicking the Vascular Morphology of the Sub Ependymal Zone

Another vessel bed that was targeted for similar vessel recapitulation was the native mouse sub ependymal zone (SEZ), which is a stem cell niche in the mouse brain. The SEZ of the brain is a known region of stem cell growth and recently has been shown to have a specific structure which is likely related to the neurogenic properties of this niche. Recreating the vascular morphology seen in the sub ependymal zone of the brain was one goal of this project, and the use of this set of techniques to induce vessels similar to those found in the sub ependymal zone is described below.

3.4.1 Methods

This similar recapitulation was run in parallel using methods from chapter two and compared to the dose escalation findings to determine the necessary doses of growth factors to recapitulate vessel parameters from the neural stem cell niche, the SEZ.

Images of the native neural stem cell niche, the subependymal zone (SEZ), were analyzed to identify the vessel density, fractal dimension and lacunarity. These measured parameters were then used as described in the previous section to calculate the dose needed to induce similar morphology vessels. New angiogenic hydrogels, with encapsulated diffusible angiogenic PDGF and FGF were then fabricated and

implanted in the mouse corneal micropocket assay containing concentrations of growth factors for induction of vessels similar to the native SEZ vessels.

Resulting induced vessels were imaged and compared to the native morphology in order to determine similarities.

3.4.2 Results

The mean fractal dimension of the SEZ fell into a range between the low and medium dose groups of combined PDGF/FGF treatment (Table 3.3).

D	Vd	Frac	Lac
High Dose	0.31±0.07	1.82±0.04	1.32±0.70
Med Dose	0.21±0.04	1.76±0.03	0.70±0.31
Low Dose	0.10±0.06	1.59±0.12	0.35±0.23
SEZ	0.12±0.02	1.66±0.03	0.48±0.09
SEZ engineered	0.14±0.02	1.65±0.04	0.39±0.11

Table 3.3: Recapitulating SEZ like vasculature. Tuning as described in the previous section was performed, and the known values for the SEZ fractal dimension were used to determine the needed dose to induce SEZ like vessels. This dose was 87.07 ng PDGF and 21.77 ng FGF, and when used, it induced vessels which had a similar density, fractal dimension and lacunarity as the native SEZ.

The dose necessary for SEZ-like fractal dimension vessels was calculated based on interpolation from the plot in figure 3.10, using a linear fit between the low and medium dose group data sets. This value was not significantly different from the dose indicated by using the logarithmic equation fit to the data (87 vs. 79ng, b= 1.68 vs. 1.66, error is 0.03). The linear fit interpolated dose from the fractal dimension data at 14 days was predicted to be 87.07 ng PDGF and 21.77 ng FGF.

SEZ-like vessels were induced in the *in vivo* model using doses of PDGF and FGF predicted to generate similar fractal dimension. Figure 3.12 shows images (A-C) of the vessels which recapitulate morphology of vasculature in the SEZ. Vessels were grown along the surface of the implants and imaged in a similar manner as the dose escalation studies. Images A-C are similar setting projections of the vessels grown in the corneal implantation method, upon the surface of the gel.

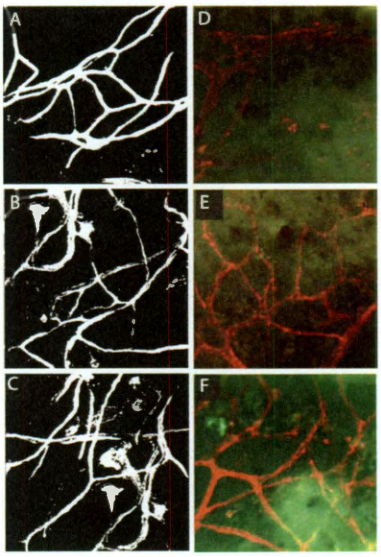

Figure 3.12: Projections of images taken of vessels grown to recapitulate the vasculature in the SEZ. A-C are representative projections of the induced vessels, while D-F are images of the induced vessels (in red) growing on the biomaterial PEG scaffolds (green). Scale bar = 50 micrometers.

Representative images of the vessels (in red) in contact with the RGDS-488 labeled hydrogels (in green) (D-F) are shown to display *in*

vivo juxtaposition with the bioactive scaffolds.

Quantitative analysis of generated SEZ-like vessels showed that recapitulation of the morphological, space-filling measures (fractal dimension, vessel density and lacunarity) measured in the SEZ (figure 3.13) was successful. The measured parameters for the engineered vessels were similar to the observed parameters from the native tissue.

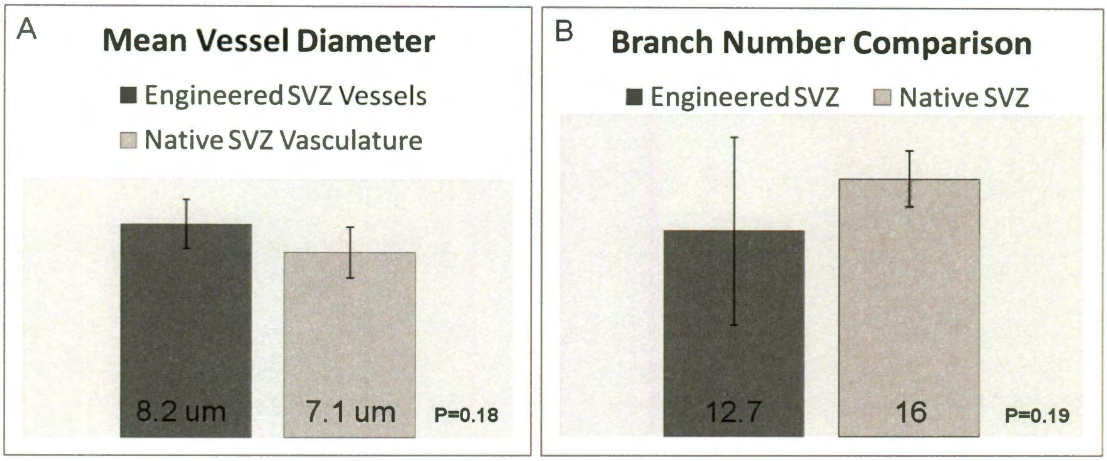

Figure 3.13: Classical methods do not distinguish engineered vessels from native vessels. This comparison with classical morphological methods helps to reinforce the concept that these microvascular constructs are similar in morphology to the natural microvascular niches. For this study n=12.

Finally, comparison of more classical methods reported in the literature, including the branch points (measured from 3d stacks) and vessel diameter between the engineered and native vessels (Fig 3.13 A, B) showed similar values. In order to assure comparison of mean diameters was valid; a histogram was generated to look at the distribution of the vessel diameters. A normal distribution was observed, and a

majority of the vessels had a diameter of 6 um, consistent with the reported mean vessel diameter in the SEZ. This comparison confirmed recapitulation of aspects of vessel morphology, as there was no significant difference between the observed branch point number and mean diameter in native versus engineered SEZ vessels.

In conclusion, the optimization of the induction of vessel morphology allowed for a fine-tuned response, in which the scale invariant measure of the fractal dimension could be used to induce mimetic vessels to match target host vessel morphology, with respect to density, fractal dimension, lacunarity, vessel diameters and branching.

3.5 Discussion

The main results of this study included that; (1) Vessels induced in response to encapsulated growth factors exhibit a tunable morphological range, and the combination treatment with PDGF and FGF provides the best range for fine tuning and optimization. (2) Induction with combination PDGF and FGF at 14 days yields vessel beds which exhibit multifractal behavior with different doses being capable of inducing vessel morphology with discrete generalized dimensions and multifractal spectra with differing heterogeneity and symmetry. (3) The optimization of the induction of vessel morphology allows for a fine-tuned response, in which the scale invariant measure, the fractal dimension can be used to induce mimetic vessels to match target host vessel morphology, with respect to density, fractal dimension, lacunarity, vessel diameters and branching.

Tuning vessel morphology as described in this study could prove valuable for several reasons. Vessel morphology differs from tissue to tissue and under different physiologic conditions. The variation among morphologies found in different tissues likely relates to the different functions of tissues, and may be a product of development and remodeling, whereby early vessel bed morphology is tuned to a certain shape to match needs of the eventual tissue. One goal of this study was to provide a better understanding of the tunability of the host vascular response in tissue engineering with a potential for broader applications in vessel remodeling in repair. These broader applications include regrowth of vessels similar to those found in

native tissues as a potential therapeutic for ischemic diseases (Li, Liu et al.; Carmeliet and Jain 2000; Ferrara and Kerbel 2005). For this reason, the findings of a tunable range in the induction of host vessels in this engineered system could prove useful in future studies.

Another reason tuning induced vessel morphology could prove useful is to address the hurdle in *tissue engineering* of the production of vascularized thick tissues (Carmeliet and Jain 2000; Griffith and Naughton 2002; Laschke, Harder et al. 2006) which exists because diffusion-based transport of most metabolic substrates is limited to 100-150 microns in human tissues (Vacanti; Vacanti, Vacanti et al. 2007). The fundamental understanding of how to shape and control vessel morphology given in this chapter could provide insight for tissue engineering, and also for the study of normal and aberrant vessel growth (Muthukkaruppan VR 1982; Less, Skalak et al. 1991; Carmeliet and Jain 2000; Sharma, Sharma et al. 2005; Goh, Sanghera et al. 2009; Adhemar Longatto Filho 2010).

In order to tune the vascular response *in vivo,* biomaterials have been tailored in this thesis to provide a robust system for vessel induction and stabilization. The rational design of bioactive scaffolds has helped to provide factors for the rapid induction of vascularization, as well as for the long term stabilization of vessels in constructs (Zhu). These scaffolds could provide a biocompatible, mechanically tunable, bioactive substrate for the delivery of cells and other factors in order to allow for induction of host vessels and perfusion (Cheung, Lau et al. 2007). One such scaffold which was described in chapter 1 and was used in this study is poly (ethylene

glycol) (PEG), a hydrophilic and biocompatible polymer, which acts as a "blank slate" by resisting protein adsorption and cell adhesion. The material was tailored in this study to incorporate desired characteristics, including cell adhesion through the addition of covalently immobilized RGD peptide (a sequence commonly found in fibronectin) which allows for integrin binding (Gunn, Turner et al. 2005). These hydrogels were also rendered degradable by incorporating matrix metalloproteinase (MMP) sensitive cleavable cross links (GGGPQGIWGQGK) into the polymer backbone (West and Hubbell 1999; Moon 2008). The degradable crosslinker within these hydrogels had been shown to allow for invading vessels which secrete MMPs, (specifically MMPs 2 and 9) to degrade this peptide sequence and therefore the hydrogel (Moon, Saik et al. 2010). The polymer was photocrosslinked by adding a photosensitive chemical initiator into the polymer solution under relatively gentle conditions, therefore, this scaffold could be used to incorporate cells in future studies (Leslie-Barbick, Moon et al. 2009). Also PEGylated growth factors could be made and incorporated in future studies to stabilize host vessel invasion. In this manner, short-term diffusible factors and covalently bound factors may have the opportunity to work in concert to help provide rapid and stable vascularization of implanted constructs.

Growth factors proved critical to the optimization of the induction and tuning of the angiogenic response. Growth factors incorporated into scaffolds in this study were carefully chosen to provide a robust vessel response. The two angiogenic growth factors which were used in this study included basic fibroblast growth factor

(FGF-2) and platelet derived growth factor-BB (PDGF-BB). These factors provided for a robust vascular host response which was optimized and proved tunable in this chapter. These growth factors had been chosen for several reasons. FGF-2 is released by macrophages in response to hypoxia and initiates vessel formation via stimulation of endothelial cell proliferation and migration (Beenken and Mohammadi 2009). FGF-2 also stabilizes vessels by inducing migration and proliferation of smooth muscle cells (Jackson and Reidy 1993) and by regulating production of angiogenic molecules, including collagenases, β1 integrins, and urokinase type plasminogen activator (Bikfalvi, Klein et al. 1997; Davis 2005; Davis 2008). When added to FGF-2, PDGF-BB helps to stabilize vessel formation (Cao 2003). The combination of PDGF-BB and FGF-2 had already been established as a synergistic combination to induce blood vessel growth and stability in the mouse cornea when used in a 4:1 ratio (Cao 2003) as compared to the use of each growth factor alone. There were other reasons that FGF-2 and PDGF-BB were desirable in vascularization of constructs in this study, including that vessels induced using Vascular Endothelial Growth Factor (VEGF) (another angiogenic factor) appear strikingly similar to tumor or diseased vasculature (Jain 2005), because they are more leaky and hemorrhagic (Jain, Au et al. 2005). In contrast, PDGF-BB and FGF-2 have been shown to create more natural appearing vessels (Cao 2003; Cao 2004). In this study, in combination, these factors proved to be best optimized and tunable to mimic normal tissue vessel beds.

The implantation method in this study was developed *in vivo* using the mouse cornea, which had previously been demonstrated as an excellent location for the study of these types of constructs (Moon, Saik et al. 2010; Poche, Saik et al. 2010). Constructs were implanted in the cornea for three reasons, which are similar to those listed by Tong et al. in their study of pathological tumor vessels (Tong and Yuan 2008). First, the assay could imitate general conditions similar to tissue scaffold implantation and vascularization. Second, induced vessels could be quantitatively examined microscopically (Gaudric, N'Guyen et al. 1992; Auerbach, Lewis et al. 2003). Third, the external nature of the cornea allowed for rapid surgical implantation and analysis.

In this group of experiments, mimetic vessels were induced to match host vessel morphology. The attempt was made to induce vessels *similar in structure* to target tissue vessels because different tissues possess different microvascular morphology, likely related to their functions in the delivery of nutrients and metabolites (Humphrey, Buschow et al. 2001). Normal tissues require a precise and unique vessel pattern to maintain an equilibrium between growth and cellular demands (Jain 2003; Jain, Au et al. 2005). Tissues possess different vessel morphology related to their initial development, metabolic need, physiological function and their ultrastructural shape and dynamics (Caplan 1985). For example, the lung provides a highly branched vascular system, which optimizes oxygen exchange and blood flow (Stenmark and Mecham 1997). Kidneys provide highly structured loops for osmotic exchange of waste products (Smith 1951). Skeletal

muscle possesses vessels that are ideal for delivery of nutrients while uniquely shaped to allow for the linear application of forces (Carlson 1973; Tong, Boucher et al. 2004). Skin possesses less vascular density, likely related to the decreased metabolic need (Jain 2003), but the microvessels are uniquely distributed to allow for the dynamic motion of the tissue (Hibbs, Burch et al. 1958). All of these tissues Have been shown to possess a network of vessels to allow for the spatial organization of the organs and the adequate delivery of nutrients to cells of an organ (Jain 2003). The importance of the microvascular vessel morphology was highlighted in the problem of the replacement and repair of skeletal muscle (Jain, Au et al. 2005). In fact, Jain postulated that the reason there was such difficulty in the development of tissue engineering strategies to repair skeletal muscle was because this tissue is densely perfused and has an extremely high metabolic rate and thus the constructs require a "rich supply of blood vessels throughout…to meet the demand for oxygen and nutrients" (Jain, Au et al. 2005). Ultimately, in this study, induced vessels were tailored to match normal tissue microvessels, and this became possible through the application of the new microvascular quantification scheme provided in chapter 2.

Novel microvascular quantification techniques were employed, along with classical measures in this study to recapitulate normal tissue microvessels. The method to quantify the microvasculature used here combined fractal dimension (Mandelbrot 1982; Sandau and Kurz 1997) and lacunarity (Landini, Murray et al. 1995; Plotnick, Gardner et al. 1996; Tolle, McJunkin et al. 2008) along with traditional diameter measurements and branching analysis (Masters 1989; J.B.

Bassingthwaighte 1994; Herman, Kocsis et al. 2001; Avakian, Kalina et al. 2002; Jain 2003; Jain, Au et al. 2005; Doubal, MacGillivray et al. 2010; Gould 2010; Grauslund, Green et al. 2010; Sng, Sabanayagam et al. 2010). This was discussed in chapters 1 and 2. The space filling methods used to quantify vascular morphology contained scale-invariant measures of vessel distribution, which could be valuable to the engineering community, because this ensures scalability in design (Baish, Gazit et al. 1996; Bianchi, Rosi et al. 2007; Bui, Šutalo et al. 2009; Liu, Wood et al. 2009).

The findings in this chapter that the morphology of induced vessels can be tuned, using space-filling parameters may prove valuable in future design of tissue engineered constructs (Bianchi, Rosi et al. 2007), therapies for ischemic disease (Cao 2003) and the induction of known vascular patterns *in vivo* (Gould 2010). The approach described here combined tailored angiogenic scaffolds with customized delivery of growth factors to induce host vascularization, and used the fractal dimension of induced vessels to *fine tune* the response. The information from the dose response allowed for the selection of the appropriate doses to recapitulate the fractal dimension and other measures of microvascular morphology of normal tissues.

In this study, one powerful observation from the vessel morphology mimicry experiments was that through simply tuning the fractal dimension of vessels formed, it was possible to induce a vascular structure with a desired fractal dimension, and to recreate the desired diameters and branch points, as well as density and lacunarity of target vessel networks. It was possible to tune the delivery of angiogenic factors to generate *specific* vascular structures; this was proven by the linear response of these

vessel parameters to loaded protein (figure 3.10). This study has gone beyond proving the tunability of the angiogenic response, and has also provided information on the range of doses of factors that may be used for angiogenesis in the corneal micropocket system. Control over microvascular morphology induced in engineered bioactive scaffolds may aid therapeutic strategies for re-vascularization. However, complex anatomical relationships seen for instance in the 3-5 tufts of capillaries surrounded by Bowman's capsule or in the juxtaglomerular apparatus in the kidney may require more complex methods to recapitulate vessel architecture. The methods described here may not be applicable to their design, because of their complex structures and extracellular matrix components as well as the importance of several specialized cell types required for physiological function. This thesis has helped to inform a formulation parameter necessary to synthesize bioactive scaffolds for a particular angiogenic application. In the future this methodology could be used to optimize other factors within bioactive scaffolds, and to study other angiogenic compounds *in vivo* in applications within tissue engineering, therapeutic angiogenesis, and other applications in regenerative medicine.

In conclusion, optimization of the modified mouse corneal micropocket angiogenesis assay in this thesis has lead to the finding that the tunability of the angiogenic response can be used to induce vessels which mimic normal tissue microvasculature. In the future this system could provide a robust tunable platform for further studies involving vessel morphology in diseased, remodeling or engineered tissues.

Chapter 4. Additional Methods for Tuning Vessel Morphology: Tethered Growth Factors and Cell Signaling Peptides

4.1 Introduction

Following the use of the growth factor customization to tune vessel morphology, several projects designed to test the effects of tethered growth and signaling factors on vessel morphology were carried out. These projects involved the use of several *in vitro* assays and several *in vivo* assays, similar to those described in the previous chapter. The methods for quantification of a response developed in chapter 2, including the scale invariant parameters were used to measure the responses to the various differing factors.

Tethered growth factors used for this purpose included PEGylated PDGF-BB and PEGylated QK which is a peptide derivative of the active signaling sequence from VEGF (Leslie-Barbick, Saik et al.). QK is an abbreviation for the sequence ac-KLTWQELYQLKYKGI-amide, which is very similar to the native VEGF-receptor binding region of VEGF15, ac- KVKFMDVYQRSYCHP-amide. This sequence has been shown to activate VEGFR-1 and 2 *in vitro* and is much more physiologically stable than complete VEGF protein. These factors were well known to be angiogenic on their own and to induce tubule formation *in vitro (D'Andrea, Iaccarino et al. 2005; Biondi, Ungaro et al. 2008)*, however they had never been studied in a tethered form bound to synthetic tissue engineering scaffolds. The key benefit of tethering the

factors is that they may serve to stimulate continuous angiogenesis, as they remain bound to the angiogenic scaffold while vessels grow into and degrade the biodegradable synthetic material. Over time, the degradation of the scaffold releases the tethered factors so that as the scaffold is degraded the factors serve to continuously stimulate angiogenesis for much longer than diffusible factors crosslinked into the gels. This acts as a slow, continuous release which is much different than the quick burst kinetics exhibited by the diffusible growth factors after implantation.

Tethered cell signals were studied *in vivo* to attempt to use native signaling and adhesion pathways to stimulate angiogenesis and to determine their effects on induced vessel morphology. A sequence from the cell signaling protein Ephrin A1 was utilized, which contained the extracellular domain of Ephrin A1plus the Fc segment. This protein had been previously shown to be critical in endothelial signaling and adhesion, and this study provided a platform to study its effects on vessel morphology *in vivo*.

This chapter presents compiled work from multiple collaborative endeavors. Within each project, my specific contribution involved the collaborative experimental design of all projects, as well as *in vivo* experimentation and analysis of the response to the biomaterials. For complete *in vivo* studies, biomaterials were synthesized and prepared in the laboratory of Jennifer West, and then the materials were cross-linked into implantable hydrogels by my collaborator, Jennifer Saik. I performed surgical implantation of these materials, as well as processing of the animal tissues, imaging

of the resulting angiogenic scaffolds, pre-processing of images for analysis, analysis of resulting images for morphological quantification of the vessel response, statistical comparison of these groups, and generation of all figures and graphs associated with these functions. I also contributed to the written manuscripts which were produced as a product of these studies, including background, methods, results and discussion of the *in vivo* findings in each manuscript, as well as editorial support and criticism of the projects. The methods that follow provide descriptions of the synthesis of these PEGylated products as well as the steps for implantation of the materials for *in vivo* studies.

4.2 Materials and Methods

4.2.1 Polymer synthesis

Poly(ethylene glycol) (PEG) diacrylate was synthesized by reacting dry PEG (MW = 6000 Da; Fluka) with acryloyl chloride (Sigma, St. Louis, MO) and triethyl amine (TEA; Sigma) in anhydrous dichloromethane (DCM; Sigma). The reaction was performed using 1:4 PEG:acryloyl chloride and 1:2 PEG:TEA molar ratios under argon gas overnight. 2 M K_2CO_3 was used to wash the solution before allowing it to separate into aqueous and organic phases. The organic phase containing PEGDA was dried using anhydrous $MgSO_4$ and filtered. PEGDA powder was obtained by

precipitating in diethyl ether, filtering, and drying overnight under vacuum and stored at -20°C under argon gas.

The cell-adhesive peptide, Arg-Gly-Asp-Ser, (RGDS, American Peptide, Sunnyvale, CA) was conjugated to a hetero-bifunctional PEG to form PEG-RGDS. RGDS peptide was dissolved into anhydrous dimethyl sulfoxide with one drop of diisopropylethylamine. The solution of RGDS was dripped onto dry acryloyl-PEG-succinimidyl carboxymethyl (PEG-SCM, Laysan, Arab, AL) using a molar ratio of 1.1:1 PEG-SCM: RGDS. The reaction was placed on a rocker overnight, followed by dialysis against water in a regenerated cellulose membrane. The final product was sterilized via filtration and lyophilized. Successful conjugation was confirmed with a gel permeation chromatography (GPC) system equipped with a PLgel column (5μm, 500Å, Polymer Laboratories, Amherst, MA) and an evaporative light scattering detector (Polymer Laboratories).

Degradable hydrogels were synthesized by incorporating a matrix metalloproteinase-sensitive peptide, GGGPQGIWGQGK (abbreviated PQ), into the backbone of the base polymer. Fmoc chemistry was used to synthesize the PQ peptide on an APEX 396 solid phase peptide synthesizer (Aapptec, Louisville, KY). Matrix-assisted laser desorption/ionisation-time of flight mass spectrometry (MALDI-ToF MS Autoflex; Bruker Daltonics, Billerica, MA, solvent: methanol) characterization confirmed successful peptide synthesis. Using a 2.1:1 molar ratio of PEG-SCM to peptide, the synthesized PQ peptide was conjugated to PEG by

following a procedure similar to that for PEG-RGDS. PEG-PQ-PEG conjugation was also confirmed using GPC.

4.2.2 Growth Factor or Cell Signaling Molecule Conjugation (PEG-ephrinA1, QK, PDGF-BB, and Laminin-Based Peptides)

Acryloyl-PEG-succinimidyl carbonate (PEG-SMC) was synthesized in house to formulate a product capable of reacting in aqueous conditions, and thus useful for protein conjugations. Synthesis followed procedures previously described by the West Laboratory (Figure 4.1). (Leslie-Barbick, Moon et al. 2009) Briefly, PEG (Fluka/Sigma, MW = 3400 Da) was reacted with Ag_2O (Sigma), acryloyl chloride (Sigma), and KI (Sigma) in anhydrous dichloromethane (DCM; Sigma) at 4 °C overnight, at molar excess ratios of 1.5, 1.1, and 0.3 respectively. The solution was filtered using Celite 521 (Spectrum Chemical Mfg Corp, Gardena, CA) and dried prior to dissolution in di H_20. The solution was adjusted to pH 3 and heated to 35 °C for 1 h. Activated charcoal (Fisher Pittsburg, PA) was used to remove iodine, and NaCl and DCM were added. Unwanted components were removed via DCM extraction and phase separation with 2 M K_2CO_3. Monoacrylated PEG was dried and concentrated followed by ethyl ether precipitation and vacuum filtration. Monoacrylated PEG in anhydrous acetonitrile (Sigma) and pyridine (Sigma) was reacted with a four molar excess of disuccinimidyl carbonate (Sigma) under argon overnight. The product was dried and dissolved in anhydrous DCM. After filtration,

PEG-SMC was purified in acetate buffer (0.1 M, pH 4.5, 15% NaCl) via phase separation. The purified PEG-SMC was dried with anhydrous $MgSO_4$ and precipitated into ethyl ether. After filtration and drying, PEG-SMC was characterized by proton nuclear magnetic resonance spectroscopy (^{1}H-NMR, Avance 400 Hz; Bruker) and stored at -80 °C under argon.

In figure 4.1 the reaction is described for EphrinA1-Fc, but this same method may be used to modify other peptides which possess a free amine in their structure, including the aminated N terminus. For each of the peptides used in these studies, the same SCM modification for PEGylation of the peptides was used. EphrinA1-Fc was obtained from R&D Systems (Minneapolis, MN) as a recombinant fusion protein containing the extracellular binding portion of ephrinA1 and the Fc fragment of human IgG. This protein was reacted with acryloyl-PEG-SMC to form PEG-ephrinA1. 200 mM sodium bicarbonate buffer (pH 8.5) was used to dissolve synthesized acryloyl-PEG-SMC. The solution was sterilized via filtration (0.2 μm) and combined with ephrinA1 at a 1:100 molar ratio of ephrinA1:PEG-SMC. In the

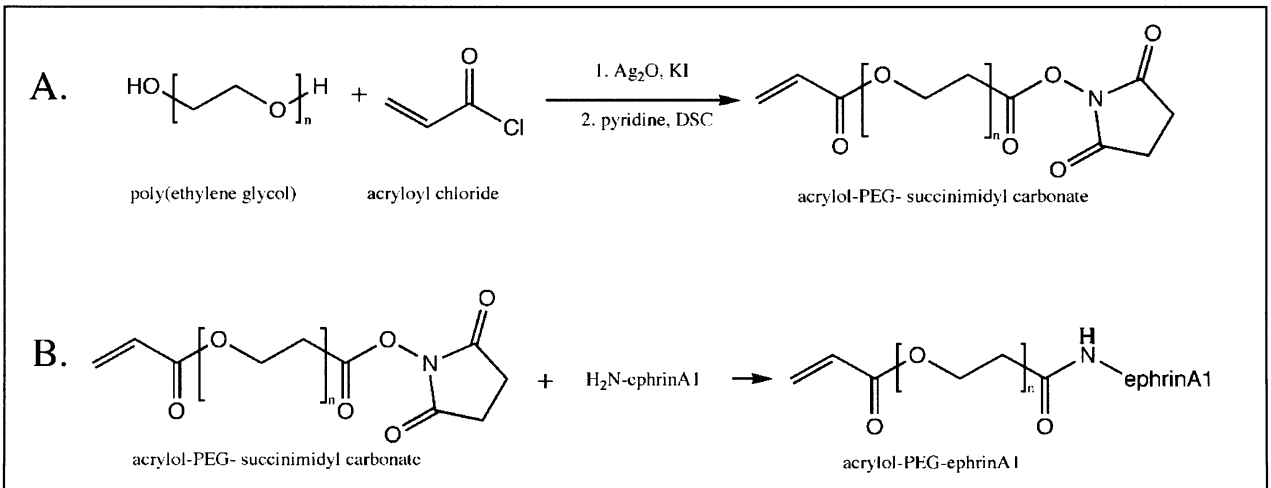

Figure 4.1: PEG-SMC for the PEGylation of growth factors and cell signaling and adhesive molecules.

synthesis of PEG-PDGF-BB, PDGF-BB was obtained from Prospec bio (Prospec bio, Israel) and was reacted in a 1:400 molar ratio, PDGF-BB:PEG-SMC in 200 mM sodium bicarbonate buffer (pH 8.5). In the case of the QK peptide, this 15 residue peptide was designed to react with PEG-SMC at the first lysine residue only by the protection of all other lysine residues with acetyl groups (Ac), so the peptide sequence is (Ac-KLTWQELYQL(K(Ac))Y(K(Ac))GI-amide. This peptide was purchased commercially from Aappatec (Aappatec, Louisville, KY). QK was reacted with PEG-SMC at a 10:1 molar ratio in the presence of DMSO via slow mixing.

In each conjugation, the reaction was placed on a rocker for four days at 4°C before lyophilization under sterile conditions. The PEG-peptide or protein (EphrinA1, QK, PDGF-BB) powder was reconstituted and stored in HEPES Buffered Saline (100 mM NaCl, 10 mM HEPES in deionized water; HBS; pH 7.4) for up to three months at 4°C. A western blot was used to confirm successful conjugation.

4.2.3 Angiogenesis Assay: Hydrogel Implantation into the Mouse Cornea

To visualize vessel invasion into the materials, hydrogels were implanted into *Flk1-myr::mCherry* transgenic mice, which express an endothelial cell specific florescent protein. (Poche, Larina et al. 2009) Hydrogel preparation and implantation followed the protocol outlined in Poche *et al.*, (Poche, Larina et al. 2009) and all animal experiments were conducted in accordance with Baylor College of Medicine Institutional Animal Care and Use Committee protocols. Briefly, hydrogels were

prepared at 10% polymer weight of degradable PEG-PQ-PEG, 3.5 μmol/ml PEG-RGDS, 10 μl/ml acetophenone stock solution, and the described concentration of PEG-peptide or protein for each set of experiments. In the case of the Ephrin A1 studies, this was 160 ng soluble platelet derived growth factor BB (PDGF-BB) per gel with or without 1.6 ng PEG-ephrinA1 (n=5 and 6, respectively). A mold of precise thickness was made by separating two glass slides with a 0.005 in polytetrafluoroethylene (PTFE) spacer and securing the glass slides with binder clips. 0.12 μl of the polymer solution was then injected between glass slides. Hydrogels were exposed to UV light (B-200SP UV lamp, 365 nm, 10mW/cm^2) for 2 min and immediately implanted into a micropocket formed in the cornea. (Poche, Saik et al. 2010) Briefly, a partial thickness incision was made in the cornea of anesthetized mice. A Von Graefe knife was used to separate the layers of the cornea stroma, creating a micropocket for hydrogel implantation. Fourteen days after implantation, mice were euthanized, and corneas were collected and fixed in 4% paraformaldehyde. The tissue was flatmounted and imaged on a Zeiss LSM 510 META confocal microscope using a Zeiss 40x/1.2NA C-Apochromat water immersion objective lens. The *mCherry* fluorophore was excited with a 543 nm laser for visualization of endothelial cells that invaded the cornea and hydrogel in response to growth factor release. Images of vessels on the hydrogel were compiled from projections of z-stacks exactly 22 μm in thickness, spaced 1.1 μm apart.

Confocal z-stacks were used to quantify vessel parameters. Vessel branch points and diameters were quantified using the image browser in the LSM software.

Fractal dimension, lacunarity, and vessel density were quantified as previously described. (Gould, Vadakkan et al. 2011) The fractal dimension was quantified to describe the complexity of the vessel network and lacunarity to examine nonuniformity of cell distribution in a scale-invariant manner (Gould, Vadakkan et al. 2011).

4.3 Tethered Growth Factors for Long-Term Stable Release

The work described below is adapted from two papers, currently in press: "Covalently immobilized platelet-derived growth factor-BB promotes angiogenesis in biomimetic poly(ethylene glycol) hydrogels". Saik JE, Gould DJ, Watkins EM, Dickinson ME, West JL. Acta Biomaterilia. 2010 Aug 27, and "An Immobilized VEGF-mimetic Peptide Promotes Microvasculature Formation in Poly(ethylene glycol) Diacrylate Hydrogels" Julia E. Leslie-Barbick, Ph.D.; Jennifer E. Saik, B.S.; Daniel J. Gould, B.S.; Mary E. Dickinson, Ph.D; Jennifer L. West, Ph.D. Biomaterials. 2011 April 20.

4.3.1 PEGylated growth factor PDGF-BB

PDGF-BB was previously shown to effect angiogenesis as described in the introduction and background sections of this thesis. Furthermore, the FDA has approved the use of PDGF-BB for use in the treatment of periodontal bone defects

and diabetic foot ulcers, making it a viable tool for tissue engineering. The goal of this project was to conjugate PDGF-BB to the PEG molecule in order to improve its delivery over time and this goal was based on previous work that has shown PEGylated PDGF-BB has improved solubility, decreased immunogenicity, and increased stability without loss of bioactivity (Veronese 2001; Roberts, Bentley et al. 2002; Fishburn 2008).

4.3.1.1 Methods

For concise methods on the in vitro aspects of these studies, please see appendix section 2. In this Methods Section, I focus on the *in vivo* experiments, as they were the primary contribution I provided to the work.

Synthesis and Purification of PEG-RGDS and Degradable PEG-PQ-PEG

PEG-RGDS was synthesized by dissolving the cell-adhesive peptide, Arg-Gly-Asp-Ser, (RGDS, American Peptide, Sunnyvale, CA) into anhydrous dimethyl sulfoxide and adding diisopropylethylamine. Dissolved RGDS was added to dry acryloyl-PEG-succinimidyl carboxymethyl (PEG-SCM, Laysan, Arab, AL) at a 1.1:1 PEG-SCM: RGDS molar ratio. This mixture was placed on a rocker overnight, dialyzed against water in a regenerated cellulose membrane to remove unwanted products, and lyophilized.

Hydrogels were rendered degradable by the incorporation of a collagenase-sensitive peptide, GGGPQGIWGQGK (abbreviated PQ), into the backbone of the PEGDA base polymer. The PQ peptide was first synthesized using Fmoc chemistry on an APEX 396 solid phase peptide synthesizer (Aapptec) and characterized using MALDI-TOF. The synthesized peptide was conjugated to PEG by following a similar procedure as above with a 2.1 molar excess of PEG-SCM. Conjugation of PEG-RGDS and PEG-PQ-PEG were confirmed using a gel permeation chromatography (GPC) system equipped with a PLgel column (5μm, 500Å, Polymer Laboratories, Amherst, MA) and an evaporative light scattering (ELS) detector (Polymer Laboratories). The PEG-RGDS was dissolved in 0.1% ammonium acetate in dimethylformamide (DMF) solvent and tested against a PEG-SCM standard.

Synthesis and Purification of acryloyl-PEG-succinimidyl carbonate (PEG-SMC)

The organic solvents needed to accommodate the short half-life of the succinimidyl carboxymethyl reactive group on the PEG-SCM, which was purchased and used for conjugation of peptides, were not compatible with proteins used in this study. It was therefore necessary to synthesize a heterobifunctional acryloyl-PEG-succinimidyl carbonate (PEG-SMC) in-house. PEG-SMC is functionally similar to the commercially available PEG-SCM, but has a longer reaction half-life and can thus be used under aqueous conditions.

PEG (Fluka/Sigma, MW = 3400 Da) was reacted with Ag_2O (Sigma, St. Louis, MO), acryloyl chloride (Sigma, St. Louis, MO), and KI (Sigma, St. Louis, MO) in anhydrous dichloromethane (DCM; Sigma, St. Louis, MO) at 4 °C overnight, at molar excess ratios of 1.5, 1.1, and 0.3 respectively. Silver was removed by filtering the solution through Celite 521 (Spectrum Chemical Mfg Corp, Gardena, CA). A Rotovap was used to dry the solution prior to dissolution in di H_20. The pH was adjusted to 3 with HCl, and the solution was heated to 35 °C for 1 h. Iodine was removed by adding activated charcoal (Fisher, Pittsburg, PA), and the solution was filtered through Celite 521. NaCl and DCM were added, followed by DCM extraction. Phase separation with 2 M K_2CO_3 was used to remove acid and chloride ions. Monoacrylated PEG was dried with sodium sulfate (Fisher, Pittsburg, PA), and a Rotovap was used to concentrate the solution followed byethyl ether precipitation and vacuum filtration. A four molar excess of disuccinimidyl carbonate (Sigma) was reacted with the monoacrylated PEG in anhydrous acetonitrile (Sigma) and pyridine (Sigma) under argon overnight. The product was dried using a Rotovap prior to dissolving in anhydrous DCM. The solution was filtered, and PEG-SMC was purified in acetate buffer (0.1 M, pH 4.5, 15% NaCl) via phase separation. The purified PEG-SMC was dried with anhydrous $MgSO_4$. PEG-SMC was precipitated into ethyl ether, filtered, and dried overnight under vacuum. PEG-SMC was characterized by proton nuclear magnetic resonance spectroscopy (^{1}H-NMR, Avance 400 Hz; Bruker, Billerica, MA, USA) and matrix-assisted laser desorption/ionisation-time of flight

mass spectrometry (MALDI-TOF; Bruker Daltonics, Dillerica, MA, USA). The final PEG-SMC product was stored at -80 °C under argon.

Synthesis of PEG-PDGF-BB and PEG-FGF-2

In-house synthesized acryloyl-PEG-SMC was dissolved in 50 mM sodium bicarbonate buffer (pH 8.5) and sterilized via filtration (0.2 μm). PDGF-BB (ProSpec Bio, Israel) was conjugated to PEG-SMC using a 400:1 PEG-SMC: PDGF-BB molar ratio in 200 mM sodium bicarbonate buffer (pH 8.5) at 4 °C for 4 d (Figure 1). The resulting PEG-PDGF-BB solution was lyophilized under sterile conditions. PEG-PDGF-BB powder was reconstituted and stored in HEPES Buffered Saline (100 mM NaCl, 10 mM HEPES in deionized water; HBS; pH 7.4) with 0.1% BSA at 4 °C for up to three months. A similar procedure was followed for PEG-FGF-2 (ProSpec Bio) at a 100:1 PEG-SMC: FGF-2 molar ratio. All growth factor conjugations were confirmed via Western Blot analysis on a 15% Tris-HCL precast polyacrylamide gel (Biorad, Hercules, CA). Primary antibodies included rabbit polyclonal anti-PDGF-B antibody (Santa Cruz Biotechnology, Santa Cruz, CA) and rabbit polyclonal anti-FGF-basic antibody (Millipore, Billerica, MA). Secondary antibody HRP-conjugated goat anti-rabbit IgG (Santa Cruz Biotechnology, Santa Cruz, CA) and an ECL™ chemiluminescent western blotting analysis system (GE Healthcare, Buckinghamshire, UK) were used. The western blot membrane was exposed to film (Kodak, Rochester, NY) for 15 s and developed using a Micromax Developer (Hope,

Seattle, WA) with T_2 developer and T_2 fixer (White Mountain Imaging, Salisbury, NY). The presence of PEG was confirmed using a PEG stain adapted from (Zhang, Wang et al. 2006), which allows barium iodine to react with PEG to form a yellow color.

Unconjugated PDGF-BB was quantified using a PDGF-BB ELISA (R&D systems, Minneapolis, MN). PEG chains mask antibody binding to PEG-PDGF, so the amount of unconjugated PDGF-BB was quantified after running a sample of the reacted solution on an ELISA. With the amount of soluble PDGF-BB quantified, appropriate concentrations of PEG-PDGF-BB were calculated.

Formation and Surface Modification of PEGDA Hydrogels

Six kDa PEGDA was dissolved in HBS to a 10% polymer weight percentage solution. A stock solution of the photoinitiator 2-dimethoxy-2-phenylacetophenone (acetophenone, Sigma) was prepared by dissolving 300 mg acetophenone in 1 ml N-vinylpyrrolidone (NVP) and then added to the polymer solution at a concentration of 10 µl/ml. The solution was vortexed and sterile filtered. Hydrogels were polymerized between two glass slides separated by a 0.75 mm thick poly(tetra fluoroethylene) (PTFE) spacer. The glass slides and spacer were secured using clips. Polymer solution was exposed to UV light (B-200SP UV lamp, UVP, 365 nm, 10 mW/cm^2) for 30 s and stored in PBS with 0.1% sodium azide.

For all studies, unconjugated PDGF-BB and PEG-SMC were removed via diffusion before the hydrogels were used. Alternatively, soluble PDGF-BB could also be left in place to act as a diffusible growth factor to encourage cell migration in the surrounding tissue for other applications.

To quantify the surface concentration of immobilized PEG-PDGF-BB, hydrogels were synthesized as described above and then degraded in 0.1 N sodium hydroxide for three days. After complete hydrogel degradation, the protein concentration was read on a Nanodrop 2000 (Thermo Scientific, Wilmington, DE).

Hydrogel Implantation into the Mouse Cornea

Hydrogels were prepared following the protocol outlined in Poche *et al.* (Poche, Larina et al. 2009). Briefly, the prepolymer solution was prepared to a 10% polymer weight percentage (100 mg/ml) of PEG-PQ-PEG, 3.5 μmol/ml PEG-RGDS, 10 μl/ml acetophenone stock solution, and 160 ng soluble PDGF-BB per gel with or without 1.6 ng PEG-PDGF-BB per gel (n=8). Hydrogels were prepared by injecting 0.12 μl polymer solution in between the glass slides spaced by a 0.005 in thick PTFE spacer secured with binder clips and exposed to UV light for two min.

Bioactive hydrogels were implanted into the cornea following a modified mouse cornea micropocket angiogenesis assay (Poche, Saik et al.). All animals were used under an approved protocol of the Institutional Animal Care and Use Committee at Baylor College of Medicine. Briefly, mice were anesthetized and a

partial thickness incision of approximately 50 μm in depth was made. The layers of the cornea stroma were separated using a Von Graff knife for immediate implantation after hydrogel crosslinking. *Flk1-myr::mCherry* transgenic mice were utilized, which enable visualization of vessel invasion via endothelial cell specific florescence [24]. Mice were euthanized and corneas were collected and fixed in 4% paraformaldehyde fourteen days after implantation. Flatmounts of tissue were made and imaged on a Zeiss 510 META confocal microscope using a 40x water immersion objective lens. A 543 nm laser was used to excite the mCherry fluorophore. Images of vessels on the hydrogel were compiled from projections of z-stacks exactly 22 μm in thickness, spaced 1.1 μm apart.

Statistics

One-way ANOVA and subsequent Tukey's Least Significant Difference (LSD) tests were used to statistically analyze the bioactivity of PEG-PDGF-BB and HUVEC tubulogenesis on surface-modified hydrogels and the movement of cells inside the hydrogels. In the tubulogenesis study, a generalized linear model in Minitab was used to analyze statistical differences in tubule formation of the co-culture of HUVEC and 10T1/2 cells. For each analysis, $p<0.05$ was considered significant.

4.3.1.2 Results

PEGylated PDGF-BB bioactivity in vitro

In vitro studies confirmed that the PEGylated PDGF-BB was bioactive by seeding hydrogels containing the PEG-PDGF-BB with 10t ½ cells and comparing them to hydrogels without PEG-PDGF-BB (figure 4.2 from (Saik, Gould et al. 2011)). The Hydrogels containing the PEGylated factor PDGF-BB exhibited robust spreading and proliferation, and the spatial distribution of this effect was confined to regions patterned with the PEGylated factor. Bioactivity of the conjugated PDGF-BB was confirmed by quantifying 10T1/2 proliferation on surfaces modified with PEG-RGDS and PEG-PDGF-BB as compared to surfaces modified with PEG-RGDS alone. Soluble PDGF-BB was added to the media of some gels modified with PEG-RGDS to serve as a positive control. As shown in Figure 4.2 A, 10T1/2 proliferation significantly increased in the presence of either soluble or bound PDGF-BB at 48 h (ANOVA, $p<0.05$). There was no significant difference in proliferation in the presence of soluble PDGF-BB compared to PEG-PDGF-BB, suggesting that conjugated PEG-PDGF-BB retained its bioactivity at levels similar to that of the soluble growth factor. The capability to spatially control immobilized PDGF-BB was demonstrated with hydrogels patterned with immobilized PDGF-BB (Figure 4.2 B-C). 10T1/2 cells were evenly seeded onto surfaces with and without PEG-PDGF-BB at 4 hours (Figure 4.2 B). By 48 hours, 10T1/2 cells seeded onto these patterned hydrogels appear to have proliferated more on areas with immobilized PDGF-BB (Figure 4.2 C).

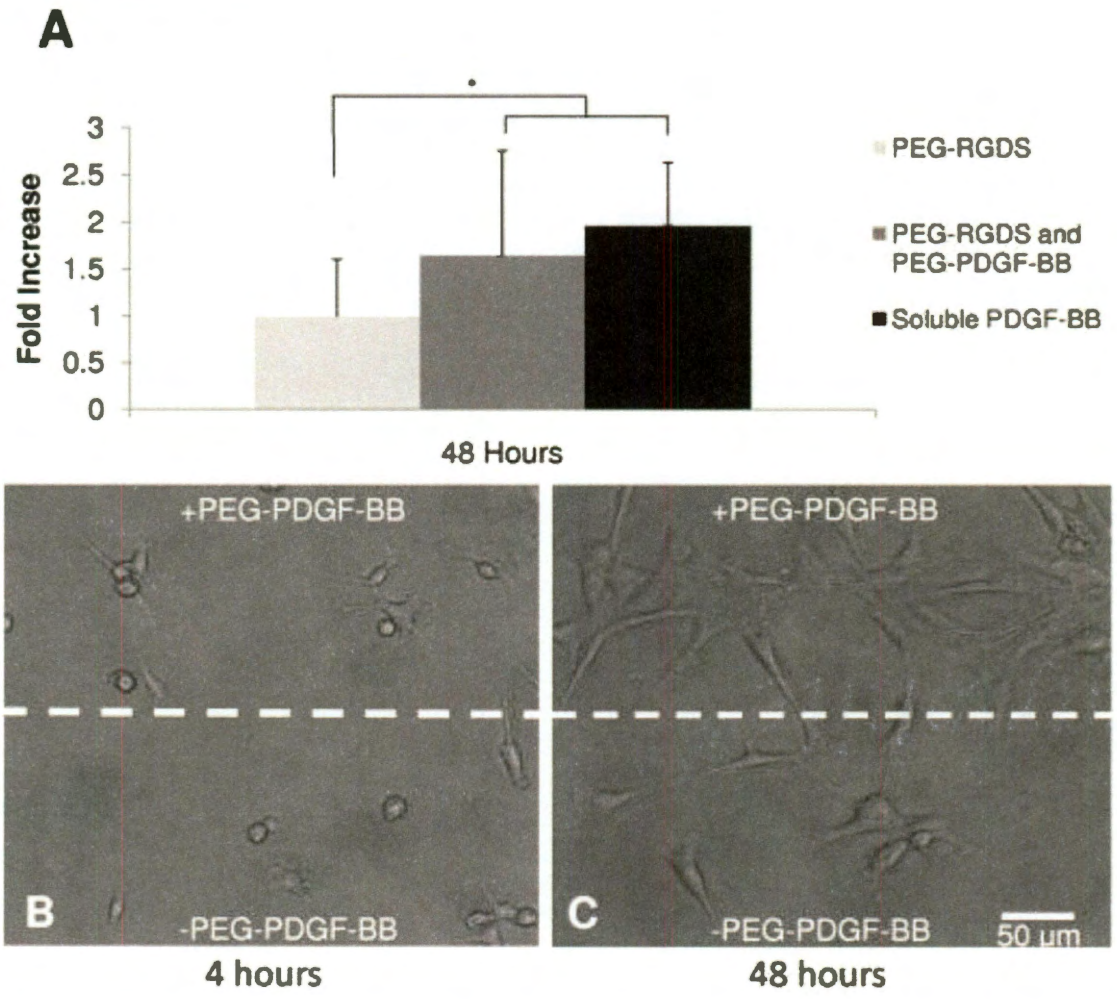

Figure 4.2: Bioactivity of PEG-PDGF was confirmed by seeding 10T1/2 cells onto modified surfaces. (A) By 48 hr, 10T1/2 proliferation had significantly increased in the presence of PDGF-BB (ANOVA, # $p<0.05$). No significant difference between soluble and bound forms of PDGF-BB indicated that covalently-immobilized PEG-PDGF-BB retained its bioactivity. (B-C) Hydrogels with patterned regions of PEG-PDGF-BB demonstrated the utility of spatial control of PDGF-BB. 10T1/2 cells seeded onto these patterned gels were evenly dispersed at 4 hours (B) but exhibited increased proliferation on regions patterned with PDGF-BB after 48 hours (C). (adapted from Saik, Gould et al 2011)

Further in vitro studies from this project confirmed that the PEG-PDGF-BB enhanced endothelial tubule formation when compared to PEG-FGF-2 and a combination of these growth factors (figure 4.3).

Thirty days after seeding HUVECs on surfaces modified with PEG-RGDS and PEG-PDGF-BB, endothelial cell tubules and branching networks were visible (Fig 4.3 A). HUVECs on surfaces modified with PEG-RGDS alone exhibited the normal cobblestone morphology of the cell type (Fig 4.3 B). Early tubulogenesis was apparent after 18 d, with robust tubulogenesis at day 30. The presence of tubulogenesis after 30 d suggests that the bioactivity of covalently immobilized PEG-PDGF-BB was maintained. Statistical analyses indicated significantly higher tubule formation on surfaces modified with PEG-RGDS and PEG-PDGF-BB as well as surfaces modified with the combination of PEG-RGDS, PEG-PDGF-BB, and PEG-FGF-2 when compared to surfaces modified with PEG-RGDS alone (ANOVA with Tukey's LSD, $p<0.05$, Fig 4.3 C).

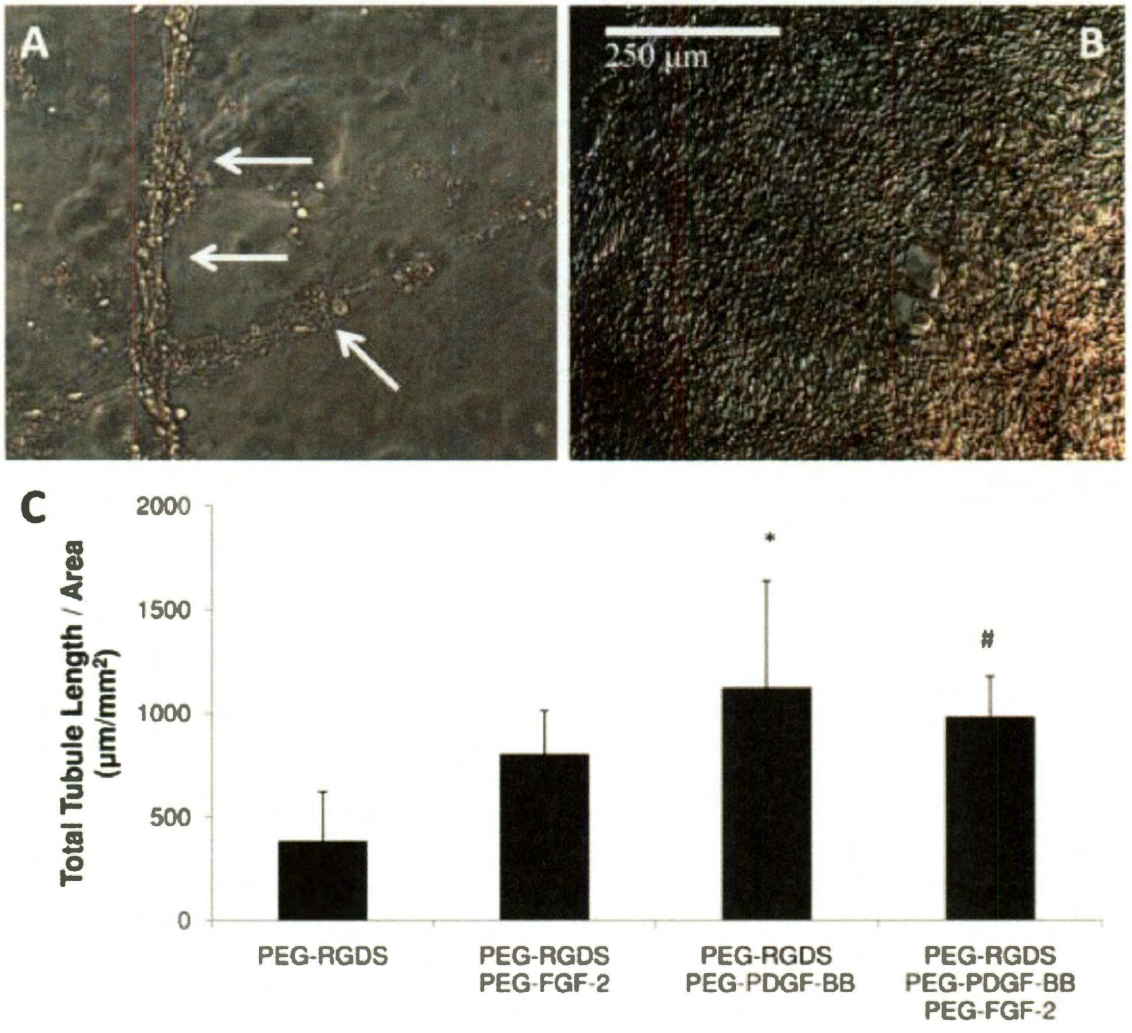

Figure 4.3: Modified surfaces significantly enhanced endothelial cell tubule formation. (A) HUVECs seeded onto modified surfaces exhibit extensive tubule formation (arrows) as early as 18 days compared to the cobblestone appearance of HUVECs seeded on surfaces with only PEG-RGDS (B). (C) A significant increase in tubule formation on surfaces with covalently immobilized PDGF-BB (* $p<0.01$) and surfaces with both covalently immobilized PDGF-BB and FGF-2 (# $p<0.05$) is seen as compared to surfaces modified with PEG-RGDS alone. (adapted from Saik, Gould et al 2011)

Tethered growth factor PEG-PDGF-BB appears to enhance the in vivo vascular response.

Bioactive hydrogels were implanted into the mouse cornea to assess the role of PEG-PDGF-BB in inducing angiogenesis *in vivo*. Hydrogels contained soluble PDGF-BB to initiate the angiogenic response by stimulating vessels from the surrounding limbus to invade into the cornea. Once vessels reached the bioactive hydrogel, the immobilized PEG-PDGF-BB (Figure 4.4) induced a more robust vascular response than hydrogels with soluble PDGF-BB alone (Figure 4.4). These *in vivo* experiments were performed with hydrogels containing 1.6 ng PEG-PDGF-BB, 160 ng diffusible PDGF-BB compared to diffusible PDGF-BB alone (Figure 4.4). There were significant differences when comparing the releasable factor to the tethered factor in concert with the releasable factor, using a t test assuming unequal variance, with a p value < 0.05. Figure 4.4 highlights the visible differences between the treatment group and the group lacking the PEGylated factor PDGF-BB in the images for comparison. The differences between vessel diameter, vessel density and fractal dimension were found to be significant, however the lacunarity comparison was not found to be significantly different (although there was a similar trend). Interestingly, the PEGylated PDGF stimulated vessel growth with a higher average vessel diameter, still within the range of physiological function, compared to the implants with only diffusible factors. Similar trends were seen where the PEGylated PDGF-BB seemed to stimulate a more robust response with greater branching and larger vascular tubules using the doses examined.

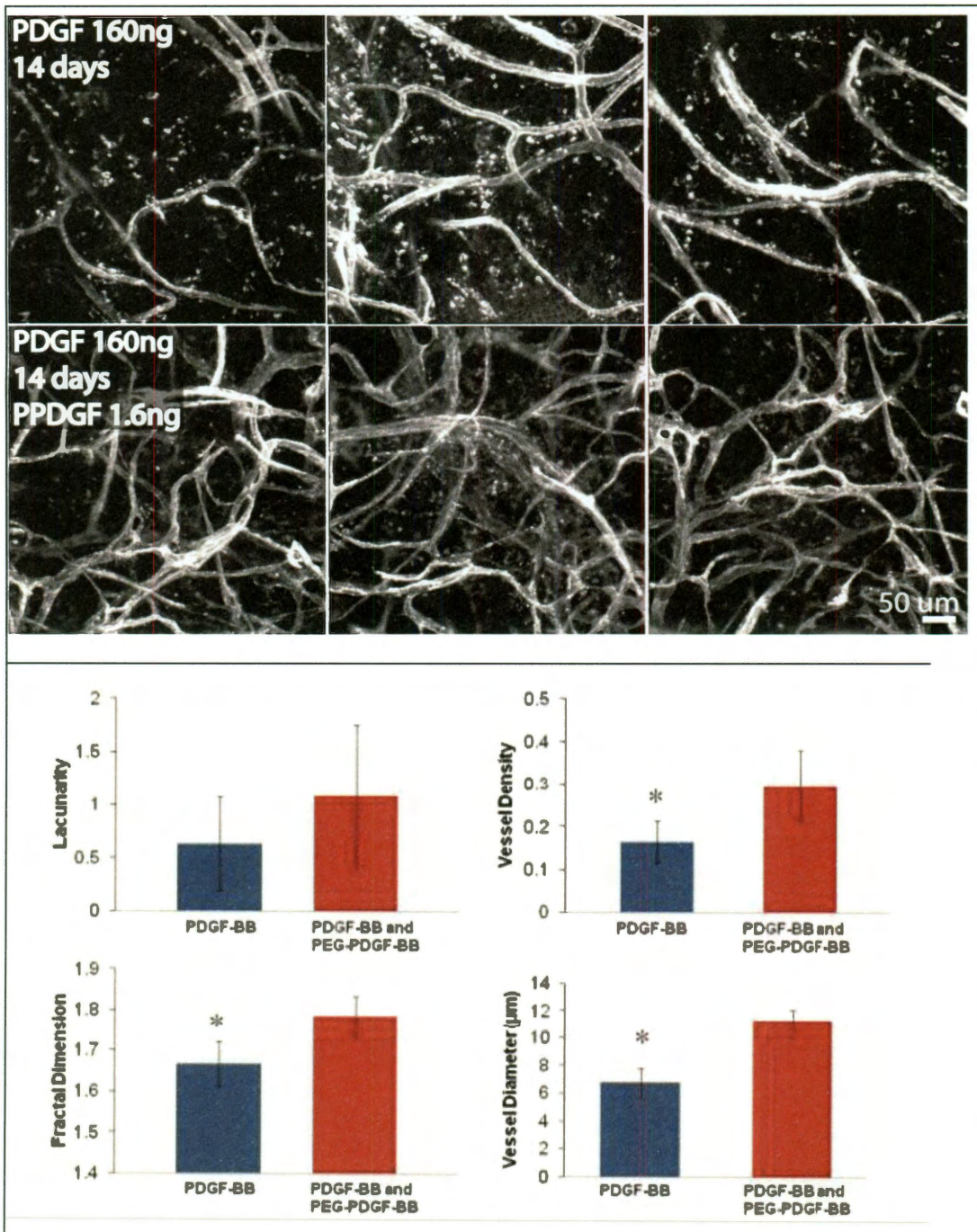

Figure 4.4: Effects of PEGylated PDGF-BB. Top panels represent vessels grown on implants with diffusible factors alone. Bottom panels are implants with 1.6ng PEGylated PDGF-BB, in addition to the 160ng diffusible PDGF-BB in both. The bar graphs show significantly different values for vessel density, fractal dimension, and vessel diameter. $P<0.05$, $n=9$. (adapted from Saik, Gould et al 2011)

Controlled delivery of PDGF-BB is particularly useful for *in vivo* applications. Soluble PDGF-BB was necessary to stimulate the initial angiogenic response of the surrounding limbic vessels into the cornea. Since soluble PDGF-BB degrades very rapidly *in vivo,* the presence of PEG-PDGF-BB enables prolonged angiogenic signaling on the hydrogel, leading to an increase in vessel density and diameter. This study presents the first work with a PEGylated growth factor *in vivo.* Furthermore, the *in vivo* data corroborated the *in vitro* studies of the PEGylated PDGF-BB and these findings provide another method for fine-tuning of the microvascular morphological parameters in angiogenic scaffolds. In the future, PEGylated PDGF-BB could be used in concert with biological scaffolds to help induce microvascular structures with high vessel density (30%, roughly double the density when using diffusible PDGF-BB alone), wide diameter (close to 11 microns), high fractal dimension approximately 1.8 (indicating complex structures) and high lacunarity parameter b, approximately 1.00 (which corresponds to a low amount of distributed empty space within the constructs). This may be useful in the design of microvascularized constructs to recapitulate skin which showed a fractal dimension of 1.8, and lacunarity parameter b of 1.03 with vessel density of 0.24 and diameters in the range of 6-10 microns (shown in chapter 2 and 3). The use of this material is not limited to the design of one microvascular type, and the value of PEG-PDGF-BB, in terms of its stability and its ability to induce a robust response should be considered in its future use.

4.3.1.3 Conclusion

Biomimetic hydrogels can be designed to incorporate cell adhesive sequences and covalently immobilized growth factors to stimulate a desired cellular response in tissue engineered constructs. This work demonstrated that PEG-PDGF-BB maintains its bioactivity and can be successfully incorporated into PEG-based hydrogels. HUVECs seeded onto hydrogel surfaces modified with covalently immobilized growth factors formed extensive and branching networks of tubules. Additionally, a co-culture of HUVEC and mouse pericyte precursor 10T1/2 cells seeded onto modified surfaces induced tubule formation independent of growth factor modification as early as two days after cell seeding. Finally, bioactive hydrogels containing both soluble PDGF-BB and immobilized PEG-PDGF-BB lead to a significant increase in vessel density and complexity when implanted into the mouse cornea angiogenesis assay as compared to hydrogels with soluble PDGF-BB alone. Further work is necessary to determine optimal combinations of cell types as well as both bound and soluble growth factors to form stable and functional vascular networks.

4.3.2 PEGylated QK (a bioactive peptide derived from VEGF) was found to effect angiogenic induction and morphology.

Another growth factor that has been previously described and is implicated in angiogenesis is VEGF. A 15 amino acid peptide sequence called QK, derived from the VEGF receptor 1 domain 2 - VEGF binding interface has been shown to bind various VEGF receptors *in vitro (D'Andrea, Iaccarino et al. 2005)*. This peptide was studied *in vitro* in the West laboratory and was shown to possess similar activity to lower concentrations of VEGF. It has been shown to activate downstream pathways of the VEGF receptor and to stimulate tubulogenesis *in vitro* (D'Andrea, Iaccarino et al. 2005). Beyond this, the peptide has appeal in bioengineering applications because it is relatively more stable and resistant to denaturation than native VEGF and it is much cheaper to synthesize than complete protein VEGF, or to produce concentrated, purified VEGF for commercial use. It can be PEGylated and covalently bound to synthetic biomaterials. This section describes a collaborative effort where I again contributed by providing the in vivo portion of the experiments as well as analysis and results for the manuscript.

4.3.2.1 Methods

In these experiments, QK was PEGylated for use in *in vitro* studies by a past student in the West lab, Julie Barbick. Her findings *in vitro* along with these *in vivo* results can be found in the manuscript listed above (Leslie-Barbick, Saik et al.). Complete methods for all in vitro experiments can be found in appendix section 3.

Preparation and Purification of PEG-QK:

The angiogenic peptide Ac-KLTWQELYQL[K(Ac)]Y[K(Ac)]GI-amide was designed to react with PEG-SCM at the first lysine (K) residue only, by protecting all other free amines with acetyl groups (represented by Ac). QK (MW=2036 Da, Aapptec, Louisville, KY) was dissolved in DMSO at a concentration of 7.4 mM. N,n-diisopropylethylamine (DIPEA, Sigma, 2 mol per mol PEG) was added to the solution to act as a base catalyst. Acryloyl-PEG-succinimidyl ester (PEG-SCM, Laysan, MW=3400 Da) was similarly dissolved at a concentration of 1.5 mM. PEG-SCM was added dropwise to QK in a 10:1 molar ratio with slow mixing and allowed to react for 4 d at 25°C. The product was precipitated in cold isopropanol and dried overnight. PEG-QK was then lyophilized and stored in HEPES buffered saline (HBS) with 0.1% bovine serum albumin (BSA) at 4°C until use. Conjugation was characterized by MALDI-TOF (MS Autoflex, solvent: methanol).

Synthesis of PEG-VEGF

In brief, $VEGF_{165}$ (Sigma) was reacted with acryloyl-PEG-SMC in a 1:200 molar ratio in sterile 50 mM sodium bicarbonate buffer (pH 8.5, 0°C) for 4 d. PEG-VEGF was then lyophilized under sterile conditions and stored in HEPES buffered saline (HBS) with 0.1% bovine serum albumin (BSA) at 4°C until use. Conjugation was confirmed via Western blot by visualizing an increase in molecular weight.

In Vivo Mouse Cornea Micropocket Angiogenesis Assay:

Hydrogels were implanted into the mouse cornea micropocket angiogenesis assay following the protocol outlined in Poche *et al.* Hydrogels were prepared by making a 10% polymer weight percentage (0.1 g/ml) prepolymer solution of PEG-PQ-PEG, 3.5 μmol/ml PEG-RGDS, 10 μl/ml acetophenone stock solution, and 640 ng soluble VEGF per gel with or without 1.6 ng PEG-VEGF or 32 ng PEG-QK per gel. Hydrogels did not contain encapsulated cells. The difference in concentration of QK and VEGF comes from the observation previously noted by D'Andrea et al. that 385 mol QK had equal bioactivity to 1 mol VEGF in a proliferation assay [2]. As a positive control, hydrogels were crosslinked with incorporation of PEG-VEGF (400 pmol/mL) instead of PEG-QK, and as a negative control, hydrogels were prepared with PEG-RGDS only. Prepolymer solution (0.12 μl) was injected in between the glass slides spaced by a

0.005 in thick PTFE spacer secured with binder clips and crosslinked via exposure to UV light for 2 min.

Bioactive hydrogels were implanted into a modified mouse cornea micropocket angiogenesis assay. All animals were used under an approved protocol of the Institutional Animal Care and Use Committee (and AALAS) at Baylor College of Medicine. *Flk1-myr::mCherry* transgenic mice were utilized, which enable visualization of vessel coverage via endothelial cell specific florescence. Briefly, a partial thickness incision of approximately 30 μm in depth was made in the cornea of anesthetized mice. A Von Graefe knife was used to separate the layers of the cornea, creating a micropocket approximately 700 microns in length where the implants could be placed approximately 3-400 microns away from the limbic vessels with great reproducibility.

Mice were euthanized 14 d after implantation, and corneas were collected and fixed in 4% paraformaldehyde. Tissue flatmounts were prepared and imaged on a Zeiss LSM 510 META confocal microscope using a 40x/1.2NA C-Apochromat water immersion objective lens corrected for UV vis IR working distance 0.28 mm with a 543 nm laser for excitation of the mCherry fluorophore. Images of vessels on the hydrogel were compiled from projections of z-stacks exactly 22 μm in thickness, spaced 1.1 μm apart. These images where then compiled into z-stacks, and the three dimensional data set was used to count branching and vessel diameters, using the image browser in the LSM software.

Next, the stacks were processed into projections using a maximum intensity projection setting in the LSM Image examiner software. Projections were then processed into grayscale images and thresholded to preserve the vessel elements without dilating or

eroding them and the images were then opened in MATLAB and analyzed for vessel density and several scale-invariant space filling parameters including fractal dimension and lacunarity using a program available free online through the MATLAB central exchange (Moisy 2006; Vadakkan 2009; Vadakkan 2009; Gould, Vadakkan et al. 2010). Briefly, the fractal dimension quantifies the amount of space filled by an object and lacunarity quantifies how it fills space, and both do this in a scale-invariant manner (Mandelbrot 1982; Lopes and Betrouni 2009; Gould, Vadakkan et al. 2010). Finally all groups were compared using anova analysis with post hoc tukeys test to identify statistically significant differences.

4.3.2.2 Results:

Briefly, the peptide was shown to stimulate tubule formation on the surface of hydrogels and in three dimensional cultures in degradable hydrogels *in vitro*. Our findings *in vivo* were similar, in that there was greater coverage of hydrogels containing the QK peptide in comparison to PEGylated whole VEGF and diffusible VEGF alone.

Immobilized VEGF and QK induce more complete vessel coverage of the hydrogel in vivo

To investigate the role of the immobilized VEGF mimicking peptide *in vivo,* bioactive hydrogels were implanted in a mouse cornea micropocket, an established, reproducible, and quantifiable assay. Hydrogels contained non-bound, diffusible VEGF to stimulate an angiogenic response from the surrounding limbus into the

normally avascular cornea. Vessel coverage of the hydrogels is illustrated with three representative images of each treatment group (Figure 4.5, A).

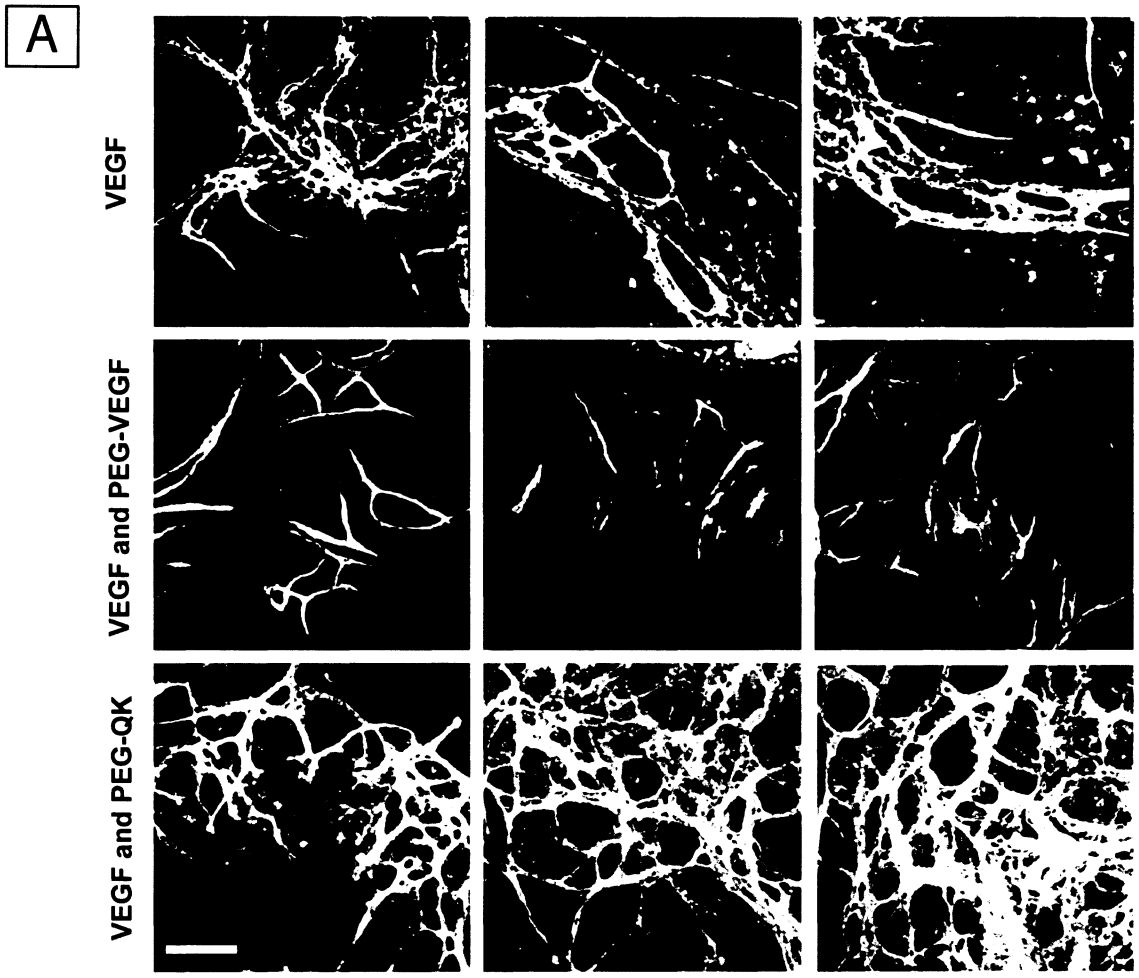

Figure 4.5 A: QK peptide with VEGF enhances angiogenesis *in vivo* when compared to VEGF alone or PEG-VEGF and VEGF. Images of the different experimental groups are shown here for visual comparison. Figure 4.4 continues below. Scale bar = 50 micrometers.

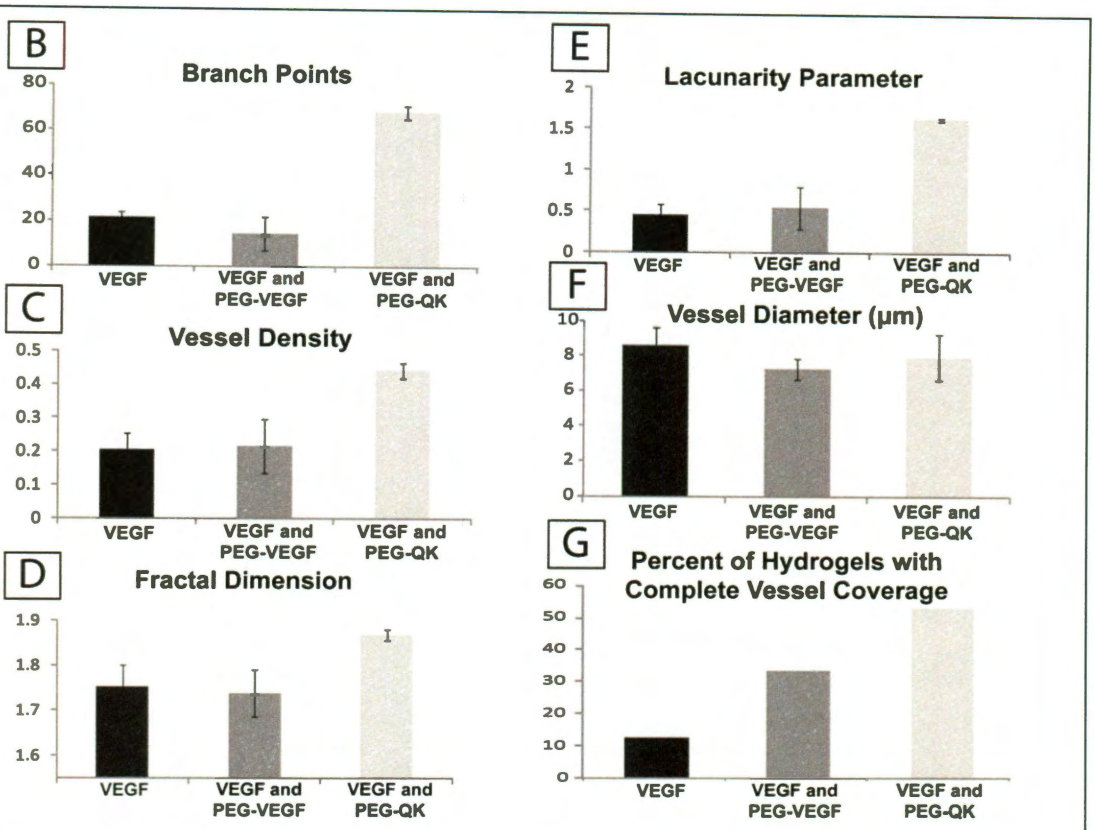

Figure 4.5 B: Morphological Parameters from QK in vivo experiments. These parameters were measured from the images of the microvessels similar to what is shown in 4.4 A. Bioactive hydrogels incorporating releasable VEGF alone and in combination with PEG-VEGF or PEG-QK were implanted into the mouse cornea micropocket and imaged fourteen days after implantation. The presence of PEG-QK significantly increased the number of branch points (B) and vessel density (C) as compared to VEGF alone and VEGF with PEG-VEGF ($p < 0.05$). Additional space filling parameters were quantified, which also showed that the presence of PEG-QK significantly increased fractal dimension (D), and the value of the lacunarity parameter (E) as compared to VEGF alone and VEGF with PEG-VEGF. No significant difference between vessel diameters existed (F). The advantage of immobilized growth factors can be seen in the percentage of hydrogels with complete vessel coverage (G), where only 12% of hydrogels with VEGF alone displayed complete vessel coverage of the hydrogel as compared to 33% in the presence of PEG-VEGF and 53% with PEG-QK.

Furthermore, PEG-QK was shown to enhance vessel branch points (B) and vessel density (C) as well as space filling properties of fractal dimension (D) and lacunarity (E). These space filling parameters provide scale invariant methods to

parse out differences in vessel morphology. Fractal dimension quantifies the complexity of the vessel network via a measurement of how much space in each image is filled with vessels (Sandau and Kurz 1997). Lacunarity quantifies the uniformity of vessels to describe how the vessels fill the image[5]. Vessel diameter (F) remained similar between all treatment groups. Although the morphological parameters do not show a significant difference between VEGF alone and VEGF with PEG-VEGF, PEG-VEGF did increase the percent of hydrogels with vessels covering the hydrogel (G). Importantly, in our study, the concentration of the QK peptide was 32ng in contrast to the concentration of tethered VEGF which was 1.6 ng. This difference in concentration coupled with the difference in PEGylation of the native VEGF could account for the more robust response seen in the QK containing group.

4.3.2.3 Discussion

D'Andrea *et al.*'s contribution of the QK peptide which binds to and activates VEGF receptors responsible for the induction of angiogenesis is a useful material for angiogenic engineering scaffolds. Although they examined the peptide in depth, they did not examine the effects of QK bound in a matrix. PEG hydrogels have been shown to support angiogenic activity when modified with bioactive peptides and proteins and this is why they were used as a matrix material to examine the angiogenic effects of covalently linked QK. In vitro results suggest that the covalent incorporation of the angiogenic peptide QK could be used to promote angiogenesis in tissue engineered matrices. The *in vivo* work using hydrogels without encapsulated cells in the mouse cornea micropocket angiogenesis assay shows that PEG-QK supports a high level of vessel coverage, outperforming that of unbound VEGF and PEG-VEGF hydrogels.

The PEG-QK containing group stimulated a more robust response than the VEGF diffusing group or the PEG-VEGF containing group. This was reflected by greater vessel branching, fractal dimension and lacunarity parameter b in the QK containing group ($p<0.05$). Interestingly the average vessel diameters were not significantly different from each other. Furthermore, the PEG-QK containing group seemed to generate excellent coverage vessels more frequently than the VEGF diffusing or the PEG-VEGF containing hydrogels, with a much higher percent of coverage in the groups containing PEGylated growth factor, in particular in the group

containing PEG-QK. The advantage of immobilized growth factors was seen in the percentage of hydrogels with complete vessel coverage (G), where only 12% of hydrogels with VEGF alone displayed complete vessel coverage of the hydrogel as compared to 33% in the presence of PEG-VEGF and 53% with PEG-QK.

In comparison to PEGylated PDGF-BB, this material produced vessels with greater density (40% compared to 30%), and higher fractal dimension (1.87 vs 1.80), yet with lower vessel diameters (8 vs 10 microns), more similar to the PDGF-BB alone and VEGF-A alone treatments. This material may prove useful in the design of microvasculature for the kidney, since the kidney was shown to have a fractal dimension of 1.89, lacunarity of 1.92 (vs 1.7 in QK) and a density of 36% (chapter 2).

This study shows the success of incorporating a covalently-linked 15-amino acid biomimetic peptide into a tissue engineering matrix to promote angiogenesis. There is no known current published research in which bioactive peptides are incorporated into tissue engineering matrices to promote angiogenesis *in vivo*.

There may be advantages to incorporating small peptides instead of large proteins for angiogenesis treatment strategies. Synthesized peptides allow more flexibility of design for bioactivity without a requirement for modifying genetic translation in bacterial production. QK was synthesized to allow only one PEG chain to be conjugated per peptide. Native VEGF protein dimers can be modified with up to 50 PEG chains, this can lead to a distribution of reaction products, where excess PEG chains may cause steric hindrance during ligand-receptor binding. Additionally,

smaller peptides may be easier to incorporate into bioactive scaffolds, as diffusion into a scaffold may be faster and more complete.

4.3.2.4 Conclusion

PEG-QK has been shown to promote angiogenesis in PEG hydrogels, without the use of sequestered growth factor proteins. Just as researchers have come to agree that it is more advantageous to include cell-adhesive peptides rather than full-sized ECM proteins in engineered matrices, this novel work introduces the use of a covalently linked angiogenic peptide, PEG-QK, as a comparable and possibly more favorable angiogenic factor than PEG-VEGF for covalent incorporation in scaffolds to promote angiogenesis.

4.4 Tethered Ephrin A1, a cell-cell signaling protein was studied for its effect on vessel morphology *in vivo*.

The work described below is adapted from the manuscript, currently available online titled: "Biomimetic Hydrogels with Immobilized EphrinA1 for Therapeutic Angiogenesis", Jennifer E. Saik[1], Daniel J. Gould[1], Aakash K. Keswani[1], Mary E. Dickinson[2], Jennifer L. West[1,†] Biomacromolecules. 2011 June 6.

4.4.1 Introduction

Ephrin A1 is a signaling molecule that signals through the EphA receptor to stimulate cell-cell adhesion, and it plays a critical role in cell guidance in development and in adult tissues (Mellitzer, Xu et al. 2000). The signaling Ephrin and the Eph receptor are both membrane bound, and signaling through the receptor is thought to effect cell adhesion and morphology through Nck and SHEP1 which directly affect cell adhesion and the cytoskeleton (Mellitzer, Xu et al. 2000). In endothelial cells, this receptor ligand pair has been shown to enhance cell-cell adhesion and signaling (Davis, Gale et al. 1994). The involvement of the ephrin-eph signaling cascade in physiology and in disease states has been recently elaborated in recent works (Pasquale 2008) and has been shown to be bidirectional. In the past, others have incorporated ephrin-A1 into synthetic hydrogels to study endothelial cell

adhesion, and have suggested that it is dependent on alpha(v)beta3 integrins (Moon, Lee et al. 2006). These studies demonstrated the angiogenic potential of synthetic materials functionalized with this protein (Moon, Lee et al. 2006). For this reason a recombinant fusion protein containing the extracellular binding portion of EprinA1 and the Fc fragment of human IgG (R&D Systems, Minneapolis, MN) was PEGylated for studies *in vitro* by Jennifer Saik, a student in the West lab, and many of the *in vitro* findings can be found in the publication related to this topic (Saik and Gould et al. 2011). Briefly, *in vitro*, the protein was found to have stimulatory effects on cell tubule formation and the deposition of extracellular matrix. The studies below represent the *in vivo* findings of the effect of the PEGylated protein on the induced vessel morphology in the modified corneal micropocket assay described previously in this chapter.

4.4.2 Methods

Conjugation of the protein and the *in vitro* methods are described briefly above and in the manuscript associated with this work (Saik, Gould et al.). *In vivo*, the micropocket surgery was performed as described above and the analysis of vessel morphology was performed as described above and in chapter 2.

In order to measure the cellular association and morphology for *in vitro* studies, three dimensional images of the cultures at several timepoints were collected, and then analyzed using Farsight software. Farshight is available free online

(http://farsight.freedesktop.org/releases/farsight2) and aids in the quantification of cellular interactions, such as the percent shared borders, which reflects cellular interconnectivity.

4.4.3 Results

PEG-Ephrin A1 in vitro

First, several comparisons were made of the PEG-Ephrin A1 *in vitro* to determine the ability of human umbilical derived endothelial cells (HUVECS) seeded on the surface of gels containing PEGylated Eprin A1 to form tubules. A dose-dependent effect was seen, where higher doses of the bound Ephrin A1 stimulated more tubule formation and this effect was shown to be long lasting in contrast to controls containing no PEGylated Ephrin A1. This effect was shown to be reversible in the presence of soluble EphA2 which is a natural binding partner for the tethered Ephrin A1, thus demonstrating the importance of the PEGylated Ephrin-A1 interaction. Next, three dimensional cultures were established using cocultures of Human Umbilical Vein Endothelial Cells (HUVECs) and Human Brain Derived Pericytes, in order to test the effects of increasing PEG-Ephrin A1 *in vitro* on cell association at different timepoints over one week. All three dimensional co-cultures containing the tethered Ephrin A1 were shown to possess more cell association in

comparison to controls (figure 4.6). Figure (4.6) demonstrates the quantification of the cellular interactions from the images of the cellular three dimensional cultures.

Measuring cell shared borders helped to demonstrate an effect of Ephrin A1 in both its concentration and over time. This type of quantification may prove useful in future *in vitro* studies of endothelial cell three dimensional cultures.

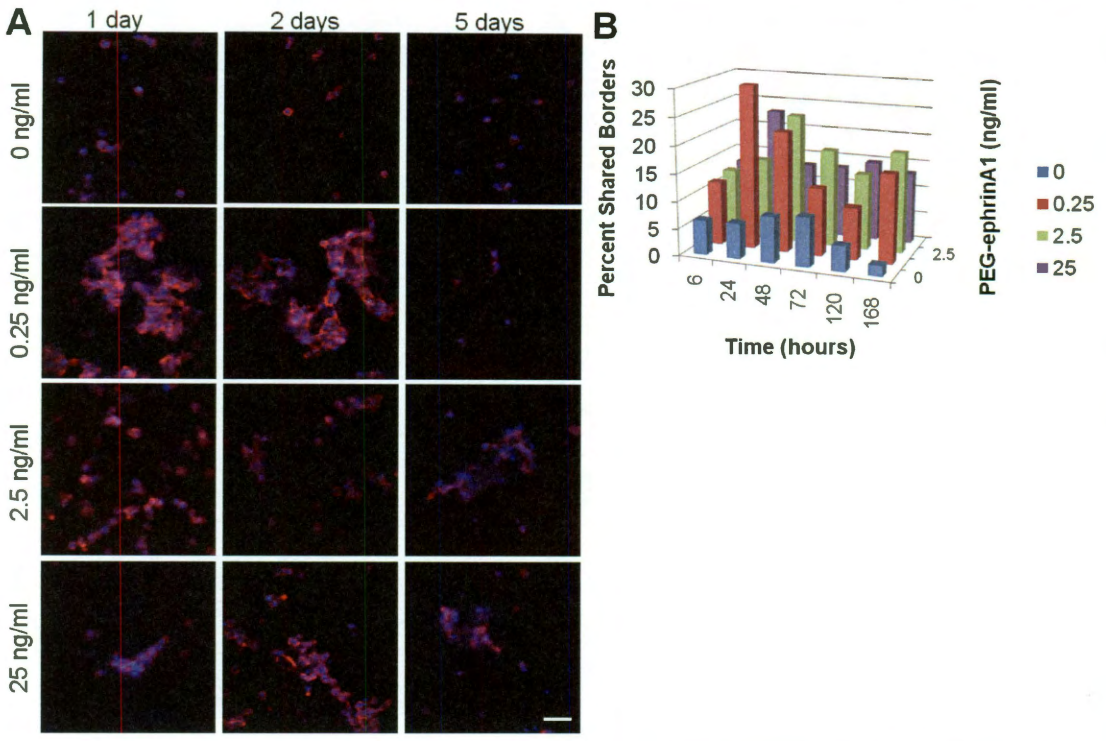

Figure 4.6: In Vitro quantification of Ephrin Effects. In order to quantify the resulting tubule formation, the parameter percent shared borders was calculated to examine the percentage of each cell's edges that were interacting with other cells to form tubule networks. Robust tubule formation was seen at early timepoints using low PEG-ephrinA1 concentrations and at late timepoints using higher PEG-ephrinA1 concentrations. A two-way ANOVA shows a significant effect of PEG-ephrinA1 concentration and time.

PEG-Ephrin A1 in vivo

Next, an evaluation of the effects of the PEGylated Ephrin A1 on vessels *in vivo* was undertaken. Small hydrogel disks were fabricated and implanted as previously described (Moon, Saik et al. 2010; Poche, Saik et al. 2010) in the flk1::myr-mCherry mouse cornea. One group contained releasable PDGF-BB alone as an angiogenic factor and the other contained releasable PDGF-BB along with tethered PEG-Ephrin A1 to stimulate angiogenesis. Implanted gels were then allowed two weeks for vessel invasion and growth, and were then harvested and resultant vessels were imaged and analyzed. Figure (4.7) describes the findings from these *in vivo* studies.

Overall, PEG-Ephrin A1 was shown to stimulate cellular interactions and tubulogenesis *in vitro* and was shown to induce vessels with more branch points, greater density and smaller diameters *in vivo*. Complete microvascular quantification from these studies was described in aforementioned manuscript and is shown

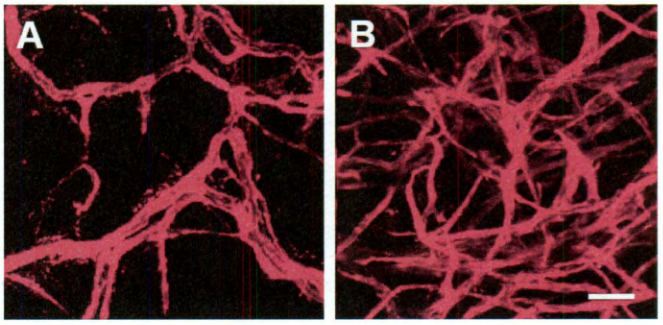

Figure 4.7: In Vivo effects of Ephrin A1. Bioactive hydrogels incorporating releasable PDGF-BB and PEG-ephrinA1 (B) showed a more robust vascular response than hydrogels with releasable PDGF-BB alone (A) when implanted into the mouse cornea.

in table 4-1 below.

In conclusion, PEG-Ephrin A1 was shown to effect the formation of endothelial tubules in co-culture systems *in vitro*. PEGylated Ephrin A1 was shown to affect blood vessel morphology. PEG-EphrinA1 in this system provided another unique pathway to control microvessel morphology, where it increased density and complexity of the network, but also stimulated formation of smaller diameter vessels. This signaling molecule may provide a unique tool in the future for patterning biomimetic hydrogels for use in the formation of microvascularized constructs with a need for high density, small-diameter microvessels.

A table was constructed to compare the resulting vessel morphologies from studies in this chapter (PEG-PDGF-BB, PEG-QK, and PEG-Ephrin A1) and the target vessel morphologies from chapter two and is shown below.

Treatment / Measured Morphology	Vessel Density	Fractal Dimension	Lacunarity	Average Vessel Diameter (um)
PDGF-BB 160ng	0.18	1.67	0.7	6.9
VEGF-A	0.2	1.75	0.5	8.5
VEGF-A and PEGVEGF-A	0.22	1.77	0.69	7
Skin	0.24	1.8	1.03	7.27
Cortex	0.24	1.75	0.97	8.45
PDGF-BB and PEGPDGF-BB	0.3	1.79	1	10.5
Kidney	0.36	1.89	1.92	8.55
VEGF-A and PEGQK	0.45	1.87	1.7	8
PDGF-BB and PEG Ephrin A1	0.5	1.9	2.5	7

Table 4.1 Comparison of covalent factors and target vessel morphologies. In this table, all the measured morphological parameters from the experiments conducted in chapter four are shown as are several of the measured parameters from kidney, skin and cortex. As described, PEG-PDGF-BB could prove valuable in the design of microvascular scaffolds for skin, while PEGQK could prove useful in design of kidney vascular scaffolds, while PEG-EphrinA1 could be used to induce extremely vascularized scaffolds with high complexity and average vessel diameters.

4.5 Conclusions

In conclusion, several different growth factors and cell signaling molecules were studied to determine their effects on cell growth *in vitro* and on host vasculature *in vivo* in the mouse corneal micropocket assay. The provision of a sensitive quantitative tool to examine the morphological properties of induced vessels allowed for sensitive statistical quantification of treatment groups, and has contributed dramatically to studies of new biomaterials and novel scaffolds. These systems can now be adapted for further use in the development of biomaterials for tissue engineering applications. The results presented here demonstrate the potential of biocompatible, PEG-based hydrogels containing immobilized growth factors as a promising methodology to engineer a microvascular system within tissue engineered constructs for regenerative medicine applications.

In this chapter, I was able to probe the effects of many different covalently bound growth factors and cell signaling ligands using the modified mouse corneal micropocket assay in conjunction with my novel microvessel quantification tool. This chapter highlights the functionality of this robust system, in exploring the host angiogenic response to biomaterials. This work should provide a platform for future studies of angiogenic biomaterials as well as for investigation of microvascular morphology. In terms of tissue engineering applications, this work has helped to provide new strategies for microvascular induction and host integration, and in the

following chapter, I explore pre-vascularization strategies *in vitro* for rapid anastomosis and integration *in vivo*.

Chapter 5: Cell-based Studies: Towards Anastomosis between the Host Vessels and Implanted Encapsulated Endothelial Cells

This final chapter is designed to reflect more recent studies involving the use of endothelial cells pre-encapsulated within hydrogel constructs for host implantation and integration. The findings of these studies are reported in the article titled

"Building Vascular Bridges: Advances in Tissue Engineering" authored by Jennifer E. Saik[1]and Daniel J. Gould[1], Mary E. Dickinson[2] and Jennifer L. West[1, †] *in preparation for submission.*

5.1 Introduction

The formation of stable and functional vessels remains a tremendous challenge for replacement of damaged or diseased tissues. Strategies developed to address this issue include those described earlier in this thesis, whereby the host vasculature is induced to grow into tissue engineered constructs to provide a rapid supply of nutrients and metabolites. Also previous studies have demonstrated the long term nature of vessels induced in response to the growth factors utilized in this project. One alternative approach involves the encapsulation of cells within constructs capable of forming vessel networks. The provision of these encapsulated cells would allow

for the rapid formation of a microvasculature *in vitro* and then the anastomosis of this pre-formed microvasculature with the host induced vessels.

This was the specific goal of the set of experiments described in this chapter: to develop a pre-vascularized construct for rapid perfusion after implantation. A deeper understanding of functional vessel anastomosis may contribute to the fields of tissue engineering, vessel biology, and cancer. Vascularized tissue constructs have a wide variety of applications in the replacement of damaged or diseased tissues including peripheral limb ischemia and chronic diabetic wounds. While many approaches utilize potent growth factors to induce angiogenesis, an alternative employs cells themselves to recruit vessels via naturally secreted chemokines. Cell-based approaches eliminate the time-delay inherent in releasing growth factors and reduce the necessary concentration of potent growth factors. In the current study, cell-laden hydrogels were evaluated using a mouse cornea micropocket angiogenesis assay (Moon, Saik et al. 2010; Poche, Saik et al. 2010), a reproducible and quantifiable assay in a normally avascular tissue (Kenyon 1996). Flk1-myr::mCherry transgenic mice were utilized, which display endothelial specific fluorescence to aid in capillary visualization (Larina 2009).

5.2 Methods

5.2.1 Cell Culture and Encapsulation

Two cell types were chosen for the *in vitro* formation of tubules for anastomosis. These included b.End3 cells (brain derived endothelial cells) and 10t ½ cells (pericytes). Previously, b.End3 cells have been demonstrated to mimic properties of the blood brain barrier in their diffusive and transport characteristics (Omidi, Campbell et al. 2003). B.End3 cells and 10t1/2 cells (Cambrex/Lonza, Walkersville, MD) were used between passages 2 and 6 and cultured. Cells were maintained in endothelial cell growth medium (EGM-2 media, Cambrex/Lonza). Before 3D encapsulation, cells were labeled with Celltracker Red CMTPX (Molecular Probes). 50 μg Celltracker Red was dissolved in 4 μl DMSO and diluted in cell media for a final concentration of 5 μg/ml. b.End3 cells were incubated in the prepared media for 45 min at 37°C. Labeling was visually confirmed via fluorescence microscopy, and labeling media was replaced with normal EGM-2 medium (without VEGF). Cells were washed with phosphate buffered saline (PBS) before enzymatic lifting using trypsin/EDTA and subsequent encapsulation as described below.

The synthetic scaffold chosen to encapsulate the cells in this study was a poly (ethylene glycol) (PEG) based hydrogel comprised of a biocompatible polymer with tunable mechanical properties (Hahn 2006). It was used to encapsulate a co-culture of bEnd.3 endothelial cells and 10T1/2 pericyte precursors under mild photocrosslinking conditions in order to retain cell viability. These PEG-based hydrogels act as a "blank slate" through their resistance to protein adsorption and

subsequent cellular adhesion. Inclusion of immobilized cell-adhesive factors such as the fibronectin-derived peptide RGDS allow for precise mediation of cell-material interactions. The hydrogels were rendered biodegradable by incorporating a matrix metalloproteinase-sensitive peptide into the polymer backbone (West and Hubbell 1999). Collagenase-degradable hydrogels with encapsulated cells (3 x 10^7 cells/mL, labeled with Celltracker Red) were prepared. Briefly, PEG-PQ-PEG (0.1 g/mL) and acryloyl-PEG-RGDS (3.5 μmol/mL) were mixed with a cell suspension and photocrosslinked by exposing to long wavelength UV (365 nm, 10 mW/cm^2) for 7 min, using eosin y as the photoinitiator (0.3% w/v).

5.2.2 Two Step Implantation

In order to provide vessels at the site of implantation for rapid anastomosis, prior to implanting the tubule containing constructs, a unique implantation scheme was developed. Mouse corneas were prevascularized by implanting hydrogels containing 320 ng of soluble platelet-derived growth factor-BB and 80 ng fibroblast growth factor-2 (see figure 5.3). In these studies, n=10, where the experiment was performed with n=5 on two separate days. Experiemental quantification for the *in vivo* tubules comes from images of these implants. For the *in vitro* tubule quantification, n=8.

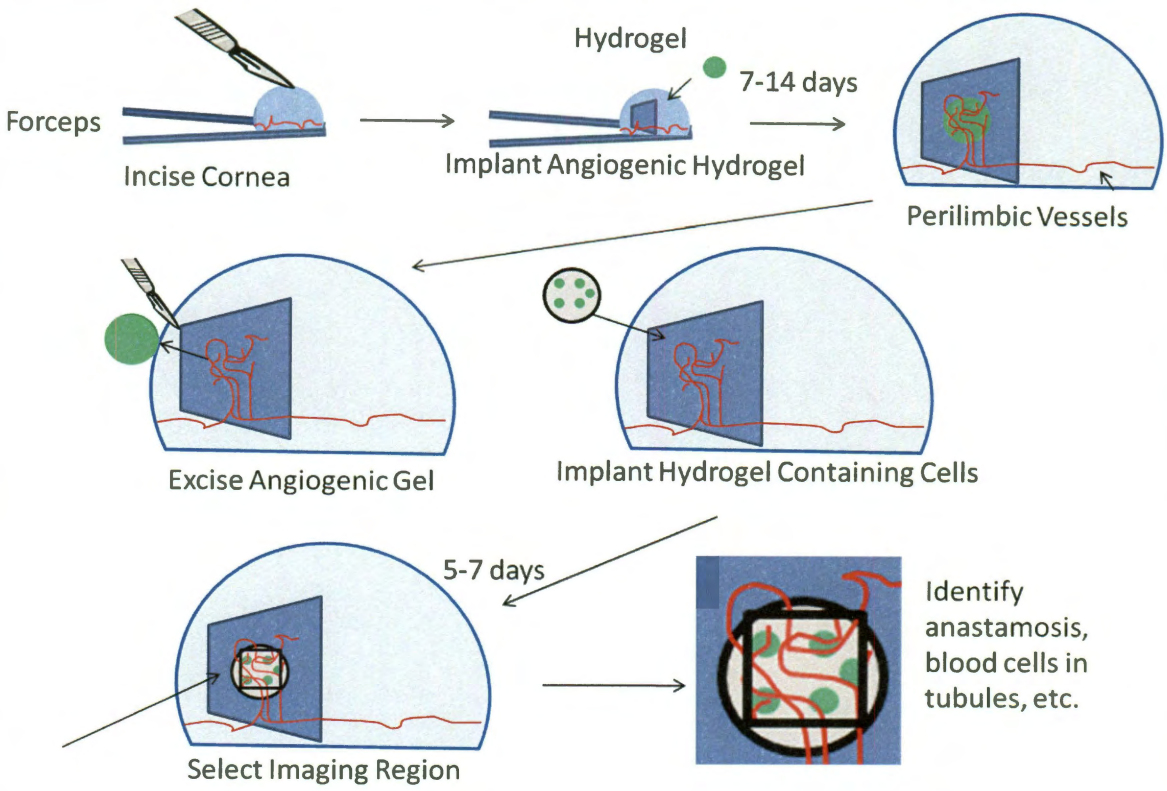

Figure 5.1: Schematic for the novel implantation scheme. First, angiogenic hydrogels are implanted in the cornea, 14 days time is allowed to pass so that induced vessels may create a vascularized pocket. Next, hydrogels with encapsulated endothelial cells are incubated in culture for 48 hours to induce formation of preformed tubules. Finally the initial hydrogels are excised and replaced with the hydrogels containing cells. The tissue is harvested at several time points and examined for tubules and anastomosis.

The new multi-step process was required for successful implantation and anastamosis because the cornea is normally an avascular site. The goal was to prime the recipient vessel bed in order to allow for a rapid anastomotic event.

5.3 Results

5.3.1 Cell Encapsulation and Tubule Formation

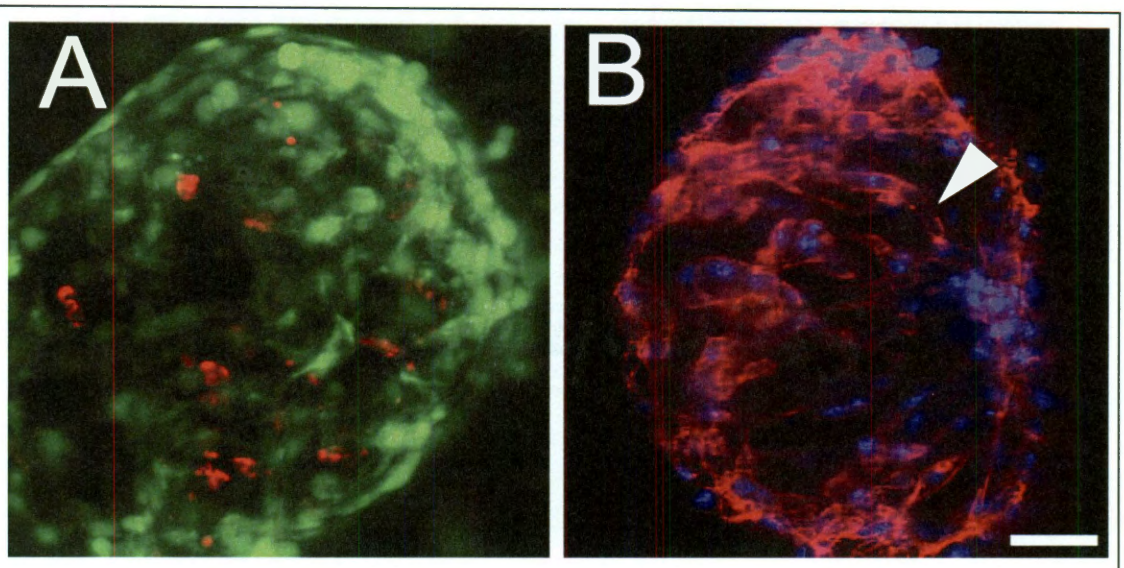

Figure 5.2: Encapsulated cells display high viability and robust tubule formation *in vitro*. A co-culture of bEnd.3 and 10T1/2 cells at a 4:1 ratio in matrix metalloproteinase-sensitive PEG-based hydrogels demonstrate 82% ± 1.5% viability (A, green= live; red = dead) after culturing for 48 hours. Cells also form robust tubules as visualized via actin (red) and nuclei (blue) staining. The white arrow highlights an example of a tubule with interconnecting cells. Scale bar = 50 um.

b.End3 cells were noted to form tubules in PEG-based hydrogels when combined with 10t1/2 smooth muscle precursor cells *in vitro* (figure 5.1). The ability to form these tubules *in vitro* is of critical importance to the success of implantation and integration. These cells proved ideal because they are observed to form tubular networks within 48 hours of *in vitro* cell culture. Encapsulated cells were allowed to culture for 48 hours before implantation, at which point staining confirmed high

viability of 82% ± 1.5%. Extensive tubule formation with branching, cell-cell interconnections, and network formation was visualized via actin staining (figure 5.1).

In addition, cell types were encapsulated alone, and examined for tubule formation and viability. When encapsulated in the hydrogel constructs and cultured *in vitro* the 10 t ½ cells remained distributed throughout the scaffolds, in a balled formation, lacking any tubulogenic structures. Likewise, the bend.3 cells alone when encapsulated did not form extensive tubular networks in comparison to the co-culture. These findings are demonstrated in figure 5.2.

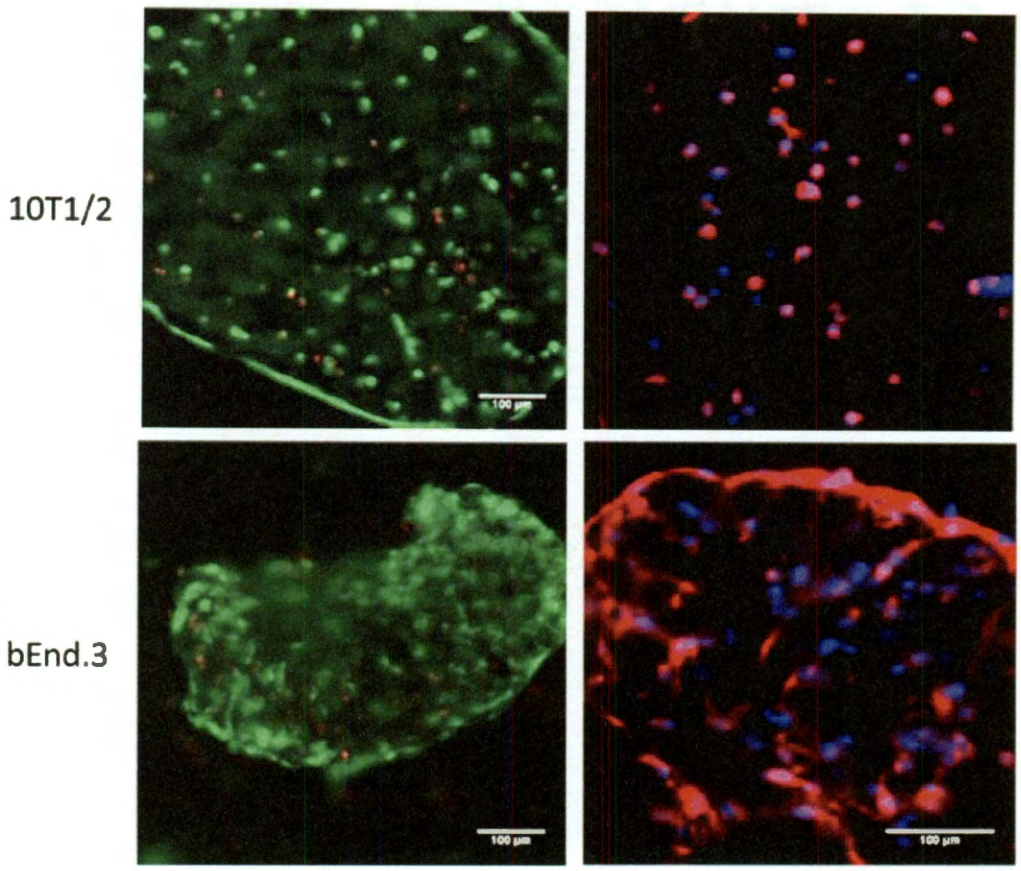

Figure 5.3: Encapsulated individual cell types do not form tubular networks *in vitro*. These cell types do demonstrate good viability, as represented by the high proportion of green cells (live stain) versus red cells dead stain) in the left live/dead staining. Frames on the right show the dapi (blue)/ phalloidin (red) images of the individual cell cultures, where there is not noticeable robust tubule formation. Given neither cell type forms reliable or robust tubules when alone in culture, the use of the co-culture system is validated for *in vitro* tubule formation.

5.3.2 Two Step Implantation and Anastomosis

Implants containing encapsulated growth factors induced an angiogenic response in the areas of the hydrogels. Two weeks after the implantation of the

growth factor containing hydrogels, the implants were surgically excised, leaving only a vascularized pocket, an ideal site for the transplantation of the cell containing implants. Cell-laden implants were soaked in media containing 12 nmol/ml PDGF for 2 hours before being inserted, in order to ensure their survival and to continue to sustain their tubulogenic potential. Three days after implantation, corneas were examined for anastomosis and perfusion using confocal microscopy. This new and unique implantation scheme represents a novel approach to creating a pre-vascularized bed for implantation, and is a valuable contribution for future cornea based implantation studies.

Cherry-labeled capillaries sprouting from red blood cell-filled arterioles were seen connecting to cell-formed tubules (Fig 5.4 A-C). The presence of the originally seeded bEnd.3 cells in the tubules was confirmed using immunohistochemistry to stain for the middle t antigen, which was used to immortalize the bEnd.3 cells (Rothermel 2005) (Fig 5.4 D-F). Image stacks of the immunohistochemistry were processed with both Imaris to provide a three dimensional image (D) and with Imera to recreate a three dimensional volume rendering (E and F) that clearly shows a region of anastomosis and red blood cells inside the encapsulated micro-tubular network. Notably, 72% of the cell-formed tubules contained red blood cells, confirming their functionality. These functional tubules had an average diameter of 8 μm while nonfunctional tubules had an average diameter of 4 μm (Fig 5.4 G).

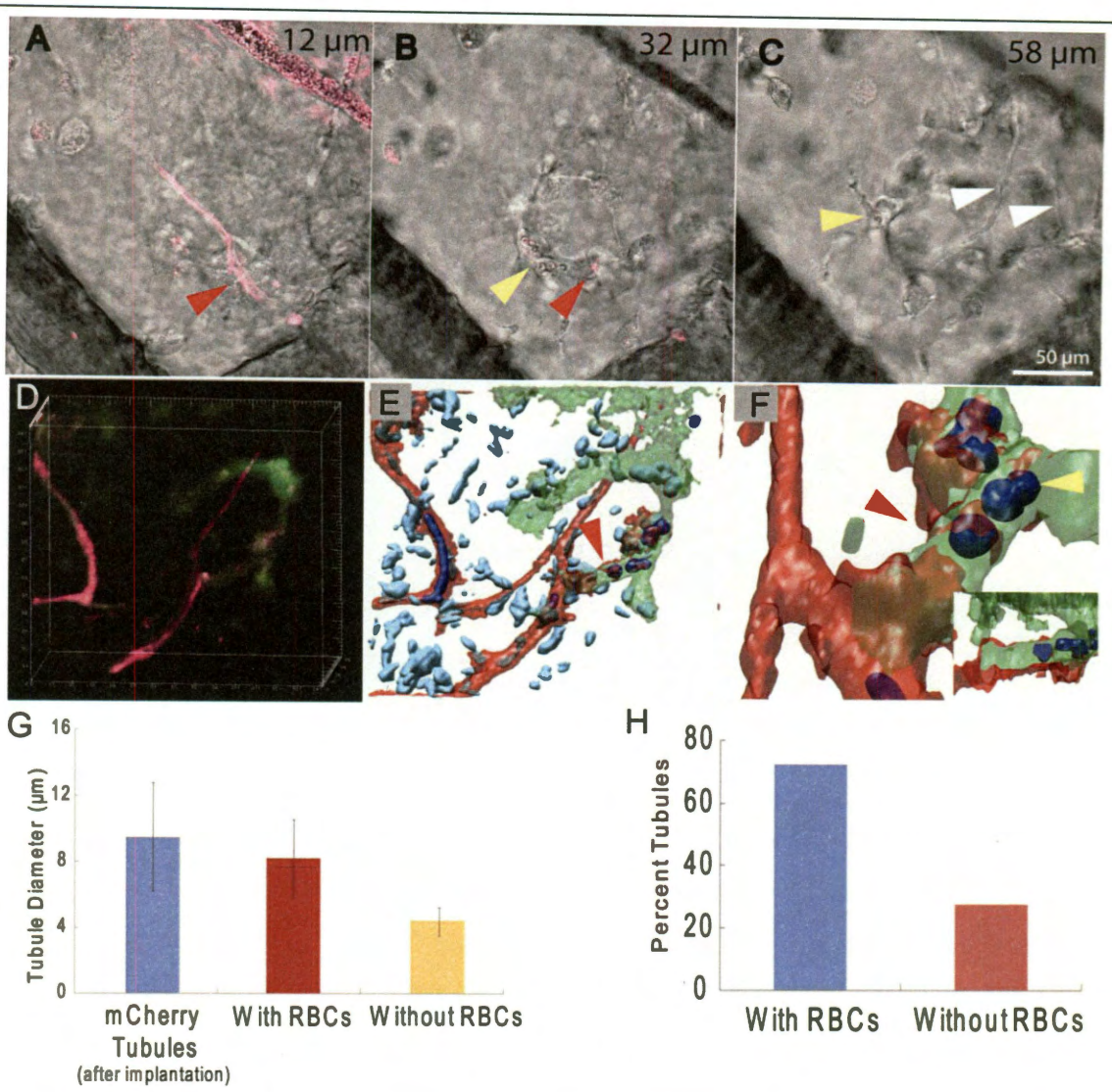

Figure 5.4: Anastomosis between cell-formed tubules and host vasculature. Transgenic mice with fluorescently-tagged endothelial cells (red) enable visualization of smaller vessels (A, red arrow) branching from red blood cell filled arterioles 12 µm into the hydrogel. B) cherry-labeled capillaries (red arrow) connect to unlabeled cell-formed tubules containing red blood cells (yellow arrow) 32 µm into the hydrogel. C) Cells are seen spreading (yellow arrow) and forming tubules as deep as 58 µm into the hydrogel. D-F) To confirm the connection between implanted cells and host vasculature, bEnd.3 cells were stained for expression of the middle t antigen (green). D) Cherry labeled vessels anastamose to middle t antigen-positive bEnd.3 cells in a 3D rendering. E) A three dimensional rendering of red labeled host vasculature connecting to green labeled bEnd.3 cells confirms the presence of red blood cells (dark blue) in the cell-formed tubule. F) Upon closer examination, the precise location of anastomosis (red arrow) and presence of red blood cells (yellow arrow) is visible. G) The tubule diameter confirms that larger diameter tubules (8 µm) are similar in size to host vasculature and contain red blood cells while smaller diameter tubules (4 µm) remain nonfunctional. H) 72% of cell-formed tubules contain red blood cells.

5.4 Discussion

The ultimate product of this study was the formation of a prevascularized tissue engineered construct, which was then successfully anastamosed to the host microvascular system and perfused with host red blood cells. This work presents the first precise visualization and confirmation of anastomosis between tubules formed by self-assembling cells *in vitro* and the host vasculature only 72 hours after implantation in a synthetic material. Additionally, the time of *in vitro* incubation was shortened to only 48 hours, and networks formed by encapsulated bEnd.3 and 10T1/2 cells were maintained once implanted *in vivo.* 72% of cell-formed tubules were perfused with red blood cells after only 3 days in the mouse cornea.

PDGF has previously been shown to induce an angiogenic response in the mouse cornea model (Saik, Gould et al. 2011) and was used to enhance vessel growth into the cornea similar to vascular endothelial growth factor significantly increasing vessel density. Previous studies had demonstrated the importance of *in vitro* incubation before implantation (Peters 2002) but required at least five to seven days incubation time prior to anastomosis (Chen, Aledia et al. 2008). For ultimate translation into clinical applications with cells derived from human patients, this work reduces the time of incubation before implantation and shortens the time to anastomosis to 72 hours. Furthermore, while long term stable vessels were formed in natural matrices (Koike, Fukumura et al. 2004), a synthetic PEG-based polymer can be used as a more advanced platform for testing and identifying key processes in

vessel development and anastomosis. This system is widely applicable to vessel development and disease, including ischemia and organ transplant, and will likely shed insight on mechanisms and therapies. Future studies of this *in vivo* assay will pinpoint the exact moment of anastomosis and the required factors. Furthermore, this technological feat will allow for greater development in complexity and scale, including expansion of incorporated cell types and implant locations.

Some limitations of this study include the two step process itself, during which, the surgical removal of the previously implanted growth factor containing hydrogel is technically very challenging, and should only be attempted after successful mastery of the primary hydrogel implantation. The site within the cornea is very different from other potential implantation sites due to it angiogenic and immune privilege. The goal of primary vessel induction is to pre-vascularize, effectively reducing the angiogenic privilege. It would be interesting to find out if the immune privilege is maintained in this setting. Furthermore, other sites will not contain the anti-angiogenic factors and stroma like the cornea possesses. This may make other sites more amenable to anastamosis and host integration, and could reduce the process to a one step implantation.

Future studies involving this system will likely focus on the anastomotic requirements, as well as long term studies of integration of these cells. Ideally, long term tracers of the cells can be incorporated to monitor the cell remodeling over time. The major leap this project demonstrates is the dramatic decrease in incubation time *in vitro* and the time required for anastomosis *in vivo*, of which both factors will be

critical to the development of clinical strategies for tissues engineering in the future. Furthermore, this technique could allow for determination if the angiogenic privilege of the cornea is coupled to the immunogenic privilege. Studies to determine this might include two step induction then implantation with hydrogels containing immunogenic stimuli, versus primary implantation without induction of vessels.

In conclusion, this study has provided insight into rapid anastamosis and integration of pre-tubularized tissue scaffolds and the host microvasculature.

Chapter 6: Conclusions and Future Directions

In this thesis, I have described a coordinated effort to optimize tissue engineering scaffolds through several approaches. These approaches included the development of a new classification system for the scale-invariant measure of vessel networks, which will provide useful scalable design parameters for microvascularized constructs. Also I have fine tuned the angiogenic response, using a combination of the new vessel morphological measurements along with classical vessel morphology measures to induce vessels with similar morphology to those found in native skin, muscle and brain. I have adapted new biomaterials and tested their feasibility and utility *in vivo* with our unique corneal micropocket assay. Finally, I have combined cells in scaffolds in order to pre-vascularize corneal implants for rapid host anastomosis and perfusion. All of these efforts were designed to help address one of the major hurdles of tissue engineering, which is microvascularization of tissue engineered constructs.

The first chapter described the incredible need for vascularized scaffolds, in order to help reduce the dramatic costs, both financially and with respect to the patients' immune suppression. It also detailed some of the most recent approaches to this problem requiring the development of a tissue engineered construct. Finally, advances in vessel biology and the use of angiogenic factors were described, in order to set up the use of these materials in this thesis.

The second chapter helped then to set up the yard stick for the measurement or quantification of the vascular response, using statistical methods to probe scale-invariant measures of vascular morphology. These methods were critical to the studies, as they helped to augment the typical measurements of vessel branching and diameter as well as density. Furthermore, these measurements became crucial to the fine tuning of the angiogenic response in the third chapter.

These studies provided information about normal early microvascular structures, but recently, other investigators have started to use the simple fractal analysis to look at vascular morphology in diseased vessels as well (Sabo, Boltenko et al. 2001; Jain 2005). Although most of the recent studies focus on tumor vessels and tumor vessel morphology, there may be other applications of the fractal analysis in non tumor vessel pathology, including stroke (Doubal, MacGillivray et al. 2010), ischemic disease, kidney disease (Sng, Sabanayagam et al. 2010) and diabetic vasculopathy (Grauslund, Green et al. 2010). The future holds promise for the application of new, scale-invariant morphological analysis of the microvasculature, not just for engineering applications, but also for therapeutic and diagnostic purposes.

In the future I would propose several studies using the expanded platform I have provided in chapter two to characterize diseased and remodeling vessels. In these studies, I would suggest examining histological samples from human tumors which are solid and are known to have a vascular component which is known to effect treatment. For instance, colon cancer is currently treated with AVASTIN, a therapeutic VEGF inhibitor, which improves survival and outcomes of effected

individuals (Labianca, Beretta et al.). It would be interesting to examine a cohort of patients who received AVASTIN therapy prior to tumor resection, and to compare them to patients who had not received neo-adjuvant therapy in order to determine the effect on vessel fractal dimension and multifractal spectra of neo adjuvant therapy. Sabo and colleagues were able to show clinical relevance of fractal dimension in the predicted morbidity and mortality of renal cell carcinoma, vascularized kidney tumor (Sabo, Boltenko et al. 2001). I would like to similarly probe colon cancer and to determine if tumor vessel fractal dimension after resection, predicts morbidity or mortality. Likewise, I would like to examine mesothelioma (Yano) , and breast adenocarcinoma (Bachelot 2007), other known vascular tumors. Ultimately if the fractal dimension ofr the multifractal spectra proved useful, it could be a clinical test worth administering to provide patients with predictive information about their disease progression. Also, if the test shows some role for its use in neoadjuvant therapy, it could provide a new outcome to measure the effectiveness of future angiostatic or angiotoxic therapy.

This method could also be used to examine remodeling in new, surgically implanted tissues. Currently, skin and soft tissue grafting is a common procedure performed in the united states, to repair tissue defects. Yet, little is known about the microvascular morphology following skin grafting. Wu and colleagues showed in 2008 using a slice by slice tomography reconstruction (Brey, King et al. 2002) that the vessels in split thickness tissue grafts remodel over time (Wu, Kathuria et al. 2008). They were only able to estimate vessel density. I think that this new

classification system could provide valuable morphological information in a similar study. I would like to examine flap vessel morphology and remodeling in the autografting and allografting of tissues for reconstructive therapy.

Ultimately the use of this system could continue to provide more utility in future angiogenic tissue engineering strategies, as described in this thesis in the third chapter. In the third chapter, I used many different doses of growth factors in several different combinations in extensive experiments involving tremendous numbers of live implantations, in order to fully characterize the vascular response in the presence of our novel biomaterial scaffolds to diffusible growth factors. This allowed for the induction of a wide array of vascular responses, which were then characterized and plotted out to try and determine the relationship between the dose concentration of a combination of factors and the morphology of vessels generated. Later, this relationship was exploited, in order to induce vessels with similar morphology to those seen in the skin, muscle and sub ependymal zone of the brain.

Importantly, in this chapter, the fine-tuning of vessel morphology allowed for the optimization of one set of inductive angiogenic factors to mimic normal host tissue morphology. This set of experiments provided a large data set for the optimization of PDGF, FGF and combinations of those factors. It could be used in future experiments where only one of the factors may be used to generate an angiogenic bed. Also the tuning has established a method for future studies, which could involve new factors or encapsulated cells to systematically implant constructs and slowly tune the desired morphological response. The utility of this tuning could

be in the mimicry of native microvessel beds, but it could also be in the identification of the minimum required dose for vessel induction and cell perfusion and survival.

Future experiments should focus on the utility of inducing microvessel morphology. This method could be combined with live imaging and fluorescent markers of metabolism to identify if set morphologies allow for better perfusion and survival of encapsulated cells and scaffolds. Also these studies could isolate other morphological effects by encapsulating materials known to affect endothelial cells or supportive pericytes to determine their role in microvascular development, perfusion and remodeling. Importantly, the study described in chapter three has helped to benchmark key morphological parameters for measurement in future studies. It has also developed an in vivo platform for future use in the development of angiogenic and cell containing tissue engineering scaffolds.

In the fourth chapter I described three recently published studies, where we examined the use of covalently bound factors, which mimic the activity of several growth and cell signaling peptides. In this section I described in depth the *in vivo* work, which represented my contribution to the projects. These studies were exciting applications for my method and they have helped to contribute to our knowledge of the use of these factors and peptides *in vivo*. These PEGylated factors will likely be used in future applications for the microvascularization of tissue engineering constructs.

Again, this fourth chapter demonstrates the utility of the system developed in the third chapter in the design of angiogenic materials. It did so by using the new

platform involving both the micropocket assay and the quantitative techniques to probe the angiogenic nature of several new tethered angiogenic peptides. PEG-PDGF-BB was one of the first demonstrations of a PEGylated angiogenic growth factor for tissue engineering design. PEG-QK provided one of the first examples of a PEGylated small peptide for angiogenic purposes for tissue engineering design. PEG-Ephrin-A1 studies demonstrated the value of the *in vivo* angiogenic platform in probing angiogenesis and helped to show that Eprin-A1 may have future utility in tissue engineering strategies. Although loose comparisons were made in the table in this chapter between the vessels seen in these studies, future projects could incorporate these covalent factors and optimize their induced vessel morphology, over time *in vivo*. Ideally, each of these factors could be optimized for vessel induction and then used in projects to induce microvascularization of tissue scaffolds in vivo for use in therapeutic human applications.

In the final portion of this project, in the fifth chapter, I describe an experiment which has delivered dramatic results. The goal was to induce *in vivo* anastomosis between host and encapsulated cells, to form a prevascularized construct for tissue engineering applications. This was possible through the use of a new commercially available cell type, the bend cell, which *in vitro* replicates some of the functions of the normal blood-brain barrier.

Critical to this aim was the development of a novel implantation scheme, which allowed for induction of a vascular bed prior to implantation of the cell-containing scaffolds in the corneal micropocket. I first implanted the cornea with an

angiogenic implant for induction of the vascular response, and then with pre-tubulogenic encapsulated brain endothelial cells. This novel two-stage implantation scheme will set the stage for future examination of the critical factors regulating host microvessel anastomosis. This two step process was critical to the success of anastamosis early in these implants, because the initial implantation of growth factor laden hydrogels helped to prime the recipient site location for implantation. The priming of the vascular response provides in intermediate step, which could be utilized in conjunction with what I developed in the third chapter, to fine tune the induced recipient bed for anastamosis. This could be valuable to induce vessels with morphology similar to normal vessels in the tissue which encapsulated cells are normally found in. In effect this allows for the priming step to induce vessels similar to the target tissues. Also, this step could be used to induce the minimum necessary vasculature to support a cell containing scaffold. This step provides one more advantage, which is the dissociation of the administration of inductive growth factors from the implantation of encapsulated cells. This could be critical in applications involving cell types which may be sensitive to growth factors, like stem cells which are desired to stay in a less differentiated success for tissue engineering applications.

Future studies should involve the use of other cell types encapsulated in the hydrogels for implantation in the second step, either alone or in conjunction with endothelial cells, to allow for rapid host integration. These studies could help to develop the platform for the integration of tissue engineered scaffolds containing cells for regenerative applications. Also other sites, like the omental cavity and the dorsal

skin fold should similarly be implanted and examined for host integration, following success in the cornea, to see if these more accessible sites, which are not normally angiogenically privileged like the cornea, could be useful for future engineering strategies.

The *in vivo* corneal micropocket assay should continue to be used to identify new angiogenic materials, and to optimize angiogenesis and cell integration. These methods should be adapted further for more cell based scaffolds, in order to test the feasibility of cell laden scaffolds for return of function or partial function of different organs, like liver, pancreas, and kidney. Cells derived from these organs or stem cells capable of differentiating to the adult cells found in these organs which are responsible for synthesis of secreted hormones and cytokines should be tested in the corneal model first, then scaled to other larger models. Also, the morphological quantification system should be used to look at diseased vessels, like those found in human tumors and in microangiopathic diseases, including diabetes and coronary artery disease. Insights into the microvascular morphology of these disease states could provide more data for models of disease pathology and could help us to better understand aberrant vessel morphology. Finally, biomaterials that were identified as valuable for tuning the angiogenic response in this thesis should be tested in other angiogenic assays and for use in tissue applications to move them towards use in humans.

Some of the future implications of this work will be in helping to design tissue engineered constructs for use in humans, for optimization of angiogenic scaffolds,

optimization of cell-laden hydrogels, and for fine tuning microvascular morphology *in vitro* and *in vivo*.

In closing, this thesis has been an excellent and rewarding opportunity to help to advance the field of tissue engineering by designing new strategies to overcome the hurdle of engineering microvascularized tissue constructs. In the future, these methods will be utilized in similar projects to create constructs for further study of tissue engineering constructs and as potential therapeutics for the use in treatment of human diseases.

Appendix

Section 1: Anova tables from dose escalation studies

	PDGF 7days 640ng	PDGF 7days 160ng	PDGF 7days 40ng	PDGF 14days 640ng	PDGF 14days 160ng	PDGF 14days 40ng	FGF 7days 640ng	FGF 7days 160ng	FGF 7days 40ng	FGF 14days 640ng	FGF 14days 160ng	FGF 14days 40ng	PDGF/ FGF 7days 640/160ng	PDGF/ FGF 7days 160/40ng	PDGF/ FGF 7days 40/10ng	PDGF/ FGF 14days 640/160ng	PDGF/ FGF 14days 160/40ng	PDGF/ FGF 14days 40/10ng	PPDGF/ FGF 14days 87/21ng	PDGF/ FGF 14days 189/47ng	PDGF/ FGF 14days 320/80ng	PDGF/ FGF 14days 88/22ng
PDGF 7days 640ng		ns	0.01	ns	0.01	0.01	ns	0.01	0.01	ns	ns	0.01	ns	0.05	0.01	ns	0.01	0.01	0.01	0.05	ns	0.01
PDGF 7days 160ng			0.01	ns	ns	0.01	ns	0.05	0.01	0.05	ns	0.01	ns	ns	0.01	ns	0.05	0.01	0.01	ns	ns	0.01
PDGF 7days 40ng				0.01	ns	ns	0.01	ns	ns	0.01	0.01	ns	0.01	0.01	ns	0.01	ns	ns	ns	0.05	0.01	ns
PDGF 14days 640ng					ns	0.01	ns	ns	0.01	ns	ns	0.01	ns	ns	ns	ns	ns	0.01	0.05	ns	ns	ns
PDGF 14days 160ng						0.05	ns	ns	0.01	ns	ns	0.05	0.01	ns	ns	ns	ns	ns	ns	ns	0.01	ns
PDGF 14 days 40ng							0.01	ns	ns	0.01	0.01	ns	0.01	0.01	ns	0.01	ns	ns	ns	0.01	0.01	ns
FGF 7days 640ng								0.05	0.01	ns	ns	0.01	ns	ns	0.01	ns	0.05	0.01	0.01	ns	ns	0.01
FGF 7days 160ng									0.05	ns	ns	ns	0.01	ns	ns	0.05	ns	ns	ns	ns	0.01	ns
FGF 7days 40ng										0.01	0.01	ns	0.01	0.01	ns	0.01	ns	ns	ns	0.01	0.01	ns
FGF 14days 640ng											ns	0.01	ns	ns	0.05	ns	0.05	0.01	0.01	ns	ns	0.05
FGF 14days 160ng												0.01	ns	ns	ns	ns	ns	0.01	0.05	ns	ns	ns
FGF 14days 40ng													0.01	0.01	ns	0.01	ns	ns	ns	0.01	0.01	ns
PDGF/FGF 7days 640/160ng														0.05	0.01	ns	0.01	0.01	0.01	ns	ns	0.01
PDGF/FGF 7days 160/40ng															ns	ns	ns	0.05	0.05	ns	ns	ns
PDGF/FGF 7days 40/10ng																0.01	ns	ns	ns	ns	0.01	ns
PDGF/FGF 14days 640/160ng																	0.01	0.01	0.01	ns	ns	0.01
PDGF/FGF 14days 160/40ng																		ns	ns	ns	0.01	ns
PDGF/FGF 14days 40/10ng																			ns	0.05	0.01	ns
PPDGF/FGF 14days 87/21ng																				0.05	0.01	ns
PDGF/FGF 14days 189/47ng																					ns	ns
PDGF/FGF 14days 320/80ng																						0.01
PDGF/FGF 14days 88/22ng																						

Table A1: Comparison of **Vessel Density** From Experimental Groups Using Analysis of Variance and Post- Hoc Tukey Test. ANOVA testing was performed on the mean values from the vessel density measurements, and then a post hoc tukey's test was applied to identify differences between the experimental groups. This table represents the output differences from the Tukey test, in the comparison of the means of each group. Differences between means that were above the score needed to signify a difference with a p value of at least 0.05 are represented by the number 0.05; those with a difference between means with a p value of at least 0.01 are represented with 0.01 in the table. Those comparisons which did not have significant differences between means are represented with ns in the table.

	PDGF 7days 640ng	PDGF 7days 160ng	PDGF 7days 40ng	PDGF 14days 640ng	PDGF 14days 160ng	PDGF 14days 40ng	FGF 7days 640ng	FGF 7days 160ng	FGF 7days 40ng	FGF 14days 640ng	FGF 14days 160ng	FGF 14days 40ng	PDGF/ FGF 7days 640/160ng	PDGF/ FGF 7days 160/40ng	PDGF/ FGF 7days 40/10ng	PDGF/ FGF 14days 640/160ng	PDGF/ FGF 14days 160/40ng	PDGF/ FGF 14days 40/10ng	PPDGF/ FGF 14days 87/21ng	PDGF/ FGF 14days 189/47ng	PDGF/ FGF 14days 320/80ng	PDGF/ FGF 14days 88/22ng
PDGF 7days 640ng		ns	0.01	ns	0.05	0.01	ns	0.05	0.01	ns	ns	0.01	ns	ns	0.01	ns	0.05	0.01	0.01	ns	ns	0.05
PDGF 7days 160ng			0.01	ns	ns	0.01	ns	ns	0.01	ns	ns	0.01	ns	ns	0.05	ns	ns	0.01	0.01	ns	ns	0.05
PDGF 7days 40ng				0.01	0.05	ns	0.01	0.01	ns	0.01	0.01	ns	0.01	0.01	ns	0.01	0.01	ns	ns	0.01	0.05	ns
PDGF 14days 640ng					ns	0.01	ns	ns	0.01	ns	ns	0.01	ns	ns	ns	ns	ns	0.01	0.01	ns	ns	0.05
PDGF 14days 160ng						0.01	ns	ns	0.01	ns	ns	0.01	0.01	ns	ns	0.05	ns	ns	ns	ns	0.05	ns
PDGF 14 days 40ng							0.01	0.01	ns	0.01	0.01	ns	0.01	0.01	0.01	0.01	0.01	ns	ns	0.01	0.05	0.05
FGF 7days 640ng								ns	0.01	ns	ns	0.01	ns	ns	ns	ns	ns	0.01	0.01	ns	ns	0.05
FGF 7days 160ng									0.01	ns	ns	0.01	0.01	ns	ns	ns	ns	ns	ns	ns	0.05	ns
FGF 7days 40ng										0.01	0.01	ns	0.01	0.01	0.01	0.01	0.01	0.05	0.05	0.01	0.05	0.05
FGF 14days 640ng											ns	0.01	ns	ns	ns	ns	ns	0.01	0.01	0.01	ns	0.05
FGF 14days 160ng												0.01	ns	ns	ns	ns	ns	0.01	0.01	ns	ns	ns
FGF 14days 40ng													0.01	0.01	0.01	0.01	0.01	ns	ns	0.01	0.05	0.05
PDGF/FGF 7days 640/160ng														ns	0.01	ns	0.05	0.01	0.01	ns	ns	0.05
PDGF/FGF 7days 160/40ng															ns	ns	ns	0.01	0.01	ns	ns	ns
PDGF/FGF 7days 40/10ng																0.01	ns	ns	ns	ns	0.05	ns
PDGF/FGF 14days 640/160ng																	ns	0.01	0.01	ns	ns	0.05
PDGF/FGF 14days 160/40ng																		ns	ns	ns	0.05	ns
PDGF/FGF 14days 40/10ng																			ns	0.01	0.05	ns
PPDGF/FGF 14days 87/21ng																				0.01	0.05	ns
PDGF/FGF 14days 189/47ng																					ns	ns
PDGF/FGF 14days 320/80ng																						0.05
PDGF/FGF 14days 88/22ng																						

Table A2: Comparison of **Fractal Dimension** From Experimental Groups Using Analysis of Variance and Post- Hoc Tukey Test. ANOVA testing was performed on the mean values from the fractal dimension measurements, and then a post hoc tukey's test was applied to identify differences between the experimental groups. This table represents the output differences from the Tukey test, in the comparison of the means of each group. Differences between means that were above the score needed to signify a difference with a p value of at least 0.05 are represented by the number 0.05; those with a difference between means with a p value of at least 0.01 are represented with 0.01 in the table. Those comparisons which did not have significant differences between means are represented with ns in the table.

	PDGF 7days 640ng	PDGF 7days 160ng	PDGF 7days 40ng	PDGF 14days 640ng	PDGF 14days 160ng	PDGF 14days 40ng	FGF 7days 640ng	FGF 7days 160ng	FGF 7days 40ng	FGF 14days 640ng	FGF 14days 160ng	FGF 14days 40ng	PDGF/ FGF 7days 640/160ng	PDGF/ FGF 7days 160/40ng	PDGF/ FGF 7days 40/10ng	PDGF/ FGF 14days 640/160ng	PDGF/ FGF 14days 160/40ng	PDGF/ FGF 14days 40/10ng	PPDGF/ FGF 14days 87/21ng	PDGF/ FGF 14days 189/47ng	PDGF/ FGF 14days 320/80ng	PDGF/ FGF 14days 88/22ng
PDGF 7days 640ng		ns	0.01	ns	0.01	0.01	ns	0.01	0.01	ns	0.05	0.01	ns	ns	0.01	ns	0.01	0.01	0.01	0.05	ns	0.01
PDGF 7days 160ng			0.01	ns	ns	0.05	ns	ns	0.01	ns	ns	0.01	0.01	ns	0.05	ns	ns	0.05	0.05	ns	ns	ns
PDGF 7days 40ng				ns	ns	ns	0.01	ns	ns	ns	ns	ns	0.01	ns	ns	0.01	ns	ns	ns	ns	0.01	ns
PDGF 14days 640ng					ns	ns	ns	ns	ns	ns	ns	ns	0.01	ns	ns	ns	ns	ns	ns	ns	0.05	ns
PDGF 14days 160ng						ns	ns	ns	ns	ns	ns	ns	0.01	ns	ns	0.01	ns	ns	ns	ns	0.01	ns
PDGF 14 days 40ng							0.05	ns	ns	ns	ns	ns	0.01	ns	ns	0.01	ns	ns	ns	ns	0.01	ns
FGF 7days 640ng								0.05	0.01	ns	ns	0.01	ns	ns	0.05	ns	ns	0.05	0.01	ns	ns	0.05
FGF 7days 160ng									ns	ns	ns	ns	0.01	ns	ns	0.01	ns	ns	ns	ns	0.01	ns
FGF 7days 40ng										0.05	ns	ns	0.01	0.05	ns	0.01	ns	ns	ns	ns	0.01	ns
FGF 14days 640ng											ns	ns	0.01	ns	ns	ns	ns	ns	ns	ns	0.05	ns
FGF 14days 160ng												ns	0.01	ns	ns	ns	ns	ns	ns	ns	0.01	ns
FGF 14days 40ng													0.01	ns	ns	0.01	ns	ns	ns	ns	0.01	ns
PDGF/FGF 7days 640/160ng														0.01	0.01	ns	0.01	0.01	0.01	0.01	ns	0.01
PDGF/FGF 7days 160/40ng															ns	ns	ns	ns	ns	ns	0.05	ns
PDGF/FGF 7days 40/10ng																0.01	ns	ns	ns	ns	0.01	ns
PDGF/FGF 14days 640/160ng																	0.01	0.01	0.01	ns	ns	0.01
PDGF/FGF 14days 160/40ng																		ns	ns	ns	0.01	ns
PDGF/FGF 14days 40/10ng																			ns	ns	0.01	ns
PPDGF/FGF 14days 87/21ng																				ns	0.01	ns
PDGF/FGF 14days 189/47ng																					0.01	ns
PDGF/FGF 14days 320/80ng																						0.01
PDGF/FGF 14days 88/22ng																						

Table A3: Comparison of **Lacunarity Parameter (*b*)** From Experimental Groups Using Analysis of Variance and Post- Hoc Tukey Test. ANOVA testing was performed on the mean values from the Lacunarity Parameter (*b*) measurements, and then a post hoc tukey's test was applied to identify differences between the experimental groups. This table represents the output differences from the Tukey test, in the comparison of the means of each group. Differences between means that were above the score needed to signify a difference with a p value of at least 0.05 are represented by the number 0.05; those with a difference between means with a p value of at least 0.01 are represented with 0.01 in the table. Those comparisons which did not have significant differences between means are represented with ns in the table.

	PDGF 7days 640ng	PDGF 7days 160ng	PDGF 7days 40ng	PDGF 14days 640ng	PDGF 14days 160ng	PDGF 14days 40ng	FGF 7days 640ng	FGF 7days 160ng	FGF 7days 40ng	FGF 14days 640ng	FGF 14days 160ng	FGF 14days 40ng	PDGF/ FGF 7days 640/160ng	PDGF/ FGF 7days 160/40ng	PDGF/ FGF 7days 40/10ng	PDGF/ FGF 14days 640/160ng	PDGF/ FGF 14days 160/40ng	PDGF/ FGF 14days 40/10ng
PDGF 7days 640ng		ns	0.01	ns	0.01	0.01	0.01	0.01	0.01	ns	ns	0.01	0.01	0.01	0.01	0.01	ns	0.01
PDGF 7days 160ng			ns	0.01	ns	0.01	0.01	ns	0.01	0.01	ns	0.01	0.01	0.01	ns	0.01	ns	0.01
PDGF 7days 40ng				0.01	ns	ns	0.01	ns	ns	0.01	ns	ns	0.01	0.01	ns	0.01	0.01	ns
PDGF 14days 640ng					ns	0.01	ns	0.01	0.01	ns	0.01	0.01	0.01	0.01	0.01	0.01	ns	0.01
PDGF 14days 160ng						ns	0.01	ns	ns	0.01	ns	ns	0.01	0.01	ns	0.01	ns	ns
PDGF 14 days 40ng							0.01	ns	ns	0.01	0.01	ns	0.01	0.01	ns	0.01	0.01	ns
FGF 7days 640ng								0.01	0.01	ns	0.01	0.01	0.01	ns	0.01	0.01	0.01	0.01
FGF 7days 160ng									ns	0.01	ns	ns	0.01	0.01	ns	0.01	ns	ns
FGF 7days 40ng										0.01	0.01	ns	0.01	0.01	ns	0.01	0.01	ns
FGF 14days 640ng											0.01	0.01	0.01	ns	0.01	0.01	0.01	0.01
FGF 14days 160ng												0.01	0.01	0.01	ns	0.01	ns	0.01
FGF 14days 40ng													0.01	0.01	ns	0.01	0.01	ns
PDGF/FGF 7days 640/160ng														0.01	0.01	ns	0.01	0.01
PDGF/FGF 7days 160/40ng															0.01	0.01	0.01	0.01
PDGF/FGF 7days 40/10ng																0.01	ns	ns
PDGF/FGF 14days 640/160ng																	0.01	0.01
PDGF/FGF 14days 160/40ng																		0.01
PDGF/FGF 14days 40/10ng																		

Table A4: Comparison of **Branch Points** From Experimental Groups Using Analysis of Variance and Post- Hoc Tukey Test. ANOVA testing was performed on the mean values from the Branch Point measurements, and then a post hoc tukey's test was applied to identify differences between the experimental groups. This table represents the output differences from the Tukey test, in the comparison of the means of each group. Differences between means that were above the score needed to signify a difference with a p value of at least 0.05 are represented by the number 0.05; those with a difference between means with a p value of at least 0.01 are represented with 0.01 in the table. Those comparisons which did not have significant differences between means are represented with ns in the table.

	PDGF 7days 640ng	PDGF 7days 160ng	PDGF 7days 40ng	PDGF 14days 640ng	PDGF 14days 160ng	PDGF 14days 40ng	FGF 7days 640ng	FGF 7days 160ng	FGF 7days 40ng	FGF 14days 640ng	FGF 14days 160ng	FGF 14days 40ng	PDGF/ FGF 7days 640/160ng	PDGF/ FGF 7days 160/40ng	PDGF/ FGF 7days 40/10ng	PDGF/ FGF 14days 640/160ng	PDGF/ FGF 14days 160/40ng	PDGF/ FGF 14days 40/10ng
PDGF 7days 640ng		ns	0.01	ns	0.01	0.01	ns	0.01	0.01	0.01	0.01	0.01	0.01	ns	0.01	0.01	0.01	0.01
PDGF 7days 160ng			0.01	0.01	0.01	0.01	ns	0.01	0.01	0.01	0.01	0.01	0.01	ns	0.01	0.01	0.01	0.01
PDGF 7days 40ng				0.01	ns	0.01	0.01	ns	ns	ns	0.01	0.01	0.01	0.01	ns	ns	0.01	ns
PDGF 14days 640ng					0.01	0.01	0.01	0.01	0.01	0.01	0.01	0.01	0.01	ns	0.01	0.01	0.01	0.01
PDGF 14days 160ng						0.01	0.01	ns	0.01	ns	0.01	0.01	0.01	0.01	ns	ns	0.01	ns
PDGF 14 days 40ng							0.01	0.01	ns	0.01	ns	ns	0.01	0.01	0.01	ns	ns	ns
FGF 7days 640ng								0.01	0.01	0.01	0.01	0.01	0.01	ns	0.01	0.01	0.01	0.01
FGF 7days 160ng									0.01	ns	0.01	0.01	0.01	0.01	ns	0.01	0.01	ns
FGF 7days 40ng										0.01	ns	ns	0.01	0.01	ns	ns	ns	ns
FGF 14days 640ng											0.01	0.01	0.01	0.01	ns	ns	0.01	ns
FGF 14days 160ng												ns	0.01	0.01	0.01	ns	ns	ns
FGF 14days 40ng													0.01	0.01	0.01	ns	ns	ns
PDGF/FGF 7days 640/160ng														0.01	0.01	0.01	0.01	0.01
PDGF/FGF 7days 160/40ng															0.01	0.01	0.01	0.01
PDGF/FGF 7days 40/10ng																ns	0.01	ns
PDGF/FGF 14days 640/160ng																	ns	ns
PDGF/FGF 14days 160/40ng																		ns
PDGF/FGF 14days 40/10ng																		

Table A5: Comparison of **Vessel Diameter** From Experimental Groups Using Analysis of Variance and Post- Hoc Tukey Test. ANOVA testing was performed on the mean values from the vessel diameter measurements, and then a post hoc tukey's test was applied to identify differences between the experimental groups. This table represents the output differences from the Tukey test, in the comparison of the means of each group. Differences between means that were above the score needed to signify a difference with a p value of at least 0.05 are represented by the number 0.05; those with a difference between means with a p value of at least 0.01 are represented with 0.01 in the table. Those comparisons which did not have significant differences between means are represented with ns in the table.

Appendix Section 2: PEG PDGF Studies In Vitro Methods

In this appendix section, the entire methods are described for the experiments pertaining to the studies on PEG PDGF.

MATERIALS AND METHODS

Cell Maintenance

HUVECs (Lonza, Walkersville, MD) were cultured in endothelial growth medium EGM-2 (Lonza), supplemented with ascorbic acid, epidermal growth factor, fibroblast growth factor (hFGF-2), heparin, hydrocortisone, insulin-like growth factor, GA-1000 (gentamicin, amphotericin-B), 2% fetal bovine serum (Bulletkit, Lonza), 2 mM L-glutamine, 1 U/ml penicillin, and 1 μg/ml streptomycin (GPS, Sigma, St. Louis, MO, USA). 10T1/2 cells (American Type Culture Collection, Manassas, VA) were cultured in Dulbecco's modified Eagle's Medium with high glucose (DMEM, Gibco, North Andover, MA) supplemented with 10% fetal bovine serum and 2 mM L-glutamine, 1 U/ml penicillin and 1 μg/ml streptomycin (GPS, Sigma). HUVECs were used from passages 4 to 6, and 10T1/2 cells were used from passages 15 to 19. Cells were maintained in an incubator at 37 ^{o}C and 5% CO_2 with media replenished every two days and subculturing as necessary.

Synthesis and Purification of Poly(ethylene glycol) Diacrylate (PEGDA)

Poly(ethylene glycol) (PEG) (MW = 6000 Da; Fluka, Milwaukee, WI) was acrylated by reacting dry PEG with acryloyl chloride (Sigma, St. Louis, MO) and triethyl amine (TEA; Sigma) in anhydrous dichloromethane (DCM; Sigma) under argon gas overnight at 1:4 PEG:acryloyl chloride and 1:2 PEG:TEA molar ratios. The resulting solution was washed with 2 M K_2CO_3 and allowed to separate into aqueous and organic phases overnight. PEGDA, in the organic phase, was dried using anhydrous $MgSO_4$ followed by filtration. The polymer was precipitated in diethyl ether, filtered, and dried overnight under vacuum. PEGDA powder was stored at -20°C under argon gas.

Synthesis and Purification of PEG-RGDS and Degradable PEG-PQ-PEG

PEG-RGDS was synthesized by dissolving the cell-adhesive peptide, Arg-Gly-Asp-Ser, (RGDS, American Peptide, Sunnyvale, CA) into anhydrous dimethyl sulfoxide and adding diisopropylethylamine. Dissolved RGDS was added to dry acryloyl-PEG-succinimidyl carboxymethyl (PEG-SCM, Laysan, Arab, AL) at a 1.1:1 PEG-SCM: RGDS molar ratio. This mixture was placed on a rocker overnight, dialyzed against water in a regenerated cellulose membrane to remove unwanted products, and lyophilized.

Hydrogels were rendered degradable by the incorporation of a collagenase-sensitive peptide, GGGPQGIWGQGK (abbreviated PQ), into the backbone of the PEGDA base polymer. The PQ peptide was first synthesized using Fmoc chemistry on an APEX 396 solid phase peptide synthesizer (Aapptec) and characterized using MALDI-TOF. The synthesized peptide was conjugated to PEG by following a similar

procedure as above with a 2.1 molar excess of PEG-SCM. Conjugation of PEG-RGDS and PEG-PQ-PEG were confirmed using a gel permeation chromatography (GPC) system equipped with a PLgel column (5μm, 500Å, Polymer Laboratories, Amherst, MA) and an evaporative light scattering (ELS) detector (Polymer Laboratories). The PEG-RGDS was dissolved in 0.1% ammonium acetate in dimethylformamide (DMF) solvent and tested against a PEG-SCM standard.

Synthesis and Purification of acryloyl-PEG-succinimidyl carbonate (PEG-SMC)

The organic solvents needed to accommodate the short half-life of the succinimidyl carboxymethyl reactive group on the PEG-SCM, which was purchased and used for conjugation of peptides, were not compatible with proteins used in this study. It was therefore necessary to synthesize a heterobifunctional acryloyl-PEG-succinimidyl carbonate (PEG-SMC) in-house. PEG-SMC is functionally similar to the commercially available PEG-SCM, but has a longer reaction half-life and can thus be used under aqueous conditions.

PEG (Fluka/Sigma, MW = 3400 Da) was reacted with Ag_2O (Sigma, St. Louis, MO), acryloyl chloride (Sigma, St. Louis, MO), and KI (Sigma, St. Louis, MO) in anhydrous dichloromethane (DCM; Sigma, St. Louis, MO) at 4 ^{o}C overnight, at molar excess ratios of 1.5, 1.1, and 0.3 respectively. Silver was removed by filtering the solution through Celite 521 (Spectrum Chemical Mfg Corp, Gardena, CA). A Rotovap was used to dry the solution prior to dissolution in di H_20. The pH was adjusted to 3 with

HCl, and the solution was heated to 35 °C for 1 h. Iodine was removed by adding activated charcoal (Fisher, Pittsburg, PA), and the solution was filtered through Celite 521. NaCl and DCM were added, followed by DCM extraction. Phase separation with 2 M K_2CO_3 was used to remove acid and chloride ions. Monoacrylated PEG was dried with sodium sulfate (Fisher, Pittsburg, PA), and a Rotovap was used to concentrate the solution followed byethyl ether precipitation and vacuum filtration. A four molar excess of disuccinimidyl carbonate (Sigma) was reacted with the monoacrylated PEG in anhydrous acetonitrile (Sigma) and pyridine (Sigma) under argon overnight. The product was dried using a Rotovap prior to dissolving in anhydrous DCM. The solution was filtered, and PEG-SMC was purified in acetate buffer (0.1 M, pH 4.5, 15% NaCl) via phase separation. The purified PEG-SMC was dried with anhydrous $MgSO_4$. PEG-SMC was precipitated into ethyl ether, filtered, and dried overnight under vacuum. PEG-SMC was characterized by proton nuclear magnetic resonance spectroscopy (^{1}H-NMR, Avance 400 Hz; Bruker, Billerica, MA, USA) and matrix-assisted laser desorption/ionisation-time of flight mass spectrometry (MALDI-TOF; Bruker Daltonics, Dillerica, MA, USA). The final PEG-SMC product was stored at -80 °C under argon.

Synthesis of PEG-PDGF-BB and PEG-FGF-2

In-house synthesized acryloyl-PEG-SMC was dissolved in 50 mM sodium bicarbonate buffer (pH 8.5) and sterilized via filtration (0.2 μm). PDGF-BB (ProSpec Bio, Israel) was conjugated to PEG-SMC using a 400:1 PEG-SMC: PDGF-BB molar ratio in 200 mM sodium bicarbonate buffer (pH 8.5) at 4 °C for 4 d (Figure 1). The

resulting PEG-PDGF-BB solution was lyophilized under sterile conditions. PEG-PDGF-BB powder was reconstituted and stored in HEPES Buffered Saline (100 mM NaCl, 10 mM HEPES in deionized water; HBS; pH 7.4) with 0.1% BSA at 4 ^{o}C for up to three months. A similar procedure was followed for PEG-FGF-2 (ProSpec Bio) at a 100:1 PEG-SMC: FGF-2 molar ratio. All growth factor conjugations were confirmed via Western Blot analysis on a 15% Tris-HCL precast polyacrylamide gel (Biorad, Hercules, CA). Primary antibodies included rabbit polyclonal anti-PDGF-B antibody (Santa Cruz Biotechnology, Santa Cruz, CA) and rabbit polyclonal anti-FGF-basic antibody (Millipore, Billerica, MA). Secondary antibody HRP-conjugated goat anti-rabbit IgG (Santa Cruz Biotechnology, Santa Cruz, CA) and an ECL^{TM} chemiluminescent western blotting analysis system (GE Healthcare, Buckinghamshire, UK) were used. The western blot membrane was exposed to film (Kodak, Rochester, NY) for 15 s and developed using a Micromax Developer (Hope, Seattle, WA) with T_2 developer and T_2 fixer (White Mountain Imaging, Salisbury, NY). The presence of PEG was confirmed using a PEG stain adapted from (Zhang, Wang et al. 2006), which allows barium iodine to react with PEG to form a yellow color.

Unconjugated PDGF-BB was quantified using a PDGF-BB ELISA (R&D systems, Minneapolis, MN). PEG chains mask antibody binding to PEG-PDGF, so the amount of unconjugated PDGF-BB was quantified after running a sample of the reacted solution on an ELISA. With the amount of soluble PDGF-BB quantified, appropriate concentrations of PEG-PDGF-BB were calculated.

Formation and Surface Modification of PEGDA Hydrogels

Six kDa PEGDA was dissolved in HBS to a 10% polymer weight percentage solution. A stock solution of the photoinitiator 2-dimethoxy-2-phenylacetophenone (acetophenone, Sigma) was prepared by dissolving 300 mg acetophenone in 1 ml N-vinylpyrrolidone (NVP) and then added to the polymer solution at a concentration of 10 µl/ml. The solution was vortexed and sterile filtered. Hydrogels were polymerized between two glass slides separated by a 0.75 mm thick poly(tetra fluoroethylene) (PTFE) spacer. The glass slides and spacer were secured using clips. Polymer solution was exposed to UV light (B-200SP UV lamp, UVP, 365 nm, 10 mW/cm^2) for 30 s and stored in PBS with 0.1% sodium azide.

The effects of PEGylated proteins in 2D were studied by modifying the surface of bulk PEGDA hydrogels as previously described (Moon, Lee et al. 2007). Briefly, 5 mm diameter circles were punched from the hydrogel slabs prepared above. A solution containing 10 µl/ml acetophenone along with PEG-RGDS and PEGylated growth factors was then added in sufficient volume to completely cover the surface of the hydrogel. The exact combination and concentrations of each factor are given in the individual experiments below. Hydrogels were then exposed to UV light for 2 min followed by soaking in sterile PBS to allow for swelling and removal of the photoinitiator solution.

Patterned hydrogel surfaces were also made to emphasize the utility of spatial control of PEG-PDGF-BB. Hydrogels were patterned by pipetting a solution containing 10 µl/ml acetophenone along with PEGylated growth factors onto the surface of a 5 mm diameter of a bulk hydrogel with a black transparency to block UV light from part of the

gel. Hydrogels were exposed to 2 min of UV light followed by extensive rinsing. PEG-RGDS was then immobilized to the entire surface by adding a solution containing 10 μl/ml acetophenone with PEG-RGDS to completely cover the surface of the hydrogel followed by 2 min UV light exposure.

For all studies, unconjugated PDGF-BB and PEG-SMC were removed via diffusion before the hydrogels were used. Alternatively, soluble PDGF-BB could also be left in place to act as a diffusible growth factor to encourage cell migration in the surrounding tissue for other applications.

To quantify the surface concentration of immobilized PEG-PDGF-BB, hydrogels were synthesized as described above and then degraded in 0.1 N sodium hydroxide for three days. After complete hydrogel degradation, the protein concentration was read on a Nanodrop 2000 (Thermo Scientific, Wilmington, DE).

Bioactivity of Conjugated PDGF-BB via 10T1/2 Proliferation

In order to evaluate the bioactivity of covalently attached PEG-PDGF-BB, 10T1/2 cells (8.5×10^4 cells/cm^2) were seeded onto gels modified with 5 mg/ml PEG-RGDS alone or in combination with 0.70 nmol/ml PEG-PDGF-BB. As a positive control, 0.70 nmol/ml soluble PDGF-BB was added to the media of gels modified with PEG-RGDS alone. Cells were imaged using an Axiovert 135 (Zeiss) inverted fluorescent microscope after 48 h of culture. Cell nuclei were visualized via incubation with Hoechst 33342 dye

(Bis- 119 Benzimide, Sigma) at a concentration of 5 μg/ml in DMEM without serum for one h at 37 °C. Four fluorescent images were taken per gel at excitation = 350 nm and emission = 460 nm. Cell nuclei were quantified using ImageJ. Cell counts in the presence of PDGF-BB were normalized to counts on surfaces modified with PEG-RGDS alone. Data from three separate experiments using gels with PEG-RGDS (n=31), PEG-PDGF-BB and PEG-RGDS (n=28), and PEG-RGDS and soluble PDGF-BB (n=18) was pooled for statistical analysis as described below.

Quantification of Tubule Formation

To investigate the impact of covalently incorporated growth factors on vascular tubulogenesis, surface-modified PEGDA hydrogels were used. Bulk hydrogels were prepared from 10% 6kDa PEGDA and surfaces were modified as described above. Four modified surfaces were investigated: (1) 50 mg/ml PEG-RGDS, (2) PEG-RGDS and 0.27 nmol/ml PEG-FGF-2, (3) PEG-RGDS and 0.70 nmol/ml PEG-PDGF-BB and (4) PEG-RGDS, PEG-PDGF-BB, and PEG-FGF-2. HUVECs (8.5×10^5 cells/cm^2) or a co-culture of HUVECs and 10T1/2 cells at a ratio of 4:1 were seeded onto the modified gels and cultured in EGM-2 media either with or without FGF-2 and imaged using an Axiovert 135 (Zeiss) inverted fluorescent microscope. Hydrogels were observed over a 30-day period and images of the entire surface of the gels were merged in Adobe Photoshop Elements. Tubules and modified surface areas were traced in Adobe Illustrator and quantified using ImageJ. For gels seeded with HUVECs alone, data from three separate experiments using gels with PEG-RGDS (n=10), PEG-FGF-2 and PEG-RGDS (n=3), PEG-PDGF-BB and PEG-RGDS (n=10), and PEG-FGF-2, PEG-PDGF-BB (n=4) was

pooled. For the co-culture of HUVEC and 10T1/2 hydrogels, data from three separate experiments using gels in media with FGF-2 with PEG-RGDS (n=10), PEG-FGF-2 and PEG-RGDS (n=3), PEG-PDGF-BB and PEG-RGDS (n=12), and PEG-FGF-2, PEG-PDGF-BB, and PEG-RGDS (n=12) was pooled. Similarly, data from three separate experiments using gels in media without FGF-2 with PEG-RGDS (n=7), PEG-FGF-2 and PEG-RGDS (n=6), PEG-PDGF-BB and PEG-RGDS (n=8), and PEG-FGF-2, PEG-PDGF-BB, and PEG-RGDS (n=7) was pooled.

Immunohistochemistry

To examine tubule morphology, immunohistochemistry was performed to identify endothelial pericyte cell markers. After 30 d in culture, gels were fixed in 4% paraformaldehyde for 30 min and washed with phosphate buffered saline (PBS). Cells were permeabilized with 0.5% Triton-X for 10 min followed by a second PBS wash. 3% normal donkey serum (Sigma) was used as a blocking agent prior to application of the primary antibodies. Gels were incubated overnight at 4 ^{o}C in a 1:200 dilution of mouse anti-alpha smooth muscle actin (R&D systems, Minneapolis, MN) and a 1:100 dilution of goat anti-PECAM-1 (Santa Cruz Biotechnology) in 3% bovine serum albumin solution in PBS. Following incubation, gels were rinsed five times in PBS for 1 h each time. A 1:400 dilution of Alexafluor 488 donkey anti-goat IgG (Invitrogen) and Alexafluor 555 donkey anti-mouse IgG (Invitrogen, Carlsbad, California) was applied overnight at 4 ^{o}C in order to visualize the primary antibodies. After washing, gels were incubated in a DAPI solution (2 μM, Invitrogen) for 45 min. Images were taken using a confocal microscope (Zeiss Live5, Plan-Apochromat 20x objective with 0.8 numerical aperture

and Plan-Apochromat oil-immersion 63x with 1.4 numerical aperture, for Alexafluor 488: excitation = 489 nm, emission BP filter = 500-525 nm; for Alexafluor 555: excitation = 532nm, emission BP filter = 560-675 nm, for DAPI: excitation = 405 nm, emission BP filter = 415-480 nm).

Cellular Encapsulation into Hydrogels

To further understand the effects of covalently immobilized growth factors on cells in 3D, HUVECs were encapsulated into MMP-sensitive hydrogels containing covalently immobilized growth factors. HUVECs were fluorescently labeled the day before encapsulation by incubation with 10 μg green CMFDA Cell Tracker® (Invitrogen, Eugene, Oregon) in the culture media for 1 h. Following incubation, cells were rinsed with PBS and fresh media was added.

Polymer solution was prepared in HBS (10 mM, pH 7.4) with a final formulation of 10% PEG-PQ-PEG, 3.5 μmol/ml PEG-RGDS, and 0.3% w/v Irgacure 2959 (Ciba Corporations, Based, Switzerland). Four treatment groups were observed, including hydrogels containing: (1) PEG-RGDS alone, (2) PEG-RGDS and PEG-FGF, (3) PEG-RGDS and PEG-PDGF-BB, and (4) PEG-RGDS, PEG-FGF-2, and PEG-PDGF-BB. 0.03 nmol/L PEG-FGF and 0.08 nmol/L PEG-PDGF-BB were used for both the individual factor groups and the combination of factors. Fluorescently-labeled HUVECs were harvested using trypsin-EDTA and counted using a Coulter counter to resuspended cells at a known concentration. 30,000 cells/μl cells were pelleted by centrifuging at 2700 RPM for 4 min. 5 μl droplets of cell-laden polymer were formed and exposed to UV

light for 7 min and the resulting cell-laden hydrogels were immediately immersed in EGM-2 media for *in vitro* analysis.

Activity of the cells in the hydrogels was monitored for 60 h using a Zeiss LSM 5Live confocal microscope. Images were captured every hour and analyzed using Logger Pro Software to track cell movement. Data from three separate experiments was pooled using hydrogels with PEG-FGF-2 and PEG-RGDS, PEG-PDGF-BB and PEG-RGDS, and PEG-FGF-2, PEG-PDGF-BB, and PEG-RGDS (n=30) for collapse data analysis.

Zymography

To determine MMP activity, media was collected from gels with encapsulated HUVECs 60 h after encapsulation. Standard zymography was performed on a 10% precast polyacrylamide gel with gelatin (Biorad, Hercules, CA) following a Millipore protocol. Briefly, after running electrophoresis, gels were immersed in a 25% triton-X-100 solution in water with gentle mixing for 30 min. After decanting the solution, a developing buffer (50 mM Tris base, 50mM Tris-HCl, 0.2 M NaCl, 5 mM $CaCl_2$, 5 mM Brij 35) was applied overnight at 37 ^{o}C. Gels were then stained with Coomassie Blue and destained with Methanol:acetic acid:water (50:10:40). Gel images were obtained using a Fujifilm LAS 4000 and analyzed for the presence of MMP bands.

Appendix section 3 : PEG-QK Methods

Cell Culture

Human umbilical vein endothelial cells (HUVEC, Cambrex/Lonza, Walkersville, MD) were used between passages 2 and 6 and cultured as previously described [10]. Cells were maintained in VEGF-free endothelial cell growth medium (EGM-2 media, Cambrex/Lonza). Before 3D encapsulation, HUVECS were labeled with Celltracker Red CMTPX (Molecular Probes). 50 μg Celltracker Red was dissolved in 4 μl DMSO and diluted in cell media for a final concentration of 5 μg/ml. HUVECs were incubated in the prepared media for 45 min at 37°C. Labeling was visually confirmed via fluorescence microscopy, and labeling media was replaced with normal EGM-2 medium (without VEGF). Cells were washed with phosphate buffered saline (PBS) before enzymatic lifting using trypsin/EDTA and subsequent encapsulation as described below.

Preparation and Purification of Poly(ethylene glycol) Derivatives

*Preparation and Purification of Poly(ethylene glycol) Diacrylate (PEGDA):*Poly(ethylene glycol) (PEG; Fluka/Sigma, MW = 6000 Da) was reacted at a 1:4 molar ratio with acryloyl chloride (Sigma) in anhydrous dichloromethane (DCM; Sigma) with triethyl amine (TEA; Sigma; 1:2 (PEG:TEA) molar ratio) overnight under argon at 25°C. PEGDA was purified by phase separation using 2 M K_2CO_3. The PEGDA-containing organic phase was dried using anhydrous $MgSO_4$ and filtered. PEGDA was precipitated in diethyl ether, filtered, and dried overnight and under

vacuum. The final product was characterized by ^{1}H-NMR and stored at -20°C under argon until use.

Preparation and Purification of PEG-succinimidyl carbonate (PEG-SMC):

Monoacrylated PEG was prepared by through a reaction of PEG (Fluka/Sigma, MW = 3400 Da) with 1.5 molar excess Ag_2O (Sigma), 1.1 molar excess acryloyl chloride (Sigma), and 0.3 molar ratio KI (Sigma) in anhydrous dichloromethane (DCM; Sigma) at 0-4°C overnight. The product was filtered in solution using Celite 521 (Spectrum Chemical Manufacturing Corp, Gardena, CA) to remove silver. The filtered product was dried *via* Rotovap, and then dissolved in DI H_20, followed by altering the pH to pH=3 using HCl. The solution was then heated to 35°C for 1 h, and activated charcoal (Fisher) was added to remove iodine. The solution was again filtered using Celite 521. NaCl was added with DCM, followed by extraction of DCM. Phase separation using 2 M K_2CO_3 removed chloride ions and acid. Resulting monoacrylated PEG was dried using sodium sulfate (Fisher), concentrated *via* Rotovap, precipitated in ethyl ether, and vacuum filtered. PEG monoacrylate was then reacted with 4 molar excess disuccinimidyl carbonate (Sigma) in anhydrous acetonitrile (Sigma) and pyridine (Sigma) overnight under argon. The resulting solution was dried *via* Rotovap, then dissolved in anhydrous DCM and filtered. PEG-SMC was isolated via phase separation in acetate buffer (0.1 M, pH 4.5, 15% NaCl), dried using anhydrous $MgSO_4$, filtered, precipitated in ethyl ether, filtered, and dried overnight and under vacuum. PEG-SMC was characterized by ^{1}H NMR and MALDI-TOF and stored at -80°C under argon until use.

Preparation and Purification of PEG-QK: The angiogenic peptide Ac-KLTWQELYQL[K(Ac)]Y[K(Ac)]GI-amide was designed to react with PEG-SCM at the first lysine (K) residue only, by protecting all other free amines with acetyl groups (represented by Ac). QK (MW=2036 Da, Aapptec, Louisville, KY) was dissolved in DMSO at a concentration of 7.4 mM. N,n-diisopropylethylamine (DIPEA, Sigma, 2 mol per mol PEG) was added to the solution to act as a base catalyst. Acryloyl-PEG-succinimidyl ester (PEG-SCM, Laysan, MW=3400 Da) was similarly dissolved at a concentration of 1.5 mM. PEG-SCM was added dropwise to QK in a 10:1 molar ratio with slow mixing and allowed to react for 4 d at 25°C. The product was precipitated in cold isopropanol and dried overnight. PEG-QK was then lyophilized and stored in HEPES buffered saline (HBS) with 0.1% bovine serum albumin (BSA) at 4°C until use. Conjugation was characterized by MALDI-TOF (MS Autoflex, solvent: methanol).

Preparation and Purification of PEG-RGDS: The cell-adhesive peptide RGDS (American Peptide, Sunnyvale, CA) was dissolved in DMSO at a concentration of 30 mM. DIPEA was added to the solution to act as a base catalyst. Acryloyl-PEG-N-hydroxysuccinimide (PEG-SCM, Laysan, MW=3400 Da) was similarly dissolved at a concentration of 30 mM. PEG-SCM was added dropwise to RGDS in a 1:1 molar ratio with slow mixing and allowed to react for 4 d at 25°C. The product was dialyzed against DI H_20 for 8 h using a membrane with a 3500 Da molecular weight cutoff (Spectrum Laboratories, Rancho Dominguez, CA). PEG-RGDS was then lyophilized and stored at -80°C under argon until use. Conjugation was characterized by gel permeation chromatography (GPC) using a PLgel column (5 μm, 500 Å, Polymer Laboratories,

Amherst, MA), 0.1% ammonium acetate in DMF solvent, and evaporative light scattering (ELS) detector (Polymer Laboratories), run against unreacted PEG-SCM for comparison.

Synthesis of Collagenase-Degradable PEG-PQ-PEG: A collagenase-sensitive peptide (PQ), GGGPQGIWGQGK, was prepared on a peptide synthesizer (Aapptec, Louisville, KY) using standard Fmoc chemistry. The peptide was cleaved from the resin using 95% trifluoroacetic acid (TFA), 2.5% triisopropylsilane (TIPS) in water and precipitated in ether. The peptide was reacted with PEG-SCM (Laysan, MW=3400 Da) in a 2:1 ratio (PEG-SCM:PQ) in DMSO and DIPEA (2 mol per mol PEG) for 4 d at 25°C to generate a PEG-diacrylate derivative with PQ in the polymer backbone. PEG-PQ-PEG was dialyzed against DI H_20 for 8 h using a membrane with a 3500 Da molecular weight cutoff (Spectrum Laboratories), and conjugation was confirmed via GPC with ELS detection as described previously.

Synthesis of PEG-VEGF: PEG-VEGF was synthesized as previously described in detail [10]. In brief, $VEGF_{165}$ (Sigma) was reacted with acryloyl-PEG-SMC in a 1:200 molar ratio in sterile 50 mM sodium bicarbonate buffer (pH 8.5, 0°C) for 4 d. PEG-VEGF was then lyophilized under sterile conditions and stored in HEPES buffered saline (HBS) with 0.1% bovine serum albumin (BSA) at 4°C until use. Conjugation was confirmed via Western blot by visualizing an increase in molecular weight as previously described in detail [10].

Bioactivity Assay

Bioactivity of PEG-QK was determined by measuring its pro-mitotic effect on endothelial cells. HUVECs were seeded at 1.05 x 10^3 cells/cm^2 in EGM-2 medium without VEGF on Day 1. On Day 4, medium was replaced with EGM-2 medium without VEGF and FGF, with an addition of either 0.13 pmol/ml VEGF (positive control), 50 pmol/ml QK, 50 pmol/ml PEG-QK, or no VEGF (negative control). The levels of QK were chosen to correspond with the bioactivity levels reported in D'Andrea's original paper on the peptide, which showed that the bioactivity of 1 mol VEGF was equal to that of 385 mol QK [D'Andrea 2005]. This medium was replaced after 4 h with EGM-2 without VEGF and FGF. On Day 6, cells were treated with a Hoechst 33342 dye (Bis-Benzimide, Sigma), which labels cell nuclei. Hoechst dye was added at a concentration of 5 μg/ml in EGM-2 without VEGF and FGF, and cells were incubated with this media for 1 h. Fluorescent images were taken immediately of each well, with 4-6 images per well, using a fluorescent microscope with excitation = 350 nm, emission = 460 nm. Cell nuclei were quantified using ImageJ. Statistical differences between groups were analyzed using ANOVA, followed by Tukey's Least Significant Difference post hoc analysis, with $p<0.05$ considered statistically significant.

Formation of Modified PEGDA Hydrogels

Formation of PEGDA Hydrogels: Hydrogels were formed as previously described in detail [10]. In brief, 6 kDa PEGDA was dissolved in HEPES buffered saline (HBS) in

a 10% w/v solution and sterile filtered. Photoinitiator, 10 μL/mL of 300 mg/mL 2,2-dimethoxy-2-phenylacetophenone in N-vinylpyrrolidone (NVP), was added to the solution. The polymer solution was pipetted into molds and crosslinked through exposure to long wavelength ultraviolet light (B-200SP UV lamp, UVP, 365 nm, 10 mW/cm^2) for 30 s. After crosslinking, the mold was removed, and the PEGDA hydrogel slab was placed in sterile PBS with 0.1% sodium azide until further use.

Surface Modification of PEGDA Hydrogels: Hydrogel slabs were soaked for 1 h in sterile PBS to remove sodium azide. 5 mm diameter circles were punched from PEGDA hydrogel slabs. A polymer solution consisting of 173 nmol/mL PEG-QK, 30 μmol/mL PEG-RGDS, 1 μmol/mL eosin Y, and 3.95 μL/mL NVP was prepared. From this solution, 10 μL was pipetted onto the top surface of the gel, completely covering the surface. The gel and polymer solution were exposed to a 532 nm laser at 30 mW/cm^2 for 30 s. Positive control hydrogels were made with 420 pmol/mL PEG-VEGF instead of PEG-QK, and negative control hydrogels contained PEG-RGDS only. Each surface-modified gel was then soaked in sterile PBS for 1 d to allow non-reacted polymer, excess photoinitiator, and residual sodium azide to diffuse from the gel.

Formation of Three-dimensional Proteolytically Degradable PEG Hydrogels: Collagenase-degradable hydrogels with encapsulated HUVEC cells (3×10^7 cells/mL, labeled with Celltracker Red) were prepared. Briefly, PEG-PQ-PEG (0.1 g/mL), acryloyl-PEG-RGDS (3.5 μmol/mL), and acryloyl-PEG-QK (152 nmol/mL or 760 nmol/mL) were mixed with a cell suspension and photocrosslinked by exposing to long

wavelength UV (365 nm, 10 mW/cm^2) for 7 min, using Irgacure 2959 as the photoinitiator (0.3% w/v). Two concentrations of PEG-QK were investigated; the lower corresponds to the bioactivity levels of comparative positive control PEG-VEGF hydrogels; the second is five times higher. As previously noted, D'Andrea et al. found that 385 mol QK had equal bioactivity to 1 mol VEGF in a proliferation assay [2]. As a positive control, hydrogels were crosslinked with incorporation of PEG-VEGF (400 pmol/mL) instead of PEG-QK, and as a negative control, hydrogels were prepared with PEG-RGDS only.

Characterization of Hydrogels

Quantification of Surface-Immobilized QK, VEGF, and RGDS: Hydrogel disks were modified with either PEG-QK, PEG-VEGF, or PEG-RGDS, and then soaked to allow unbound peg-modified factor to diffuse from the hydrogel. The amount of PEG-QK bound to the hydrogel was determined by measuring the absorbance of PEG-QK in the soak solution after hydrogel modification. The absorbance of PEG-QK, which includes a tryptophan amino acid residue, was measured at 280 nm spectrophotometrically (Vivian) and compared to prepolymer solution standards. Similarly, an ELISA assay was used to determine the amount of VEGF that was covalently immobilized on positive control hydrogel surfaces as previously described by measuring the amount of PEG-VEGF removed by soaking [10]. A ninhydrin assay was used to quantify the amount of covalently-linked PEG-RGDS on the surface of the gels, as previously described [10].

Biological Activity on Hydrogels

Endothelial Tubule Formation on Surface of Hydrogels: HUVECs were seeded (8.5×10^4 cells/cm^2) onto gels with either PEG-RGDS and PEG-QK, PEG-RGDS and PEG-VEGF, or only PEG-RGDS covalently attached to the surface. HUVEC tubulogenic response on the gels was monitored and EGM-2 medium changed every other day. Three experimental groups were observed: QK- and RGDS-modified hydrogels cultured in EGM-2 medium (without soluble VEGF), VEGF- and RGDS-modified hydrogels cultured in EGM-2 medium (without soluble VEGF), and RGDS-modified hydrogels cultured in EGM-2 medium (without soluble VEGF). Images were taken of each entire gel and merged using Photoshop Elements software. Tubules were

traced using Adobe Illustrator software, and length of each tubule was calculated in ImageJ software (NIH, Bethesda, Maryland). The total sum of tubule length per area was calculated for each sample. Data from separate experiments was pooled, and ANOVA followed by Tukey's Least Significant Difference post hoc analysis was performed to determine significant differences between groups, with $p<0.05$ considered statistically significant. All data are presented as mean $\pm$ standard deviation.

In some samples, cells were permeabilized with 0.1% Tween-20 for 30 min, blocked with BSA for 30 min, then treated with Alexafluor 488-conjugated phalloidin (10 U/mL, Molecular Probes) and DAPI (2 μM, Invitrogen, Carlsbad, California) for 45 min to label cell actin filaments and nuclei, and visualized using confocal microscopy (Zeiss Live5, Plan-Apochromat 20x objective with 0.8 numerical aperture and digital zoom of 1 or 2, for Alexafluor 488 phalloidin: excitation = 489 nm, emission BP filter = 500-525 nm; for DAPI: excitation = 405 nm, emission BP filter = 415-480 nm, pinhole = 7 μm). Tubules stained with phalloidin/DAPI were captured via z-stack images.

Time Lapse Study of Endothelial Tubulogenesis in Three-dimensional Degradable PEG Hydrogels: Three-dimensional collagenase-degradable constructs were transferred to a confocal microscope (Zeiss Live5, Thornwood, NY) with a stage chamber providing a regulated environment (37°C and 5% CO_2). No additional proteolytic enzymes or protease inhibitors were added to the culture. Z-stack images were collected every hour for 60 h using the Multi Time Series macro (Zeiss), Plan-Apochromat 20x objective with 0.8 numerical aperture, and excitation wavelength = 532 nm, emission bandpass (BP) filter = 560-675 nm, and pinhole = 7 μm. Time lapse movies were analyzed for tubule

formation, cell migration, and cell-cell contact formation. For tubule formation, tubules were traced at 22 h and 32 h time points and quantified. Total tubule length per viewing field was analyzed. For cell migration quantification, the movement of three randomly selected cells per viewing field was tracked using Logger Pro software, which allows the tracing and quantification of cell paths through timeframe progression. For cell-cell contact formation quantification, the number of all cell-cell contacts formed within the viewing field was counted by timeframe progression using Zeiss LSM5 Image Browser. The number of cell-cell contacts formed was normalized by the number of cells present in the first frame analyzed. Data from separate experiments was pooled, and ANOVA, followed by Tukey's Least Significant Difference, was performed to determine significant differences between groups, with $p<0.05$ considered statistically significant.

References:

Adhemar Longatto Filho, J. M. L., and Fernando C. Schmitt (2010). ""Angiogenesis and Breast Cancer."" Journal of Oncology **vol. 2010,** (Article ID 576384): 7 pages.

Al-Kadi, O. S. and D. Watson (2008). "Texture Analysis of Aggressive and Nonaggressive Lung Tumor CE CT Images." Biomedical Engineering, IEEE Transactions on **55**(7): 1822.

Ambati, B. K., Nozaki, M., Singh, N., Takeda, A., Jani, P. D., Suthar, T., Albuquerque, R. J., Richter, E., and E. Sakurai, Newcomb, M. T. et al. (2006). "Corneal avascularity is due to soluble VEGF receptor-1." Nature **443**: 993-7.

Atala, A., Bauer, S. B., Soker, S., Yoo, J. J. and Retik, A. B. (2006). "Tissue-engineered autologous bladders for patients needing cystoplasty." Lancet **367**: 1241-6.

Au, P., J. Tam, et al. (2008). "Bone marrow-derived mesenchymal stem cells facilitate engineering of long-lasting functional vasculature." Blood **111**(9): 4551-4558.

Auerbach, R., R. Lewis, et al. (2003). "Angiogenesis assays: A critical overview." Clinical Chemistry **49**(1): 32.

Avakian, A., R. E. Kalina, et al. (2002). "Fractal analysis of region-based vascular change in the normal and non-proliferative diabetic retina." Current Eye Research **24**(4): 274-280.

Bachelot, T. (2007). "[Angiogenesis and breast cancer]." Bulletin du cancer **94 Spec No**: S203.

Baish, J. W., Y. Gazit, et al. (1996). "Role of Tumor Vascular Architecture in Nutrient and Drug Delivery: An Invasion Percolation-Based Network Model." Microvascular Research **51**(3): 327.

Baish, J. W. and R. K. Jain (2000). "Fractals and Cancer." Cancer Res **60**(14): 3683-3688.

Bautch, V. L., James, Jennifer M. (2009). "Neurovascular Development." Cell Adhesion and Migration **3**(2): 199-204.

Beenken, A. and M. Mohammadi (2009). "The FGF family: biology, pathophysiology and therapy." Nature Rev. Drug Discov. **8**: 235.

Bemis, R. (2005). "Thresholding Tool." MATLAB Central.

Bergman, D. L. and U. Ullberg (1998). "Scaling properties of the placenta's arterial tree." J Theor Biol **193**: 731 - 738.

Bianchi, F., M. Rosi, et al. (2007). "Microfabrication of fractal polymeric structures for capillary morphogenesis: Applications in therapeutic angiogenesis and in the engineering of vascularized tissue." Journal of Biomedical Materials Research Part B: Applied Biomaterials **81B**(2): 462.

Bikfalvi, A., S. Klein, et al. (1997). "Biological roles of fibroblast growth factor-2." Endocr Rev **18**(1): 26-45.

Biondi, M., F. Ungaro, et al. (2008). "Controlled drug delivery in tissue engineering." Advanced Drug Delivery Reviews **60**(2): 229.

Block, A., W. von Bloh, et al. (1990). "Efficient box-counting determination of generalized fractal dimensions." Physical Review A **42**(4): 1869.

Bohnsack, B. L. a. H., K. K. (2003). "The FAKs about blood vessel assembly." Circ Res **92**: 255-7.

Brey, E. M., T. W. King, et al. (2002). "A Technique for Quantitative Three-Dimensional Analysis of Microvascular Structure." Microvascular Research **63**(3): 279.

Bui, A., I. Šutalo, et al. (2009). "Dynamics of pulsatile flow in fractal models of vascular branching networks." Medical and Biological Engineering and Computing **47**(7): 763.

Cao, R., Anna Eriksson, Hajime Kubo, Kari Alitalo, Yihai Cao and Johan Thyberg (2004). "*Comparative Evaluation of FGF-2–, VEGF-A–, and VEGF-C–Induced Angiogenesis, Lymphangiogenesis, Vascular Fenestrations, and Permeability*." Circ. Res. **94**: 664-670.

Cao, R., E. Brakenhielm, et al. (2003). "Angiogenic synergism, vascular stability and improvement of hind-limb ischemia by a combination of PDGF-BB and FGF-2." Nat Med **9**(5): 604-13.

Cao, R., Brakenhielm, E., Pawliuk, R., Wariaro, D., Post, M. J., Wahlberg, E., Leboulch, P. and Cao, Y. (2003). "Angiogenic synergism, vascular stability and improvement of hind-limb ischemia by a combination of PDGF-BB and FGF-2." Nat Medicine **9**: 604-13.

Cao, R., Meit A. Björndahl, Piotr Religa, Steve Clasper, Stina Garvin, Dagmar Galter, Björn Meister, Fumitaka Ikomi, Katerina Tritsaris, Steen Dissing, Toshio Ohhashi, David G. Jackson and Yihai Cao (2004). "PDGF-BB induces intratumoral lymphangiogenesis and promotes lymphatic metastasis." cancer cell **6**(4): 333-345.

Cao, Y., R. Cao, et al. (2008). "R Regulation of tumor angiogenesis and metastasis by FGF and PDGF signaling pathways." J Mol Med **86**(7): 785-9.

Caplan, A. I. (1985). "The vasculature and limb development." Cell Differentiation **16**(1): 1.

Carlson, B. M. (1973). "The regeneration of skeletal muscle — a review." American Journal of Anatomy **137**(2): 119.

Carmeliet, P. (2005). "Angiogenesis in life, disease and medicine." Nature **438**(7070): 932.

Carmeliet, P. and R. K. Jain (2000). "Angiogenesis in cancer and other diseases." Nature **407**(6801): 249.

Cascone, M. G., B. Sim, et al. (1995). "Blends of synthetic and natural polymers as drug delivery systems for growth hormone." Biomaterials **16**(7): 569.

Chang, J.-H., E. E. Gabison, et al. (2001). "Corneal neovascularization." Current Opinion in Ophthalmology **12**(4): 242-249.

Chaudhari, A., C.-C. Sanders Yan, et al. (2002). "Effect of surface roughness on diffusion limited reactions, a multifractal scaling analysis." Chemical Physics Letters **351**(5-6): 341.

Chen, X., A. S. Aledia, et al. (2008). "Prevascularization of a Fibrin-Based Tissue Construct Accelerates the Formation of Functional Anastomosis with Host Vasculature." Tissue Eng Part A.

Cheung, H.-Y., K.-T. Lau, et al. (2007). "A critical review on polymer-based bio-engineered materials for scaffold development." Composites Part B: Engineering **38**(3): 291.

Chhabra, A. B., and R.V. Jensen. 1989. (1989). "Direct determination of the f(a) singularity spectrum." Phys. Rev. Lett. **62**: 1327-1330.

Claudio, D., C. Anna, et al. (1999). "Prognostic and predictive value of intratumoral microvessels density in operable non-small-cell lung cancer." Lung cancer (Amsterdam, Netherlands) **24**(2): 81.

Cosgriff-Hernandez, E., M. Hahn, et al. "Bioactive hydrogels based on Designer Collagens." Acta Biomaterialia **In Press, Uncorrected Proof**.

Cursiefen, C. (2007). "Immune privilege and angiogenic privilege of the cornea." Chem Immunol Allergy **92**: 50-7.

D'Andrea, L. D., G. Iaccarino, et al. (2005). "Targeting angiogenesis: Structural characterization and biological properties of a de novo engineered VEGF mimicking peptide." Proceedings of the National Academy of Sciences of the United States of America **102**(40): 14215-14220.

Dajnowiec, D. and B. L. Langille (2007). "Arterial adaptations to chronic changes in haemodynamic function: coupling vasomotor tone to structural remodelling." Clinical Science **113**(1): 15-23.

Davies, N., S. Dobner, et al. (2008). "The dosage dependence of VEGF stimulation on scaffold neovascularisation." Biomaterials **29**(26): 3531-8.

Davis, G. E. a. S., **D. R.** (2005). "Endothelial extracellular matrix: biosynthesis, remodeling, and functions during vascular morphogenesis and neovessel stabilization." *Circ Res* **97**: 1093-107.

Davis, G. E. a. S., **D. R.** (2008). "Extracellular matrix mediates a molecular balance between vascular morphogenesis and regression." *Curr Opin Hematol* **15**: 197-203.

Davis, S., N. W. Gale, et al. (1994). "Ligands for EPH-related receptor tyrosine kinases that require membrane attachment or clustering for activity." Science **266**(5186): 816-819.

Delcroix, G. J. R., P. C. Schiller, et al. "Adult cell therapy for brain neuronal damages and the role of tissue engineering." Biomaterials **31**(8): 2105.

DeLong, S. A., A. S. Gobin, et al. (2005). "Covalent immobilization of RGDS on hydrogel surfaces to direct cell alignment and migration." Journal of Controlled Release **109**(1-3): 139.

Doubal, F. N., T. J. MacGillivray, et al. (2010). "Fractal analysis of retinal vessels suggests that a distinct vasculopathy causes lacunar stroke." Neurology **74**(14): 1102-1107.

Eddins, S. (2007). "Imclose." MATLAB Central.

Efron, B. (1979). "Bootstrap Methods: Another Look at the Jackknife." The Annals of Statistics **7**(1): 1.

Ellenberg, D., D. T. Azar, et al. "Novel aspects of corneal angiogenic and lymphangiogenic privilege." Progress in Retinal and Eye Research **29**(3): 208.

Ferrara, N. and R. S. Kerbel (2005). "Angiogenesis as a therapeutic target." Nature **438**(7070): 967.

Fishburn, C. S. (2008). "The pharmacology of PEGylation: Balancing PD with PK to generate novel therapeutics." Journal of Pharmaceutical Sciences **97**(10): 4167.

Fontanini G, B. D., Vignati S, Basolo F, Mussi A, Lucchi M, Chinè S, Angeletti CA, Harris AL, Bevilacqua G (1995). "Microvessel count Predicts metastatic disease and survival in non-small cell lung cancer." J Pathol **117**: 57-63.

Gaengel, K., G. Genove, et al. (2009). "Endothelial-Mural Cell Signaling in Vascular Development and Angiogenesis." Arterioscler Thromb Vasc Biol **29**(5): 630-638.

Gaudric, A., T. N'Guyen, et al. (1992). "Quantification of angiogenesis due to basic fibroblast growth factor in a modified rabbit corneal model." Ophthalmic Research **24**(3): 181.

Gilmore, S., R. Hofmann-Wellenhof, et al. (2009). "Lacunarity Analysis: A Promising Method for the Automated Assessment of Melanocytic Naevi and Melanoma." PLoS ONE **4**(10): e7449.

Glodbaum, M. (2010). Structured analysis of the Retina.

Gobin, A. S. a. W., J. L. ((2002)). "Cell migration through defined, synthetic ECM analogs." Faseb J **16**: 751- 3.

Goh, V., B. Sanghera, et al. (2009). "Assessment of the spatial pattern of colorectal tumour perfusion estimated at perfusion CT using two-dimensional fractal analysis." European Radiology **19**(6): 1358.

Gonzalez, A. L., A. S. Gobin, et al. (2004). "Integrin Interactions with Immobilized Peptides in Polyethylene Glycol Diacrylate Hydrogels." Tissue Engineering **10**(11-12): 1775-1786.

Gould, D. (2010). "Overlap Program." MATLAB Central.

Gould, D., Vadakkan, Tegy, Poche, Ross, Dickinson, Mary (2010). "Multifractal Analysis of Vessel Morphology and Remodelling." Microcirculation.

Gould, D., Vadakkan, Tegy, Poche, Ross, Dickinson, Mary (Submitted- In preparation). "Multifractal Analysis of Vessel Morphology and Remodelling." Microcirculation.

Gould, D. J., T. J. Vadakkan, et al. (2011). "Multifractal and lacunarity analysis of microvascular morphology and remodeling." Microcirculation **18**(2): 136-51.

Gould, D. J., T. J. Vadakkan, et al. (2010). "Multifractal and Lacunarity Analysis of Microvascular Morphology and Remodeling." Microcirculation **18**(2): 136.

Graham, W. (2010). "Organ Facts." United Network of Organ Sharing.

Grauslund, J., A. Green, et al. (2010). "Retinal Vascular Fractals and Microvascular and Macrovascular Complications in Type 1 Diabetes." Ophthalmology **In Press, Corrected Proof**.

Grayson, W. L., T. P. Martens, et al. (2009). "Biomimetic approach to tissue engineering." Seminars in Cell & Developmental Biology **20**(6): 665.

Greisler, H. P. (1996). "Growth factor release from vascular grafts." Journal of Controlled Release **39**(2-3): 267.

Griffith, L. G. and G. Naughton (2002). "Tissue Engineering--Current Challenges and Expanding Opportunities." Science **295**(5557): 1009-1014.

Gunn, J. W., S. D. Turner, et al. (2005). "Adhesive and mechanical properties of hydrogels influence neurite extension." J Biomed Mater Res A **72**(1): 91-7.

Haas, T. L. (2005). "Endothelial cell regulation of matrix metalloproteinases." Canadian Journal of Physiology and Pharmacology **83**(1): 1-7.

Hahn, M. S., MELISSA K. MCHALE,* EVA WANG, RACHAEL H. SCHMEDLEN, and JENNIFER L. WEST (2006). "Physiologic Pulsatile Flow Bioreactor Conditioning of Poly(ethylene glycol)-based Tissue Engineered Vascular Grafts." Annals of Biomedical Engineering, **Vol. 35**(No. 2): pp. 190-200.

Harris, D. C. (1998). "Nonlinear Least-Squares Curve Fitting with Microsoft Excel Solver." Journal of Chemical Education **75**(1): 119.

Heldin, C. H. and B. Westermark (1999). "Mechanism of action and in vivo role of platelet-derived growth factor." Physiol Rev **79**(4): 1283-316.

Herman, P., L. Kocsis, et al. (2001). "Fractal Branching Pattern in the Pial Vasculature in the Cat." J Cereb Blood Flow Metab **21**(6): 741.

Hibbs, R. G., G. E. Burch, et al. (1958). "The fine structure of the small blood vessels of normal human dermis and subcutis." American Heart Journal **56**(5): 662.

Hoganson, D. M., H. I. Pryor, II, et al. (2008). "Tissue Engineering and Organ Structure: A Vascularized Approach to Liver and Lung." Pediatric Research **63**(5): 520-526 10.1203/01.pdr.0000305879.38476.0c.

Horsfield, K. (1978). "Morphometry of the small pulmonary arteries in man." Circ Res **42**(5): 593-597.

Humphrey, J. D., K. H. J. Buschow, et al. (2001). Blood Vessels, Mechanical and Physical Properties of. Encyclopedia of Materials: Science and Technology. Oxford, Elsevier**:** 748.

Isner, J. M. and T. Asahara (1999). "Angiogenesis and vasculogenesis as therapeutic strategies for postnatal neovascularization." The Journal of Clinical Investigation **103**(9): 1231.

J.B. Bassingthwaighte, L. S. L., B.J. West (1994). Fractal Physiology. New York, NY, Oxford University.

Jackson, C. L. and M. A. Reidy (1993). "Basic fibroblast growth factor: its role in the control of smooth muscle cell migration." Am J Pathol **143**(4): 1024-31.

Jain, R. K. (2003). "Molecular regulation of vessel maturation." Nat Med **9**(6): 685.

Jain, R. K. (2005). "Normalization of tumor vasculature: an emerging concept in antiangiogenic therapy." Science **307**: 58 - 62.

Jain, R. K., P. Au, et al. (2005). "Engineering vascularized tissue." Nat Biotech **23**(7): 821.

Jain, R. K., K. Schlenger, et al. (1997). "Quantitative angiogenesis assays: Progress and problems." Nat Med **3**(11): 1203.

Kats, B. M. and V. V. Kutarov (1996). "Fractal Dimension of Polymer Sorbents." Langmuir **12**(11): 2762.

Kenyon, B. M., Voest, E. E., Chen, C. C., Flynn, E., Folkman, J. and D'Amato, R. J. (1996). "A model of angiogenesis in the mouse cornea." Invest Ophthalmol Vis Sci **37**: 1625-32.

Kim, K. J., B. Li, et al. (1993). "Inhibition of vascular endothelial growth factor-induced angiogenesis suppresses tumour growth in vivo." Nature **362**(6423): 841.

Kimelman, D. and M. Kirschner (1987). "Synergistic induction of mesoderm by FGF and TGF-[beta] and the identification of an mRNA coding for FGF in the early Xenopus embryo." Cell **51**: 869.

Kirbas C, Q., F. (2004). "A Review of Vessel Extraction Techniques and Algorithms." Computing Surveys **36**(2): 81-121.

Kovacic, J., Boehm, Manfred (2009). "Resident Vascular Progenitor Cells: an emerging role." Stem Cell Res. **2**(1): 2-15.

Kurz, H., & Sandau, K. ((1997)). "Modeling of blood vessel development - bifurcation pattern and hemodynamics, optimality and allometry." *Comments on Theoretical Biology* ***4***: 261-291.

Labianca, R., G. D. Beretta, et al. "Colon cancer." Critical Reviews in Oncology/Hematology **74**(2): 106.
Lam, N. S. N., De Cola, Lee (1993). Fractals in Geography. Englewood Cliffs, N.J, Prentice Hall.
Landini, G., P. I. Murray, et al. (1995). "Local connected fractal dimensions and lacunarity analyses of 60 degrees fluorescein angiograms." Invest. Ophthalmol. Vis. Sci. **36**(13): 2749-2755.
Lang, R. A. and J. M. Bishop (1993). "Macrophages are required for cell death and tissue remodeling in the developing mouse eye." Cell **74**(3): 453.
Langer, R. and J. P. Vacanti (1993). "Tissue engineering." Science **260**(5110): 920-926.
Langer, R. and J. P. Vacanti (1993). "Tissue Engineering." Science **260**(5110): 920.
Larina, I. V., Shen, W., Kelly, O. G., Hadjantonakis, A. K., Baron, M. H., & Dickinson, M. E. (2009). "A membrane associated mCherry fluorescent reporter line for studying vascular remodeling and cardiac function during murine embryonic development." *The Anatomical Record*(292): 333-341.
Laschke, M. W., Y. Harder, et al. (2006). "Angiogenesis in Tissue Engineering: Breathing Life into Constructed Tissue Substitutes." Tissue Engineering **12**(8): 2093-2104.
Lee, J. and H. E. Stanley (1988). "Phase Transition in the Multifractal Spectrum of Diffusion-Limited Aggregation." Physical Review Letters **61**(26): 2945.
Leslie-Barbick, J. E., J. J. Moon, et al. (2009). "Covalently-Immobilized Vascular Endothelial Growth Factor Promotes Endothelial Cell Tubulogenesis in Poly(ethylene glycol) Diacrylate Hydrogels." Journal of Biomaterials Science, Polymer Edition **20**: 1763.
Leslie-Barbick, J. E., J. J. Moon, et al. (2009). "Covalently-immobilized vascular endothelial growth factor promotes endothelial cell tubulogenesis in poly(ethylene glycol) diacrylate hydrogels." J Biomater Sci Polym Ed **20**(12): 1763-79.
Leslie-Barbick, J. E., J. E. Saik, et al. "The promotion of microvasculature formation in poly(ethylene glycol) diacrylate hydrogels by an immobilized VEGF-mimetic peptide." Biomaterials **32**(25): 5782.
Less, J. R., T. C. Skalak, et al. (1991). "Microvascular Architecture in a Mammary Carcinoma: Branching Patterns and Vessel Dimensions." Cancer Research **51**(1): 265-273.
Li, M., C. Liu, et al. "Mutant hypoxia inducible factor-1[alpha] improves angiogenesis and tissue perfusion in ischemic rabbit skeletal muscle." Microvascular Research **81**(1): 26.
Lin, K. Y., Maricevich, Marco, Nabeel Bardeesy, Ralph Weissleder, and Umar Mahmood (2008). "In Vivo Quantitative Microvasculature Phenotype Imaging of Healthy and Malignant Tissues Using a Fiber-Optic Confocal Laser Microprobe." Transl Oncol. **2**: 84-94.
Liu, C., Z. Xia, et al. (2007). "Design and Development of Three-Dimensional Scaffolds for Tissue Engineering." Chemical Engineering Research and Design **85**(7): 1051.
Liu, D., N. B. Wood, et al. (2009). "Computational Analysis of Oxygen Transport in the Retinal Arterial Network." Current Eye Research **34**(11): 945-956.
Lopes, R. and N. Betrouni (2009). "Fractal and multifractal analysis: A review." Medical Image Analysis **13**(4): 634-644.
Lucitti, J. L., E. A. V. Jones, et al. (2007). "Vascular remodeling of the mouse yolk sac requires hemodynamic force." Development **134**(18): 3317-3326.
Lutolf, M. P., J. L. Lauer-Fields, et al. (2003). "Synthetic matrix metalloproteinase-sensitive hydrogels for the conduction of tissue regeneration: Engineering cell-invasion characteristics." Proceedings of the National Academy of Sciences **100**(9): 5413-5418.
Mandelbrot, B. B. (1963). "the variation of certain speculative prices." J. of buisiness **36**: 394-419.
Mandelbrot, B. B. (1982). The Fractal Geometry of Nature. New York, Freeman.
Mann, B. K., A. S. Gobin, et al. (2001). "Smooth muscle cell growth in photopolymerized hydrogels with cell adhesive and proteolytically degradable domains: synthetic ECM analogs for tissue engineering." Biomaterials **22**(22): 3045.

Margolis, D. J., T. Crombleholme, et al. (2000). "Clinical Protocol: Phase I trial to evaluate the safety of H5.020CMV.PDGF-B for the treatment of a diabetic insensate foot ulcer." Wound Repair and Regeneration **8**: 480.

Mary, B. V., A. K. Patricia, et al. (2009). "VESGEN 2D: Automated, User-Interactive Software for Quantification and Mapping of Angiogenic and Lymphangiogenic Trees and Networks." The Anatomical Record: Advances in Integrative Anatomy and Evolutionary Biology **292**(3): 320-332.

Masters, B., Family, F., Platt, DE. (1989). "Fractal analysis of human retinal vessels." Biophys J. **55**(575a).

Masters, B. R. (2004). "Fractal Analysis of the Vascular Tree in the Human Retina." Annual Review of Biomedical Engineering **6**(1): 427-452.

Matsushita, M., M. Sano, et al. (1984). "Fractal Structures of Zinc Metal Leaves Grown by Electrodeposition." Physical Review Letters **53**(3): 286.

McKay, T. L., D. J. Gedeon, et al. (2008). "Selective Inhibition of Angiogenesis in Small Blood Vessels and Decrease in Vessel Diameter throughout the Vascular Tree by Triamcinolone Acetonide." Invest. Ophthalmol. Vis. Sci. **49**(3): 1184-1190.

Meakin, P., H. E. Stanley, et al. (1985). "Surfaces, interfaces, and screening of fractal structures." Physical Review A **32**(4): 2364.

Mellitzer, G., Q. Xu, et al. (2000). "Control of cell behaviour by signalling through Eph receptors and ephrins." Current Opinion in Neurobiology **10**(3): 400.

Meneveau, C. and K. R. Sreenivasan (1991). "The multifractal nature of turbulent energy dissipation." Journal of Fluid Mechanics Digital Archive **224**(-1): 429.

Mikos, A. S. H., Pannee Ochareon, Jennifer Elisseeff, Helen Lu, Rita Kandel (2006). "Engineering Complex Tissues." Tissue Engineering **12**(12): 3307.

Miller, J. S., C. J. Shen, et al. "Bioactive hydrogels made from step-growth derived PEG-peptide macromers." Biomaterials **31**(13): 3736.

Milne, B. T. (1991). "The utility of fractal geometry in landscape design." Landscape and Urban Planning **21**(1-2): 81.

Moisy, F. (2006). "Boxcount." MATLAB Central.

Montesano, R., M. S. Pepper, et al. (1990). "Increased proteolytic activity is responsible for the aberrant morphogenetic behavior of endothelial cells expressing the middle T oncogene." Cell **62**(3): 435.

Moon, J. J., S.-H. Lee, et al. (2006). "Synthetic Biomimetic Hydrogels Incorporated with Ephrin-A1 for Therapeutic Angiogenesis." Biomacromolecules **8**(1): 42.

Moon, J. J., S. H. Lee, et al. (2007). "Synthetic biomimetic hydrogels incorporated with ephrin-A1 for therapeutic angiogenesis." Biomacromolecules **8**(1): 42-9.

Moon, J. J., Ph.D., Mariah S. Hahn, Ph.D., Iris Kim, B.S., Barbara A. Nsiah, B.S., and Jennifer L. West, Ph.D. (2008). "Micropatterning of Poly(Ethylene Glycol) Diacrylate Hydrogels with Biomolecules to Regulate and Guide Endothelial Morphogenesis." TISSUE ENGINEERING: Part A **Volume 14**: 1-7.

Moon, J. J., J. E. Saik, et al. (2010). "Biomimetic hydrogels with pro-angiogenic properties." Biomaterials **31**(14): 3840.

Murray, C. D. ((1926)). "The physiological principle of minimum work: I. The vascular system and the cost of blood volume." *PNAS* ***12***: 207-214.

Muthukkaruppan VR, K. L., Auerbach R. (1982). " Tumor-induced neovascularization in the mouse eye." J Natl Cancer Inst. **69**(3): 699-708.

Nillesen, S. T. M., P. J. Geutjes, et al. (2007). "Increased angiogenesis and blood vessel maturation in acellular collagen-heparin scaffolds containing both FGF2 and VEGF." Biomaterials **28**(6): 1123.

Nimni, M. E. (1997). "Polypeptide growth factors: targeted delivery systems." Biomaterials **18**(18): 1201.

Nomi, M., H. Miyake, et al. (2006). "Role of growth factors and endothelial cells in therapeutic angiogenesis and tissue engineering." Curr Stem Cell Res Ther **1**(3): 333-43.

Omidi, Y., L. Campbell, et al. (2003). "Evaluation of the immortalised mouse brain capillary endothelial cell line, b.End3, as an in vitro blood-brain barrier model for drug uptake and transport studies." Brain Research **990**(1-2): 95.

Ori, A., M. C. Wilkinson, et al. (2008). "The heparanome and regulation of cell function: structures, functions and challenges." Front. Biosci. **13**: 4309.

Parsons-Wingerter, P., K. E. Elliott, et al. (2000). "Fibroblast Growth Factor-2 Selectively Stimulates Angiogenesis of Small Vessels in Arterial Tree." Arterioscler Thromb Vasc Biol **20**(5): 1250-1256.

Pasquale, E. B. (2008). "Eph-Ephrin Bidirectional Signaling in Physiology and Disease." Cell **133**(1): 38.

Penn, J. S. and C. A. Gay (1992). "Computerized digital image analysis of retinal vessel density: Application to normoxic and hyperoxic rearing of the newborn rat." Experimental Eye Research **54**(3): 329.

Plotnick, R. E., R. H. Gardner, et al. (1996). "Lacunarity analysis: A general technique for the analysis of spatial patterns." Physical Review E **53**(5): 5461.

Poche, R. A., I. V. Larina, et al. (2009). "The Flk1-myr:mCherry mouse as a useful reporter to characterize multiple aspects of ocular blood vessel development and disease." Dev Dyn.

Poche, R. A., J. E. Saik, et al. "The mouse cornea as a transplantation site for live imaging of engineered tissue constructs." Cold Spring Harb Protoc **2010**(4): pdb prot5416.

Poche, R. A., J. E. Saik, et al. (2010). "The mouse cornea as a transplantation site for live imaging of engineered tissue constructs." Cold Spring Harb Protoc **2010**(4): pdb prot5416.

Poche, R. A., J. E. Saik, et al. (2010). "The Mouse Cornea as a Transplantation Site for Live Imaging of Engineered Tissue Constructs." Cold Spring Harb Protoc **2010**(4): pdb.prot5416-.

Poché, R. A. L., Irina V. Scott, Melissa L. Saik, Jennifer E. West, Jennifer, L. Dickinson, Mary, E. (2009). "The Flk1-myr:mCherry mouse as a useful reporter to characterize multiple aspects of ocular blood vessel development and disease." Developmental Dynamics **238**(9): 2318-2326.

Posadas, A. N. D., D. Gimenez, et al. (2001). "Multifractal Characterization of Soil Particle-Size Distributions." Soil Sci Soc Am J **65**(5): 1361-1367.

Posadas, A. N. D., D. Gimenez, et al. (2003). "Multifractal Characterization of Soil Pore Systems." Soil Sci Soc Am J **67**(5): 1361-1369.

Rasband, W. (2010). Image J plugin, NIH.

Roberts, M. J., M. D. Bentley, et al. (2002). "Chemistry for peptide and protein PEGylation." Advanced Drug Delivery Reviews **54**(4): 459.

Rogers, M. S., Birsner, A. E. and D'Amato, R. J. (2007). "The mouse cornea micropocket angiogenesis assay." Nat Protoc **2**: 2545-50.

Rothermel, T. A., Engelhardt, B. & Sheibani, N. (2005). "Polyoma virus middle-T-transformed PECAM-1 deficient mouse brain endothelial cells proliferate rapidly in culture and form hemangiomas in mice." J Cell Physiol **202**: 230-239.

Sabo, E., A. Boltenko, et al. (2001). "Microscopic Analysis and Significance of Vascular Architectural Complexity in Renal Cell Carcinoma." Clinical Cancer Research **7**(3): 533-537.

Saik, J. E., D. J. Gould, et al. "Biomimetic Hydrogels with Immobilized EphrinA1 for Therapeutic Angiogenesis." Biomacromolecules **12**(7): 2715.

Saik, J. E., D. J. Gould, et al. (2011). "Covalently immobilized platelet-derived growth factor-BB promotes angiogenesis in biomimetic poly(ethylene glycol) hydrogels." Acta Biomater **7**(1): 133-43.

Sandau, K. and H. Kurz (1997). "Measuring fractal dimension and complexity - an alternative approach with an application." J Microsc **186**: 164 - 176.

Schroeder-Tefft, J. A., H. Bentz, et al. (1997). "Collagen and heparin matrices for growth factor delivery." Journal of Controlled Release **48**(1): 29.

Sharma, S., M. C. Sharma, et al. (2005). "Morphology of angiogenesis in human cancer: a conceptual overview, histoprognostic perspective and significance of neoangiogenesis." Histopathology **46**(5): 481.

Silva, E. A. and D. J. Mooney "Effects of VEGF temporal and spatial presentation on angiogenesis." Biomaterials **31**(6): 1235-41.

Smith, H. W. (1951). The kidney: structure and function in health and disease, Oxford University Press.

Sng, C. C. A., C. Sabanayagam, et al. (2010). "Fractal analysis of the retinal vasculature and chronic kidney disease." Nephrol. Dial. Transplant.: gfq007.

Soo-Hong, L., S. M. Jordan, et al. (2005). "Proteolytically Degradable Hydrogels with a Fluorogenic Substrate for Studies of Cellular Proteolytic Activity and Migration." Biotechnology Progress **21**(6): 1736-1741.

Stenmark, K. R. and R. P. Mecham (1997). "CELLULAR AND MOLECULAR MECHANISMS OF PULMONARY VASCULAR REMODELING." Annual Review of Physiology **59**(1): 89-144.

Stephan, B., S. Olivera, et al. (2008). "Growth factors and cytokines in wound healing." Wound Repair and Regeneration **16**(5): 585-601.

Stosic, Tatijana, et al. (2006). Multifractal analysis of human retinal vessels. New York, NY, USA, Institute of Electrical and Electronics Engineers.

Streilein, J. W. (2003). "Ocular immune privilege: the eye takes a dim but practical view of immunity and inflammation." J Leukoc Biol **74**(2): 179-185.

Tayalia, P. and D. J. Mooney (2009). "Controlled growth factor delivery for tissue engineering." Adv Mater **21**(32-33): 3269-85.

Tolle, C. R., T. R. McJunkin, et al. (2008). "An efficient implementation of the gliding box lacunarity algorithm." Physica D: Nonlinear Phenomena **237**(3): 306.

Tong, R. T., Y. Boucher, et al. (2004). "Vascular Normalization by Vascular Endothelial Growth Factor Receptor 2 Blockade Induces a Pressure Gradient Across the Vasculature and Improves Drug Penetration in Tumors." Cancer Research **64**(11): 3731-3736.

Tong, S. and F. Yuan (2008). "Dose response of angiogenesis to basic fibroblast growth factor in rat corneal pocket assay: I. Experimental characterizations." Microvascular Research **75**(1): 10.

Turner, N. and R. Grose "Fibroblast growth factor signalling: from development to cancer." Nat Rev Cancer **10**(2): 116.

Uzzan, B., P. Nicolas, et al. (2004). "Microvessel Density as a Prognostic Factor in Women with Breast Cancer." Cancer Research **64**(9): 2941-2955.

Vacanti, J. "Tissue engineering and regenerative medicine: from first principles to state of the art." Journal of Pediatric Surgery **45**(2): 291.

Vacanti, J., C. A. Vacanti, et al. (2007). The history and scope of tissue engineering. Principles of Tissue Engineering (Third Edition). Burlington, Academic Press**:** 3.

Vadakkan, T. (2009). "Lacunarity of a binary image." MATLAB Central.

Vadakkan, T. (2009). "Multifractal spectrum of a binary image." MATLAB Central.

Veronese, F. M. (2001). "Peptide and protein PEGylation: a review of problems and solutions." Biomaterials **22**(5): 405.

Vicsek, T. and et al. (1990). "Multifractal Geometry of Diffusion-Limited Aggregates." EPL (Europhysics Letters) **12**(3): 217.

W. E. Higgins, W. J. T. S., E. L. Ritman, Y. Kim, and F. A. Spelman, (1989). " "Automatic extraction of the arterial tree from 3-d angiograms"." in IEEE Conf. Eng. in Medicine and Bio.**, vol. 2**: pp. 563-564.

Wang, Z. Z., P. Au, et al. (2007). "Endothelial cells derived from human embryonic stem cells form durable blood vessels in vivo." Nat Biotech **25**(3): 317.

Welm, B. E. (2002). "Inducible dimerization of FGFR1: development of a mouse model to analyze progressive transformation of the mammary gland." J. Cell Biol. **157**: 703.

Werner, S. and R. Grose (2003). "Regulation of wound healing by growth factors and cytokines." Physiol. Rev. **83**: 835.

West, G. B., J. H. Brown, et al. (1997). "A General Model for the Origin of Allometric Scaling Laws in Biology." Science **276**(5309): 122-126.

West, J. L. (2006). *Bioactive Hydrogels: Mimicking the ECM with Synthetic Materials. Scaffolds in Tissue Engineering.* Boca Raton, Florida, Taylor Francis Group.

West, J. L. and J. A. Hubbell (1998). "Polymeric Biomaterials with Degradation Sites for Proteases Involved in Cell Migration." Macromolecules **32**(1): 241.

West, J. L. and J. A. Hubbell (1999). "Polymeric biomaterials with degradation sites for proteases involved in cell migration." Macromolecules **32**: 241-244.

Wiedemann, M. and B. Trueb (2000). "Characterization of a novel protein (FGFRL1) from human cartilage related to FGF receptors." Genomics **69**: 275.

Wolf, M. (1996). "Multifractility of snowflakes." Fractals **4**(4): 477-493.

Wu, X., N. Kathuria, et al. (2008). "Quantitative analysis of the microvasculature growing in the fibrin interface between a skin graft and the recipient site." Microvascular Research **75**(1): 119.

Xu, Y., H. Ji, et al. (2009). "Viewpoint Invariant Texture Description Using Fractal Analysis." International Journal of Computer Vision **83**(1): 85.

Yang, J., L. X. Yu, et al. (2010). "Comparative structural and hemodynamic analysis of vascular trees." Am J Physiol Heart Circ Physiol **298**(4): H1249-1259.

Yano, S. "Antiangiogenic therapies for malignant pleural mesothelioma." Frontiers in bioscience **16**: 740.

Yao, C., M. Roderfeld, et al. (2006). "The impact of proteinase-induced matrix degradation on the release of VEGF from heparinized collagen matrices." Biomaterials **27**(8): 1608-1630.

Zaia, A., R. Eleonori, et al. (2006). "MR Imaging and Osteoporosis: Fractal Lacunarity Analysis of Trabecular Bone." Information Technology in Biomedicine, IEEE Transactions on **10**(3): 484.

Zhang, G., X. Wang, et al. (2006). "A PEGylated fibrin patch for mesenchymal stem cell delivery." Tissue Eng **12**(1): 9-19.

Zhu, J. "Bioactive modification of poly(ethylene glycol) hydrogels for tissue engineering." Biomaterials **31**(17): 4639.

Zhu, M., M. C. Madigan, et al. (2000). "The Human Hyaloid System: Cell Death and Vascular Regression." Experimental Eye Research **70**(6): 767.

Zisch, A. H., M. P. Lutolf, et al. (2003). "Cell-demanded release of VEGF from synthetic, biointeractive cell ingrowth matrices for vascularized tissue growth." FASEB J. **17**(15): 2260-2262.

Zisch, A. H., M. P. Lutolf, et al. "Biopolymeric delivery matrices for angiogenic growth factors." Cardiovascular Pathology **12**(6): 295.

Zisch, A. H., M. P. Lutolf, et al. (2003). "Biopolymeric delivery matrices for angiogenic growth factors." Cardiovascular Pathology **12**(6): 295.